

Flow and Deposition of Colloidal Suspensions through Porous Media and on Model Surfaces

by

Hafez Balavi

A thesis submitted in partial fulfilment of the requirements for the degree of

Doctor of Philosophy

Department of Civil and Environmental Engineering  
University of Alberta

© Hafez Balavi, 2017

## Abstract

Operations with drilling fluids require multiple performance requirements. Among those, fluid loss issue is a very severe problem that is encountered in many drilling operations. Rheological and transport properties of drilling muds in porous media control the fluid loss behavior in reservoir formations. Additionally, some kinds of drilling fluids especially those formulated with hydrocarbons, oils, etc. are strongly contaminating. Therefore, it is essential to introduce drilling fluids of very low or negligible contaminating potential for sustainable development in oilfields. In the formulation of such muds it is becoming increasingly common to use cellulose-based materials as additives, due to their low cost, rheological properties, and scant environmental impact. Cellulose-based materials have been used to control water loss for many years. In addition, the rheological behavior of drilling muds can be optimized with cellulose-based polymers of different chain lengths and properties. Cellulose nanocrystal particles (CNC) and carboxymethyl cellulose polymer (CMC) are typical examples of such materials. This research is about the preparation of water-based drilling fluid formulations enhanced by CNC and CMC, selecting optimal preparation for a field test at an actual drilling site, and investigation of cross-flow filtration mechanisms of cellulose-formulated bentonite suspensions. Filtration and rheological properties of cellulose-bentonite suspensions were investigated and CNC/CMC functions in bentonite particles deposition and suspension stability were highlighted by dynamic filtration tests, flow stability of the drilling fluid and rheological experiments, colloidal deposition studies and assessing and characterizing filter cake properties.

**Keywords:** drilling fluids, porous media, fluid loss, cellulose nanocrystals, cross-flow filtration, bentonite, colloidal deposition.

## **Dedication**

*To my beloved parents,*

*Lovely wife,*

*And my supportive supervisor*

*Without whom none of my success would be possible*

# Acknowledgements

I would like to express the deepest appreciation to my lovely parents for their infinite support and unlimited love especially to my mother for her spiritual support throughout my life.

I am greatly thankful to my supervisor, Professor Yaman Boluk, for his endless sincere support, patience, motivation, enthusiasm and immense knowledge. He continually and convincingly conveyed a spirit of adventure through my personal and professional life. Without his guidance and persistent help this dissertation would not have been possible.

I would like to thank my committee members, Dr. Zaher Hashisho, Dr. Rick Chalaturnyk, and Dr. Cagri Ayrançi for their suggestions and recommendations. I am also grateful to have Professor John Simonsen from Oregon State University for serving as my external committee member.

I am deeply thankful to ArboraNano, the Canadian Forest NanoProducts Network and Network of Centres of Excellence (NCE), Alberta Innovates – Bio Solutions, and Alberta Innovates Technology Future for funding and supporting my project. In addition, I am grateful to National Institute for Nanotechnology (NINT) for providing me lab equipment and facilities to accomplish my project objectives. Materials supply by Marquis Alliance – SECURE Energy Systems is highly acknowledged.

I would like to appreciate all my colleagues and research group team for their cooperation, help and positive comments through my research.

The last but not least, I would like to express my special thank-you to my lovely wife, Behnaz, for her endless patience, support and encouragement through this journey.

# Table of Contents

1. Introduction .....	1
1.1. Drilling fluids functions, compositions, and issues .....	1
1.2. Fluid loss issue in drilling operations .....	3
1.3. Filtration of drilling fluids formulated with cellulose nanocrystals .....	5
2. Background and literature review .....	11
2.1. Filtration .....	11
2.1.1. Filtration theory.....	14
2.1.2. Static vs. dynamic filtration .....	20
2.1.3. Mathematical models in cross-flow filtration .....	22
2.2. Flow in porous media.....	26
2.2.1. Basic forces involved in flow in porous media.....	27
2.2.2. Porosity .....	27
2.2.3. Darcy's law .....	28
2.2.4. Kozeny's equation.....	29
2.2.5. Modifications on Kozeny's equation .....	31
2.2.6. Flow behaviour of polymer-based fluids in porous media.....	34
2.3. Rheology of mud suspensions.....	37
2.3.1. Laminar flow of Newtonian fluids.....	38
2.3.2. Bingham plastic model.....	39
2.3.3. Pseudoplastic fluids.....	40
2.3.4. The generalized power law .....	40
2.3.5. Rheology of bentonite clay suspension.....	41

2.3.6.	Rheology of CMC suspension .....	42
2.3.7.	Rheology of bentonite-CMC suspension .....	43
2.3.8.	Rheology of CNC suspensions .....	45
3.	Materials and methods.....	46
3.1.	Materials.....	46
3.1.1.	Clay minerals .....	46
3.1.2.	Carboxymethyl cellulose (CMC).....	47
3.1.3.	Cellulose nanocrystals (CNC).....	47
3.1.4.	Sample preparation.....	48
3.2.	Rheological experiments .....	50
3.3.	Dynamic filtration experiments.....	51
3.4.	Quartz crystal microbalance with dissipation (QCM-D) experiments ...	55
3.5.	Characterization methods .....	59
4.	Dynamic filtration properties .....	60
4.1.	Flow regime between the drilling bit and porous media.....	61
4.2.	Flow through porous media .....	63
4.3.	Pressure gradient (differential pressure) effect in fluid loss .....	67
4.4.	Temperature effect in fluid loss .....	71
4.5.	Filter pore size effect in fluid loss.....	72
4.6.	Drilling bit speed (shear rate) effect in fluid loss.....	74
4.7.	Mud formulation (CNC/CMC) effect in fluid loss .....	75
4.8.	Governing filtration mechanisms .....	77
4.9.	Best mathematical model to fit fluid loss data.....	81
4.10.	CNC effect in comparison to other commonly used additives .....	85

4.11. Summary .....	86
5. Rheology of water-based drilling muds .....	87
5.1. Rheology of CNC suspensions.....	87
5.2. Rheology of CMC polymer suspensions .....	90
5.2.1. Molecular weight calculation for CMC suspension.....	91
5.2.2. Rheological properties of CMC solutions.....	92
5.3. Rheology of clay suspensions .....	94
5.4. Rheology of CNC/CMC-rich drilling mud suspensions.....	99
5.4.1. Effect of cellulose nanocrystals (CNC).....	100
5.4.2. Effect of carboxymethyl cellulose (CMC) polymer.....	104
5.4.3. Rheology of drilling mud containing both CMC and CNC .....	106
5.5. Best rheological models for cellulose-based drilling mud.....	112
5.6. Summary .....	114
6. Particle deposition onto model surfaces: A microscopic approach .....	116
6.1. Experimental set-up for bentonite – CNC particles system.....	122
6.2. Particle deposition onto uncoated quartz sensor (similarly charged particles and collector).....	124
6.2.1. Similarly charged particles and collectors interactions.....	124
6.2.2. QCM-D experimental data.....	127
6.2.3. Effect of CNC particles on clay particles deposition .....	129
6.3. Particle deposition onto coated quartz sensor (oppositely charged particles and collector).....	132
6.3.1. Oppositely charged particles and collectors interactions .....	132
6.3.2. QCM-D experimental data.....	133

6.3.3.	Effect of CNC particles on clay particles deposition.....	137
6.3.4.	Effect of surface potentials and ionic strength on deposition of colloidal particles	141
6.4.	Summary .....	141
7.	Morphology of filter cake and structure analysis.....	142
7.1.	The origin of fibrous structure in dried filter cakes .....	142
7.2.	Elemental analysis of dried cake filters and filtrate suspension .....	145
7.3.	Summary .....	147
8.	Conclusions and recommendations for future work .....	149
	References.....	155
	Appendix A: Cross-flow and porous media calculations .....	164
	Cross-flow calculations in concentric cylinders geometry.....	164
	Taylor number for experimental data (FANN90 device) .....	164
	Taylor number for industrial data (Example) .....	164
	Porous media calculations .....	165
	Appendix B: CMC characterization via intrinsic viscosity .....	167
	Appendix C: Sensor surface coverage calculations.....	168
	Uncoated silica surface and bentonite particles coverage .....	168
	Uncoated silica surface and bentonite + CNC particles coverage .....	168
	Coated silica surface and bentonite particles coverage .....	169
	Coated silica surface and CNC particles coverage.....	169
	Coated silica surface and bentonite + CNC particles coverage .....	169

## List of Tables

<b>Table 2.1. Empirical values for different retention mechanisms.....</b>	<b>15</b>
<b>Table 2.2. Experimental/computational Kozeny constant values [36] .....</b>	<b>30</b>
<b>Table 2.3. Cross model constants of CMC suspensions [46] .....</b>	<b>43</b>
<b>Table 2.4. Rheological parameters of Oswald model for bentonite-CMC suspension [45] .....</b>	<b>44</b>
<b>Table 3.1. Filter core(s) specifications .....</b>	<b>52</b>
<b>Table 3.2. HPHT Fann 90 Dynamic Filtration Apparatus Specifications .....</b>	<b>53</b>
<b>Table 3.3. Dynamic Filtration Experimental Condition.....</b>	<b>54</b>
<b>Table 3.4. QCM-D instrument specifications .....</b>	<b>57</b>
<b>Table 4.1. Flow regime parameters for concentric cylinders geometry.....</b>	<b>61</b>
<b>Table 4.2. Practical specifications for flow regime calculations in drilling operation.....</b>	<b>62</b>
<b>Table 4.3. Porous media specifications and results.....</b>	<b>65</b>
<b>Table 4.4. Parameters for flow of polymer-based fluids in porous media.....</b>	<b>67</b>
<b>Table 4.5. Filtration rate data for different differential pressures.....</b>	<b>69</b>
<b>Table 4.6. Average filtration rates for different temperatures .....</b>	<b>71</b>
<b>Table 4.7. Filtration rate data for different filter porosities .....</b>	<b>73</b>
<b>Table 4.8. Filtration rate values for different shear rates .....</b>	<b>75</b>
<b>Table 4.9. Dynamic Filtration data for different mud formulations.....</b>	<b>76</b>
<b>Table 4.10. Filtrate volume loss modeling parameters at different differential pressures .....</b>	<b>82</b>
<b>Table 4.11. CNC performance in fluid loss control in comparison to other nanoparticles .....</b>	<b>85</b>
<b>Table 5.1. Viscosity values for bentonite clay suspensions at different shear rates and mud concentrations.....</b>	<b>98</b>
<b>Table 5.2. Viscosity values for suspensions including CNC at different shear rates .....</b>	<b>100</b>
<b>Table 5.3. Anticipation of interaction mechanisms based on saturated polymer concentration .....</b>	<b>106</b>
<b>Table 5.4. Rheological data for different mud formulations.....</b>	<b>112</b>
<b>Table 6.1. QCM-D experimental parameters .....</b>	<b>123</b>

<b>Table 6.2. DLVO parameters for Bentonite-CNC-Silica system .....</b>	<b>125</b>
<b>Table 6.3. Deposition of bentonite/CNC particles on uncoated silica surface .....</b>	<b>130</b>
<b>Table 6.4. Particle deposition studies for oppositely charged particles and collector ...</b>	<b>136</b>
<b>Table 7.1. Inductively Coupled Plasma (ICP) elemental analysis results.....</b>	<b>146</b>

# List of Figures

Figure 1.1. Schematic pattern of fluid loss issue in drilling operation .....	3
Figure 1.2. Methodology flowchart.....	10
Figure 2.1. A schematic of typical filtration process.....	11
Figure 2.2. Dead-end vs. cross-flow filtration.....	13
Figure 2.3. Filtration data and regression to find filter and cake resistances .....	17
Figure 2.4. A schematic depiction of cake layer thickness and the flux in equilibrium and non-equilibrium regions [8].....	20
Figure 2.5. Schematic of formation invasion by mud particles [16] .....	21
Figure 2.6. System geometry .....	23
Figure 2.7. Taylor vortices in concentric cylinders geometry [18] .....	25
Figure 2.8. Kozeny model .....	31
Figure 2.9. Schematic diagram of pore model.....	36
Figure 2.10. Schematic illustration of laminar flow of a Newtonian fluid.....	38
Figure 2.11. Schematic of different rheological models.....	39
Figure 3.1. Carboxymethyl cellulose (CMC) structure .....	47
Figure 3.2. SEM (a) and TEM (b) images of CNC particles [55] .....	48
Figure 3.3. Materials dispersion in water before final mixing.....	49
Figure 3.4. Drilling fluid suspension.....	49
Figure 3.5. (a) TA Rheology instrument-model AR-G2, (b) Cone & plate geometry .....	51
Figure 3.6. FANN 90 Dynamic Filtration apparatus .....	52
Figure 3.7. Schematic of dynamic filtration apparatus .....	55
Figure 3.8. Q-Sense E4 instrument.....	56
Figure 3.9. Parallel-plate geometry .....	57
Figure 4.1. A typical casing design and drilling specifications [63].....	63
Figure 4.2. Schematic of dynamic filtration apparatus .....	64
Figure 4.3. Darcy calculations flowchart .....	66
Figure 4.4. Total volume loss in dynamic filtration for different differential pressures. 68	
Figure 4.5. Permeate flux as a function of differential pressure for shear rate = $10 \text{ s}^{-1}$ ..	70
Figure 4.6. Permeate flux as a function of differential pressure for shear rate = $100 \text{ s}^{-1}$	70

<b>Figure 4.7. Dynamic filtration data for different temperatures .....</b>	<b>72</b>
<b>Figure 4.8. Total volume loss in dynamic filtration for different filter porosities .....</b>	<b>73</b>
<b>Figure 4.9. Total volume loss during dynamic filtration for different shear rates .....</b>	<b>74</b>
<b>Figure 4.10. Filtration rate during dynamic filtration for different shear rates.....</b>	<b>75</b>
<b>Figure 4.11. Dynamic filtration data for clay w/o additives.....</b>	<b>77</b>
<b>Figure 4.12. Filtration rate inverse vs. volume loss per unit area for shear rate <math>10 \text{ s}^{-1}</math> ...</b>	<b>78</b>
<b>Figure 4.13. Filtration rate inverse vs. time for shear rate <math>10 \text{ s}^{-1}</math>.....</b>	<b>78</b>
<b>Figure 4.14. Filtration rate inverse vs. volume loss per unit area for shear rate <math>100 \text{ s}^{-1}</math> .</b>	<b>79</b>
<b>Figure 4.15. Filtration rate inverse vs. time for shear rate <math>100 \text{ s}^{-1}</math>.....</b>	<b>79</b>
<b>Figure 4.16. Filtration rate inverse vs. volume loss for different filter pore sizes.....</b>	<b>80</b>
<b>Figure 4.17. Filtration rate inverse vs. time for different filter pore sizes.....</b>	<b>81</b>
<b>Figure 4.18. Fluid loss data at (a,b) 0.7 MPa, (c,d) 1.0 MPa, and (e,f) 1.7 MPa differential pressure .....</b>	<b>84</b>
<b>Figure 5.1. Rheological behaviour of CNC suspensions with DS = 0.85% at different concentrations [71] .....</b>	<b>88</b>
<b>Figure 5.2. Viscosity vs. shear rate of CNC dispersions at various concentrations without electrolyte addition [53] .....</b>	<b>89</b>
<b>Figure 5.3. Relative viscosity of CNC suspension vs. volume fraction (legends: NaCl concentrations) [53].....</b>	<b>90</b>
<b>Figure 5.4. Viscosity vs. shear rate for different CMC solution concentrations (No salt)93</b>	
<b>Figure 5.5. Relative zero-shear viscosity of CMC suspensions as a function of volume fraction. The dashed lines are guides for the eye. ....</b>	<b>94</b>
<b>Figure 5.6. Rheological behaviour of bentonite suspensions with different concentrations .....</b>	<b>96</b>
<b>Figure 5.7. Bentonite suspension viscosity as a function of concentration. ....</b>	<b>97</b>
<b>The dashed lines are guides for the eye.....</b>	<b>97</b>
<b>Figure 5.8. Low shear viscosity values for bentonite suspensions at shear rate = <math>0.1 \text{ s}^{-1}</math>. 98</b>	
<b>Figure 5.9. Potential mechanisms for different mud formulations .....</b>	<b>99</b>
<b>Figure 5.10. Rheological behaviour of bentonite suspensions containing 1% CNC .....</b>	<b>101</b>
<b>Figure 5.11. Low shear viscosity values for CNC enhanced bentonite suspensions at shear rate = <math>0.1 \text{ s}^{-1}</math> .....</b>	<b>101</b>

<b>Figure 5.12. Effect of 1% CNC addition in rheological behaviour of clay suspensions at shear rate = 0.1 s<sup>-1</sup> .....</b>	<b>102</b>
<b>Figure 5.13. Effect of CNC addition in rheological behaviour of bentonite suspensions at different volume fractions .....</b>	<b>103</b>
<b>Figure 5.14. Bentonite - CNC depletion interaction.....</b>	<b>103</b>
<b>Figure 5.15. Bridging mechanism between bentonite platelets and CMC polymer chains .....</b>	<b>105</b>
<b>Figure 5.16. Depletion mechanism between bentonite platelets and CMC polymer chains .....</b>	<b>105</b>
<b>Figure 5.17. Viscosity vs. shear rate for different suspensions .....</b>	<b>107</b>
<b>Figure 5.18. Aggregation of bentonite platelets by CNC-CMC, CNC-bentonite, and CMC-bentonite depletion .....</b>	<b>108</b>
<b>Figure 5.19. Aggregation of bentonite platelets by CNC-CMC, and CNC-bentonite depletion, and CMC-bentonite bridging.....</b>	<b>108</b>
<b>Figure 5.20. Synergistic effect of CMC/CNC addition to bentonite suspension.....</b>	<b>110</b>
<b>Figure 5.21. Schematic overview for different mechanisms colloids - polymer suspensions [84] .....</b>	<b>111</b>
<b>Figure 5.22. Herschel - Bulkley schematic model.....</b>	<b>113</b>
<b>Figure 5.23. Herschel - Bulkley rheological behaviour of mud suspensions .....</b>	<b>114</b>
<b>Figure 6.1. The schematic relationship between microscopic and macroscopic studies of cake formation .....</b>	<b>116</b>
<b>Figure 6.2. Schematic of a suspension containing spherical particles of different radii interacting with a collector surface [1].....</b>	<b>117</b>
<b>Figure 6.3. 2-D parallel-plate channel; large and small spheres represent bentonite and CNC particles, respectively .....</b>	<b>119</b>
<b>Figure 6.4. Interaction potentials between bentonite/CNC particles and uncoated quartz surface .....</b>	<b>127</b>
<b>Figure 6.5. Deposition of similarly charged clay particles on uncoated silica surface (The line is guide for the eye.....</b>	<b>128</b>
<b>Figure 6.6. Effect of CNC on deposition of similarly charged clay particles on uncoated silica surface (The lines are guide for the eye).....</b>	<b>129</b>

<b>Figure 6.7. Initial deposition rates for bentonite particles with and without CNC particles .....</b>	<b>131</b>
<b>Figure 6.8. Interaction potentials between bentonite/CNC particles and PEI-coated silica surface .....</b>	<b>133</b>
<b>Figure 6.9. Particle mass deposition on PEI-coated silica surface.....</b>	<b>135</b>
<b>Figure 6.10. Initial deposition rates for oppositely charged particles and collector .....</b>	<b>136</b>
<b>Figure 6.11. Schematic representation of adsorbed polyelectrolyte (a) on the particle; (b) on a collector surface [103].....</b>	<b>139</b>
<b>Figure 6.12. (a) Progressive and (b) steady-state regions of deposition .....</b>	<b>140</b>
<b>Figure 7.1. SEM images of filter cake .....</b>	<b>144</b>
<b>Figure 7.2. EDX elemental analysis for filter cake.....</b>	<b>145</b>
<b>Figure 7.3. The shear forces in A develop the bentonite particle into the fiber in B .....</b>	<b>146</b>
<b>Figure 7.4. Rope-like structure in clay due to shear force effect .....</b>	<b>147</b>

# **1. Introduction**

Drilling fluids and their properties impose a considerable effect on the completion of an oil-well and its relevant costs. The cost of the drilling mud is relatively small, but how to select the right fluid and maintain the right properties while drilling will completely influence the total well costs. For example, the number of rig days needed to drill depends significantly on the penetration rate of the bit. It also depends on the prevention of delays caused by several issues such as caving shales, stuck drilling pipe, fluid loss, etc., all of which are affected by the composition and properties of drilling fluid [1]. The US Energy Information Administration (EIA) performed a study of upstream drilling and production costs released in March 2016. Their report assessed capital and operating costs associated with drilling, completing, and operating wells and facilities. Based on their report, Rig and drilling fluids costs make up 15% of total costs. In addition, fracturing pumps and equipment costs make up 24% of total costs. Within onshore basins drilling comprises about 30 – 40% of total well costs along with 55 – 70% for completion, and 7 – 8% for facilities and operation expenses [2]. Another well cost study carried out in 2015 by Petroleum Services Association of Canada (PSAC) reveals considerable cost assumptions associated with drilling and completion operations [3]. In addition to all of the aforementioned costs, the drilling fluid affects formation evaluation and the consequent productivity of the well. Therefore, the selection of a workable drilling fluid the daily maintenance of its properties is the great concern of not only the mud engineer, but also of the drilling supervisor, the drilling chief, and drilling, logging and production engineers. It is crucial to understand some basic principles associated with choosing a suitable composition for drilling fluids as well as controlling their flow properties while drilling.

## **1.1. Drilling fluids functions, compositions, and issues**

Drilling fluids are widely used in oil-well operations to perform several functions such as:

- Removing and carrying cuttings from below the drill bit,
- Transporting the cuttings up the annulus and permitting their separation at the surface,
- Reducing friction between the drilling string and the hole sides,
- Cooling, cleaning, and lubricating the drill bit,
- Maintaining the stability of the borehole,
- Preventing the fluids invasion into permeable rocks and minimizing formation damage, and
- Forming a thin, low permeable filter cake and sealing permeable formations to control fluid loss.

Drilling fluids can be categorized according to their base:

- Water – base fluids, when solid particles are suspended in water or brine.
- Oil – base fluids, when solid particles are suspended in oil.
- Gas fluids, when drill cuttings are removed by a high-velocity stream of air or natural gas.

Water – base muds consist of clays and some organic additives in order to provide the required rheological and filtration properties. Some weighing agents such as barite could also be added to increase the density of the mud. In the interest of well safety, there is a natural trend to keep the mud density above that actually required to control the formation fluids, but it has some disadvantages. First of all, excessive mud density may increase the borehole pressure and causes induced fracturing. In this scenario, mud is lost into the formed fracture. In addition, excessive mud densities may have an impact on drilling rate that may lead to high overbalance pressure and increases the risk of sticking the drill pipe. Finally, it increases the mud cost not only by the initial cost of the barite, but also by the increased cost of maintaining suitable flow properties due to increase in viscosity [1].

In addition to the issues associated with mud density, the flow properties of the drilling fluid play a significant role in the successful progress of the drilling operation. They are mainly responsible for removal of the drill cuttings and transporting them up the annulus. The flow behaviour of drilling fluids is controlled by the flow regimes and pressure – velocity

relationships. This behaviour is could be measured and investigated by analyzing the rheological and filtration properties of the drilling fluid. Unacceptable flow performance may lead to such serious issues as bridging the hole, unsatisfactory transporting the drill cuttings from the bottom of the hole, reduced drilling rate, stuck pipe, and fluid loss.

## 1.2. Fluid loss issue in drilling operations

Fluid loss during drilling operation has been one of the great concerns through decades. Figure 1.1 shows a schematic pattern of drilling fluid loss in operation. Loss of circulation is defined as the uncontrolled flow of drilling mud into a formation. It imposes cost increase to the whole drilling operation as well as environmental side effects to the formation [4-7]. It has been estimated to cost the drilling industry over one billion dollars annually in rig time, materials and other financial resources. Invasion of drilling fluid filtrate and suspended solids into a near wellbore region during drilling operations causes formation damage and wellbore instability. This may lead to a substantial decline in production. Therefore, it is very crucial to investigate the fluid loss problem and understand the mechanisms involved and to find an applicable solution in order to control it.

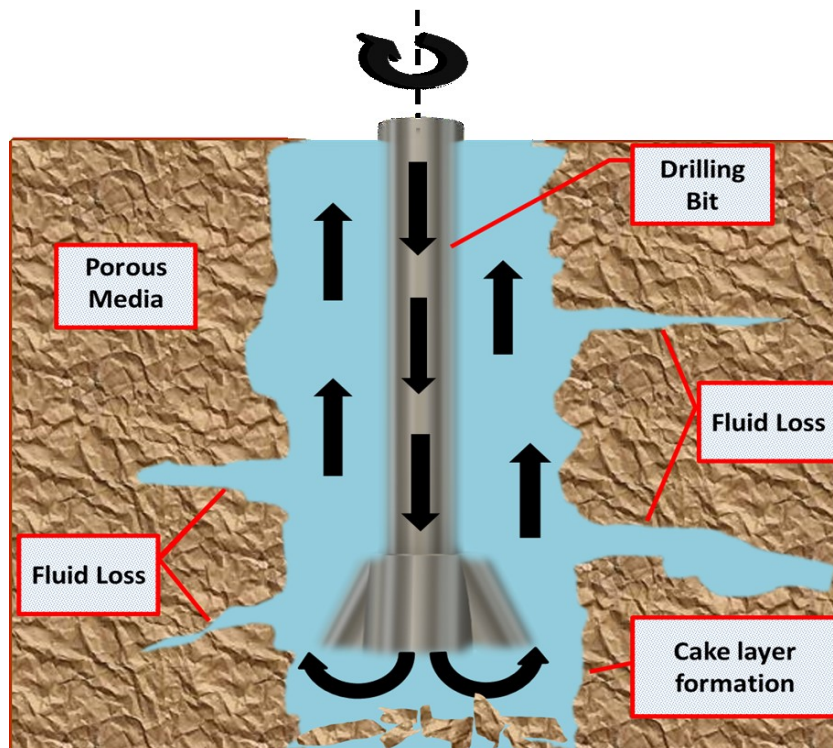


Figure 1.1. Schematic pattern of fluid loss issue in drilling operation

Fluid loss during drilling operations is a typical filtration problem. Filtration can be carried out under static or dynamic conditions. Static filtration refers to the filtration that occurs when the mud circulation stops. It is also known as dead-end filtration. During this type of filtration, the thickness of mud cake around the inner side of the filter gradually increases and the rate of filtration diminishes. On the other hand, dynamic filtration takes place when the drilling fluid is circulated continuously and the formed mud cake is partially swept away and reformed over time. The growth of the filter cake is limited by the erosive action of the drilling mud flow. This type of filtration is also called cross-flow (tangential) filtration. Dynamic filtration rates and fluid loss volumes are much higher than the static ones due to higher fluid invasion to the formations. Under dynamic equilibrium conditions, filtration rate is governed by Darcy's law, while under static conditions, cake thickness is gradually increases to infinity. The type of filter cake is also different in dynamic versus static filtration. Static filter cakes consist of soft surface layers, while dynamic filter cake surfaces are more eroded due to the hydrodynamic forces of the mud flow stream. In order to simulate filtration in the drilling well more closely, it is vital to limit the filter cake growth by liquid or mechanical erosion. More meaningful results could be obtained in systems that either closely simulated conditions in a drilling well, or that allowed the rate of shear at the surface of the cake to be calculated.

In the formulation of drilling fluids, bentonite is the main constituent because it shows excellent colloidal properties, nevertheless high dosage of bentonite in drilling mud can decrease the drilling efficiency, damage the formations, etc. Hence, it is recommended to use other additives to enhance drilling mud workability and performance. Nanoparticles have attracted an increasing attention as additives in drilling fluids. Their small dimensions, high surface area to volume ratio, and other unique characteristics make them essential to be used in drilling fluids formulation technology. They are being used to enhance drilling performance, maintain borehole stability, reduce fluid loss, increase mud viscosity, and enhance oil and gas recovery. Some examples of these nanoparticles are graphene oxide, carbon nanotubes, copper oxide, nanosilicacomposite, zinc oxide and titanium dioxide [8-12]. They all exhibit improved rheology, filtration, and desirable performance. However, most of them are expensive, nonrenewable, and nonbiodegradable. Also, from environmental point of view, these nanoparticles are potentially pollutants. Therefore, it is vital to utilize more

environmentally friendly and cost-effective materials as additives. Among all the options available, there is an increasing trend to utilize natural polymers and nanoparticles. They are renewable, environment friendly, and cost effective.

### **1.3. Filtration of drilling fluids formulated with cellulose nanocrystals**

Cellulose is the most abundant renewable biopolymer. Cellulose nanoparticles (CNC) are crystalline rod-like nanoparticles which are obtained by acid hydrolysis of cellulose fibers. They are typically 6-10 nm in width and 80-200 nm in length [13]. They have high aspect ratios. They can be dispersed in aqueous medium. They are negatively charged particles with zeta potential of -51.5 mV determined by zetasizer [13].

People have seen special interactions with CNC and some polysaccharide polymers such as carboxymethyl cellulose (CMC) and hydroxyethyl cellulose (HEC) [13-15]. The steady-state shear and linear viscoelastic deformations of semidilute suspensions of CNC particles in HEC and CMC solutions were investigated. The low shear viscosity values of polymer solutions were increased 20 – 490 times by the addition of CNC. It also increased the yield stress of polymer solutions up to 7.12 Pa. The addition of nonadsorbing HEC and CMC polymers caused depletion-induced interaction among CNC particles leading to the flocculation of these rod-like particles. Consequently, it increased the viscosity of the suspensions [13]. Oguzlu et al. investigated the non-Newtonian behaviour of dilute and semidilute CMC solutions in the presence of CNC particles. Drastic viscosity increase was observed originating from the nematic flocculation of CNC particles in the presence of non adsorbing CMC polymer that made the CNC flocs entrapped in pockets. Consequently, a highly concentrated network solutions state was observed that resulted in both high viscosity and high degree of shear thinning behaviour [15]. Lu et al. also observed a sol-gel transition in positively charged HEC aqueous solution with an addition of negatively charged CNC suspension due to the electrostatic adsorption interactions. They investigated the scaling law application on gelation of oppositely charged CNC particles and HEC polyelectrolyte [14]. Moreover, flocculation of *Pseudomonas aeruginosa* (PA) bacteria due to the rod-shaped CNC particles was investigated by Boluk et al. [16, 17]. The impact of cellulose nanocrystals on the

aggregation and initial adhesion of the bacteria was explained by the depletion interaction induced by CNC particles. They indicated that the CNC particles can induce bacterial aggregation, and consequently prevent the bacterial initial adhesion on solid surfaces [17].

Some researchers investigated the effect of CMC polymer in rheological and static filtration properties of bentonite-based drilling fluids [5, 18, 19]. They exhibited that the rheological and filtration properties of drilling fluids were modified with CMC polymer. The drilling fluids dosed with CMC were found to be non-Newtonian and show pseudo-plastic behaviour. Iscan and Kok investigated the effect of CMC concentration on rheological and fluid loss parameters in water-base drilling fluids. An optimization of the fluid loss control due to the addition of CMC was made; however, not many people investigated the dynamic filtration of drilling fluids and CMC effect in fluid loss control [7, 20] up to the author's knowledge. In addition, an investigation on the effect of cellulose nanocrystals (CNC) on the rheological and filtration properties of bentonite water-base drilling fluids was carried out recently [21]. However, not a clear understanding of why CNC enhances the rheological and filtration properties of drilling muds was achieved yet. Moreover, the effect of CNC on filtration properties of bentonite-base drilling fluids under dynamic conditions was not investigated yet.

In this study, we are interested in understanding if CNC is suitable to be used as fluid loss additive to the CMC-dosed bentonite drilling fluids. In other words, it is hypothesized that CNC is an effective fluid loss additive in drilling fluid formulation. Afterwards, the possible mechanisms involved in dynamic filtration and rheological properties of drilling fluids are investigated. This work is an initiative to use CNC in CMC-dosed bentonite-base drilling fluids. The objectives of this work are to understand:

- **The dynamic filtration mechanisms involved:** It is crucial to know how filtration proceeds in order to control the fluid loss and prevent high formation damage. The most important aspects of a drilling mud from a formation damage standpoint are to prevent loss of the drilling mud filtrate and to make sure that the filtrate that is lost will not react with the formation to reduce permeability. Fluid loss control is accomplished by rapidly sealing off the permeable pores of the formation. This is carried out by creating an almost impermeable cake of particles on the surface of the

formation where leak-off happens. Therefore, there is a necessary need to know and understand the governing mechanisms involved in dynamic filtration of drilling fluid. Moreover, understanding the filtration mechanisms can be helpful in order to recommend special fluid treatment such as manipulating fluid formulation to minimize torque and drag, prevent excessive drag and low production rates. Plotting the inverse of filtration rate data versus time and total volume loss could be a quantifying tool to understand which mechanism is governing the filtration process. More detailed information is presented in Chapter 2 of this thesis.

- **The effect of CNC to enhance dynamic filtration and rheological properties of drilling fluids:** The question of “Is CNC an effective fluid loss additive?” must be answered. To answer this question, dynamic filtration and rheological experiments must be carried out under various conditions and the results must be compared with sole bentonite-based drilling muds and other common nanoparticle additives that are already used in industry. In addition, filtration theories must be applied to dynamic filtration data to determine how effectively drilling fluid additives (CMC/CNC) block porous filter media.
- **The type of interactions between CNC, CMC and bentonite:** If the use of CNC in drilling fluid formulation is successful regarding fluid loss control, the reason(s) behind it should be thoroughly understood. In other words, the interactions involved when CNC is added to a CMC-dosed bentonite suspension must be quantified in order to highlight the CNC impact on rheological and dynamic filtration properties of bentonite drilling fluids. To do so, colloidal deposition experiments using Quartz Crystal Microbalance with Dissipation (QCM-D) must be carried out. The mass of deposited particles with/without CNC addition must be compared during experiments and logical conclusions must be drawn from the results. Moreover, morphology study of the cake will be a great opportunity to investigate the structure of the cake taken from dynamic filtration experiments.

In Chapter 4 of this research, dynamic filtration tests are carried out under different temperature, pressure, shear rate, medium permeability and drilling mud formulation. The effect of each parameter on fluid loss volume and filtration rate is investigated. Among the mentioned parameters, temperature, pressure, shear rate and porosity are proportional to the

fluid loss. In other words, increasing these parameters leads to an increase in fluid loss volume over time. The effect of mud formulation is included in the investigation of CNC impact to improve dynamic filtration of drilling fluids. Flow behaviour through porous media and in the wellbore will be simulated using FANN 90 Dynamic Filtration apparatus and governing mechanisms involved in the process will be analyzed. Cake formation and particle pore plugging are the main possible mechanisms that may govern the filtration process. They can be analyzed by plotting the inverse of filtration rate versus time and total volume loss separately. The linear relationship confirms the governing mechanism in dynamic filtration results. Finally, different mathematical models to explain fluid loss behaviour are analyzed and the best is selected for the current experimental data.

The stability of the drilling mud under unfavorable borehole conditions is another matter of fact that must be investigated in order to assess drilling mud performance. The drilling engineer must control mud rheological properties to minimize pumping costs, lift drill cuttings efficiently, minimize hole erosion, and separate drill solids and entrained gas at the surface. The transport capacity of drilling fluids is mainly related to their rheological properties. Therefore, it is crucial to optimize the mud properties in order to obtain the best overall performance. In Chapter 5, the rheological behaviour of bentonite suspensions dosed with CNC is investigated. Also, rheological properties of CNC suspensions and CMC solutions are measured and analyzed separately. The effect of each additive on the rheology of bentonite suspensions will be discussed and highlighted. Finally, the best rheological model to interpret the experimental data will be proposed.

Governing interactions between particles and pore surfaces through flow in porous media and filtration could be investigated through particle deposition study. In other words, particle deposition study onto different model surfaces will lead us to know more about what mechanism(s) are involved in interactions between particles and pore surfaces. Role of particle deposition in dynamic filtration results can be investigated by observing it in microscopic level. When filtration happens, particles move towards the inner surface of filter core due to hydrodynamic forces. A portion of them passes through the filter and transports through porous medium of the filter, while the other portion may be deposited onto the inner surface of the filter. In Chapter 6, particle deposition studies are carried out using Quartz

crystal microbalance with dissipation (QCM-D) technique to investigate dynamic filtration mechanisms of cellulose-based drilling mud suspensions. Governing interactions between clay particles and pore surfaces were studied thoroughly. Cellulose nanocrystals (CNCs) play a significant role to enhance clay particles deposition onto silica collector surface. They improve fluid loss control in dynamic filtration of drilling muds by enhancing the deposition of clay particles onto filter surface. The depletion interaction induced by rod-like shape CNCs pushes the bentonite particles toward the collector surface. Bentonite particles plug the pores at the beginning and start to form a cake gradually. As a result, fluid loss issue (large permeate flow from filter) will be controlled and the involved mechanisms will be investigated completely.

The drilling mud formulation consisting of Wyoming bentonite, cellulose nanocrystal particles, and carboxymethyl cellulose polymer exhibits acceptable performance in dynamic filtration and rheological experiments under different experimental conditions. Not only it is required to investigate the mechanism of clay particles deposition from a flow onto a model surface, but also a thorough fundamental knowledge of clay mineralogy is required to investigate filtration and rheological properties of drilling muds in a more comprehensive way. Clay is the basic component of approximately all aqueous muds. The stability of borehole depends largely on interactions between the drilling fluid and the exposed formation surface. Moreover, colloid chemistry is of great importance in drilling fluid technology, as clays form colloidal suspensions in water. Both clay mineralogy and colloid chemistry are significant topics to investigate the drilling mud behaviour under wellbore condition. In Chapter 7, morphology and mineralogy of filter cakes collected from dynamic filtration experiments are investigated. Scanning electron microscopy (SEM) images of the dried filter cakes are analyzed and elemental analysis is carried out on mud suspensions before and after dynamic filtration tests. Possible scenarios for observing fibrous structure in the filter cake samples are stated and investigated.

The aforementioned objectives were satisfied by the investigation of dynamic filtration, rheology and transport phenomena through porous media for colloidal and polymer solutions through Chapters 4 – 7. Figure 1.2 illustrates the methodology followed in order to investigate fluid loss issue and propose scientific suggestions to control it. It shows the

pathway to understand and investigate the significant parameters controlling fluid loss in drilling fluids.

Fluid Loss During Oil Well Drilling							
Mud Formulation			Filtration Properties	Mud Stability	Colloidal Deposition	Filter Cake Structure	
Bentonite	CNC	CMC	Dynamic Filtration	Rheology	QCM-D	Morphology	Elemental Analysis
<ul style="list-style-type: none"> <li>• Excellent Colloidal Properties</li> <li>• Swelling Capability</li> <li>• Main Component</li> </ul>	<ul style="list-style-type: none"> <li>• High Aspect Ratio</li> <li>• Rod-Like Nanoparticle</li> <li>• Depletion Interaction</li> <li>• Filtration Control</li> <li>• -62.8 mV Zeta Potential</li> </ul>	<ul style="list-style-type: none"> <li>• Non-Adsorbing Anionic Polymer</li> <li>• Viscosity Modifier</li> <li>• <math>M_w</math> 700-900K</li> </ul>	<ul style="list-style-type: none"> <li>• Total Volume Loss</li> <li>• Filtration Rate</li> <li>• Spurt Loss Volume</li> <li>• Mechanisms</li> <li>• Experimental Conditions</li> </ul>	<ul style="list-style-type: none"> <li>• Viscosity vs. Shear Rate</li> <li>• Flow Behaviour Model</li> </ul>	<ul style="list-style-type: none"> <li>• Mass Deposition vs. Time</li> <li>• Initial Deposition Rate</li> <li>• Model Surface Coverage</li> <li>• Colloidal Interactions</li> </ul>	SEM	<ul style="list-style-type: none"> <li>• ICP</li> <li>• EDX</li> </ul>

Figure 1.2. Methodology flowchart

## 2. Background and literature review

### 2.1. Filtration

The separation of fluid-solid system involving passage of most of the suspension through a porous media which retains a portion of solid particles contained in the mixture is defined as filtration. A filter is a piece of unit-operations equipment by which filtration is performed. The **filter medium** is the barrier that lets the liquid pass while holding most of the solids; it may be a screen, cloth, paper, membrane, or bed of solids. The liquid that passes through the filter medium is called the **filtrate**. The solids remain behind the filter are called retentate (cake) [22]. Figure 2.1 shows a typical filtration process.

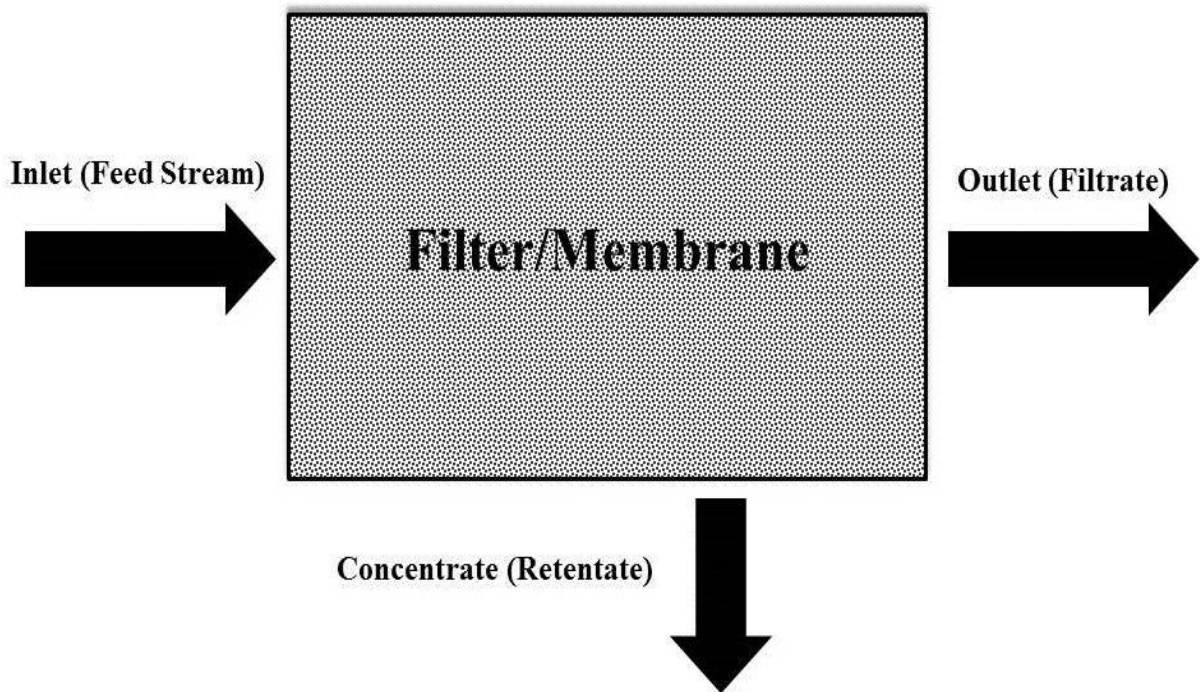


Figure 2.1. A schematic of typical filtration process

Filtration can be classified based on (1) driving force, (2) target of filtration, (3) operation kind, (4) nature and size of the solids, (5) the geometry of filtration and (6) filtration mechanisms:

1. Filtration can be affected by different driving forces such as gravity (hydrostatic head), applied pressure upstream of the filter medium, reduced applied pressure downstream of the filter, or centrifugal force across the medium.
2. Depending on what is the goal of filtration (product of value), dry solids (cake) or clarified liquid (the filtrate), filtration may be accomplished by different ways.
3. If the filtration is batch or continuous, both the filter and filtration equipment are different due to requiring different filter area and solids loading.
4. Compressibility of the cake (solids) is very significant as it changes the rigidity (deformability) of the solid particles under filtration process. Additionally, particles may range from nanometers to micrometers (same order of magnitude as common filter pore sizes) that will change the type of filtration accordingly.
5. Based on the direction of feed stream, filtrate, and retentate, filtration can be accomplished by dead-end (conventional) and cross-flow filtration. A schematic of the dead-end vs. cross-flow filtration is illustrated in Figure 2.2.

The **dead – end filtration** is a type of filtration where the flow is perpendicular to the filter surface. The fluid is pushed through the membrane by pressure. All the fluid that is introduced in the dead-end-cell passes through as permeate. In other words, there is no rejected fluid. In dead-end filtration the retained particles build up with time on or within the filter. In either cases, the particles accumulation results in an increased resistance to filtration and causes the permeate flux to decline; therefore, this type of filtration requires shut down of filtration in order to clean or replace the filter. This type of filtration is also called batch filtration. There are two types of filtration which can be employed in a dead end cell unit; dead-end microfiltration with constant flux and dead-end microfiltration with constant pressure drop. The dead end microfiltration with constant flux ensures that the permeate flux through the filter remains constant. As the cake build-up increases with time, the pressure drop must be increased to maintain constant flux. In dead-end microfiltration with constant pressure, as the cake builds up with time, the permeate flux decreases.

The **cross – flow filtration**, also known as tangential flow filtration, is a flow through a filter module in which the feed flow and permeate flow are perpendicular in direction. In

other words, while the fluid stream moves parallel to the filter surface, the permeate flow moves away from the filter in the direction normal to the filter surface. The main advantage of cross flow filtration is the filter cake formation, which is substantially washed away during the filtration process, and it can increase the length of time that a filter unit can be operational. This system can be a continuous process, unlike batch-wise dead-end filtration. To explain more, with cross flow filtration, the tangential motion of the bulk of the fluid across the filter causes trapped particles on the filter surface to be washed away that makes it a non-stop continuous process. Traditionally, cake filtration is carried out with the direction of the feed (suspension) flow coinciding with that of the filtrate flow and cake growth taking place along the opposite direction. However, one may carry out cake filtration by passing the suspension to be treated along the filter medium such that the direction of the filtrate flow is normal to that of the suspension flow. In both dead-end and cross-flow filtration, particle separation leads to the formation of filter cakes which contribute resistance to filtrate flow. There are, however, significant differences between the two types of operations. For example, regular dead-end filtration may operate under relatively high pressure. In contrast, the operating pressure (the so-called transmembrane pressure) in cross-flow filtration, in most cases, is not very high [22, 23].

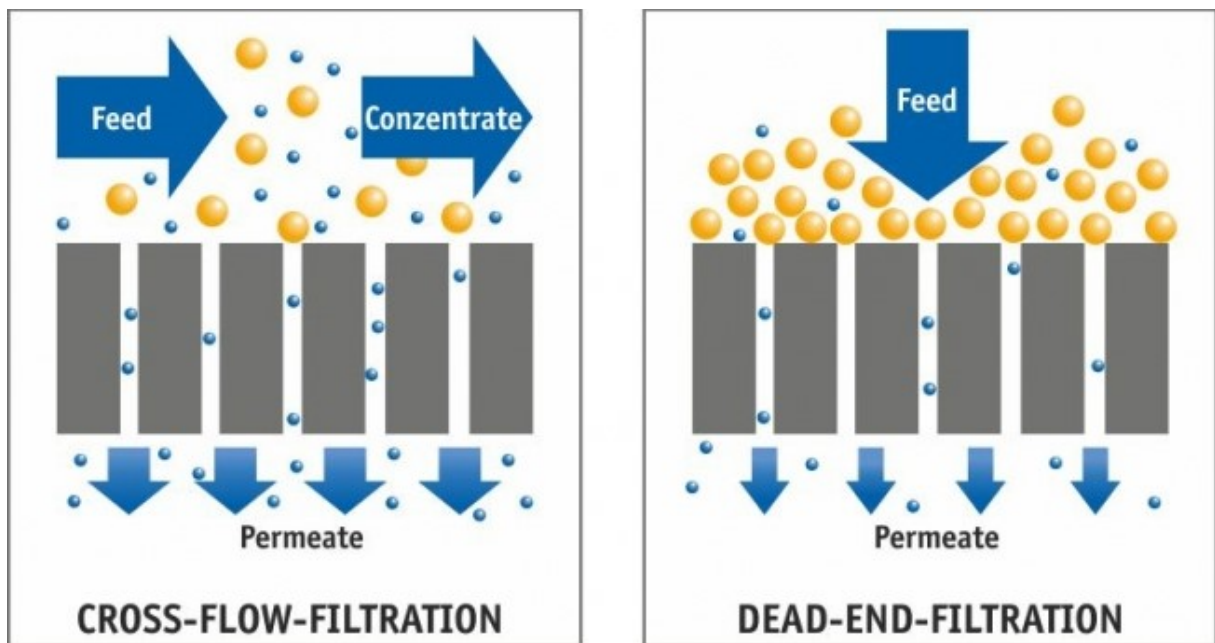


Figure 2.2. Dead-end vs. cross-flow filtration

6. The last but not least is the classification according to the filtration mechanism. In other words, what mechanisms are governing the filtration from the early stage to the end of process? The three known mechanisms, cake formation, particle pore plugging and concentration polarization, are introduced in the following section.

### **2.1.1. Filtration theory**

Based on filtration mechanisms, filtration can be classified as (1) cake formation, (2) clarifying filtration (particle pore plugging), and (3) concentration polarization (gel-layer formation). When solids are stopped at the surface of a filter medium and pile upon one another to form a cake of increasing thickness, the separation is called cake filtration [22]. That is due to several hydrodynamic effects as well as interaction forces between surface and particles. Gravitational, depletion, and van der Waals interactions may be included in this category. In cake filtration, the filter medium acts as a screen, therefore particles of the suspension to be treated are kept by the medium, resulting in the formation of filter cakes. In contrast, in deep bed filtration, separation is affected by particle deposition throughout the whole depth of the medium. In other words, the individual entities constituting the medium act as particle collectors. Hence, cake filtration is also known as surface filtration while deep bed filtration is often referred to as depth filtration [23].

Over the years, researchers have investigated the mechanisms of cake formation. Beginning with Hermans and Bredee (1935), the so-called "laws of filtration" were advanced. In 1982, Hermia proposed a later version of filtration laws. His theory was based on the mechanism in which particle deposition happens; therefore cake filtration was classified into four different types: (1) complete blocking, (2) intermediate blocking, (3) bridging and standard blocking and (4) cake filtration. Complete blocking refers to the action of every retained particle to block a medium pore. In intermediate blocking stage, there is a possibility for a retained particle to block medium pores. In standard blocking, particle retention happens within medium that results in narrowing the medium pores. Finally, cake filtration refers to the cake formation and growth caused by particle retention. It is important to note that "standard blocking" is an operative retention mechanism in deep bed filtration while complete and intermediate blocking are taking place in the initial stages of cake filtration [24].

The dynamics of filtration based on four assumed filtration rate expressions corresponding to each of the four retention mechanisms mentioned above is given as:

$$\frac{d^2t}{dV^2} = k_1 \left( \frac{dt}{dV} \right)^{k_2} \quad [2.1]$$

where V is the total filtrate volume per medium surface area collected, t the time, and  $k_1$  and  $k_2$  are empirical constants. It was suggested that the value of  $k_2$  characterizes the types of cake formation corresponding to (1) bridging (proper cake filtration), (2) intermediate blocking, (3) standard blocking and (4) complete blocking, respectively (Table 2.1).

**Table 2.1. Empirical values for different retention mechanisms**

<b>Retention Mechanism</b>	<b>Value of <math>k_2</math></b>
Cake filtration	0.0
Intermediate blocking	1.0
Standard blocking	1.5
Complete blocking	2.0

Hermia version of the filtration equation was based completely on spontaneous argument with some arbitrary assumptions. Both complete blocking and bridging lead to cake formation. Furthermore, since in practical situations, the medium pores and particles are probably not uniform in sizes, different types of deposition may happen at the same time [23, 24].

#### **2.1.1.1. Cake Filtration**

In cake or surface filtration, there are two primary areas of consideration: (1) continuous filtration, in which the resistance of the filter cake (deposited process solids) is very large with respect to that of the filter media and filtrate drainage, and (2) batch pressure filtration, in which the resistance of the filter cake is not very large with respect to that of the filter media and filtrate drainage. Basic equations in filtration theory originate from some basic assumptions and writing the one-dimensional continuity equations of particles and fluid.

It is assumed that the suspended particles cannot penetrate into the medium and are retained on the upstream side of the medium to form a cake. The suspending fluid passes through the medium as filtrate. The thickness of the cake increases with time as filtration proceeds. Simplified theory for both batch and continuous filtration is based on the time-honored Hagen-Poiseuille equation [25]:

$$\frac{1}{A} \frac{dV}{dt} = \frac{P}{\mu(\alpha w V/A + r)} \quad [2.2]$$

where  $V$  is the volume of filtrate,  $t$  the filtration time,  $A$  the filter area,  $P$  the total pressure across the system,  $w$  the weight of cake solids/unit volume of filtrate (filtrate density),  $\mu$  the filtrate viscosity,  $\alpha$  the cake-specific resistance, and  $r$  the resistance of the filter medium.

For constant-pressure filtration Equation [2.2] can be integrated to give the following relationship between elapsed time and filtrate measurements:

$$\frac{t}{V/A} = K_1 V/A + K_2 \quad [2.3]$$

Equation [2.3] is known as Ruth's Law. Knowing filter area ( $A$ ), values of  $\frac{t}{V/A}$  can be plotted for various values of  $V/A$  resulting in a straight line having the slope  $K_1 = \frac{\mu\alpha w}{2P}$  and an intercept on the vertical axis of  $K_2 = \frac{\mu r}{P}$ . Since  $\mu$ ,  $w$ , and  $P$  are known,  $\alpha$  and  $r$  can be calculated as shown in Figure 2.3.

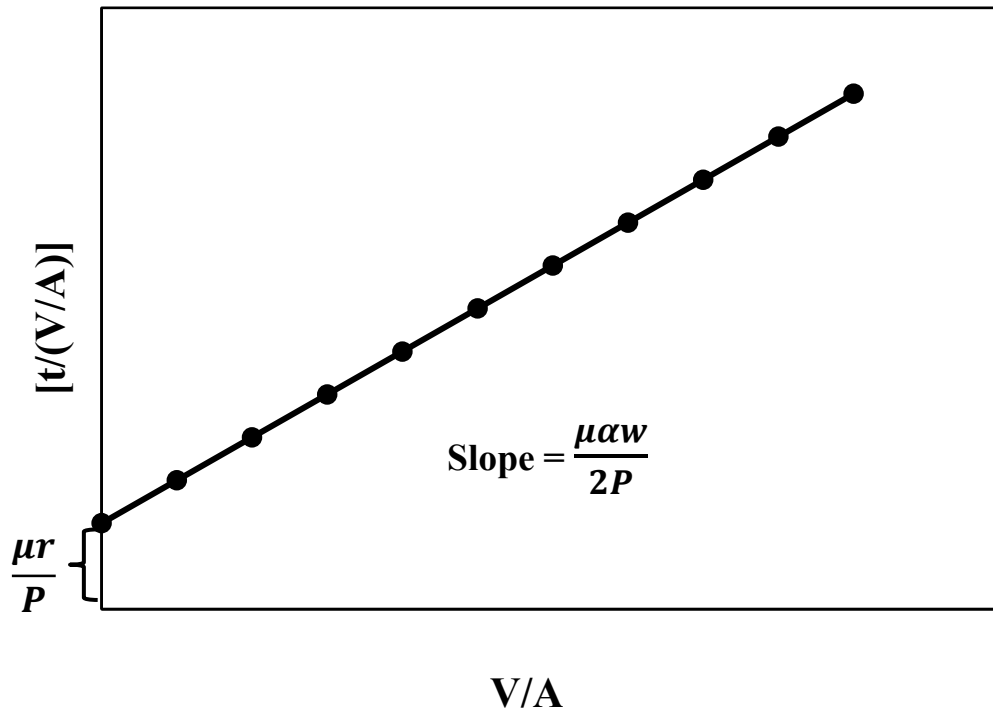


Figure 2.3. Filtration data and regression to find filter and cake resistances

The symbol  $\alpha$  represents the average specific cake resistance, which is a constant for the particular cake in its immediate condition. In the usual range of operating conditions it is related to the pressure by the following equation:

$$\alpha = \alpha' P^s \quad [2.4]$$

where  $\alpha'$  is a constant determined by the size of the particles forming the cake,  $s$  the cake compressibility, varying from 0 for rigid, incompressible cakes to 1.0 for very highly compressible cakes. For most industrial slurries,  $s$  takes values between 0.1 and 0.8. It should be noted also that the intercept is difficult to determine accurately because of large potential experimental error in observing the time of the start of filtration and the time-volume correspondence during the first moments when the filtration rate is high. The value of  $r$  calculated from the intercept may vary appreciably from test to test, and will almost always be different from the value measured with clean medium in a permeability test [25].

### 2.1.1.2. Pore Plugging

Particle pore plugging is another mechanism that happens when solids are trapped within the pores or body of the filter medium. Solids smaller than the pores are often trapped in the filter medium, which reduces the medium's permeability. Research shows that pore plugging occurs during the first few minutes of filtration. This internal pore blockage by solids in suspension slows down filtration [26]. In reality, when the collector surface is covered with deposited particles, its capture efficiencies alter with the extent of particle coverage. When the deposited particles prevent from further deposition, the process is called blocking. There might be another outcome of these transient variations while the deposited particles enhance further deposition which is referred to as ripening. The basic physics of blocking involves reduction in the available surface sites on the collector grains (filter pores) because of the deposited particles. Also, knowing the fact of electrostatic repulsion interaction between similarly charged particles makes it more perceptible that blocking is caused by two main mechanisms: First by physical reduction of the available collector (filter) surface area and second by rendering the collector surface less electrostatic attractive or favorable for further deposition. On the other hand, ripening is engendered by increase in the net capture cross section of the filters, leading to a greater interception of flowing particles in the bulk [27].

Equation [2.5] describes particle plugging mechanism in porous filter media.

$$\frac{t}{V/A} = K_3 t + K_4 \quad [2.5]$$

Equation [2.5] is the solution of a second-order differential equation, developed by Hermans and Bredee [26] and is known as standard blocking law. If plots of  $[t/(V/A)]$  vs.  $t$  are linear and have a positive slope, pore blocking is governing the filtration.

With Equations [2.3] and [2.5], cake formation can be separated from pore plugging mechanism during filtration. Both cake filtration and particle plugging occur during drilling. It is possible to evaluate fluid-loss additives on their ability to block pore space and to form highly compressible low-permeability filter cakes.

Over the past several decades, the dynamics of filter blocking by deposited particles has received considerable attention. One of the most outstanding researches in this case is named as the random sequential adsorption (RSA) model [28]. The RSA model provides a relationship between the deposition efficiency and the extent of collector surface coverage by deposited particles in the form of a chemical kinetic equation. Song also formulated the flux decline behaviour for cross flow filtration considering the pore blocking and cake formation models as the mechanisms of particle depositions on filter surface [29]. The paper discussed the three main resistances appearing during cross-flow filtration including pore blocking, cake formation and concentration polarization. The rapid initial decline in the flux is attributed to the quick blocking of the membrane/filter pores. Following the pore blocking process is the gradual cake formation as particles tend to deposit and form layers on top of each other. Afterwards, the flux reaches a steady state where there is no change with time. As it can be observed in Figure 2.4, different behaviours in terms of permeation flux and cake growth are observed if the deposition region is divided into equilibrium and non-equilibrium regions. In the equilibrium region, particle deposition rate on the membrane surface is zero due to the equilibrium thickness of the cake layer, while particle deposition rate is not zero in non-equilibrium region. This rate is equal to the particle flux into the concentration polarization layer.

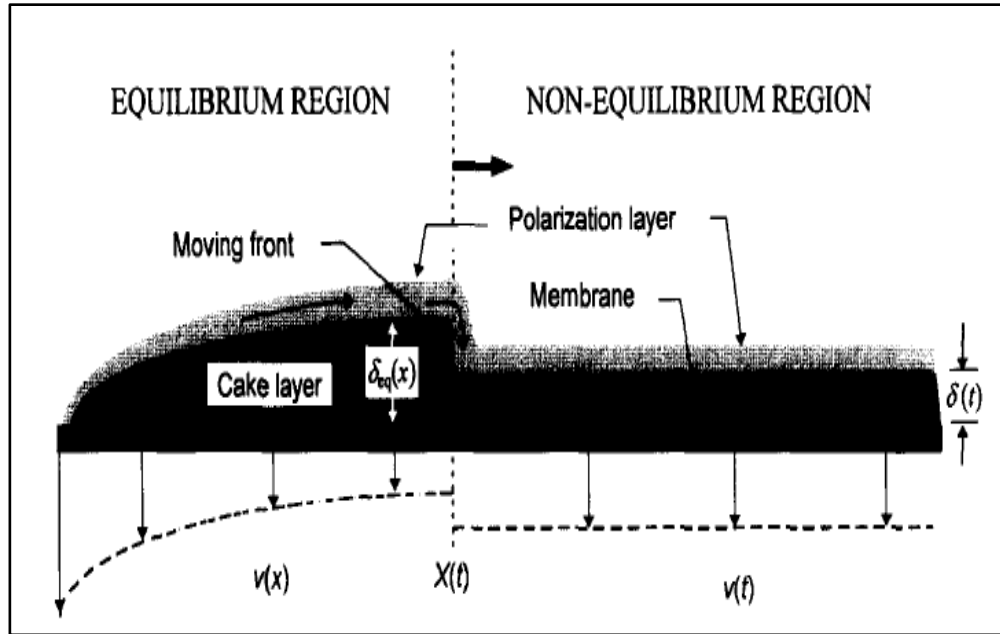


Figure 2.4. A schematic depiction of cake layer thickness and the flux in equilibrium and non-equilibrium regions [8]

### 2.1.1.3. Concentration Polarization

The third mechanism is the concentration polarization phenomenon in which the particle concentration in the vicinity of the membrane surface is higher than that in the bulk. This phenomenon occurs due to different permeability of the membrane/filter for various components of the suspension and results in the formation of a concentrated layer called concentration polarization layer. This layer increases the filter resistance and accordingly decreases the permeate flux through the filter [30].

## 2.1.2. Static vs. dynamic filtration

Static filtration happens when mud is not circulated after the bit has drilled out the formation. The filter cake grows undisturbedly as a result. On the other hand, mud circulation between the drill bit and borehole wall continues in dynamic filtration. Therefore, the flow of mud across the borehole wall causes erosion of the deposited cake and increases the fluid loss

to the formation. If the circulation time is extended, the deposition and erosion processes reach an equilibrium state which constant cake thickness and filtration rate is achieved.

It is obvious that there is a mud spurt at the beginning of a filtration process before it properly starts. More permeable rocks result in larger mud spurt loss volume. After this short period, depending on the size of particles and permeability of borehole wall, internal and external layers of cake are formed. As a result, three zones are established as follows:

- i. External filter cake on the walls of the borehole;
- ii. Internal filter cake due to deposited particles;
- iii. An invaded zone by the fine particles during the mud spurt period.

Figure 2.5 illustrates the invasion of permeable formation by mud solid particles.

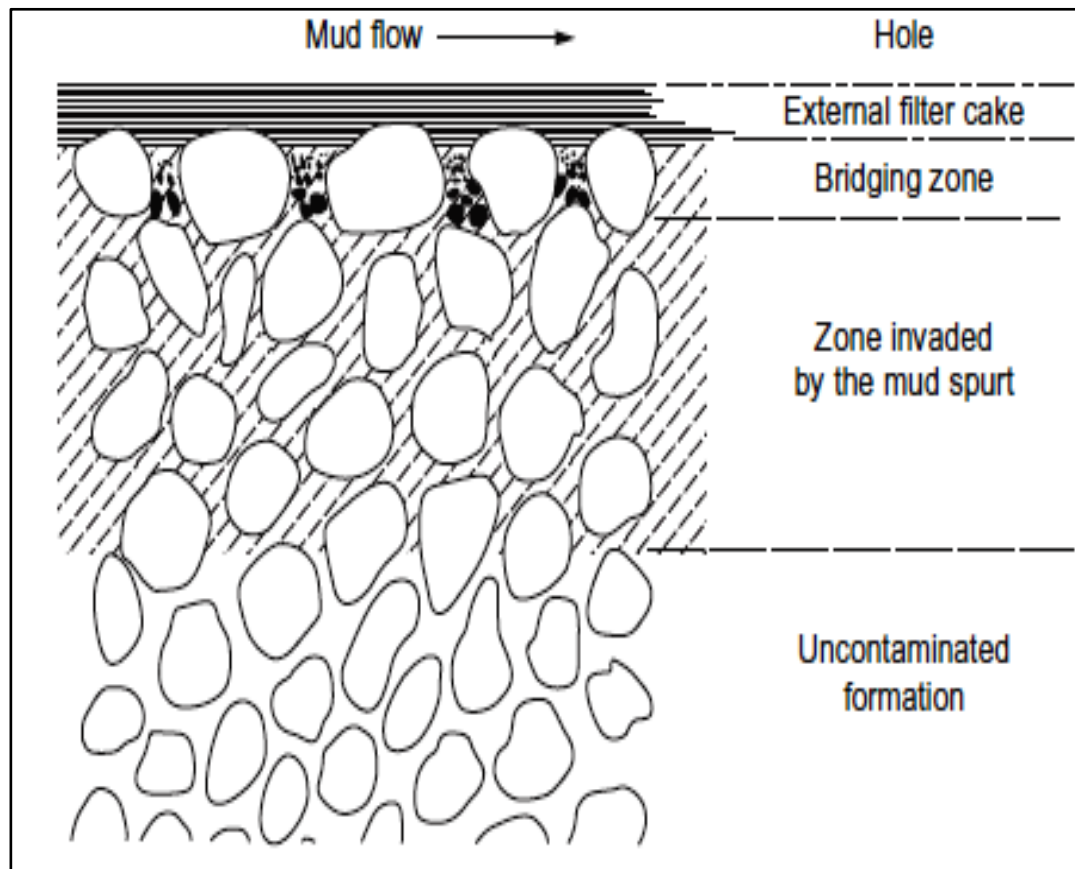


**Figure 2.5. Schematic of formation invasion by mud particles [16]**

## 2.1.3. Mathematical models in cross-flow filtration

### 2.1.3.1. Models for dynamic fluid loss

Modeling of fluid loss is important for obtaining reasonable estimates of fracture geometry. The fluid-loss process is complicated and difficult to accurately model theoretically since many of the parameters are difficult to evaluate. Modeling is even more complicated when non-Newtonian fluids are used and the thickening agent (typically a water soluble polymer) may or may not pass through the filter cake, and the extent to which the polymer does penetrate the filter cake is unknown. Moreover, dynamic fluid loss makes it more difficult to model because filter-cake erosion must be taken into account [31]. Typically, the volume is plotted versus the square root of time and a slope and intercept determined.

For static filtration, the volume versus square-root-of-time data can be described by Equation [2.6] for drilling muds.

$$V_{fl} = V_{sp} + m\sqrt{t} \quad [2.6]$$

Where  $V_{fl}$  is the fluid loss volume,  $V_{sp}$  the spurt loss volume,  $m$  the initial slope of the linear part of the curve, and  $t$  the time.

Equation [2.6] does not work satisfactorily for dynamic fluid loss data. Different models were proposed during 1983 to 1996. Gulbis suggested that using time instead of square root of time results in better curve fits for dynamic fluid loss data. Equation [2.7] describes the suggested model.

$$V_{fl} = V_{sp} + mt \quad [2.7]$$

Roodhart proposed that both time and square root of time should be included in order to cover both short-time wall-building phase and long-time equilibrium region. Equation [2.8] describes his analysis.

$$V_{fl} = V_{sp} + m\sqrt{t} + Bt \quad [2.8]$$

Where  $B$  is a fitting parameter relating to the equilibrium flow region. A power law model can also be used in this type of analysis as follows:

$$V_{fl} = V_{sp} + mt^n \quad [2.9]$$

Using the exponential  $t^n$  instead of  $t$  works better at longer times.

To better explain both early-time and equilibrium stages of dynamic filtration, another model was proposed by Clark and Barkat that includes the term  $(1 - e^{-c_b t})$ . This term approaches one as time increases, so it includes the square-root-of-time portion.  $C_b$  determines how fast this occurs. The model is explained in Equation [2.10].

$$V_{fl} = V_{sp}(1 - e^{-c_b t}) + mt \quad [2.10]$$

One or a combination of these semi empirical models can be used to describe fluid loss behaviour in dynamic filtration process [31].

### 2.1.3.2. *Flow regime and geometry of the system in cross-flow filtration*

As shown in Figure 2.6, the geometry of the cross-flow filtration can be depicted as two co-axial cylinders (Inner moving and outer stationary) and the flow regime between the cylinders is called the Taylor flow.

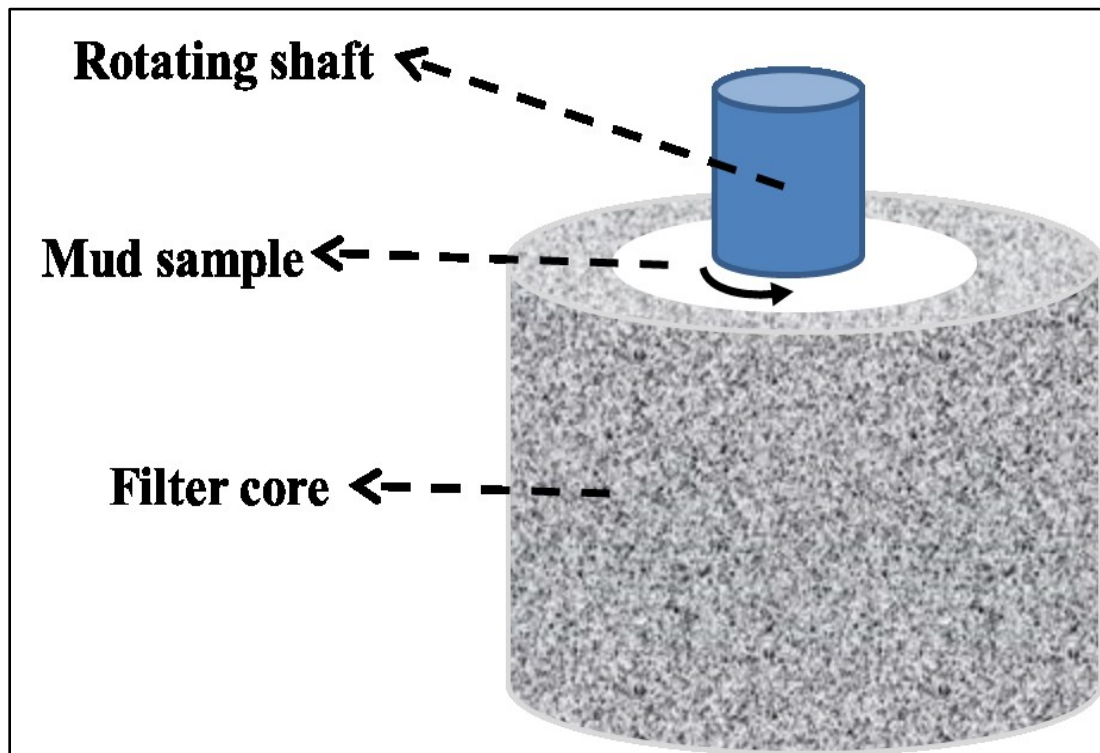


Figure 2.6. System geometry

Researchers studied the effects of different parameters such as the gap size between the inner and outer cylinder, feed concentration, feed rate, and rotation speed of the inner cylinder on the filtrate/permeate flux experimentally [32]. Taylor vortex phenomena can be explained as dimensionless Taylor number,  $T_a$  as follows:

$$Ta = \frac{\omega r_i d}{\nu} \sqrt{\frac{2d}{r_i + r_o}} \quad [2.11]$$

$$Ta_c = 41.1 + 13.1 \frac{d}{r_i} \quad [2.12]$$

$$\omega = \frac{\dot{\gamma}}{c} \quad [2.13]$$

$$c = \frac{2r_i^2 r_o^2}{r_a^2 (r_o^2 - r_i^2)} \quad [2.14]$$

$$r_a = \frac{r_i + r_o}{2} \quad [2.15]$$

where  $\omega$  is the angular velocity,  $r_i$  the radius of the rotating shaft,  $r_o$  the inside radius of the filter core,  $d$  the width of the gap,  $\dot{\gamma}$  the shear rate, and  $\nu$  the kinematic viscosity of the mud.

As clearly observed, Taylor number definition is another explanation of Reynolds number for a different geometry (concentric cylinders). Both dimensionless numbers explain the ratio of inertia forces to the viscous forces. By defining the critical Taylor number at which the Taylor vortex begins (Taylor-Couette flow), one can state that if the Taylor number calculated for a specific problem is greater than critical one, Taylor vortices and high turbulence exist in the system. Figure 2.7 illustrates the Taylor-Couette flow.

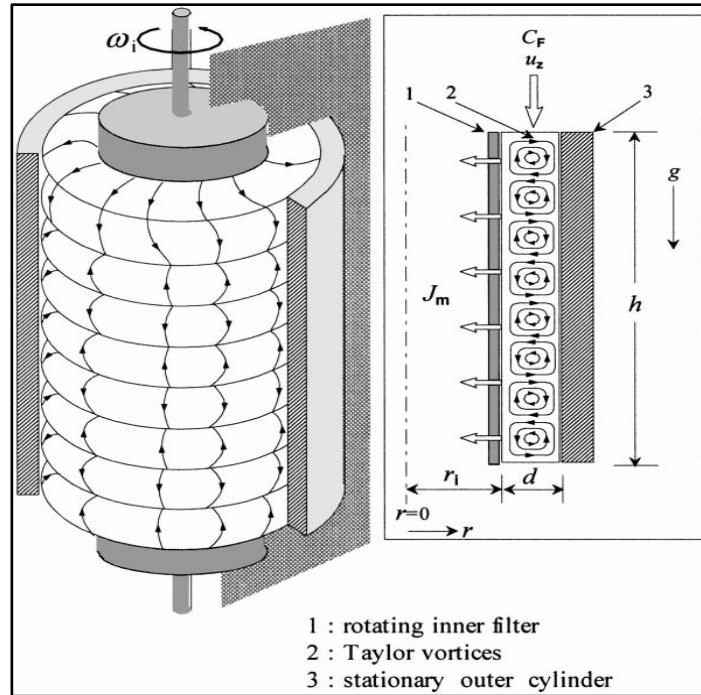


Figure 2.7. Taylor vortices in concentric cylinders geometry [18]

Critical Taylor number was given in Equation [2.12]. This equation is valid when no axial flow exists in the system. For further assumptions and equations, please refer to the original article [33]

### 2.1.3.3. Key parameters and conditions in cross-flow filtration

Cross-flow filtration tests are affected by different experiment conditions such as differential pressure, temperature, angular velocity, filter porosity, and etc. Increase in differential pressure (pressure between inside and outside of the filter), results in an increment in permeate flux. Additionally, when speed of rotation increases under constant pressure, the permeate flux also increases.

In 1988, Kroner et al. observed secondary flow phenomena, the so-called “Taylor vortices” in their experiments and the flow regime was described as Taylor-Couette flow. They described the effect of transmembrane pressure (TMP), or differential pressure, on permeate flux with the following equation:

$$J = \frac{TMP}{\mu R_t} \quad [2.16]$$

where  $\mu$  is the viscosity of the suspension and  $R_t$  is the total resistance of the system. It is clearly understood that increase in transmembrane pressure is proportional to the permeate flux increase [34]. The permeate flux is also proportional to temperature increase and higher porous filters. They need to be discussed further in Chapter 4.

## 2.2. Flow in porous media

The dynamics of large fluid sections such as oceans or atmosphere is often dominated by inertia term, which causes turbulence, while the dynamics of fluids in porous media is generally dominated by porous matrix, which permeates the entire volume and results in an efficient dissipation of the fluid's kinetic energy. The transport and deposition behaviour of colloidal particles in saturated porous media is of great importance in various natural and engineering processes. The necessity of predicting the transport of microbial particles, such as bacteria, viruses, and protozoan cysts as well as colloid-bound pollutants in subsurface environments is an appropriate example of the importance of particle deposition/filtration studies. Additionally, granular filtration unit, used in water and wastewater treatment and other industrial separations is another typical instance of the significance to know more about particle transport and deposition, specifically in porous media [35].

Filtration in a macroscopic scale is a special example of flow through porous media, where the flow resistance increases with time as the filter medium becomes clogged or a filter cake builds up. It is usually classified into dead-end filtration and cross-flow filtration as discussed earlier. Most commonly, the pressure drop is held constant which is called constant pressure filtration. The total resistance of the system consists of the filter resistance and the resistance of the deposited particles (cake resistance). The first one is usually constant and is important only during the early steps of cake filtration, but the resistance of deposited particles is related to the frictional drag force in the transverse flow of permeate through the dense layer of deposited particles and is zero at the start, increases with time as filtration progresses [30].

### 2.2.1. Basic forces involved in flow in porous media

Cake filtration was selected as an appropriate and relevant example of flow in porous media. It is clear that solid particles form a filter cake on the filter medium and liquid flows through the interstices of the cake in the direction of decreasing hydraulic pressure. Each particle is subjected to skin and form drag. Surface forces on the particles generate internal forces which are transferred from particle to particle at points of contact. Since the solid particles are considered as points, the hydraulic pressure  $P_L$  is effective over the entire cross-sectional area  $A$ . By neglecting inertia forces, one can write a force balance over a portion of the filter cake in a finite length:

$$F_s + AP_L = AP \quad [2.17]$$

where  $F_s$  is the accumulated drag force on the particles and  $P$  is the applied pressure. Dividing by  $A$  yields:

$$P_s + P_L = P \quad [2.18]$$

where  $P_s$  is the compressive drag force or effective solid pressure. As it is clear, the applied pressure is only a function of time while the hydraulic and compressive drag pressures are dependent on time and distance. Therefore, taking the differential of Equation [2.18] with respect to the distance at constant time yields:

$$dP_L + dP_s = 0 \quad [2.19]$$

This equation implies that the drop in hydraulic pressure is exactly equal to the rise in solid compressive pressure.

### 2.2.2. Porosity

One of the significant parameters in filtration and flow in porous media is the so-called "Porosity". It is a measure of the void or empty spaces in a material, and is a fraction of the volume of voids over the total volume. Porosity of the cake (deposited particles) and of the filter medium are two separated topics. The first one is described here. The filter medium porosity and its influence on filtration properties are well discussed in results and discussion Chapter 4.

As the cake thickness increases with time during filtration, the cake near the filter medium is dry and compact while the cake near surface is wet and highly porous. Particle size and particle size distribution control the porosity of the cake. Minimum porosities are obtained when there is an even gradation of particle sizes (a linear particle size distribution curve) , because the smaller particles then packed most densely in the pores between the larger particles. Additionally, mixtures with a wide range of particle sizes have lower porosities than mixtures with the same size distribution but narrower size range. Porosity of the cake may vary due to the change in solid compressive pressure. As the filter medium is approached from the surface of the cake, increase in compressive pressure results in porosity decrease. These changes may have significant effect on filtration results (See Chapter 4).

### 2.2.3. Darcy's law

Darcy's law is used to study flow of liquids through porous media. It basically states that the superficial velocity (Darcy flux) of the fluid is proportional to the hydraulic pressure gradient and inversely proportional to the liquid viscosity.

$$q = -\frac{k}{\mu} \nabla P \quad [2.20]$$

where  $q$  is the darcy flux (m/s),  $\nabla P$  the pressure gradient (Pa/m),  $k$  the intrinsic permeability of the medium ( $m^2$ ), and  $\mu$  the liquid viscosity (Pa.s). The fluid velocity can be linked to the darcy flux by dividing it by porosity.

$$u = \frac{q}{\epsilon} \quad [2.21]$$

In filtration, Darcy's law is usually written with material coordinates in the form of:

$$\frac{dP_L}{dw} = -\frac{dP_s}{dw} = \mu \alpha q \quad [2.22]$$

where  $w$  is the mass of dry cake per unit area deposited in thickness  $x$  from the medium and  $\alpha$  is the local specific flow resistance (m/kg). We also have  $dw$  and  $k$  as:

$$dw = \rho_s(1 - \epsilon)dx \quad [2.23]$$

$$k = \frac{1}{\rho_s} \alpha (1 - \epsilon) \quad [2.24]$$

With compressible cakes, the solid moves toward the medium as the cake is compressed, so Darcy's law must be modified to account for relative velocity of the liquid with respect to solids. This is not significant in fixed bed systems as the solid particles are stationary. Due to the fact that the solid velocity is not large in most filtrations, this modification can be neglected.

#### 2.2.4. Kozeny's equation

Josef Kozeny (1889-1967), an Austrian physicist, modified Darcy's simple formula and developed an analytical expression for the permeability or the specific resistance based on Poiseuille equation. The Poiseuille equation for flow through a circular pipe is written as:

$$\frac{\Delta P}{L} = - \frac{32\mu u'}{D^2} \quad [2.25]$$

where  $\frac{\Delta P}{L}$  is the pressure gradient,  $\mu$  the viscosity of the fluid,  $u'$  the mean velocity in the tube and D tube diameter.

It is possible to write Equation [2.20] in terms of porous media parameters by introducing the hydraulic radius  $R_H$  in place of D and then relating it to porosity  $\epsilon$  and specific surface S. The hydraulic radius is defined as:

$$R_H = \frac{\text{flow area}}{\text{wetted perimeter}} \quad [2.26]$$

For circular pipe,  $R_H$  is D/4. The hydraulic radius may also be rewritten as:

$$R_H = \frac{\text{void volume}}{\text{surface area of solids}} \quad [2.27]$$

The void volume is related to porosity by:

$$\text{void volume} = \frac{\epsilon}{1 - \epsilon} (\text{volume of solids}) \quad [2.28]$$

Then,

$$R_H = \frac{\epsilon}{1 - \epsilon} \frac{\text{volume of solids}}{\text{surface area of solids}} \quad [2.29]$$

Knowing the definition of specific surface area as:

$$S = \frac{\text{surface area of solids}}{\text{volume of solids}} \quad [2.30]$$

The hydraulic radius may be expressed as:

$$R_H = \frac{\epsilon}{1 - \epsilon} \frac{1}{S} \quad [2.31]$$

Substituting Equation [2.21] and Equation [2.31] into Equation [2.25] yields:

$$\frac{dP_L}{dx} = kS^2 \frac{(1 - \epsilon)^2}{\epsilon^3} \mu q \quad [2.32]$$

Equation [2.32] is known as Kozeny's equation, and k is Kozeny's constant. Kozeny's constant is a function of the shape of particles, the arrangement of particles, the shape of the cross-sectional area of flow, and the ratio of the length of the actual path to the thickness of the bed. Some of the k values are given in Table 2.2.

**Table 2.2. Experimental/computational Kozeny constant values [36]**

<b>Porous medium</b>	<b>Proposed constant</b>
Uniform spheres	K=4.8±0.3
Fibrous and granular beds	K=12.81
Random porous media constructed with square obstacles	6.5<K<10.4
Circular cylinders in cross flow	K=9
Square rods in cross flow	K=7.5

He also derived a fundamental relationship between permeability and porosity [37]. Equation [2.33] expresses the relationship between permeability and porosity of the porous media consisting of capillary tubes.

$$k = \left( \frac{1}{2S_{Vgr}^2} \right) \frac{\epsilon^3}{(1 - \epsilon)^2} \quad [2.33]$$

### 2.2.5. Modifications on Kozeny's equation

When a fluid passes through a porous material, it flows through long thin tortuous passages of varying cross section. Kozeny and Carman tackled the problem of how to calculate the flow rate based on nominal thickness of the layer. The important assumption to be taken into account before reviewing their models is that the passage between the particles is so small that the velocity in them is small and flow is well and truly laminar ( $Re < 1$ ). As it is shown in Figure 2.8, Kozeny modelled the layer as many small capillary tubes of diameter  $D$  making up a layer of cross-sectional area  $A$ . The actual cross-sectional area for the flow path is  $A'$ . The ratio of  $A'/A$  is the porosity of the material. The volumetric flow rate through the layer is  $Q$ .

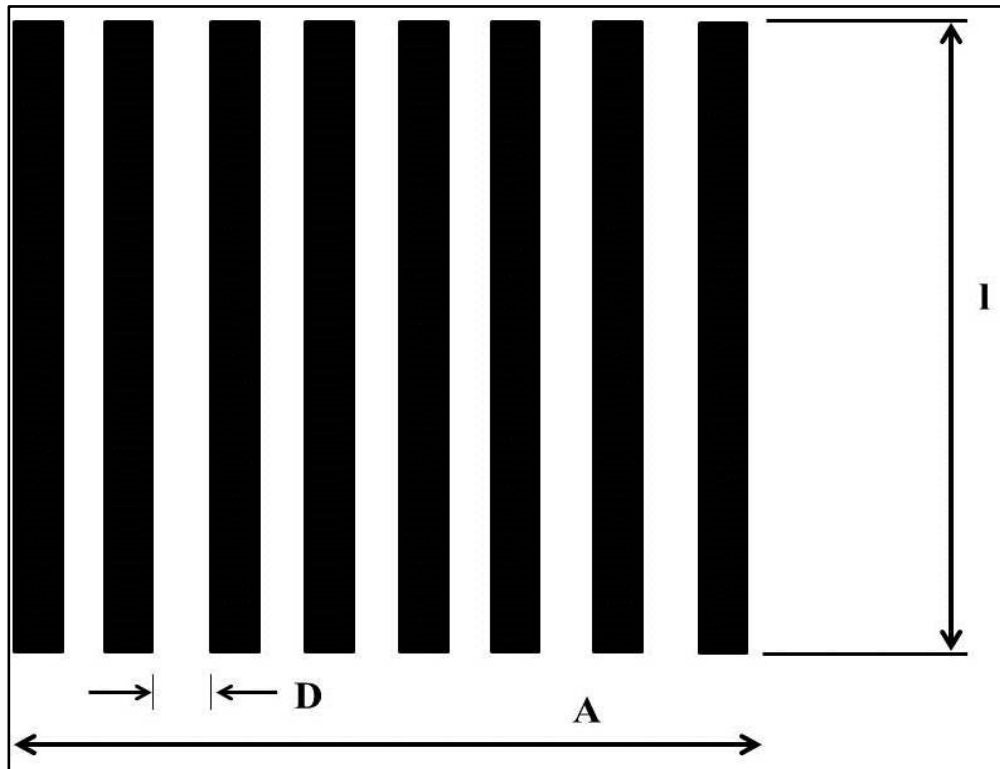


Figure 2.8. Kozeny model

By knowing  $Q=Au$  and  $Q=A'u'$ , we have:

$$\dot{u} = \frac{A}{A'}u = \frac{u}{\epsilon} \quad [2.34]$$

Carman modified this formula when he realised that the actual velocity inside the tubes must be proportionally larger because the actual length is longer than the layer thickness. In other words, all the above equations were based on the assumption that the porous medium can be represented by a bundle of straight capillary tubes. However, the actual length the fluid passes through is greater than the length  $L$  of the capillary tubes. Therefore:

$$\dot{u} = \frac{u \dot{l}}{\epsilon l} \quad [2.35]$$

Substituting in Equation [2.25], Poiseulle equation can be modified as:

$$\frac{\Delta P}{l} = \frac{dP}{dx} = -\frac{32\mu u \dot{l}}{\epsilon D^2} \quad [2.36]$$

We can define the porosity in terms of cross-sectional surface area and consequently volume of solids and tubes as follows:

$$\epsilon = \frac{\dot{A}}{A} = \frac{\dot{A}}{\dot{A} + A_s} \quad [2.37]$$

Where  $A_s$ ,  $\dot{A}$ , and  $A$  are cross-sectional areas of the solids, the tubes, and the layer, respectively. Multiplying numerator and denominator of Equation [2.37] by the length 'l' results in:

$$\epsilon = \frac{\dot{Q}}{\dot{Q} + Q_s} \quad [2.38]$$

By rearranging Equation [2.38]:

$$\dot{Q} = \frac{\epsilon}{1 - \epsilon} Q_s \quad [2.39]$$

Dividing both sides by  $S$ :

$$\frac{\dot{Q}}{S} = \frac{\epsilon}{1 - \epsilon} \frac{Q_s}{S} \quad [2.40]$$

Where

$$\dot{Q} = \frac{n\pi D^2 \dot{l}}{4} \quad [2.41]$$

And

$$S = 2\pi n R \dot{l} = n\pi D \dot{l} \quad [2.42]$$

Substituting Equations [2.41] and [2.42] into Equation [2.40] yields:

$$D = \frac{4\epsilon Q_s}{S(1 - \epsilon)} \quad [2.43]$$

For spherical solids,

$$Q_s = \frac{\pi d_s^3}{6} \quad [2.44]$$

And

$$S = \pi d_s^2 \quad [2.45]$$

Hence, Equation [2.43] may be rewritten as:

$$D = \frac{2}{3} \frac{\epsilon d_s}{(1 - \epsilon)} \quad [2.46]$$

Substituting this into Equation [2.36], one can write:

$$\frac{dP}{dx} = - \frac{72\mu u \dot{l} (1 - \epsilon)^2}{l \epsilon^3 d_s^2} \quad [2.47]$$

Finally, research has shown that the ratio of ( $\dot{l}/l$ ) is about 2.5, so:

$$\frac{dP}{dx} = - \frac{180\mu u (1 - \epsilon)^2}{\epsilon^3 d_s^2} \quad [2.48]$$

This equation is known as Kozeny-Carman equation.

The same calculations were done in order to find the relationship between the permeability and the porosity of the porous medium. Equation [2.49] is the modified form of Kozeny's model.

$$k = \left( \frac{1}{5S_{V_{gr}}^2} \right) \frac{\epsilon^3}{(1 - \epsilon)^2} \quad [2.49]$$

where  $S_{V_{gr}}$  is the specific surface area of the grains.

### **2.2.6. Flow behaviour of polymer-based fluids in porous media**

The flow of polymer solutions in porous media is considered in many technologies nowadays such as filtration, polymer processing and enhanced oil recovery. Important information in all these applications is the relationship of pressure drop and flow rate (velocity) of the flow in the porous medium that can be related to the characteristics of the porous medium and that of polymer solution. The first and simplest way to describe the flow in porous medium is to assume Newtonian behaviour for the flow as mentioned earlier. Darcy's law has proven to be an excellent model for this case. Darcy's law states that with known permeability and solution viscosity, the pressure drop can be calculated as a function of the superficial velocity. The higher the velocity, the larger the pressure drop.

The case of flowing in porous media is not as simple for non-Newtonian fluids such as polymer solutions [38]. Sometimes the size of polymer molecules is as large as the pores that results in interaction between polymer molecules and wall. This interaction can be adsorption, mechanical entrapments and etc. That is why the first assumption to develop a model for the flow of non-Newtonian solutions in porous media would be a high permeable porous medium where the molecule-pore wall interactions can be neglected.

The situation is still complicated, because some polymers such as polyacrylamide and polyethylene oxide exhibit viscoelastic behaviour and excess pressure drops may happen. In addition, inertial effects may alter the behaviour of all solutions in porous media including Newtonian ones due to high flow rates.

Having considered all these limits, the ideal model for the flow of polymer solution through porous media neglects elastic effects as well as inertial and molecule-wall

interactions. In other words, the ideal situation is considering a polymer solution with short relaxation time flowing at low velocities (creeping flow) in high permeability porous media.

Attempts were made to modify the Darcy equation to make it applicable for non-Newtonian polymer solution. First of all, the pore structure was assumed as a group of capillary tubes that shows similar resistance to flow as the porous medium. This modelling technique is presented by Bird et al in 1960. This led to the well-known Blake-Kozeny-Carman equation that was discussed in detail above.

One can add the flow rheological behaviour to the approach to consider the flow of purely viscous non-Newtonian solution. Power-law and Ellis model fluids are examples of this modification. The pressure drop-flow rate relationships for these rheological behaviours were tabulated in Duda et al work [38].

Most studies have used the power-law model suggested by Duda et al as this model is based on the coupling of the capillary model for the porous medium and the power-law model for the fluid rheology. However, some experiments exhibit that the predicted pressure drop based on this model is lower than experimental one [39]. That may be due to the viscoelastic properties of the polymer solutions. Polymer solutions such as CMC, Hydroxyethyl cellulose (HEC), xanthan gum, and cellulose sulphate ester in porous media are in good agreement with the capillary models as reported by Wang et al. However, polymer solutions containing polyacrylamide and polyethylene oxide (PEO) exhibited larger pressure drops than those of predicted.

First of all, most porous media do not follow capillary tubes model and consist of many sharp bottlenecks. In other words, porous media are cavities connected by pores. It is obvious that excess pressure drops happen at these points of contraction and expansion when fluid velocity is high. Even under creeping flow conditions, excess pressure drops occur at sharp expansions and contractions. That means, regardless of the effect of inertial or viscous forces, excess pressure drops happen at abrupt contractions and expansions. This reveals the inadequacy of capillary models for the flow of polymer solutions in porous media [38]. If the failure is related to the excess pressure drop near contraction and expansion regions, a new model which incorporates this expansion-contraction effect should be proposed. The porous

media can be modeled as a group of non-uniform conduits with the periodic geometry as shown in Figure 2.9.

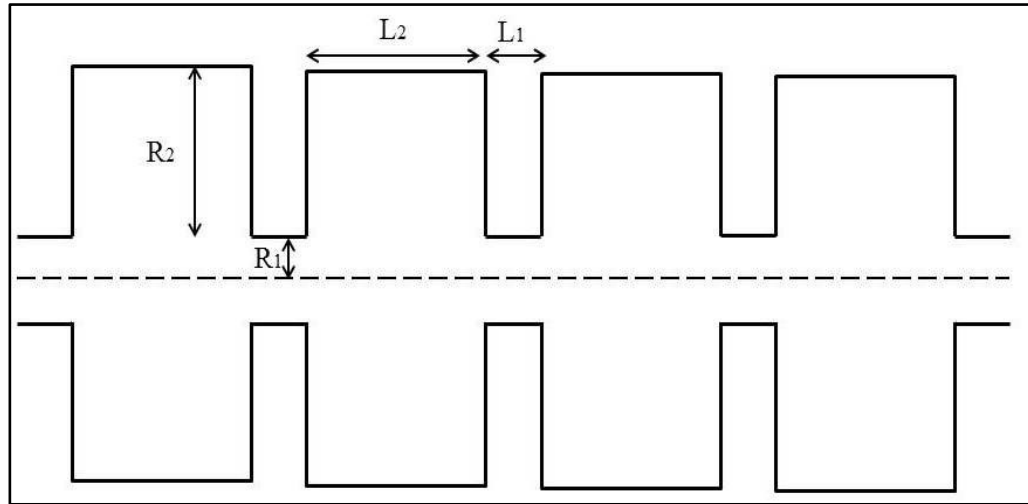


**Figure 2.9. Schematic diagram of pore model**

Additionally, the rheological model for the fluid must include the transition from Newtonian behaviour at low shear rates to shear thinning behaviour at high shear rates. It was reported that the Ellis rheological model altogether with a non-uniform pore model (Figure 2.9) has the capacity of being used to describe the flow of polymer solutions in porous media [38].

The pressure drop in polymer flow through porous media is attributed to shear and elongational forces as reported by Gonzalez et al. [40]. Most real flows have both shear and elongational elements. Elongation is important when the fluid passes through changing cross-sectional area such as porous media or diverging-converging channel. Therefore shear and elongation should be investigated separately in order to study of the polymer flow through porous media. The pressure drop between the entrance and exit sections was measured as a function of flow rate and results are reported in terms of the dimensionless resistance coefficient,  $\Lambda$ , as follows:

$$\Lambda = \frac{d^2 \phi^3 \left( \frac{\Delta P}{L} \right)}{\mu \nu (1 - \phi)^2} \quad [2.50]$$

where  $\Delta P$  is the pressure drop over a length  $L$  of porous medium,  $\phi$  the medium porosity,  $d$  the particle diameter,  $\mu$  the viscosity of solvent and  $\nu$  is the superficial velocity.

If shear flow dominates the behaviour of the solutions in porous media at low Reynolds number, the dimensionless resistance coefficient is proportional to the shear viscosity [40]. In other words,

$$\frac{\Lambda}{\Lambda_w} = \frac{\eta}{\eta_w} \quad [2.51]$$

where  $\Lambda_w$  is the resistance coefficient of water at low Reynolds numbers and is about 200 [40]. Based on these theories, one can compare different flow formulations in terms of their pressure drop and resistance in porous media.

### 2.3. Rheology of mud suspensions

The rheology of mud suspensions is of great importance to predict their behaviour in different borehole conditions. This science is concerned with the deformation of all forms of matter, but it is more significantly developed in the study of fluid flow in pipes. Based on two different flow regimes, laminar and turbulent flow, several pressure-velocity relationships are developed. The laminar flow regime happens at low flow velocities, while the turbulent flow is dominant at high velocities [1].

Certain flow models are relating flow behaviour to the flow characteristics in laminar flow such as the Newtonian, the Bingham plastic, the pseudoplastic, and the dilatant. We consider the first three models in drilling fluid technology.

Most mud suspensions do not fit exactly to any of these models, but their behaviour can be predicted sufficiently by one or more of them. Flow behaviour can be visualized by plotting shear stress versus shear rate, or flow pressure versus flow rate for example.

### 2.3.1. Laminar flow of Newtonian fluids

As illustrated in Figure 2.10, if a force,  $F$ , is applied to the end of the top plane, and if, due to friction, the velocity of each lower planes decrease by a constant,  $dv$ , from  $v$  to zero, then we have:

$$\frac{F}{A} = \tau = -\mu \frac{dv}{dr} \quad [2.52]$$

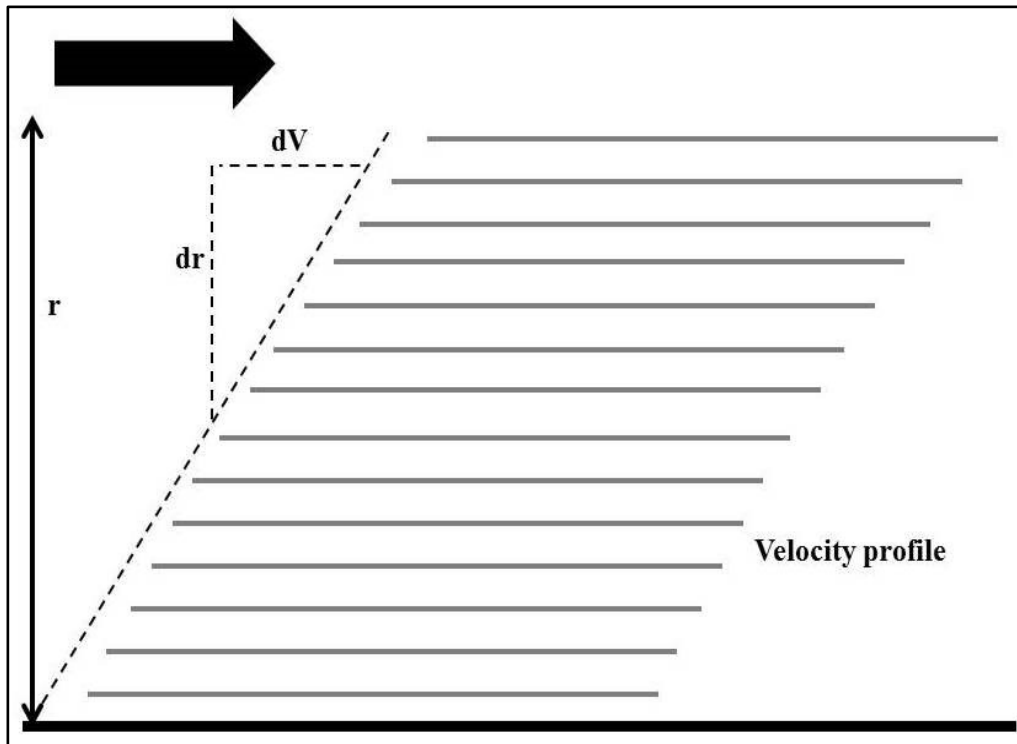


Figure 2.10. Schematic illustration of laminar flow of a Newtonian fluid

Where  $A$  is the surface area,  $r$  the thickness of the deck,  $dv$  the difference in velocity between the planes,  $\mu$  the frictional resistance to movement between planes,  $\tau$  the shear stress, and  $dv/dr$  the shear rate.

The consistency curve, the so-called flow model curve, of different rheological models is illustrated in Figure 2.11. As it can be seen, the Newtonian fluid behaviour is straight line passing through the origin, and the slope of the curve defines the viscosity.

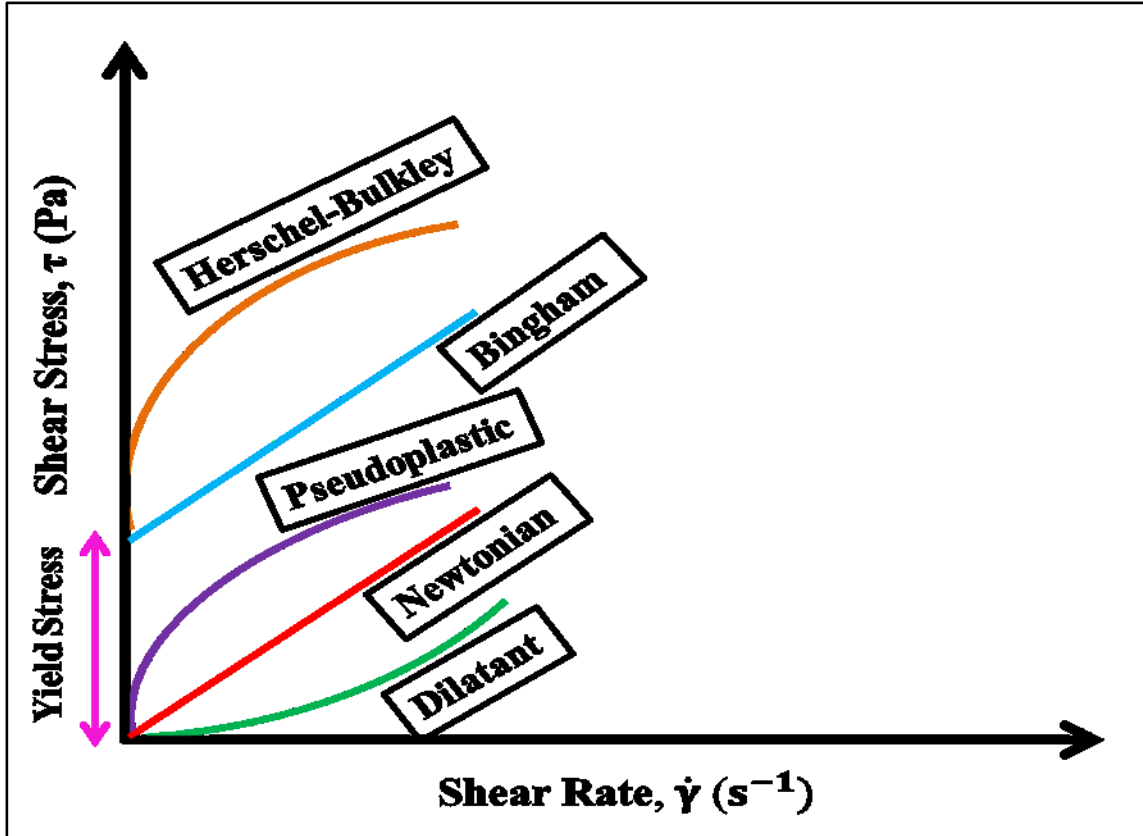


Figure 2.11. Schematic of different rheological models

### 2.3.2. Bingham plastic model

Bingham plastic fluids are distinguished from Newtonian fluids in that they require a finite stress to initiate flow. The relationship is as follows:

$$\tau - \tau_0 = -\mu_p \frac{dv}{dr} \quad [2.53]$$

where  $\tau_0$  is the stress required to initiate flow, and  $\mu_p$  is the plastic viscosity. Studies showed that drilling fluids are not ideal Bingham plastics, and they deviate from linearity at low shear rates [1]. This behaviour can be explained as follows: Ideal Bingham plastic

behaviour happens when a high concentration of approximately equidimensional particles exists in the suspension. This concentration is high enough to build a structure by grain-to-grain contact. This structure resists shear due to attractive inter-particle friction. Once the yield point is exceeded, and laminar flow begins, there is no longer interaction between particles and viscosity is only affected by the volume the particles occupy.

### 2.3.3. Pseudoplastic fluids

The “pseudoplastic” term originates from the fact that if stress readings taken at high shear rates are extrapolated back to the axis, there appears to be a yield point similar to that of a Bingham plastic. However, these fluids have no yield point and their consistency curves pass through the origin. The curves are nonlinear, but approach linearity at high shear rates. Suspensions of long-chain polymers are typically pseudoplastics. The chains are entangled at rest, but they do not form a structure because of repulsive electrostatic forces. The chains tend to align themselves parallel to the flow direction when the fluid is in motion. Increase in shear rate results in more parallel alignment that leads to viscosity decrease. An empirical equation describes this behaviour, the so-called power law model, as follows:

$$\tau = K \left( \frac{dv}{dr} \right)^n \quad [2.54]$$

where K is the viscosity at a shear rate of 1 sec<sup>-1</sup>, and n is the flow behaviour index. This index indicates the degree of shear thinning. Less value of n results in greater shear-thinning characteristic. As a recall, the viscosity of shear thinning fluids decreases with shear rate increase, while the viscosity of shear thickening fluids increases when the shear rate increases. Thixotropic fluids are also categorized under shear thinning fluids with time dependency property.

### 2.3.4. The generalized power law

The ideal power law describes three flow models based on the n value:

1. Pseudoplastic for n<1,
2. Newtonian for n=1, and
3. Dilatant for n>1.

Equation [2.54] may be expressed as:

$$\log \tau = \log K + n(\log \dot{\gamma}) \quad [2.55]$$

where  $\dot{\gamma}$  is the shear rate (dv/dr).

Plotting a logarithmic curve of shear stress versus shear rate results in a linear line for pseudoplastic fluid; however, these curves are not linear for most drilling fluids, contrary to the ideal power law. The consistency curves of most drilling fluids are intermediate between the ideal Bingham plastic and the ideal pseudoplastic flow models. Therefore, it can be expressed as follows:

$$\tau = \tau_0 + \mu \dot{\gamma}^n \quad [2.56]$$

This model is known as Herschel-Bulkley and is very precise for modelling drilling fluids rheological behaviour. It will be discussed with more detail in Chapter 5.

### **2.3.5. Rheology of bentonite clay suspension**

Clay suspensions frequently exhibit a time dependent, the so-called thixotropy, flow behaviour. After mixing the suspension, the yield stress and viscosity decrease but will recover with time if left standing. Concentrated clay suspensions are very sensitive to shear, therefore their rheological properties will change with time. If the shear rate is strengthened and immediately decreased, the stresses recorded for each shear will be lower. This phenomenon happens because of the required time for broken fragments of the network to be linked again to a three-dimensional network. When the clay system is subjected to a constant shear rate, the viscosity decreases with time because the gel structure is collapsed, until an equilibrium viscosity is reached. Different factors affect the flow behaviour of clay suspensions. Due to the negatively charged particles and double-layer structure, the yield stress and viscosity vary with changes in pH of the suspension and electrolyte concentration. When temperature increases, it leads to an increase in inter-particle attractive forces those results in enhanced particle-particle interactions. Viscosity of clay suspension is dependent on the viscosity of the medium which is also temperature dependent. In addition, the liquid viscosity increases exponentially and clays and liquids are compressed differentially with pressure that may alter the flow properties [41].

Some studies show the flow behaviour of sodium montmorillonite suspensions are in relatively good agreement with Bingham model [42, 43]. Some others exhibit the flow behaviour as Herschel-Bulkley model. The advantage of using the latter model is that it covers a broader shear rate scope, giving a better estimate of the yield stress. Also, it is useful for obtaining other parameters such as the flow behaviour index  $n$ , consistency factor  $k$ , and effective viscosity  $\mu$  [44].

Increase in electrolyte concentration leads to double-layer compression. The result is the network break down accompanied by the lowering of the rheological properties.

Based on another study, from 3% of bentonite suspension, the non-Newtonian behaviour becomes more visible. This yield stress is strengthened with increase in bentonite concentration [45].

### 2.3.6. Rheology of CMC suspension

Many studies have been done on CMC rheological properties [46]. It was reported that Newtonian behaviour at the lowest concentration and pseudoplastic, thixotropic behaviour at the higher-end concentration were observed in the concentration range 1-5%. By increasing CMC concentration at a constant shear rate, the apparent viscosity increases. This is because of the increase in the intermolecular interactions between CMC molecules. The rheological behaviour of CMC suspensions can be expressed by Cross model as follows:

$$\frac{\mu - \mu_{\infty}}{\mu_0 - \mu_{\infty}} = \frac{1}{1 + (\lambda_c \cdot \dot{\gamma})^n} \quad [2.57]$$

where  $\mu$  is the viscosity at any shear rate  $\dot{\gamma}$ ,  $\mu_0$  and  $\mu_{\infty}$  are viscosities at zero and infinite shear rates, respectively,  $\lambda_c$  is a time constant with the dimensions of time and  $n$  is the degree of dependence of viscosity on shear rate (flow behaviour index). As “ $n$ ” increases, CMC suspension flow behaviour tends to more shear thinning manner. Cross model parameters are given in Table 2.3.

**Table 2.3. Cross model constants of CMC suspensions [46]**

<b>CMC (%)</b>	<b><math>\lambda_c</math> (sec)</b>	<b>n</b>	<b><math>\mu_0</math> (Pa.s)</b>	<b><math>\mu_\infty</math> (Pa.s)</b>
0.2	0.010	0.67	0.019	0.001
0.4	0.016	0.65	0.045	0.001
1.0	0.088	0.61	0.530	0.003
2.0	0.287	0.66	6.355	0.024
3.0	0.865	0.69	48	0.040
5.0	1.804	0.67	200	0.045

CMC suspensions are strongly time-dependent materials, so they are strongly thixotropic. This dependency is due to the changes occurring in the inner structure of the fluid caused by particle interaction forces such as van der Waals forces. These forces act in microscopic scale and lead to the formation of a rigid continuous particle network which can resist the flow.

### **2.3.7. Rheology of bentonite-CMC suspension**

The addition of cellulose-based additives to clay suspensions has been taken into account significantly due to their colloidal and rheology modifying capacity. Their applications in cosmetics, chemical paints, food products, and specifically in water-based drilling fluids make them interesting materials to work with [41]. They enable clay-based drilling mud to fulfill its functions such as stabilizing the borehole (cake formation), cleaning the hole (evacuating the cuttings), and cooling and lubricating the string and the bit. Among many cellulose-based additives, CMC is a great material for increasing the viscosity, controlling the mud fluid loss, and maintaining enough flow properties at high temperature-high pressure (HPHT) condition.

The effect of CMC addition on the rheological properties of bentonite clay suspensions has been studied and experimented thoroughly [45, 47]. An increase in apparent viscosity is observed by increase in CMC concentration. This is because of more polymer chain entanglements due to concentration increment. All flow curves show a shear-thinning behaviour [45]. One can use the power law model of Oswald-de Waele within a wide scope of

shear rates ( $\geq 10 \text{ s}^{-1}$ ). The Oswald model is defined in Equation [2.58] and its parameters are tabulated in Table 2.4.

$$\tau = k. \gamma^n \quad [2.58]$$

**Table 2.4. Rheological parameters of Oswald model for bentonite-CMC suspension [45]**

CMC (%)	$\tau_0$ (Pa)	k (Pa.s <sup>n</sup> )	n
0.00	0.19	0.0011	1.28
0.10	0.0	0.0132	1.01
0.25	0.0	0.0976	0.78
0.50	0.0	0.5511	0.63
1.00	0.0	1.5571	0.59
2.00	0.0	14.1038	0.47

As it is obvious in Table 2.4, increase in CMC concentration results in flow index reduction and disappearance of the yield stress,  $\tau_0$ . That is due to the chemical structure of CMC, which allows the full dispersion of the clay particles.

In conclusion, the rheological behaviour of the anionic polymer solution (additives), predominates that of the bentonite suspension alone. The addition of merely a small amount of these additives in the suspension makes a considerable increase in viscosity value that makes cellulose-based polymers (CMC) interesting in water-based drilling mud.

First and foremost is the formulation and composition of drilling suspension. Drilling fluids are basically composed of clay minerals including sodium or calcium montmorillonite plus some additives. Additives can serve as corrosion control, emulsifiers, lubricants, thinners and deflocculants, weighting and filtration control agents, and viscosifiers. In this research, CNC rod-like particles and CMC polymer were utilized in order to enhance filtration, stability and rheological behaviour of Wyoming clay water-based drilling mud.

Secondly, rheological stability of drilling mud was investigated in the presence of CNC and CMC. Rheological behaviour of drilling mud is one of the necessary parameters affecting its performance in drilling operation [48].

### **2.3.8. Rheology of CNC suspensions**

Rod-like CNC particles are prepared by acid hydrolysis of dissolved pulp or cotton with concentrated (65%) sulfuric acid [49-51]. This process produces CNC particles of typically 5 – 10 nm width and 100 – 300 nm length. High aspect ratio in these materials is expected consequently. There are many comprehensive studies reviewed on CNC and its applications in nanocomposites, films, and coatings [52]. Rod-like CNC particles in aqueous solutions are negatively charged due to the formation of sulfate groups on their surface. Similar to other types of nanoparticles, the surface charge on CNC particles and organization of counter and co-ions in electrolyte solution form an electric double layer around the particles. Therefore at low ionic strength, electrostatic repulsion of thick double layers around these particles produces stable CNC dispersions in aqueous solutions [53]. Rheological properties of aqueous suspensions of cellulose nanocrystals were investigated in the literature [53-55], but not a quite understanding of CNC effect in rheological behaviour of bentonite suspensions is achieved yet.

In this study, the effect of carboxymethyl cellulose and cellulose nanocrystals on the rheology of bentonite suspensions will be investigated. Moreover, the synergistic behaviour of CNC rods and CMC in rheology of bentonite suspension is discovered. Finally, the effect of these cellulose derivatives on the flow parameters of bentonite suspension will be discussed.

## **3. Materials and methods**

The target of this research is to achieve a workable formulation of clay mud and to optimize it based on considering the effects of other experimental conditions such as temperature, differential pressure, shear rate, and porosity of filters. Achieving a reliable feasible formulation makes it possible to implement filtration and rheological experiments and to understand filtration mechanisms in microscopic level that results in better control over fluid loss issue.

### **3.1. Materials**

#### **3.1.1. Clay minerals**

Clay minerals are of a crystalline nature, and the atomic structure of their crystals is the prime factor that determines their properties. Most clays have a mica-type structure. The unit layers are stacked together face-to-face to form what is known as the crystal lattice. The sheets in the unit layer are tied together by covalent bonds, so that the unit layer is stable. On the other hand, the layers in the crystal lattice are held together only by van der Waals forces and secondary valences between juxtaposed atoms. Consequently, the lattice cleaves readily along the basal surfaces, forming tiny mica-like flakes. The degree of substitution, the atoms involved, and the species of exchangeable cations are of enormous importance in drilling fluids technology because of the influence they exert on such properties as swelling, dispersion, and rheological and filtration characteristics.

Among the clay mineral groups of interest, the Smectites are of great importance. Smectites have an expanding lattice, which greatly increases their colloidal activity, because it has the effect of increasing their specific surface many times over. Montmorillonite is by far the best known member of the Smectite group, and has been extensively studied because of its common occurrence and economic importance. It is the principal constituent of Wyoming clays, and of many other clays added to drilling fluids.

Other clay mineral groups are Kaolinites, Chlorites, Attapulgites and Sepiolites. Layers of different clay minerals are sometimes found stacked in the same lattice. The last two groups are completely different in structure and shape from the mica-type minerals

discussed so far. They consist of bundles of fibers, which separate to individual laths when mixed vigorously with water [1]. Sepiolite is a fibrous clay mineral similar to Attapulgite. When slurries of Sepiolite are subjected to high shear rates, the bundles of fibers separate to innumerable individual fibers. Mechanical interference between these fibers is primarily responsible for the rheological properties, and Sepiolite muds are therefore little affected by the electrochemical environment.

The experimental clays are readily available in Sigma Aldrich. 3% w/v composition was selected for clay portion in drilling mud suspension as an optimum value.

### 3.1.2. Carboxymethyl cellulose (CMC)

Figure 3.1 illustrates carboxymethyl cellulose molecular structure. Carboxymethyl cellulose (CMC), a non-adsorbing anionic polymer, is obtained by the reaction of celluloses with chloroacetic acid. It has a very high water-bonding capacity, good compatibility with skin and, because it is physiologically harmless, is used widely in pharmacy, cosmetics and the food industry in order to improve the consistency and flow properties. Its molecular weight ranges from 700-900 kDa. 0.25% w/v concentration of CMC was used in the experiments for stability and viscosity modification. It is readily available to purchase from Sigma Aldrich.

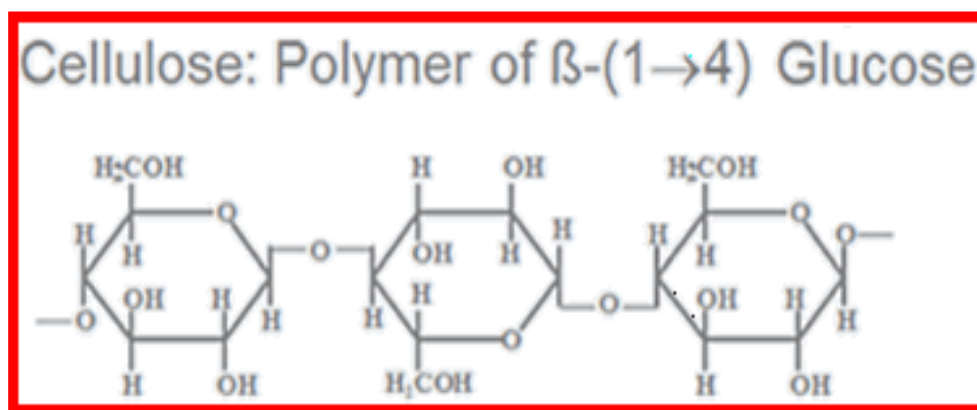
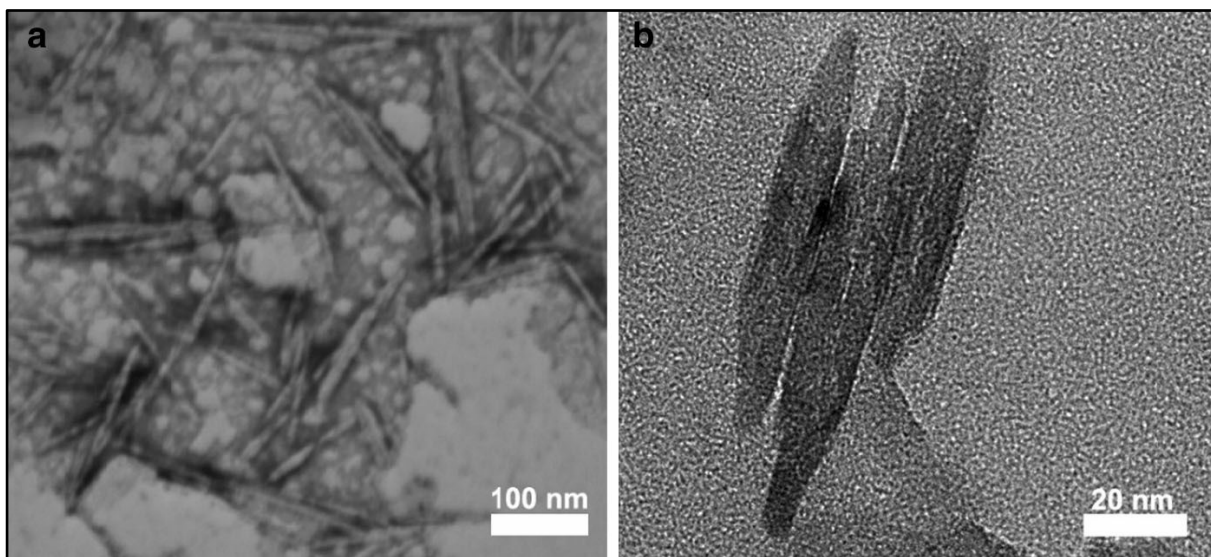


Figure 3.1. Carboxymethyl cellulose (CMC) structure

### 3.1.3. Cellulose nanocrystals (CNC)

Rod-shaped CNC was prepared by acid hydrolysis of dissolving pulp or cotton with concentrated (65%) sulfuric acid. This process generates CNC particles with typically 5–10

nm width and 100–300 nm length. CNC particles in aqueous solutions carry negative electrical charges due to the formation of sulfate groups on their surface. The CNC particles have zeta potential of  $-62.8\text{mV}$  without any addition of electrolyte reported by Boluk et al [53]. 1% (w/v) CNC suspensions were prepared for the experiments. The CNC particles were provided from Alberta Innovates-Future Technology (AITF). Figure 3.2 (a,b) shows SEM and TEM images of these rod-like nanoparticles.



**Figure 3.2. SEM (a) and TEM (b) images of CNC particles [55]**

### **3.1.4. Sample preparation**

Colloidal suspensions were prepared with the formulation including 3% w/v Wyoming clay in tap water with or without 0.25% w/v carboxymethyl cellulose (CMC) and/or cellulose nanocrystal (CNC) rod-shaped particles in diluted concentrated regimes. The maximum percentage of CNC used was 1% w/v. All the materials are readily available at Sigma Aldrich. As it is observed in Figure 3.3, each material (bentonite, CMC, CNC) was dispersed separately in tap water using a high shear (2500-3000 RPM) mechanical stirrer until a homogeneous solution of each was achieved. Afterwards, all solutions were added to another beaker and mixed completely till a homogeneous stable suspension was achieved. Figure 3.4 is a homogeneous, stable suspension of bentonite clay containing CMC and CNC. Mixing

technique requires a lot of attention, because the filtration process requires a well-mixed viscous suspension to obtain more realistic filtration data.



**Figure 3.3. Materials dispersion in water before final mixing**



**Figure 3.4. Drilling fluid suspension**

## 3.2. Rheological experiments

Rheology measurements of colloidal suspensions were carried out on a TA Instruments AR-G2 rheometer as illustrated in Figure 3.5. Four different formulations were tested as follows:

- Bentonite clay
- Bentonite clay + CMC
- Bentonite clay + CNC
- Bentonite clay + CMC + CNC

The rheometer is equipped with 2° cone and plate geometry of 60 mm in diameter. The torque resolution is 0.1 $\mu$ N. The temperature was controlled by a water bath with an accuracy of 0.1 °C. For each sample, at least three measurements were made to obtain an average flow time. Standard deviations were calculated based on the triplication of experimental data. All rheology measurements were performed at ambient temperature.



(a)

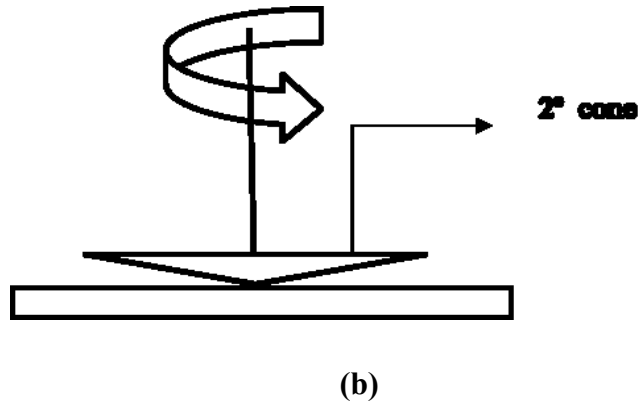


Figure 3.5. (a) TA Rheology instrument-model AR-G2, (b) Cone & plate geometry

### 3.3. Dynamic filtration experiments

As it is shown in Figure 3.6, the FANN 90 Dynamic Filtration apparatus was used for simulating high pressure-high temperature (HPHT) dynamic filtration. It is a computerized instrument for conducting filter cake formation, fluid loss, and permeability analysis. Utilizing a selection of available Filter Core mediums and selecting one that closely resembles the formation of interest, the Model 90 simulates the downhole conditions of pressure, temperature and shear rate. Test parameters input into the Model 90 will optimize the test simulation. The Filter Core medium is a thick walled cylinder with formation-like characteristics to simulate the depositing and build-up of cake on the formation. Nominal core dimensions are tabulated along with the mean pore sizes and porosity values in Table 3.1. The porosity and permeability simulates the fluid loss to the formation. The fluid loss rate can be tracked and calculated as well as the fluid loss volume measured. High static pressure of maximum 7238 kPa and differential pressure of up to static test pressure as well as temperature range of ambient to 260° C can be provided by The FANN 90 Dynamic Filtration apparatus to simulate high pressure high temperature (HPHT) conditions. The specifications of Dynamic Filtration apparatus are tabulated in Table 3.2.



**Figure 3.6. FANN 90 Dynamic Filtration apparatus**

**Table 3.1. Filter core(s) specifications**

<b>Nominal core dimensions</b>	<b>Porosity (mean pore diameter)</b>	<b>Permeability (air)</b>
Inside Diameter: 2.57 cm	10 micron	950 milli-Darcy
Outside Diameter: 3.83 cm	35 micron	5.5 Darcy
Length: 2.83 cm	90 micron	13.5 Darcy

**Table 3.2. HPHT Fann 90 Dynamic Filtration Apparatus Specifications**

<b>Specification</b>	<b>Range</b>
Temperature	Ambient-260° C
Static Pressure	Max. 7238 KPa
Differential Pressure	Up to static pressure limited by strength of the filter
Shear Rate	8.1-269 s <sup>-1</sup> (30-1000 RPM)
Filtrate Volume	Max. 50 ml
Sample Volume	275 ml
Filter Core Pore Sizes	5-90 micron (0.75-75 darcy)

Dynamic filtration tests were carried out using high temperature, high pressure cross flow dynamic filtration apparatus. Static pressure of 4.1 MPa was selected as a constant value. All the other test conditions such as differential pressure, temperature, shear rate, and filter pore sizes were selected according to the water phase diagram and shown in Table 3.3. The selected values confirm that the experiments were carried out in liquid phase and no phase change occurred. Filtration properties such as total volume loss, filtration rate and spurt loss volume were tabulated for the given drilling fluid formulations in Table 4.9 in Chapter 4. Spurt loss volume, which is considered as the volume of filtrate, obtained initially when filtration begins for the 10 first seconds, is one of the key parameters that should be lowered to optimize the filtration. In addition, filtration rate, which is the rate of change in the filtrate volume vs. time, is essential under in situ condition particularly in dynamic state. The lower the filtration rate, the better for most oil well drilling fluid systems (less than 0.2 ml/min). Moreover, the amount of mud filtrate must be lowered to decrease the probability of borehole instability problems and damage to permeable formations [56]. Similar formulations were used for colloidal suspensions. All data were obtained based on API standard dynamic filtration process in 30 minutes. The total volume loss is presented as a ratio percentage.

**Table 3.3. Dynamic Filtration Experimental Condition**

<b>Experimental Condition</b>	<b>Range</b>
Hydrostatic Pressure (HP)	4.1 MPa
Differential Pressure (DP)	0.69 – 1.7 MPa
Temperature (T)	29 – 150 °C
Shear Rate	10 , 100 s <sup>-1</sup>
Filter Mean Pore Size	10 , 35 , 90 micron

Filtration properties of drilling muds such as spurt loss volume, filtration rate, and the amount of drilling fluid invasion through porous media are the key properties to be determined and optimized in order to make a safe and productive operation. The lower the total volume loss and the filtration rate, the better for most oil well drilling fluid systems (usually filtration rate of less than 0.2 ml/min is acceptable). Moreover, the amount of mud filtrate must be lowered to decrease the probability of borehole instability problems and damage to permeable formations.

The schematic of dynamic filtration apparatus is illustrated in Figure 3.7 . The main advantage of dynamic filtration, the so-called “cross flow filtration”, is the formation of filter cake, which is substantially detached and reattached during the filtration process, and it can increase the length of time that a filter unit can be operational. To better explained, this system is a continuous process unlike the batch-wise dead-end filtration. Filtration phenomenon of drilling fluid in borehole is static if the filtration happens after stopping the mud circulation. Under static filtration conditions, the filtration and cake properties are not well determined, while the measurement of dynamic filtration under continuous mud circulation and dynamic borehole conditions is particularly significant in order to mimic actual downhole conditions.

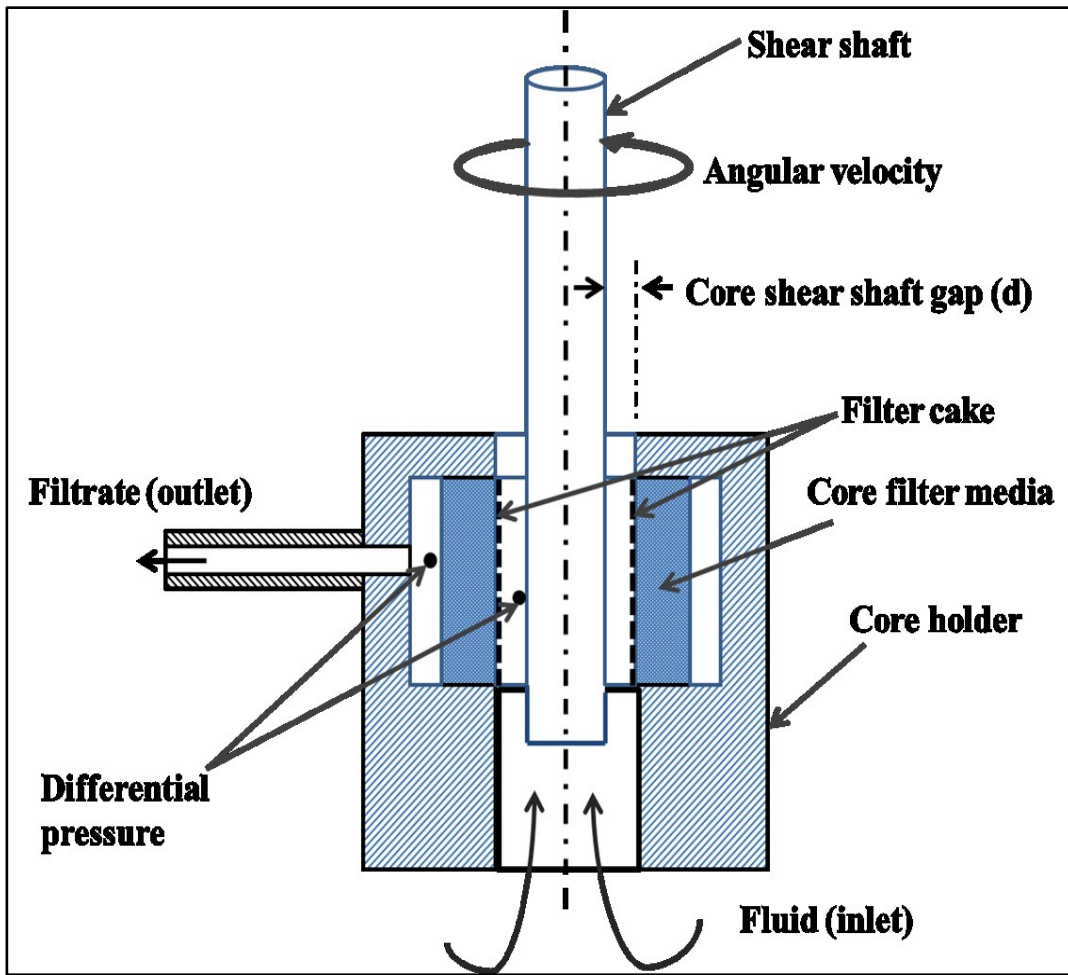


Figure 3.7. Schematic of dynamic filtration apparatus

### 3.4. Quartz crystal microbalance with dissipation (QCM-D) experiments

Quartz crystal microbalance with dissipation (QCM-D) is an advanced technology for the study of surface interactions and deposition behaviour of colloidal particles. Based on piezoelectric effect, the frequency change of a quartz crystal sensor is related to the mass loading on the quartz surface; the change of the dissipation indicating the energy dissipation response of the freely oscillating sensor is corresponding to the viscoelastic properties of molecular layers when they are built up or changed on the sensor surface. The QCM-D technology can provide sensitivity to nano-grams of mass and can be applied to in situ

structural arrangements; therefore, it is a useful technique to study small colloidal particles deposition on different model surfaces. It was recently shown that data obtained from QCM-D could be used to determine the size of particles deposited on a surface as well [57]. This technique may be disadvantageous when operated in liquids in biological systems, because both the bound mass and the bulk solution properties such as viscosity, pH, density, etc. may provide a decrease in the frequency, falsifying the results.

Q-Sense E4 instrument as shown in Figure 3.8 was used to carry out QCM-D measurements for real-time studies of surface or surface-bound processes such as interactions and changes of mass. The instrument is the second generation of Q-Sense instruments based on the patented QCM-D technique, and constitutes a complete turnkey system including everything needed to quickly get started and produce high quality data. Some remarkable features of this instrument are tracking mass changes, real-time presentation of data, no need for labeling of molecules, flexible choice of surfaces, flow measurements, 4-sensor chamber, and easy cleaning.



**Figure 3.8. Q-Sense E4 instrument**

As illustrated in Figure 3.9, parallel-plate model surface geometry was selected for QCM-D experiments. Parallel-plate channels have been used in several theoretical and experimental studies of particle deposition. Its simplicity makes it a considerable tool to investigate the kinetics of particle deposition onto stationary surfaces [58]. Instrument specifications and experimental conditions are tabulated in Table 3.4.

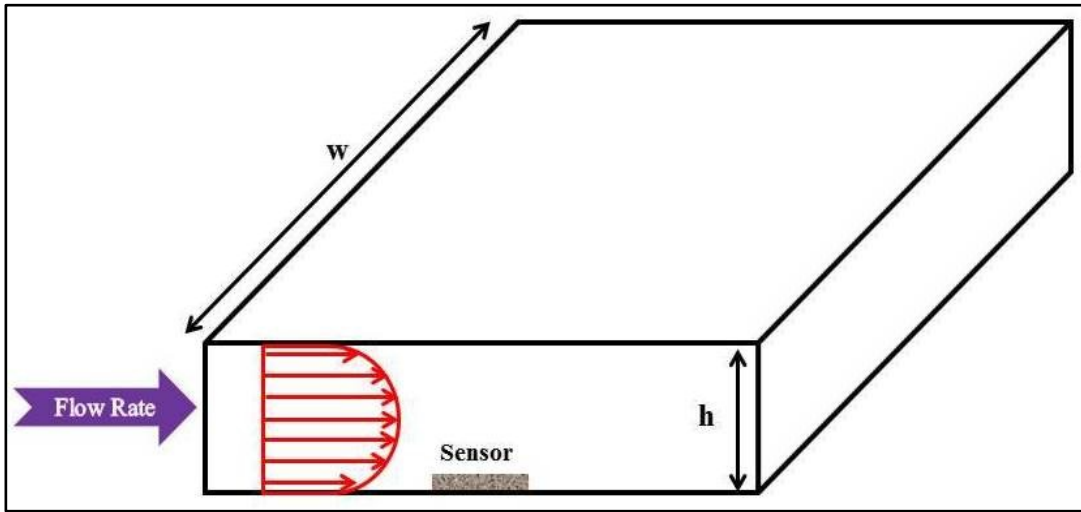


**Figure 3.9. Parallel-plate geometry**

**Table 3.4. QCM-D instrument specifications**

Specifications	Description/value
Channel width (W)	1 cm
Channel height (h)	0.2 cm
Sensor type	Silicon dioxide (SiO <sub>2</sub> )
Flow Rate (Q)	0.3 ml/min (Re = 0.5)

Due to flow rate scope limit of 0-1 ml/min, flow rate of 0.3 ml/min was selected for consistency of all the experiments that yields in  $Re = 0.5$ . In other words, laminar flow was chosen as the flow regime.

Preparation of the sensor is very significant and includes all the following steps:

- UV/ozone treat for 10 min,
- Immersing the sensor in 2% sodium dodecyl sulphate (SDS) for 30 minutes and in room temperature,
- Immediately rinsing the sensor in mili-Q water,
- Drying the sensor with nitrogen gas, and
- UV/ozone retreat for 10 minutes.

The sensor type used in experiments was silicon dioxide ( $\text{SiO}_2$ ) due to its availability and several reported usages [57, 59-61]. The surface of the sensor was also washed in 2% polyethylenimine (PEI) solution to form a positively charged layer on the sensor surface. This was carried out to stabilize the obtained deposition data and smoother behaviour (fewer fluctuations).

PEI is a cationic polymer with repeating unit composed of amine group. It has been known to effectively interact with nanomaterials via physisorption. It has worked as a coating, controlling and enhancing the deposition of nanomaterials on the model surfaces. Due to the high content of amine groups, it can link with negatively charged colloids. This polymer is pH sensitive as its chains are fully extended at low pH due to electrostatic repulsion between the protonated amine groups [62].

Bentonite suspension was prepared by dispersing 0.1% w/v Wyoming Gel in water. Also, 0.1 % w/v cellulose nanocrystal (CNC) rod-shaped particles were dissolved in water. Each material (bentonite, CNC) was dispersed separately in tap water using sonication method until a homogeneous solution of each was obtained. Three samples were prepared as follows:

- 0.1% (wt) bentonite,
- 0.1% (wt) CNC, and
- 0.1% (wt) bentonite + 0.1 % (wt) CNC in water.

Mixing technique needs a lot of attention, because the deposition process requires a well-mixed viscous suspension to obtain realistic and reliable data. Dilute solutions of each bentonite or CNC made it possible to assume no intermolecular interactions.

### **3.5. Characterization methods**

The morphologies of the samples (dried cakes) were investigated by high resolution SEM using a Hitachi model S-5500 and SEM using a Hitachi model S-4800 apparatus equipped with a field emission source and operating at an accelerating voltage of 5 kV or 30 kV in transmission mode. The samples were stained by depositing a drop of uranyl acetate solution (2 wt. % in water) on the grid for 5 min. The grid was dried at room temperature for at least 24 h prior to imaging.

Elemental analysis and chemical characterization of the dried cake was carried out using energy dispersive X-Ray spectroscopy (EDX) analytical technique. This add-on to SEM apparatus was used to screen the distribution of each element in the filter cake.

Inductively coupled plasma mass spectrometry (ICP) was carried out using Perkin Elmer Elan 6000 quadrupole ICPMS for elemental analysis specifically presence of iron (Fe) in the samples.

## 4. Dynamic filtration properties

Both static and dynamic filtrations happen during a drilling operation. Filtration takes place under dynamic conditions while the mud is circulating and under static conditions when circulation is ceased for different reasons such as making a connection, changing bits, etc [1]. Therefore, the static cake layer is on top of dynamic one, so the filtration rate decreases and the filter cake thickness increases. Moreover, dynamic filter cakes differ from static ones in that the soft surface layers of the static cake are not present in the dynamic cake. This originates from the fact that the cake surface is eroded to an extent that depends on the shear stress exerted by the hydrodynamic force of the mud stream. Additionally, the amount of filtrate invasion is considerably smaller under static conditions. Under dynamic filtration condition, the growth of the filter cake is limited by the erosive action of the mud stream. In the beginning, when the surface of the rock is first exposed, the rate of filtration is very high, and the cake grows quickly. Afterwards, the rate of cake growth decreases with time, until eventually it is equal to the erosion rate and the thickness of the cake is constant. Under equilibrium dynamic conditions, the rate of filtration depends on the thickness and permeability of the cake and is governed by Darcy's law.

To be concluded, flow behaviour calculations under dynamic condition is of great importance as the data obtained are closer to the real drilling operation. In this chapter, drilling fluid (bentonite + CMC/CNC) flow behaviour is investigated during two separate stages: 1) between the drilling pipe and porous media (concentric annuli) and 2) through porous media (filter pores). A proper mathematical model to fit dynamic fluid loss data will be achieved. Effect of different physical/chemical parameters on the volume loss and filtration rate of drilling mud will be investigated. At the end, governing filtration mechanisms will be discussed.

## 4.1. Flow regime between the drilling bit and porous media

Equations [2.11] to [2.15] were used to calculate the Taylor number for the present ceramic filters used in FANN 90 dynamic filtration apparatus. Table 4.1 illustrates the parameters required in order to calculate Taylor number.

**Table 4.1. Flow regime parameters for concentric cylinders geometry**

Specification	Description	Value
$r_i$	Radius of rotating shaft	9.52 mm
$r_o$	Inner radius of filter core	12.87 mm
$r_a$	Average radius	11.20 mm
$d = r_o - r_i$	Width of the gap between shaft and inner surface	3.35 mm
$c = \frac{2r_i^2 r_o^2}{r_a^2 (r_o^2 - r_i^2)}$	Constant parameter	3.19
$Ta_c$	Critical Taylor number	45.7
$\nu @ 10 \text{ s}^{-1}$	Kinematic viscosity of mud at shear rate of $10 \text{ s}^{-1}$	$4.2 \times 10^{-4} \text{ m}^2/\text{s}$
$\nu @ 100 \text{ s}^{-1}$	Kinematic viscosity of mud at shear rate of $100 \text{ s}^{-1}$	$7.8 \times 10^{-5} \text{ m}^2/\text{s}$
$Ta @ 10 \text{ s}^{-1}$	Calculated Taylor number at shear rate of $10 \text{ s}^{-1}$	0.13
$Ta @ 100 \text{ s}^{-1}$	Calculated Taylor number at shear rate of $100 \text{ s}^{-1}$	7.05

Taylor numbers were calculated as 0.13 and 7.05 for shear rates of 10 and  $100 \text{ s}^{-1}$ , respectively. Both numbers are lower than the critical Taylor number that confirms no

turbulence flow regime exists in the system. In other words, laminar flow regime assumption is confirmed. As illustrated in Figure 4.1, in real operations, the standard size of bit and casing or drill pipe is related to well depth. Concerning the bit speed, it shall be noted that the driver is a variable speed electrical motor. For example for model TDS 8A developed by Varco, the maximum speed is 270 rpm. However in normal operations the speed may be around 50-100 rpm. Table 4.2 illustrates the Taylor numbers calculated at conventional drilling operations.

**Table 4.2. Practical specifications for flow regime calculations in drilling operation**

Specification	Description	Value
$r_i$	Radius of rotating shaft	0.381 m (15")
$r_o$	Inner radius of wellbore at surface	0.457 m (18")
$r_a$	Average radius	0.419 m (16.5")
$d = r_o - r_i$	Width of the gap between shaft and inner surface	0.076 m (3")
$c = \frac{2r_i^2 r_o^2}{r_a^2 (r_o^2 - r_i^2)}$	Constant parameter	5.46
$Ta_c$	Critical Taylor number	43.7
$\nu @ 50 \text{ rpm } (0.83 \text{ s}^{-1})$	Kinematic viscosity of mud at shear rate of 50 rpm	$4.8 \times 10^{-3} \text{ m}^2/\text{s}$
$\nu @ 100 \text{ rpm } (1.67 \text{ s}^{-1})$	Kinematic viscosity of mud at shear rate of 100 rpm	$2.4 \times 10^{-3} \text{ m}^2/\text{s}$
$Ta @ 50 \text{ rpm}$	Calculated Taylor number at shear rate of 50 rpm	0.38
$Ta @ 100 \text{ rpm}$	Calculated Taylor number at shear rate of 100 rpm	1.59

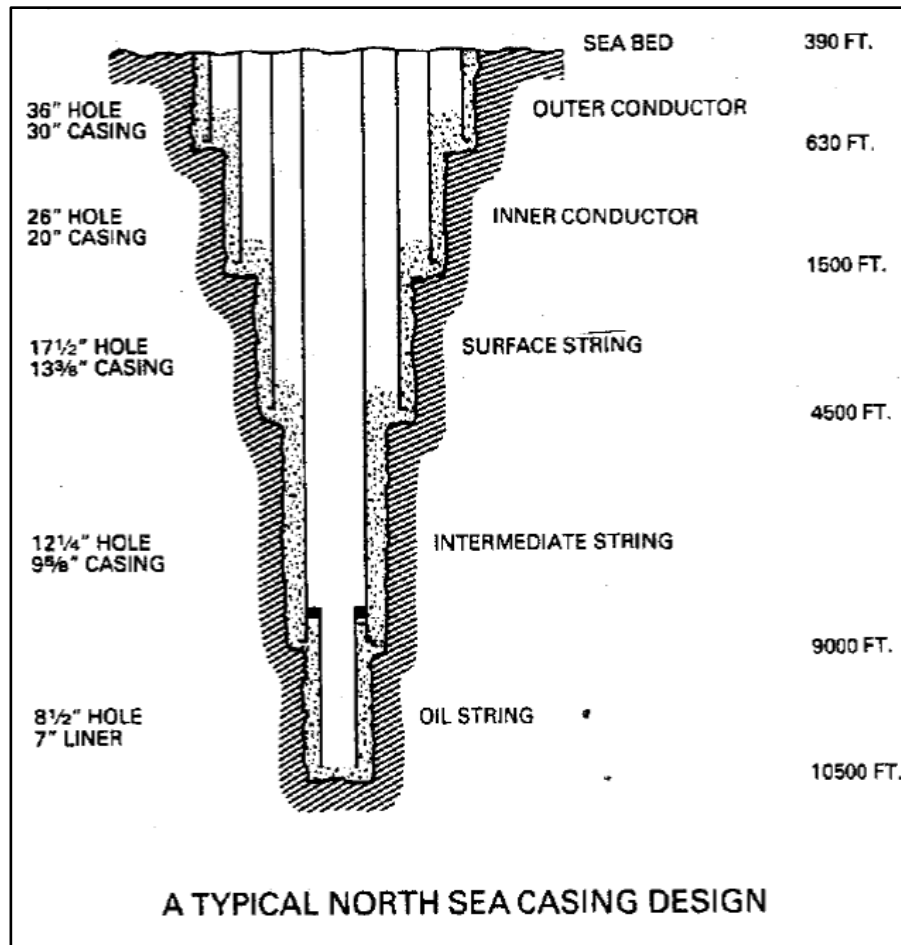


Figure 4.1. A typical casing design and drilling specifications [63]

As it is shown in Table 4.2, Taylor numbers calculated at 50 and 100 rpm drilling speeds are very lower than the critical Taylor number. Laminar flow is established like the calculations of dynamic filtration apparatus. The Taylor numbers calculated in Table 4.2 are very close in magnitude to the ones in Table 4.1. This confirms that our calculations are in good agreement with real drilling data.

## 4.2. Flow through porous media

As discussed previously in Section 2.2.3, Darcy's law is used to investigate the flow of liquids in porous media. Equation [2.20] states that the flux of the fluid is proportional to the pressure gradient between the inlet and outlet of the medium (through the length of the filter) and inversely to the fluid viscosity. Figure 4.2 illustrates the two stages involved in dynamic filtration experiments. First, the fluid flows in a concentric geometry between the filter and

the outer cylindrical cell (section 4.1). Second, it flows through porous medium of filter and is partially collected in filtrate cell (section 4.2).

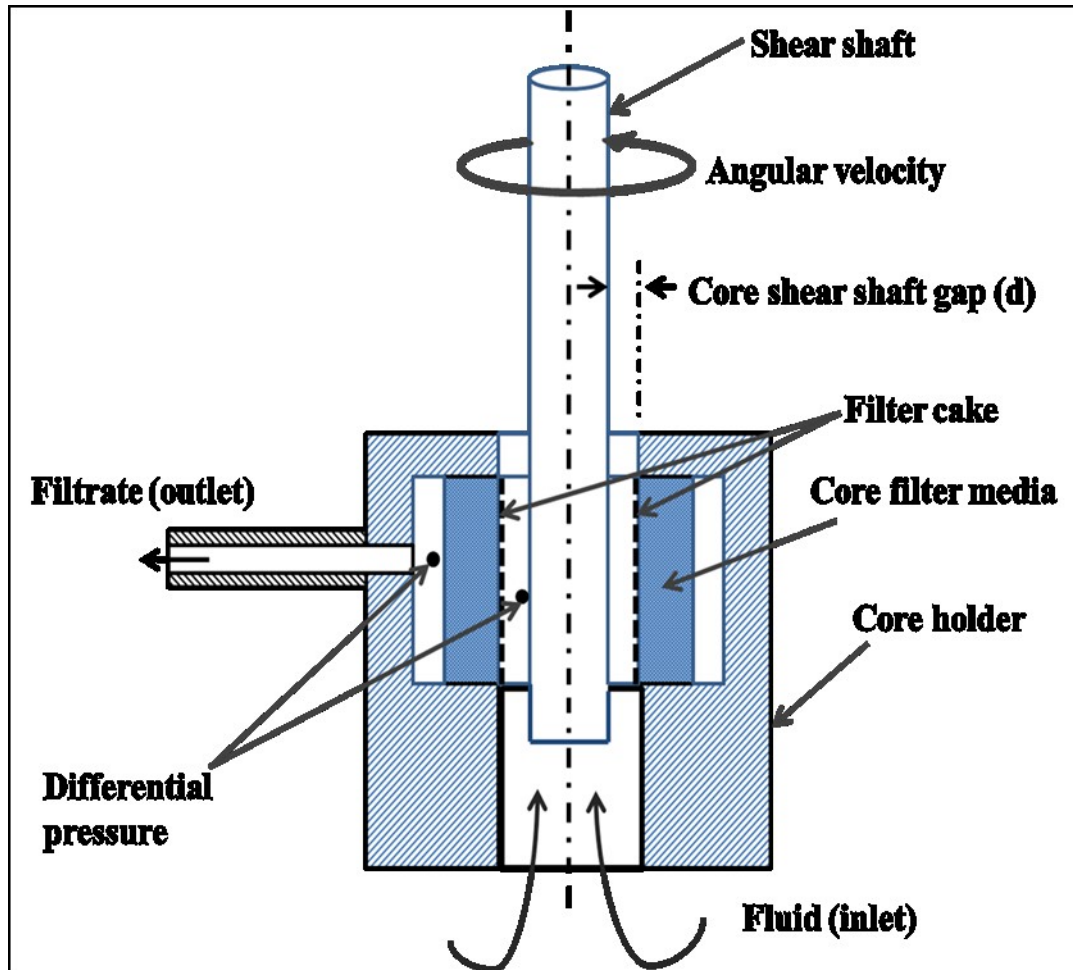


Figure 4.2. Schematic of dynamic filtration apparatus

Table 4.3 shows the specifications of the filter medium, and test conditions in order to calculate the Darcy flux (fluid superficial velocity) and all calculated parameters are tabulated.

**Table 4.3. Porous media specifications and results**

Specifications/calculated parameters	Description	Value
k for 35 micron filter core <sup>a</sup>	Permeability of the filter with 35 micron mean pore size	5.5 Darcy ( $5.43 \times 10^{-12} \text{ m}^2$ )
$L = R_o - R_i$ <sup>a</sup>	Length of the filter core (Outside radius minus inside)	$6 \times 10^{-3} \text{ m}$
$\Delta P$	Differential pressure	100 psi ( $6.9 \times 10^5 \text{ Pa}$ )
$\nabla P = dP/dx$	Pressure gradient	$1.15 \times 10^8 \text{ Pa/m}$
$d_{gr}$	Diameter of the grains	35 micron
$S_{Vgr}$	Specific surface area of the grains	$1.71 \times 10^5 \text{ m}^{-1}$
$\epsilon$	Porosity	0.55
q	Darcy flux	3.47 mm/s
u	Fluid velocity in porous medium	6.31 mm/s

**Note:** <sup>a</sup>: Taken from FANN 90 HPHT Dynamic Filtration Apparatus Manual

According to Equation [2.20], the Darcy flux is calculated as  $3.47 \times 10^{-3} \text{ m/s}$  (3.47 mm/s). To find the real fluid velocity, the Darcy flux should be divided by the porosity. Equation [2.49] is used to convert the permeability of the filter core to the porosity. Assuming that the pore grains are spherical, the specific surface area of the grains can be estimated as follows:

$$S_{Vgr} = \frac{6}{d_{gr}} \quad [4.1]$$

Where  $d_{gr}$  is equal to 35 micron. Having the specific surface area of the grains and the porosity, the real fluid velocity in the porous filter core is calculated as 6.31 mm/s using Equation [2.49]. All the parameters calculated in a step-by-step procedure are shown in Figure 4.3.



**Figure 4.3. Darcy calculations flowchart**

To better investigate the drilling mud behavior (flow of polymer-based fluids) through porous media (filter), a dimensionless resistance coefficient can be defined by:

$$\Lambda = \frac{d^2 \epsilon^3 \left( \frac{\Delta P}{L} \right)}{\mu v (1 - \epsilon)^2} \quad [4.2]$$

where  $\Delta P$  is the pressure drop over a length  $L$  of the porous medium,  $\epsilon$  the porosity,  $d$  the particle diameter,  $\mu$  the viscosity of solvent (water), and  $v$  the superficial velocity. This resistance is originated from a shear flow contribution and an extensional flow contribution. Studies have shown that the pressure gradient of the polymer-based fluids in porous media is more than expected by simple capillary models [64].

Reynolds number can also be expressed as:

$$Re = \frac{\bar{V}_m \cdot d \cdot \rho}{\mu} \quad [4.3]$$

where  $\bar{V}_m$  is the filtration flux,  $d$  the mean pore size of the filter,  $\rho$  the density of the fluid and  $\mu$  the viscosity of the fluid.

Two different samples were investigated. The first one had 3% bentonite and 0.25% CMC while the second one has 3% bentonite, 0.25% CMC, and 1% CNC. Their  $Re$  numbers at shear rate =  $100 \text{ s}^{-1}$  and their pressure gradient ratio at low  $Re$  number and low shear viscosities were compared using the previous equations. The results were tabulated in Table 4.4.

**Table 4.4. Parameters for flow of polymer-based fluids in porous media**

Sample name	Viscosity, $\mu$ (Pa.s)	Density <sup>d</sup> , $\rho$ (kg/m <sup>3</sup> )	Mean velocity, $V_m$ (m/s)	Re	Pressure gradient ( $\Delta P/L$ )
B – C <sup>a</sup>	0.09	2300	$2.2 \times 10^{-6}$	$1.96 \times 10^{-6}$	-
B – C – CN <sup>b</sup>	0.18	2300	$1.8 \times 10^{-6}$	$8.05 \times 10^{-7}$	-
B-C/B-C-CN ratio	0.5	1	1.22	$2.4^c$	$0.38^c$

**Notes:** a: B represents bentonite; b: C represents CMC and CN represents CNC sample; c: calculations are in Appendix A. d: densities are considered approximately constant due to low dosages of additives.

A brief look at Table 4.4 reveals interesting results regarding CNC effect. The addition of CNC decreases the Reynold number. This is due to an increase in sample viscosities from 0.09 Pa.s for B – C to 0.18 Pa.s for B – C – C at shear rate =100 s<sup>-1</sup>. This shear viscosity increase is more considerable at low shear rates when Re number is 0.1. Viscosity of the B – C sample is 0.14 Pa.s compared to 0.37 Pa.s for the B – C – C sample. This viscosity increase acts as a resistance against the fluid flow through the porous filter and increases the pressure drop. As shown in Table 4.4, the pressure gradient is 2.6 times larger when CNC is included in the bentonite drilling fluid suspension.

### **4.3. Pressure gradient (differential pressure) effect in fluid loss**

Figure 4.4 illustrates the effect of differential pressure on volume loss and filtration rate. Filtration rate values calculated from Figure 4.4 are tabulated in Table 4.5. Increase in differential pressure results in higher amounts of volume loss and filtration rate. This is also predicted and expected from theory [1]. Table 4.5 illustrates that working with differential

pressure of more than 1 atm increases the filtration rate twice, which is not desirable. The effect of differential pressure (the so-called trans-membrane pressure) in cross-flow filtration rate is expressed in Equation [4.4].

$$J = \frac{\Delta P_m}{\mu R_t} \quad [4.4]$$

In Equation [4.4], J is the permeate flux,  $\Delta P_m$  the differential pressure,  $\mu$  the viscosity of suspension, and  $R_t$  the total resistance of the system.

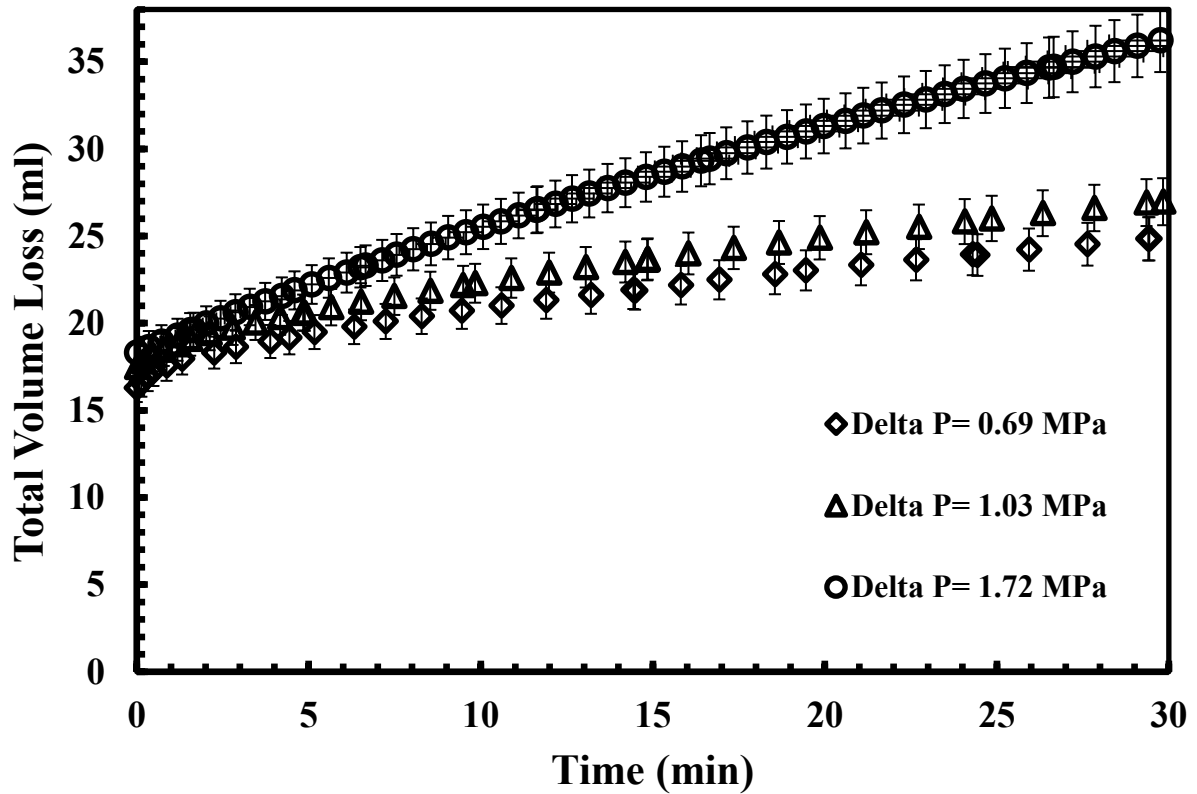


Figure 4.4. Total volume loss in dynamic filtration for different differential pressures

**Table 4.5. Filtration rate data for different differential pressures**

Differential Pressure (MPa)	Filtration Rate (ml/min)
0.69	0.25
1.03	0.30
1.72	0.60

**Note:** All experiments are carried out according to API standard time of 30 min.

The total resistance,  $R_t$ , is calculated by replotting the permeate flux,  $J$ , values obtained from Figure 4.4 versus different differential pressures,  $\Delta P$ . Knowing the filter surface area,  $A = 2.3 \times 10^{-3} \text{ m}^2$ , and fluid viscosities,  $\mu = 0.98 \text{ Pa}\cdot\text{s}$  (for shear rate =  $10 \text{ s}^{-1}$ ) and  $\mu = 0.18 \text{ Pa}\cdot\text{s}$  (for shear rate =  $100 \text{ s}^{-1}$ ), the total resistance of the system (filter and cake resistance) can be calculated from the slope of  $J$  vs.  $\Delta P$  graph. Figure 4.5 and Figure 4.6 illustrate the permeate flux as a function of differential pressure for shear rates of 10 and  $100 \text{ s}^{-1}$ , respectively. The total resistance for shear rates =  $10 \text{ s}^{-1}$  and  $100 \text{ s}^{-1}$  is calculated as  $2.4 \times 10^{-12} \text{ m}$ , and  $4.7 \times 10^{-13} \text{ m}$ , respectively. Higher resistance (approximately 5 times) is observed with shear rate =  $100 \text{ s}^{-1}$ . In other words, the total resistance of both filter and cake increases by increasing the shear rate. This phenomenon can be explained as follows: higher shear rate increases the velocity of depositing particles. Therefore, a more compressed cake is expected due to the pressure induced by depositing particles. As a result, higher cake resistance is predicted when higher shear rate is applied. Filter resistance should not change because same material with same porosity was used in the experiments.

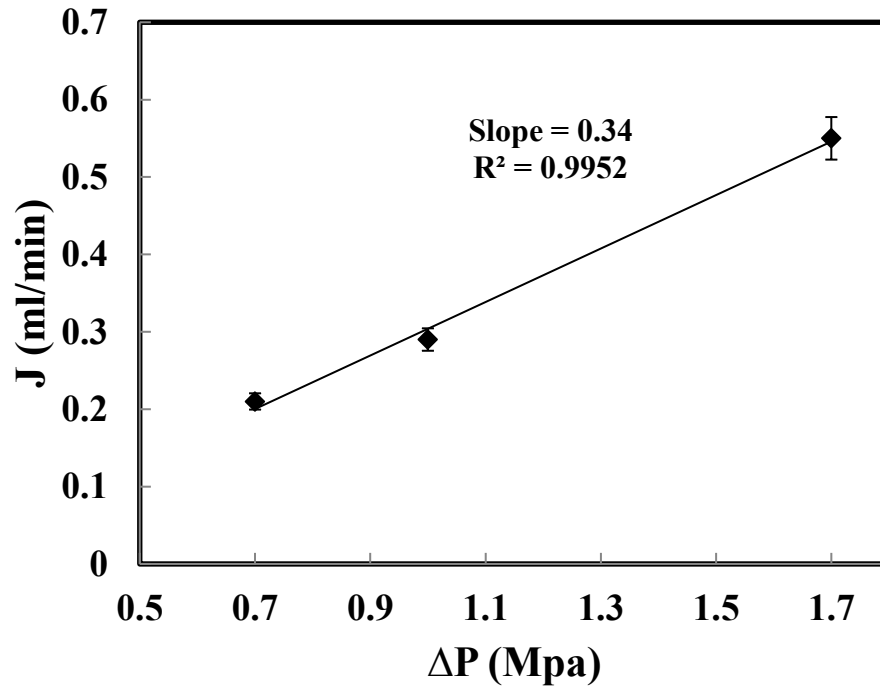


Figure 4.5. Permeate flux as a function of differential pressure for shear rate =  $10 \text{ s}^{-1}$

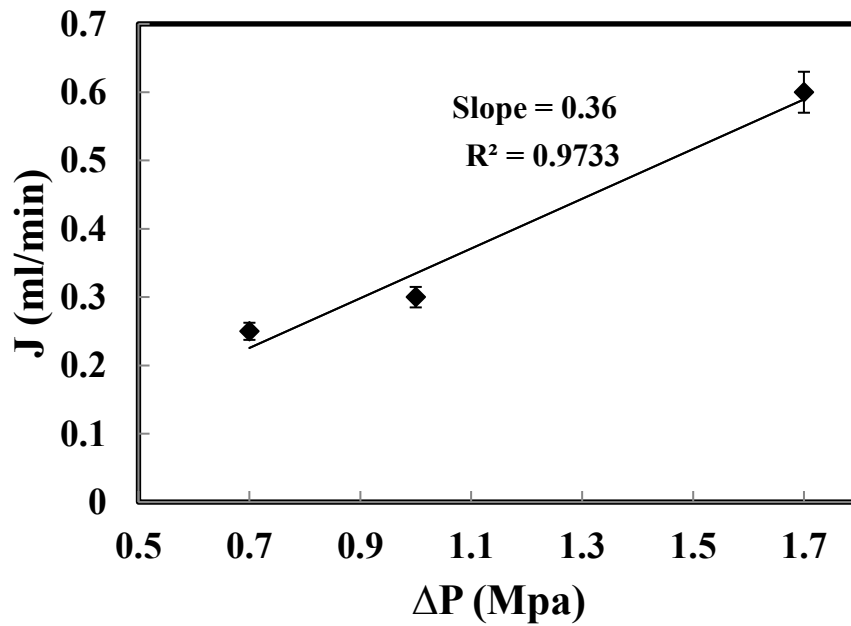


Figure 4.6. Permeate flux as a function of differential pressure for shear rate =  $100 \text{ s}^{-1}$

## 4.4. Temperature effect in fluid loss

Figure 4.7 illustrates the effect of temperature on filtration rate of drilling mud. It is shown that increasing temperature results in higher fluid loss and filtration rate. That may be due to the effect of temperature on fluid viscosity. An increase in temperature may increase the filtrate volume in several ways. First of all, as temperature elevates, it reduces the viscosity of the filtrate, and therefore the filtrate volume increases. Temperature changes inversely with square root of viscosity [1]. For example, if the water viscosity at  $T = 20^\circ \text{C}$  is 1.00 cP and at  $T = 100^\circ \text{C}$  is 0.28 cP, then the filtrate volume at  $T = 100^\circ \text{C}$  would be about  $\sqrt{\frac{1.00}{0.28}} = 1.88$  times larger than the one at  $T = 20^\circ \text{C}$ . In addition, changes in temperature may affect filtration rate and volume by changing the electrochemical equilibria that control the degree of flocculation and aggregation. As a result, the permeability of the filter cake changes and filtrate volume may be increased. Moreover, chemical degradation of one or more components of the mud is another mechanism by which high temperatures can affect filtrate properties. Many organic filtration control agents start to degrade significantly at relatively high temperatures (above  $100^\circ\text{C}$ ) and the rate of degradation increases with further increase in temperature until filtration properties cannot be adequately maintained [1]. The degradation of CMC polymer chains and some clay minerals (mostly bentonite type) may happen at high temperatures.

The average filtration rates at different temperatures are given in Table 4.6. As shown in the table, unacceptable rate of filtration happens at  $T = 150^\circ\text{C}$ .

**Table 4.6. Average filtration rates for different temperatures**

Temperature ( $^\circ\text{C}$ )	Filtration Rate (ml/min)
29	0.16
65	0.24
150	0.54

**Note:** All experiments are carried out according to API standard time of 30 min.

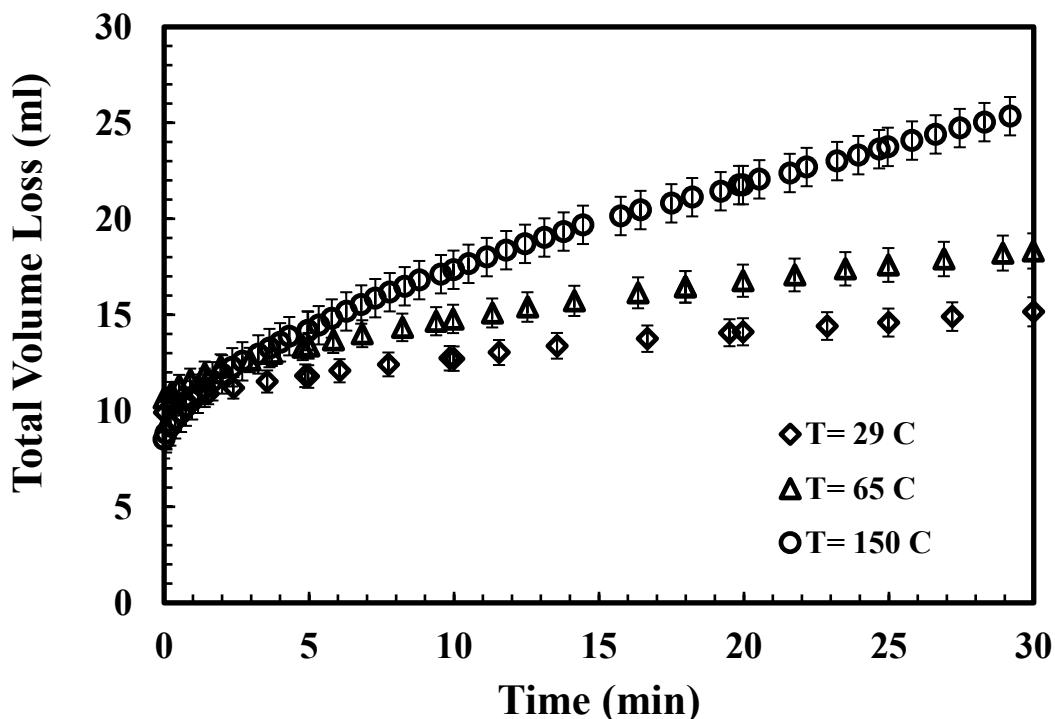


Figure 4.7. Dynamic filtration data for different temperatures

#### 4.5. Filter pore size effect in fluid loss

The role of porosity (filter pore sizes) has been investigated numerically and experimentally by other researchers [65, 66]. As expected, larger pore sizes should increase the permeate flux and therefore result in higher volume loss and filtration rate, but surprisingly, this trend was different in values for 10 and 35 micron filter cores. The filter cores with mean pore sizes of 35 micron worked better (lower filtration rates and volume loss) in all the experiments compared to 10 micron size. There is possibility of non-homogeneous pore size distribution in the used filter cores. Additionally, mud particles may have been plugged the pores in the early stages of filtration when filters of 35 and 10 microns were used, but 90 micron filter is large enough not to let the particles plugging the pores early. However, mercury porosimetry can be carried out on the filters to accept or deny the homogeneity of pore size distribution. Figure 4.8 illustrates the effect of filter pore sizes on dynamic filtration properties of drilling mud. Average filtration rate values are tabulated in Table 4.7.

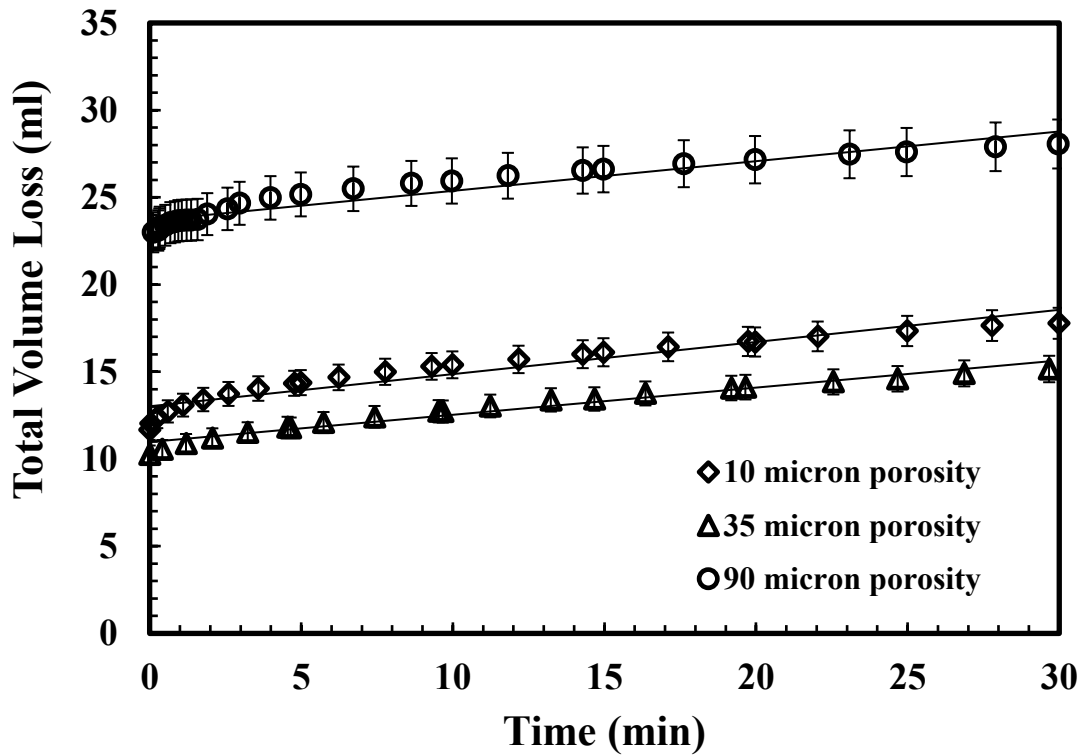


Figure 4.8. Total volume loss in dynamic filtration for different filter porosities

Table 4.7. Filtration rate data for different filter porosities

Filter porosity (Permeability), micron	Filtration Rate (ml/min)
10 (0.95 darcy)	0.18
35 (5.5 darcy)	0.16
90 (13.5 darcy)	0.24

**Note:** All experiments are carried out according to API standard time of 30 min.

The industry-accepted rules for selecting the size and concentration of clay minerals in drilling mud suspension are based on the theory indicating that the average particle size of the clay used in drilling mud has to be equal or slightly greater than one-third the filter pore size [20]. Once the mean pore diameter is known, the particle size distribution of the bridging solids in the mud (clay minerals) must be adjusted to meet the required specifications.

Optimized particle size distribution results in minimum filtration rates. Due to better filtration rates with 35 micron filter pore size, an average grain size of around 12 microns for clay particles is expected.

#### 4.6. Drilling bit speed (shear rate) effect in fluid loss

Effect of shear rate (or cross-flow velocity) is illustrated in Figure 4.9 & Figure 4.10. Higher shear rate results in increasing filtration rate. That is possibly due to the higher numbers of washed away particles from the surface as shear rate increases. This phenomenon leads to the decrease in filter cake growth rate. This was experimentally and numerically confirmed by previous works [67]. Average filtration rates for shear rates of 10 and 100  $\text{s}^{-1}$  are presented in Table 4.8.

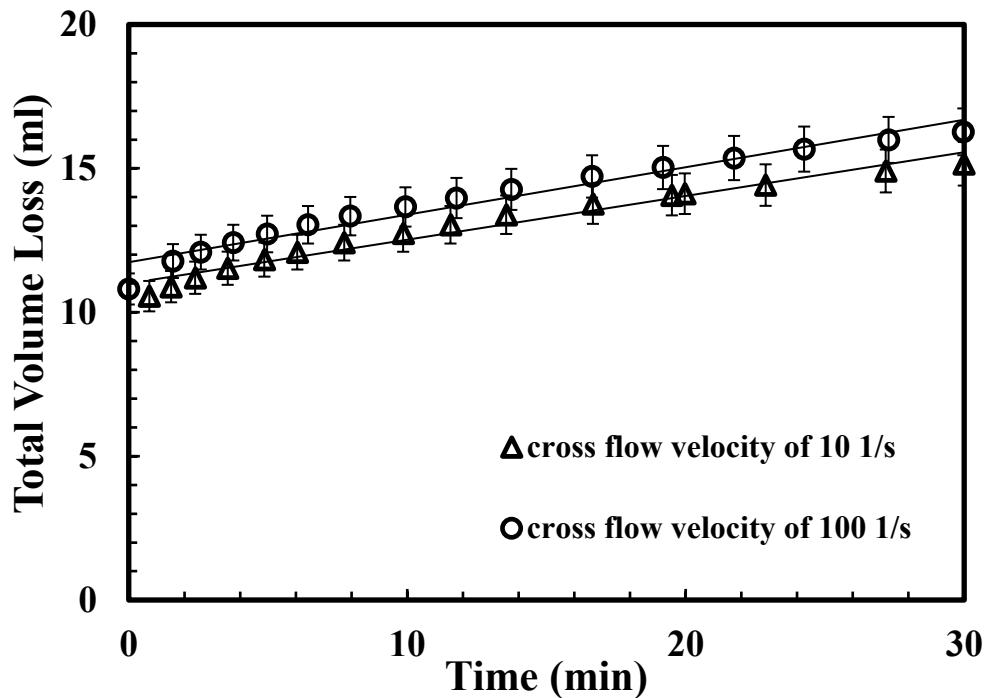


Figure 4.9. Total volume loss during dynamic filtration for different shear rates

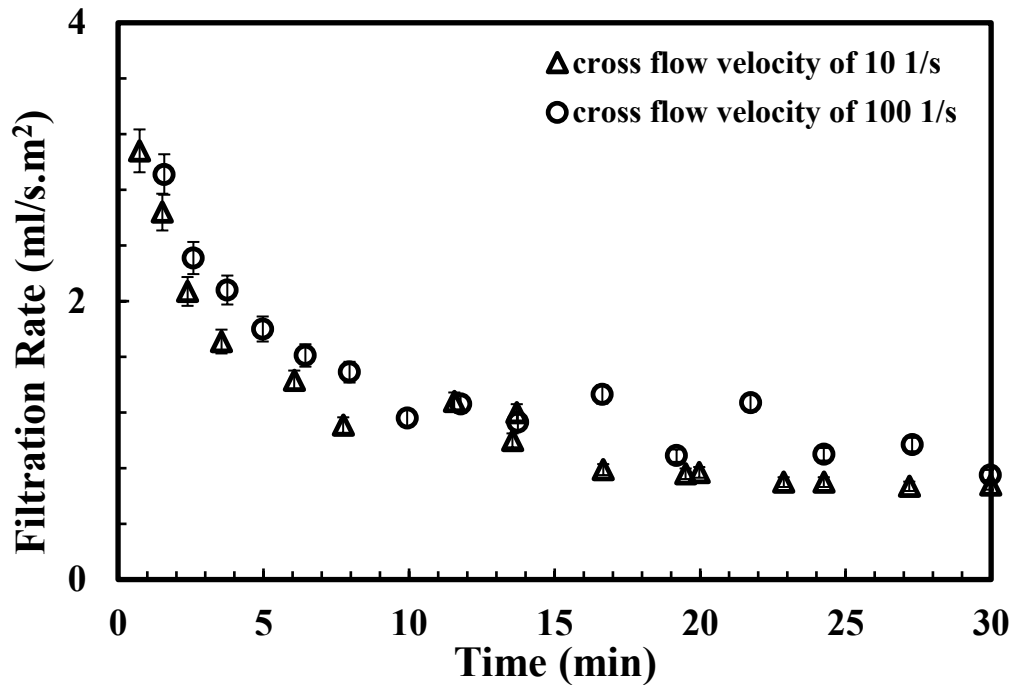


Figure 4.10. Filtration rate during dynamic filtration for different shear rates

Table 4.8. Filtration rate values for different shear rates

Shear Rate ( $s^{-1}$ )	Filtration Rate (ml/min)
10	0.16
100	0.17

**Note:** All experiments are carried out according to API standard time of 30 min.

#### 4.7. Mud formulation (CNC/CMC) effect in fluid loss

Figure 4.11 and Table 4.9 illustrate the considerable effect of CNC particles and CMC polymer on dynamic filtration properties of drilling mud suspension. It is observed that none of CNC or CMC can enhance the dynamic filtration properties alone, but the addition of very low dosages of CNC (1 wt %) and CMC (0.25 wt %) reduces the filtration rate by 64% of the bare clay solution. It also decreases the total volume loss by 56% lower than using the bare clay solution. This is a significant effect that made us motivated to investigate it in more

details. Many researchers worked on the so-called “depletion” effects of CNC in particle suspensions. One probable scenario is that the clay particles are depleted by CNC rods and pushed to the surface (filter pores). The other scenario talks about the agglomeration of clay particles due to the CNC repulsive forces. To investigate these two probabilities, quartz crystal microbalance with dissipation (QCM-D) technique was carried out on clay suspensions with and without CNC. It was observed that clay particles were deposited so much better in the presence of CNC compared to when there was no CNC in the system. CMC effect is considerable as a viscosity modifier in the system, and enhancing the suspension stability specially when working with CNC, but not to enhance filtration properties. Its significant effect in rheological properties of clay suspensions will be discussed in Chapter 5.

**Table 4.9. Dynamic Filtration data for different mud formulations**

<b>Wyoming Clay (%)</b>	<b>Additives (CMC - CNC) (%)</b>	<b>Spurt loss volume (ml)</b>	<b>Total volume loss (%)</b>	<b>Filtration Rate (ml/min)</b>	<b>Comments</b>
3	0.00 - 0.00	21.01	69	0.45	High fluid loss
3	0.25 - 0.00	11.39	46	0.38	Unstable and no filter cake formation
3	0.00 - 1.00	12.48	47	0.38	Semi stable cake formation
3	0.25 - 1.00	9.91	30	0.16	Controlled filtration and cake formation

**Note:** All experiments are carried out according to API standard time of 30 min.

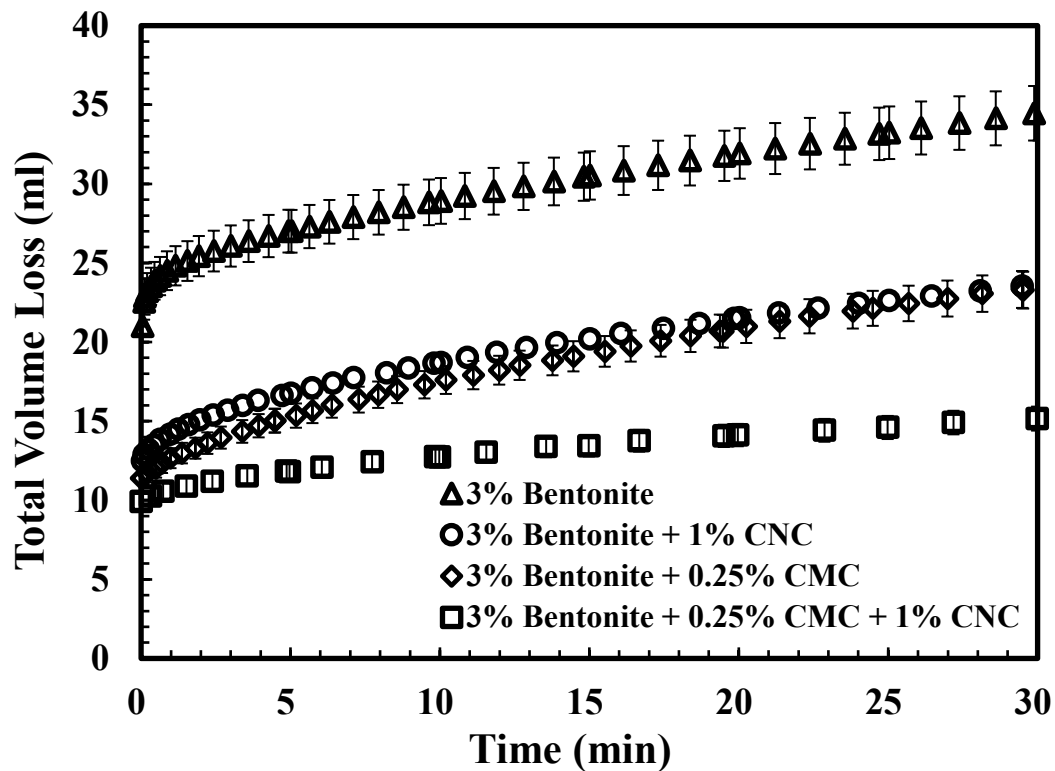


Figure 4.11. Dynamic filtration data for clay w/o additives

## 4.8. Governing filtration mechanisms

To investigate the filtration mechanism of clay suspension with regards to shear rate change, inverse of filtration rate vs. time and volume loss per unit area are plotted in Figure 4.12, Figure 4.13, Figure 4.14, and Figure 4.15. Linear behaviour confirms the governing filtration mechanism. As it is illustrated, no matter which shear rate used, the governing mechanism is pore plugging. In other words, rotation of the shear shaft creates a shear rate that applies a pressure on the particles and pushes them into the filter pores. The swept particles into the pores block them and control filtration consequently.

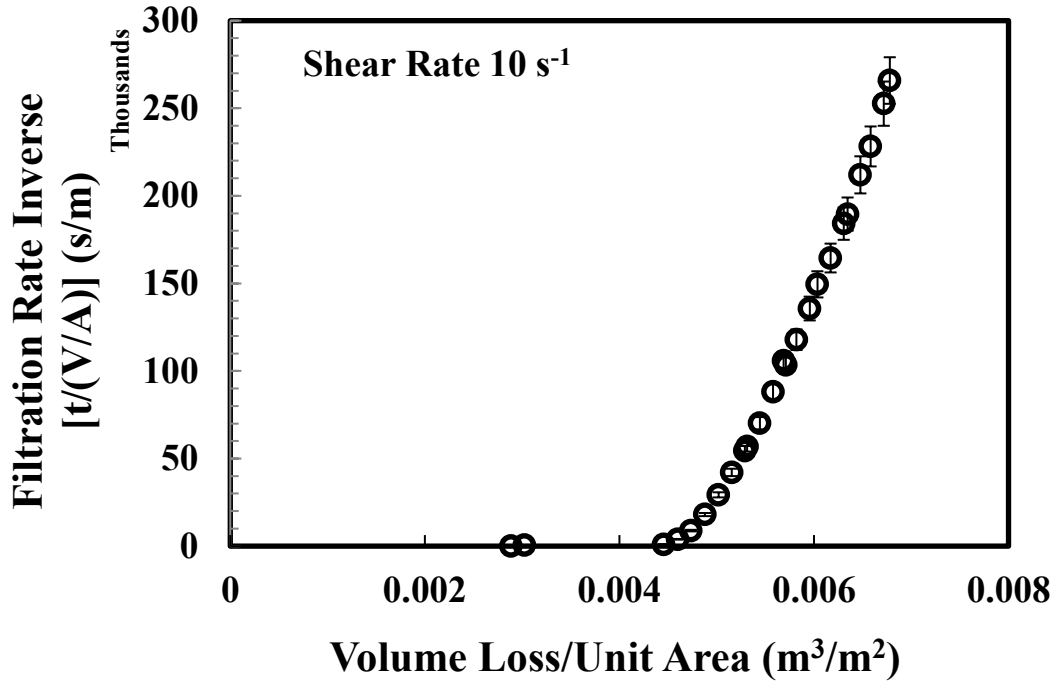


Figure 4.12. Filtration rate inverse vs. volume loss per unit area for shear rate  $10 \text{ s}^{-1}$

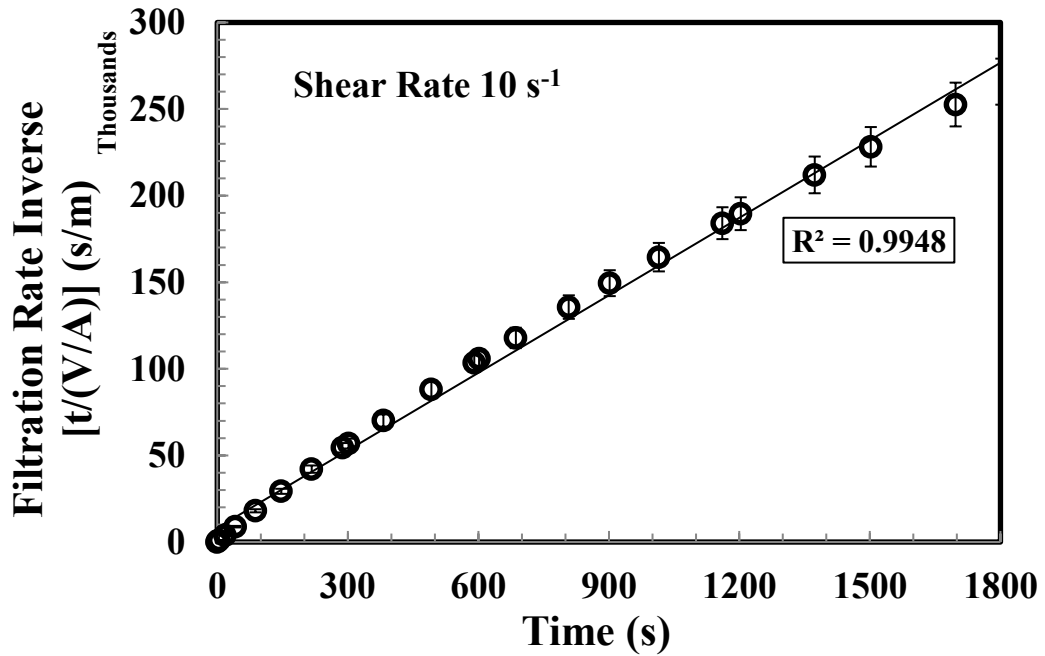


Figure 4.13. Filtration rate inverse vs. time for shear rate  $10 \text{ s}^{-1}$

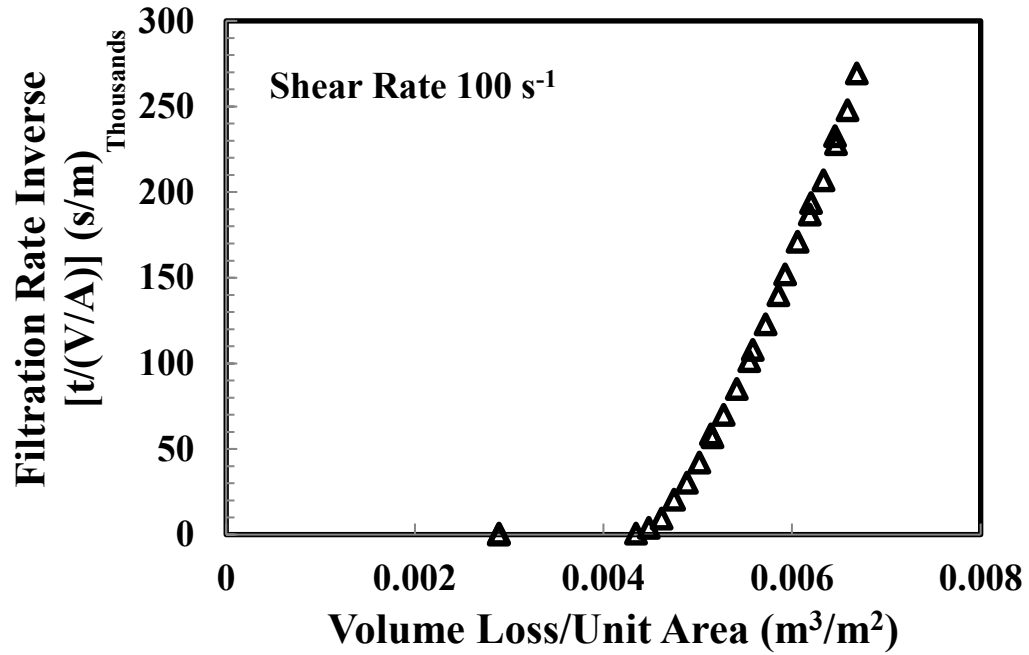


Figure 4.14. Filtration rate inverse vs. volume loss per unit area for shear rate  $100 \text{ s}^{-1}$

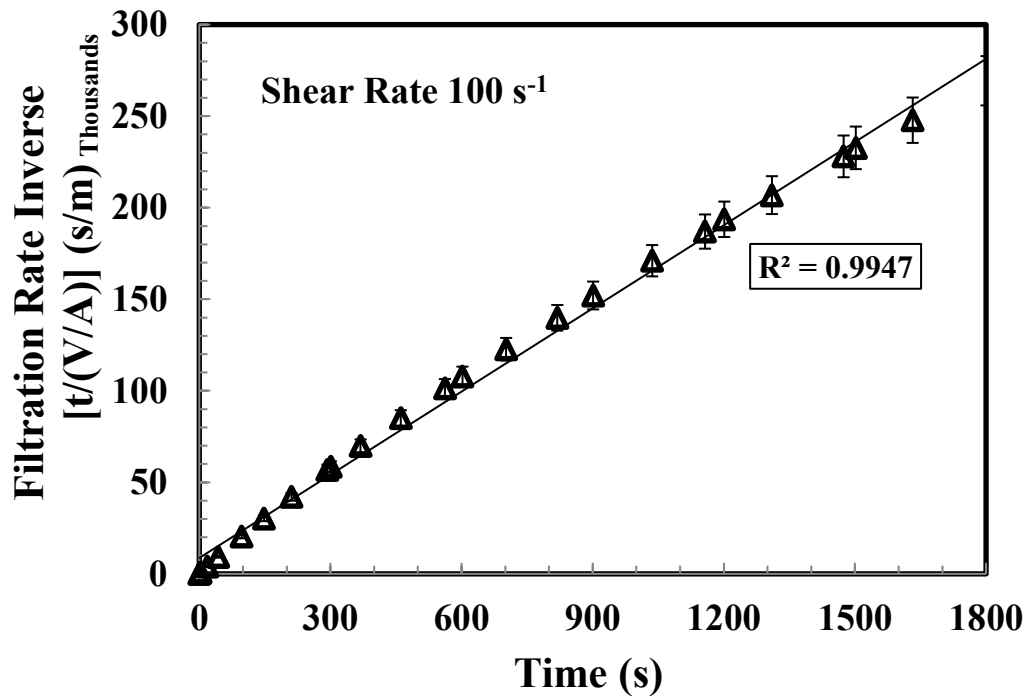


Figure 4.15. Filtration rate inverse vs. time for shear rate  $100 \text{ s}^{-1}$

Moreover, inverse of filtration rate vs. time and volume loss graphs were plotted for different filter mean pore sizes at constant differential pressure and shear rate. Figure 4.16 and Figure 4.17 illustrate that the governing mechanism is still pore plugging for all different filter mean pore sizes. Additionally, Figure 4.17 shows that the pore size of 90 micron has the highest linear regression correlation of  $R^2 = 0.9992$ . It implies the fact that the mud had a greater tendency to block the filter pore size of 90 micron compared to the 10 and 35 micron.

Reviewing Figures 5.9 – 5.14 indicates that the current drilling mud formulation had a greater tendency to block pore spaces than to form filter cake during the dynamic filtration period under different experimental conditions such as different shear rate and filter mean pore sizes. In conclusion, there are various mechanisms governing dynamic filtration of drilling muds. As discussed previously in Chapter 2, two main mechanisms are involved during filtration: particles pore plugging and cake formation. Previous studies have shown that one or both mechanisms occur during drilling.

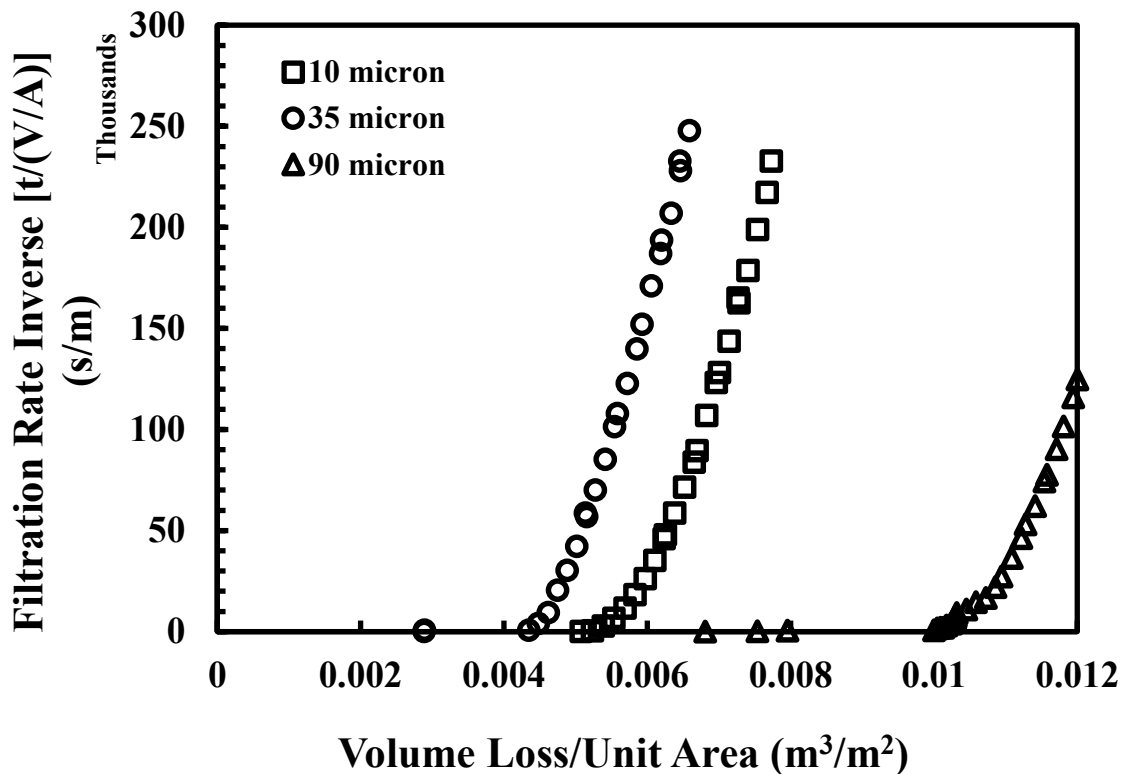


Figure 4.16. Filtration rate inverse vs. volume loss for different filter pore sizes

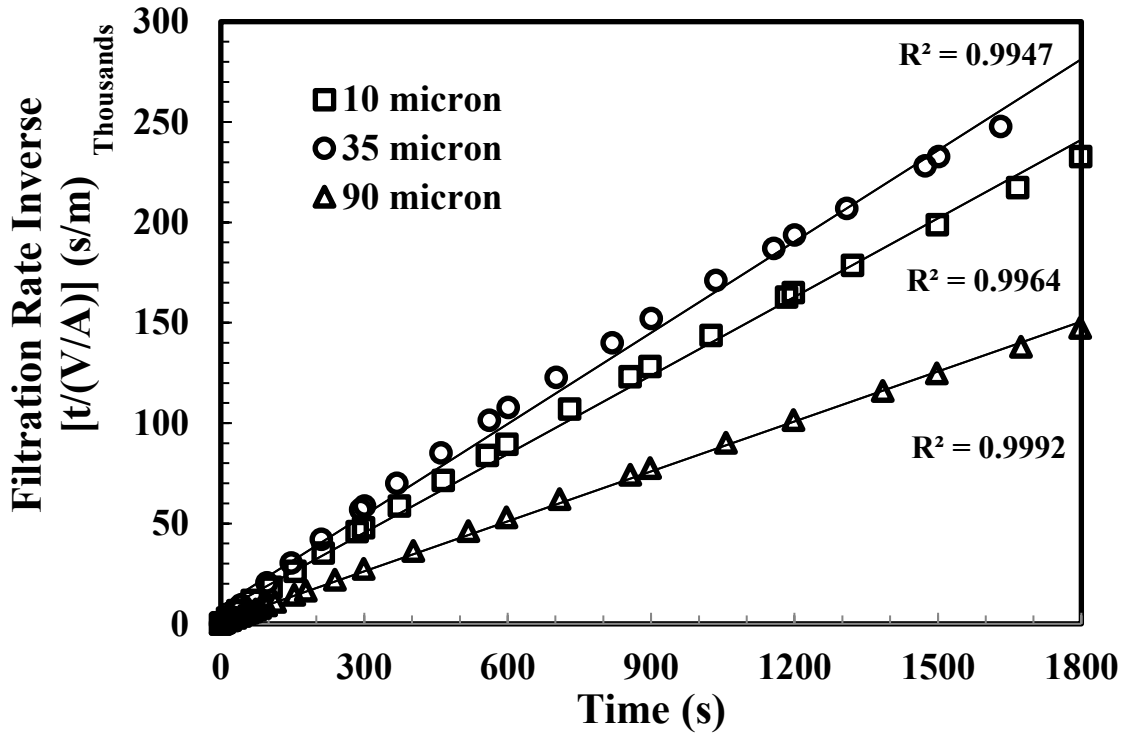


Figure 4.17. Filtration rate inverse vs. time for different filter pore sizes

## 4.9. Best mathematical model to fit fluid loss data

Different mathematical models were examined in order to find the best fit for dynamic fluid loss data. Fluid loss volume in different differential pressures was plotted vs. time and square root of time. It was found that none of the above mentioned models accurately described the fluid behavior. In one of the most complete experimental studies of dynamic fluid loss [66], the authors proposed a piecewise function. This function separates the experiment time into two periods and sums up the fluid loss in each part.

$$V_{fl} = V_{sp} + m\sqrt{t}|_{V_{sp}}^{V_e} + \beta t|_{V_e}^{\infty} \quad [4.5]$$

where the second term ( $m\sqrt{t}$ ), describes the short time wall-building phase (cake deposition) and the third term ( $\beta t$ ), includes the longer time equilibrium flow region. In other words, this equation quantizes the application of each period of fluid loss process. Here, the equilibrium volume,  $V_e$ , needs to be identified. Afterwards, the volume loss behavior can be described as a combination of short term deposition and long term levelling off period.  $V_e$  represents the point on the volume – time curve when equilibrium flow is established. This

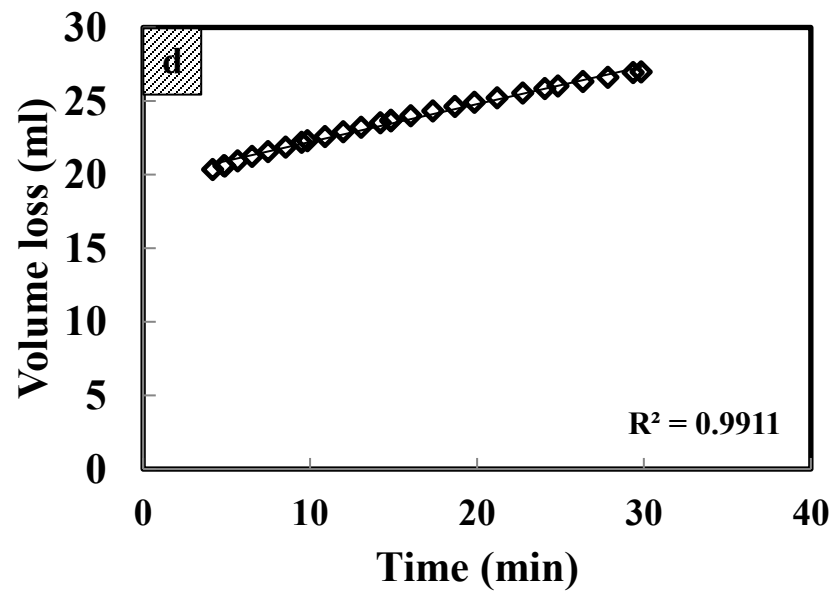
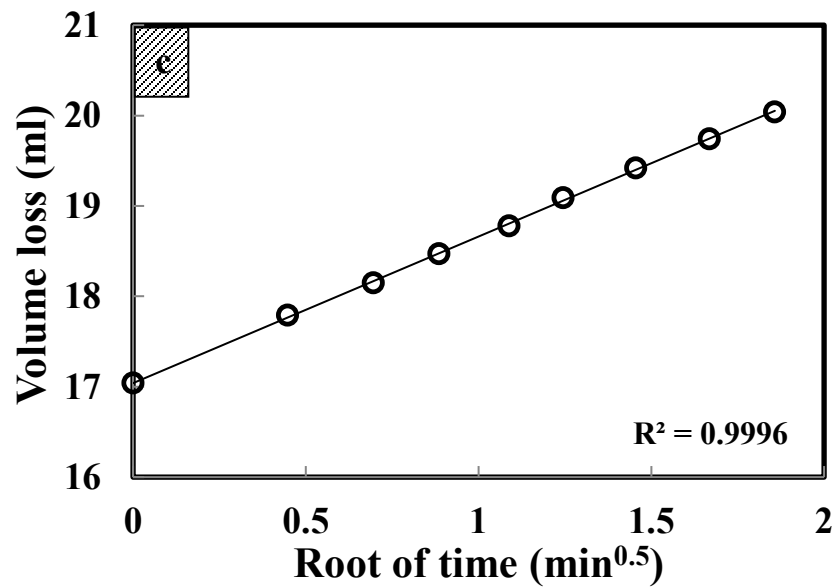
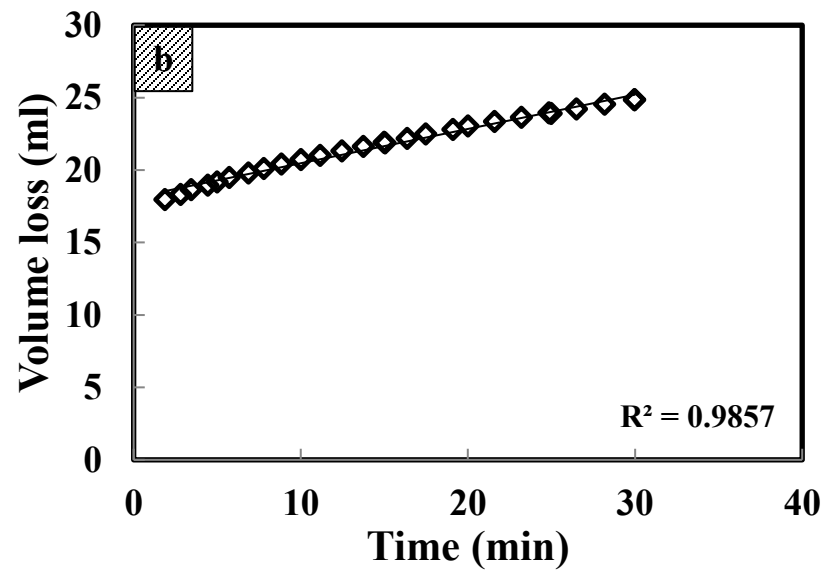
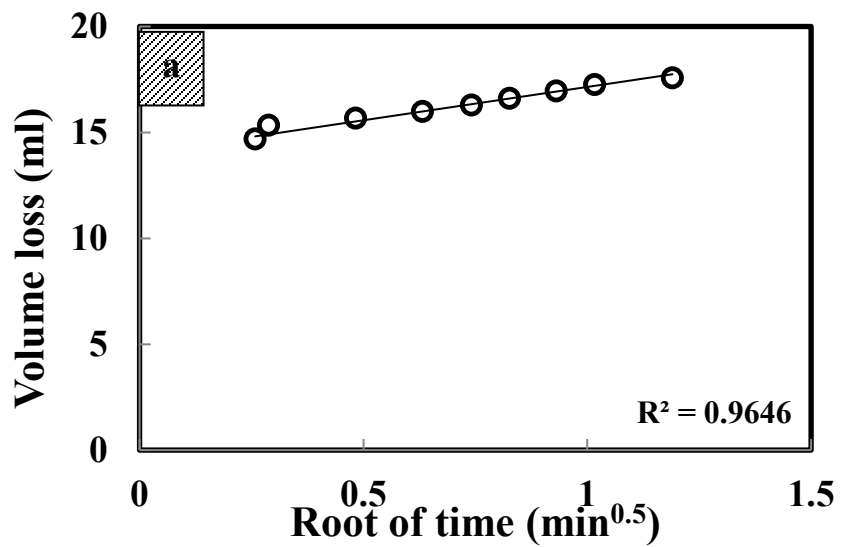
implies the fact that the filter cake growth has stopped to change in thickness or permeability and the rate of growth is equal to the rate of erosion for filter cake.

Figures 4.15 [a – f] illustrate that the suggested equation matches reasonably with the experimental data for fluid loss volume. The wall-building period of filtration are exhibited in Figures 4.15 [a], [c], and [e], while the equilibrium stage of filtration is shown in Figures 4.15 [b], [d], and [f].

The coefficients “m” and “ $\beta$ ” were calculated by fitting the model with fluid loss data and tabulated in Table 4.10. Increase in differential pressure results in slight increase in spurt loss volume. It also increases the equilibrium volume loss and filtration rate ( $\beta$ ), but we do not observe a uniform ascending/descending trend in early stage wall-building period. The coefficient m decreases when differential pressure changes from 0.7 to 1.0 MPa; Afterwards, m increases again when differential pressure goes higher. This might be due to the experimental error by operator or apparatus. It might also because of the presence of a critical pressure in the system.

**Table 4.10. Filtrate volume loss modeling parameters at different differential pressures**

$\Delta P$ (MPa)	$V_{sp}$ (ml)	$V_e$ (ml)	m (ml.s <sup>-0.5</sup> )	$\beta$ (ml/s)
0.7	14.0	17.57	3.15	0.24
1.0	17.1	20.04	1.62	0.26
1.7	17.4	20.63	1.81	0.58



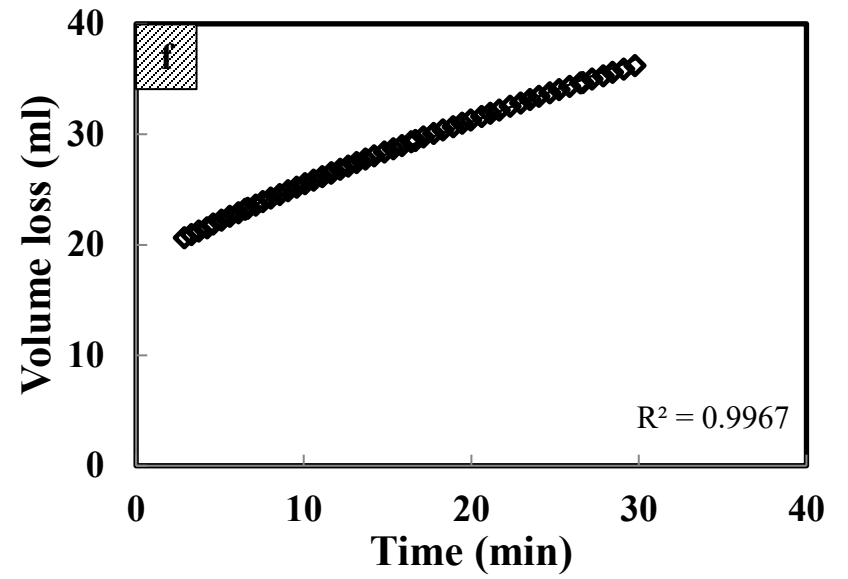
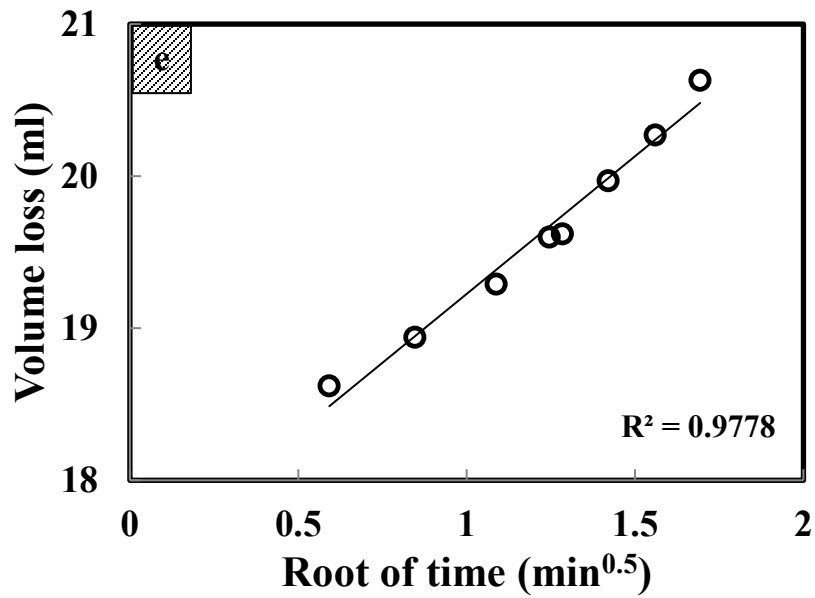


Figure 4.18. Fluid loss data at (a,b) 0.7 MPa, (c,d) 1.0 MPa, and (e,f) 1.7 MPa differential pressure

## 4.10. CNC effect in comparison to other commonly used additives

Some typical examples of nanoparticles used as viscosity modifier and fluid loss control are graphene oxide, carbon nanotubes, nanosilica composites, and iron (III) hydroxide. They all exhibited improved rheology, filtration, and desirable performance [4, 8-10, 68]. However, most of them are expensive, nonrenewable, and nonbiodegradable. Also, from environmental point of view, these nanoparticles are potentially pollutants. But the most important thing to note is all filtration experiments were carried out under static conditions. In other words, lower filtrate loss volumes in these works is due to the static conditions while filtration progresses. On the other hand, our filtration data with CNC-dosed drilling fluids were obtained under dynamic conditions and still comparable with previous reported data. Table 4.11 illustrates the total volume loss, and the fluid loss reduction percentage for different drilling fluids dosed with various nanoparticles.

**Table 4.11. CNC performance in fluid loss control in comparison to other nanoparticles**

Additive (%)	CNC (1%)	GO <sup>a</sup> (0.2%)	NSC <sup>b</sup> (0.5%)	Fe(OH) <sub>3</sub> (0.74%)	CNT <sup>c</sup> (1%)
Type of Filtration	Dynamic	Static	Static	Static	Static
API Total Volume Loss (ml)	15.2	6.1	16.0	1.1	26.3
Fluid Loss Reduction	60%	15%	40%	70%	7.0%

**Note:** All experiments were carried out under API standard (30 min); a Graphene Oxide; b Nanosilica Composite; c Carbon Nanotube.

Experimental data were collected for thermal conductivity, viscosity/yield point, and filtrate amount in samples dosed with 1% vol. carbon nanotubes (CNT). The rheological results followed an analogous improvement trend. The amount of filtrate for drilling muds

after 30 min (in accordance with the API filtration test) was 28.4 ml, while this parameter became 26.3 ml after the addition of 1 vol. % functionalized CNTs to the sample. This means that the amount of filtrate decreases by 7 % after using CNTs [9]. In case of graphene oxide nanoparticles (GO), it was found that a combination of large-flake GO and powdered GO in a 3:1 ratio performed best in the API filtration tests, allowing an average fluid loss of 6.1 ml over 30 min and leaving a filter cake  $\sim 20$   $\mu\text{m}$  thick. In comparison, a standard suspension of clays and polymers used in the oil industry gave an average fluid loss of 7.2 ml and a filter cake  $\sim 280$   $\mu\text{m}$  thick [8]. When iron (III) hydroxide was used, the API fluid loss of the samples indicated a decreasing trend in fluid loss over a period of 30 min as around 70% when lost circulation materials and 0.74 % iron (III) hydroxide nanoparticles were used together.

## **4.11. Summary**

In this chapter, drilling mud flow behaviour was investigated during two separate stages: between the drilling bit and porous media (concentric annuli), and through porous media (filter pores). Flow regime was laminar in both stages and laminar flow assumptions were used to develop fundamental transport equations. Darcy flow through porous media was established and pressure loss through the filter was compared between in the presence/absence of CNC particles. Effect of different physical/chemical parameters such as differential pressure, temperature, porosity of filters, shear rate, and mud formulation on the total volume loss and filtration rate of drilling mud was investigated. Finally, governing filtration mechanisms was discussed under different experimental conditions. Pore plugging due to the invasion of particles was confirmed to be the main and governing mechanism during filtration. A proper mathematical model to fit dynamic fluid loss data was achieved, which covered both early wall-building and equilibrium periods during dynamic filtration.

In the next chapter, rheology of the drilling mud and its flow behaviour will be discussed in further detail.

## **5. Rheology of water-based drilling muds**

As discussed previously in Chapter 1, drilling operation is the most important significant phase of oilfield operations. Drilling is considered successful based on the proper choice of the drilling mud used. An optimized composition of drilling fluid allows to considerably reducing the overall cost of a drilling process. The drilling fluid must ensure several performances such as carrying cuttings from the hole, cooling and lubricating the drill bit, maintaining the stability of the wellbore, and form a thin filter cake (controlling fluid loss). To this end and simultaneously preserve the environment, a water-based drilling mud is used. It consists of Wyoming clay, cellulose nanocrystals (CNC), and carboxymethyl cellulose polymer (CMC). These natural polysaccharides affect the rheological properties of the drilling fluids. Thus, understanding the effect of each component on the rheological properties of the mud is crucial to guarantee the smooth running of drilling.

In this chapter, the rheological behaviour of cellulose nanocrystal particles and CMC polymer are discussed. Afterwards, their highlighted effect to enhance rheological properties of clay suspensions will be presented. Finally, the best fit rheological model for different mud samples containing CMC/CNC will be proposed.

### **5.1. Rheology of CNC suspensions**

The rheological behaviour of CNC particles is of great importance especially when drilling mud fluid loss is studied. In Chapter 4, dynamic filtration tests on different drilling mud formulations were carried out. The addition of CNC results in better fluid loss control. Since rheological and filtration properties of drilling mud are related in regards to control the fluid loss, an understanding of how CNC particles change the rheology of the suspension is necessary. Recent investigations showed that CNC suspensions exhibited thixotropic shear thinning behaviour depending on particle concentration, aspect ratio and degree of sulfation [54, 69-71]. Shafiei-Sabet et al. investigated the rheology of cellulose nanocrystals under different conditions such as CNC particles concentration, temperature, ultrasound energy (sonication) and degree of sulfation (DS) [54, 71]. Their results indicated that CNC particles with aspect ratio (L/D) of 13 – 20 and zeta potential value of -31.5 mV exhibited non-Newtonian shear thinning behaviour in the concentration range from 1% to 7%. According to

their results, the 1% sample exhibits a Newtonian behaviour at low shear rates followed by a shear thinning trend at intermediate shear rates. Sonication effect was more highlighted at higher concentrations ( $> 3\%$ ). For example, 3 orders of magnitude decrease in viscosity was observed for 7% concentration. The observed shear thinning behaviour is attributed to a combination of two different mechanisms called gel breakage and domain deformation [54]. They also investigated the effect of sulfur content on the rheological properties of CNC suspensions in a wide range of concentrations (1 – 15 %) [71]. Two sets of CNC suspensions were prepared with 0.85 and 0.69 wt% sulfur content. Higher degree of sulfation results in lower viscosities at certain shear rates. Lower surface charges cause a decrease in electrostatic repulsion (stability) of the nanoparticles, which leads to a higher probability of aggregation. Applied ultrasound energy breaks all these aggregates, and the viscosity then drops significantly. Likewise their previous work, shear thinning behaviour was observed for all the concentrations of CNC. Figure 5.1 illustrates the shear thinning behaviour of the CNC suspensions with degree of sulfation 0.85%. Davis et al. investigated the rheology and phase behaviour of cellulose nanocrystal suspensions [70] with concentrations ranging from 3.07 to 17.3 volume percent. They showed that the behaviour of CNC suspensions at the lowest concentration (3.07 vol%) was nearly Newtonian with the inception of a shear thinning region at  $30 \text{ s}^{-1}$ .

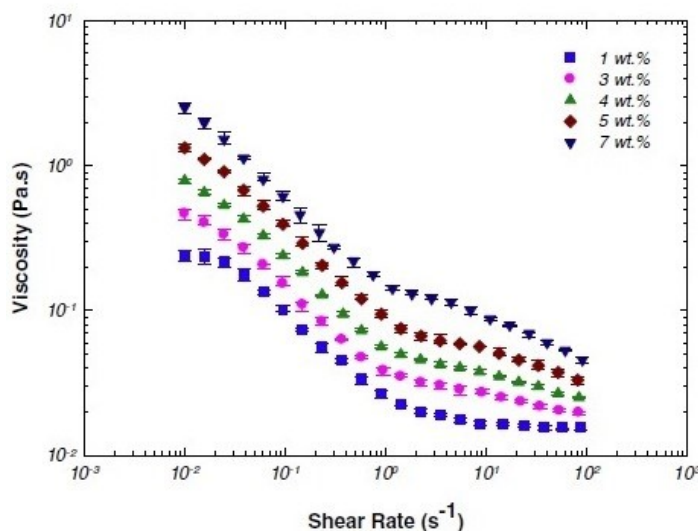


**Figure 5.1. Rheological behaviour of CNC suspensions with DS = 0.85% at different concentrations [71]**

CNCs are considered as an effective rheological modifier to enhance the rheological function of water-based drilling fluids. Boluk et al. investigated the rheological behaviour of CNC suspensions containing CNCs with aspect ratio of  $30 \pm 14$  and zeta potential of  $-62.8$  mV without any addition of electrolyte. The viscosity of CNC suspensions was reported Newtonian at concentrations below 1% (w/v) or 1 g/dl [53]. Figure 5.2 illustrates the viscosity vs. shear rate of CNC suspensions at 0.25, 0.50, 0.75, and 1.0 % concentrations without any electrolyte addition. Boluk et al. found out that all of the CNC concentrations were above the minimum overlap concentration,  $\phi_c$ , and it is expected that inter-particle interactions should be taken into account. The minimum overlap concentration for dispersions of CNC rods is given by Equation [5.1]:

$$\phi_c = \frac{d^2L}{L^3} \quad [5.1]$$

where  $d$  and  $L$  are the diameter and length of CNC rods, respectively.

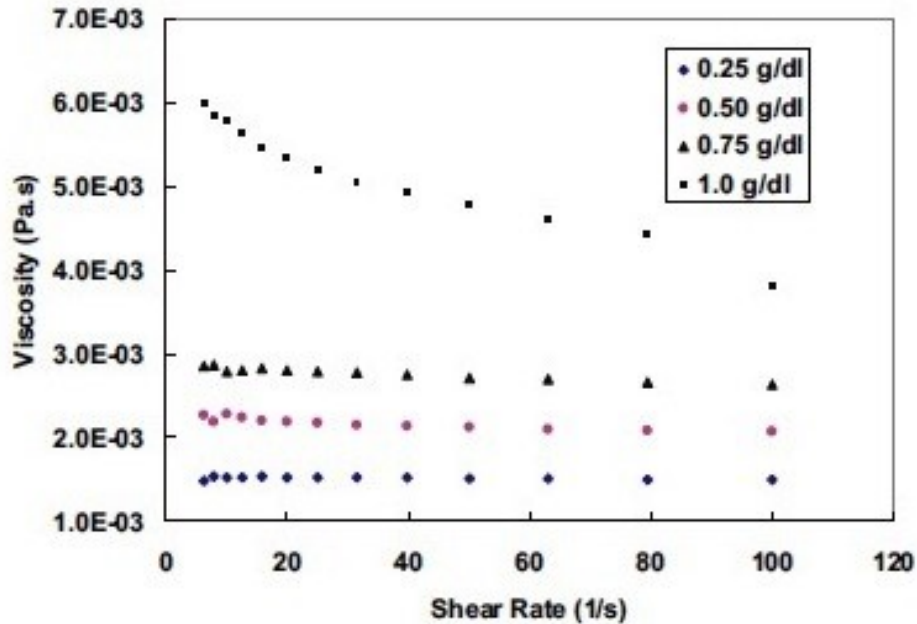


**Figure 5.2. Viscosity vs. shear rate of CNC dispersions at various concentrations without electrolyte addition [53]**

As shown in Figure 5.2 shear thinning non-Newtonian behaviour is clearly revealed only at 1.0 g/dL (1%) concentration. However, this behaviour disappears and becomes

Newtonian by addition of NaCl electrolyte to the CNC suspension. Figure 5.3 exhibits relative viscosity (viscosity of suspension to water ratio) as a function of volume fraction of CNC particles. As it is observed, with no addition of electrolyte, a non-linear behaviour is observed, but addition of electrolyte to the CNC suspension reduces the slope (intrinsic viscosity of CNC particles) and results in linear behaviour. The double layer thickness is compressed with an increase in ionic strength that results in CNC intrinsic viscosity decrease.

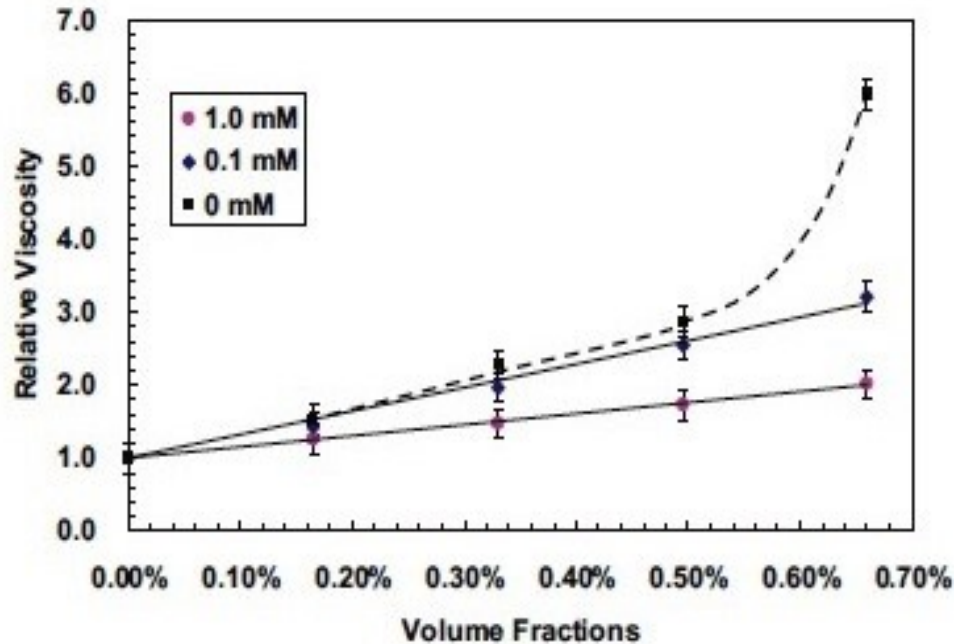


**Figure 5.3. Relative viscosity of CNC suspension vs. volume fraction (legends: NaCl concentrations) [53]**

The viscosity of 1% CNC suspension decreases consistently with increase in shear rate. 1% (w/v) CNC (volume fraction of 0.67%) identical to the CNC in Boluk et al. work was selected for the drilling fluids composition in both dynamic filtration and rheology experiments in order to consume CNC as low as possible and efficiently.

## 5.2. Rheology of CMC polymer suspensions

Likewise the effect of CNC particles on the rheological behaviour of drilling muds, the addition of CMC to clay suspensions is of great importance [46]. Precisely, in such materials, where clay is a major component, CMC works considerably to increase the

viscosity and control the mud fluid loss. CMC is used in many other industries including cosmetics, textile, pulp and paper, etc. It is frequently the product of choice because of its desirable price-to-performance ratio.

The rheological behaviour of CMC solutions has been investigated in several works [46, 72-75]; however, none of them was comprehensive enough to address the questions of CMC solutions rheological trend over a wide range of concentrations and molecular weight. For example, Ghannam [72] investigated the rheological properties of CMC solutions in the concentration scale of 1-5%, while lower percentages of 1% were not considered in his paper. Moreover, he did not report the molecular weight of the CMC used, which is crucial to know especially to compare different experimental results.

In this section, we first calculate the molecular weight of the CMC used in our experiments using intrinsic viscosity method, because the CMC polymer used in the experiments was not well characterized. Afterwards, rheological behaviour of CMC solutions will be discussed.

### 5.2.1. Molecular weight calculation for CMC suspension

It has been reported that the molecular weight of a polymer can be calculated based on its intrinsic viscosity and the empirical Mark-Houwink-Sakurada equation [76, 77]. The general equation takes the form:

$$[\eta]_w = K q_w M_w^a \quad [5.2]$$

where  $[\eta]_w$  is the experimentally measurable weight-average intrinsic viscosity,  $q_w = \left(\frac{M_v}{M_w}\right)^a$  the polydispersity correction factor, and  $M_w$  the molecular weight of the polymer.  $K$  and  $a$  are the constants that can be measured from intrinsic viscosity and molecular weights of polymer samples. These two constants vary depending on the polyelectrolyte concentration in the solution.

Equation [5.3] represents the  $[\eta] - M_w$  relationship for CMC solution in 0.01 M NaCl solvent,  $T = 298$  K, and molar masses 200000 – 2000000  $\text{g mol}^{-1}$  [77]:

$$[\eta] = 1.43 \times 10^{-2} M_w^{0.90} (\text{cm}^3 \text{g}^{-1}) \quad [5.3]$$

To obtain intrinsic viscosity, low shear viscosities of CMC samples were measured for 0.01 M NaCl at 298 K. Dilute CMC solutions were prepared in the concentration range of 0.1 – 0.6% w/v (0.001 g/ml – 0.006 g/ml). Viscosities at low shear rate (0.01 – 1 s<sup>-1</sup>) were measured and recorded. Equations [5.4] and [5.5] [77] were used to do a linear regression for reduced viscosity vs. solution concentration and yield intrinsic viscosity from the intercept:

$$\eta_{sp} = \frac{\eta_0}{\eta_{LM}} - 1 = c[\eta] + K_H(c[\eta])^2 + B_n(c[\eta])^n \quad [5.4]$$

$$\eta_r = \frac{\eta_{sp}}{c} = [\eta] + K_H[\eta]^2 c \quad [5.5]$$

where  $\eta_{sp}$ ,  $\eta_r$ ,  $\eta_0$ , and  $\eta_{LM}$  are specific, reduced, low shear, and solvent viscosities, respectively. C represents the concentration of CMC solutions, and  $K_H = 0.281$ ,  $B_n = 4.80 \times 10^{-4}$ , and  $n = 4.34$  are constants for CMC in 0.01 M NaCl solution at T = 298 K. The complete calculations can be found in Appendix B. Intrinsic viscosity and the consequent molecular weight of the CMC polymer were calculated as 3466.3 cm<sup>3</sup>/g and 961 kDa, respectively.

### 5.2.2. Rheological properties of CMC solutions

Figure 5.4 illustrates the viscosity change with CMC solution concentration without any electrolyte addition. It is shown that when CMC concentration increases from 0.1% to 0.6% (w/v), low shear viscosity increases by more than one order of magnitude. In addition, as CMC concentration increases, shear thinning behaviour will be more highlighted. For CMC concentration of 0.1%, approximately no shear thinning behaviour is observed. This is in good agreement with the recent work on rheological properties of carboxymethyl cellulose solutions [46]. CMC solutions are strongly thixotropic materials, which mean that they exhibit a viscosity – time relationship [46, 72, 73]. This behaviour is attributed to the inner structure of the fluid due to particle interactions such as van der Waals interactions that are responsible for the formation of flocs and aggregates. It was found that no yield stress was observed for the CMC solutions and the experimental results were found to be well correlated by the Cross model, as discussed earlier in Chapter 2. CMC solutions exhibit viscoelastic properties with a dominant viscous behaviour at low concentrations and a governing elastic behaviour at relatively high concentrations [46].

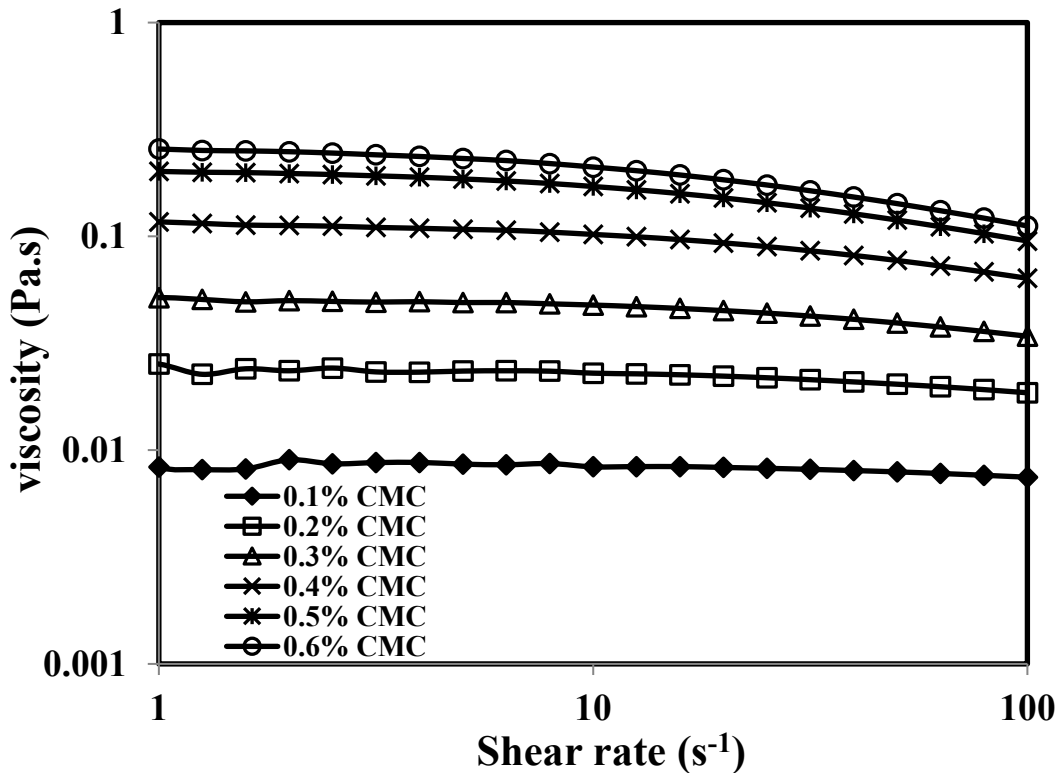


Figure 5.4. Viscosity vs. shear rate for different CMC solution concentrations (No salt)

Figure 5.5 illustrates the viscosity change as a function of CMC volume fraction at shear rate =  $1 \text{ s}^{-1}$ . As discussed earlier, increase in polymer concentration results in more entanglements of polymer chains. Consequently, higher viscosity is expected. For example, increasing volume fraction of CMC from 0.000625% to 0.00375 (6 times) results in an increase in relative viscosity from 10 to 500 (50 times). This reveals the high concentration dependency of CMC suspensions. Figure 5.5 demonstrates two separate regions based on the CMC polymer concentrations. The sets of points with connected with a straight line show the dilute region where inter-particle interactions are ignored. The concentrations below the critical concentration,  $C^*$ , are considered in dilute regime. The concentrations above this critical value have non-linear behaviour and are considered as semi-dilute regime points and change the rheological properties of suspension.

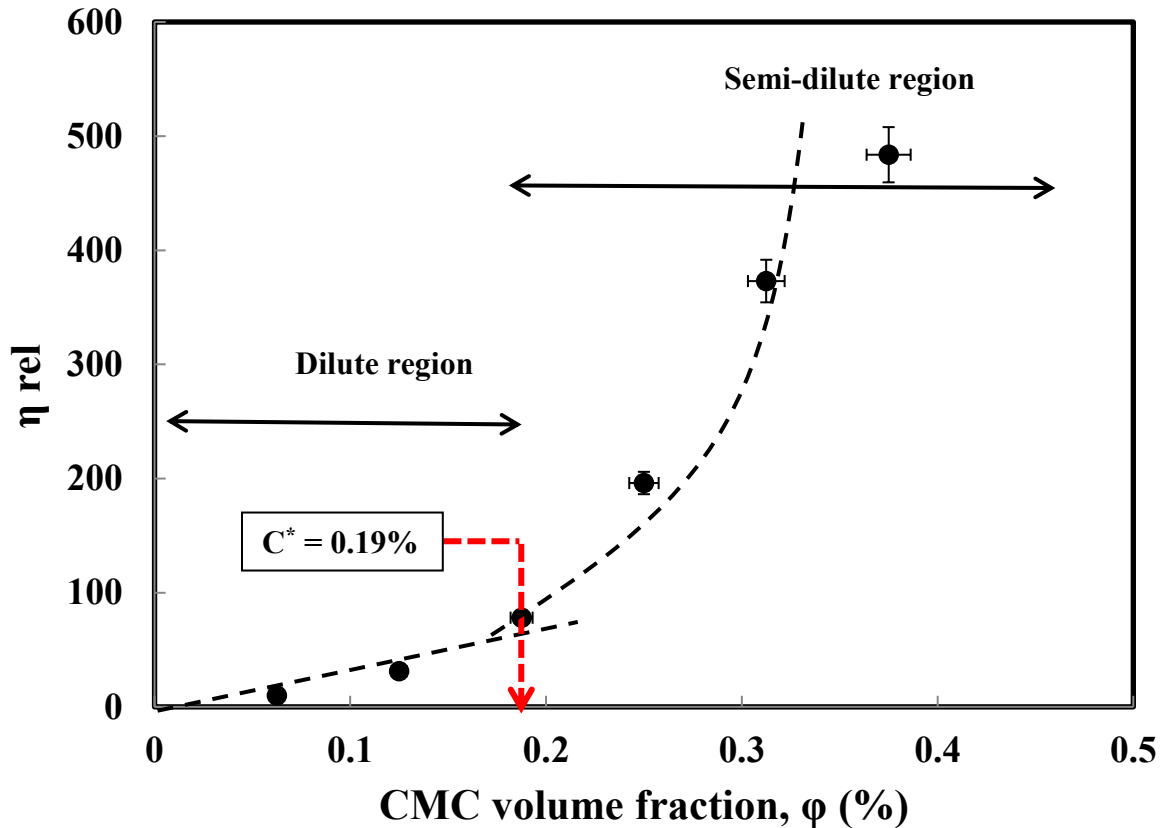


Figure 5.5. Relative zero-shear viscosity of CMC suspensions as a function of volume fraction. The dashed lines are guides for the eye.

It can be observed from the graph that 0.25% w/v concentration of CMC ( $\phi = 0.16\%$ ) is located in the dilute suspension region (linear behaviour). That implies the fact that the choice of 0.16 vol% for CMC is appropriate.

### 5.3. Rheology of clay suspensions

Rheological behaviour of bentonite suspensions (sodium/calcium montmorillonite) were investigated in several researches [18, 21, 41, 43-45]. Benyounes et al. carried out the rheological experiments over the range of 2 – 8% sodium bentonite. They noticed that from 3% of bentonite, the non-Newtonian behaviour became more visible. In addition, presence of yield stress in bentonite suspensions was confirmed and strengthened with the concentration of bentonite. This yield stress is attributed to inter-particle attractive energy that governs the

cohesion of bentonite-water system. This yield stress is highly dependent on the clay concentration and caused by the presence of an open three-dimensional network created by the contact of clay particles [45].

Rheological behaviour of clay (Wyoming Gel) suspensions is illustrated in Figure 5.6. Wyoming gel is sodium montmorillonite clay that is used primarily for filter-cake building, filtration control, and suspension agent in freshwater systems. As illustrated, an increase in bentonite concentration from 3% to 8% results in low shear viscosity increase by more than two orders of magnitude. All concentrations reveal the shear thinning behaviour, but more shear thinning behaviour is observed for higher percentage of bentonite. It is clearly indicated that the increasing of the bentonite weight percentage will increase the viscosity of the solution in each shear rate level. Moreover, it can be seen that the slope of the Viscosity – Shear rate data increases as the bentonite concentration is low, then gets stable when bentonite concentration is getting higher. The possible reason could be that in high – concentration region, the solubility of bentonite in water is close to its saturation limit, so the addition of more bentonite will not strongly influence the rheological properties of the solution. However, when the concentration of bentonite is low, the water has strong ability to keep dissolving bentonite in the solution; hence the rheological properties of the solution might be easily changed.

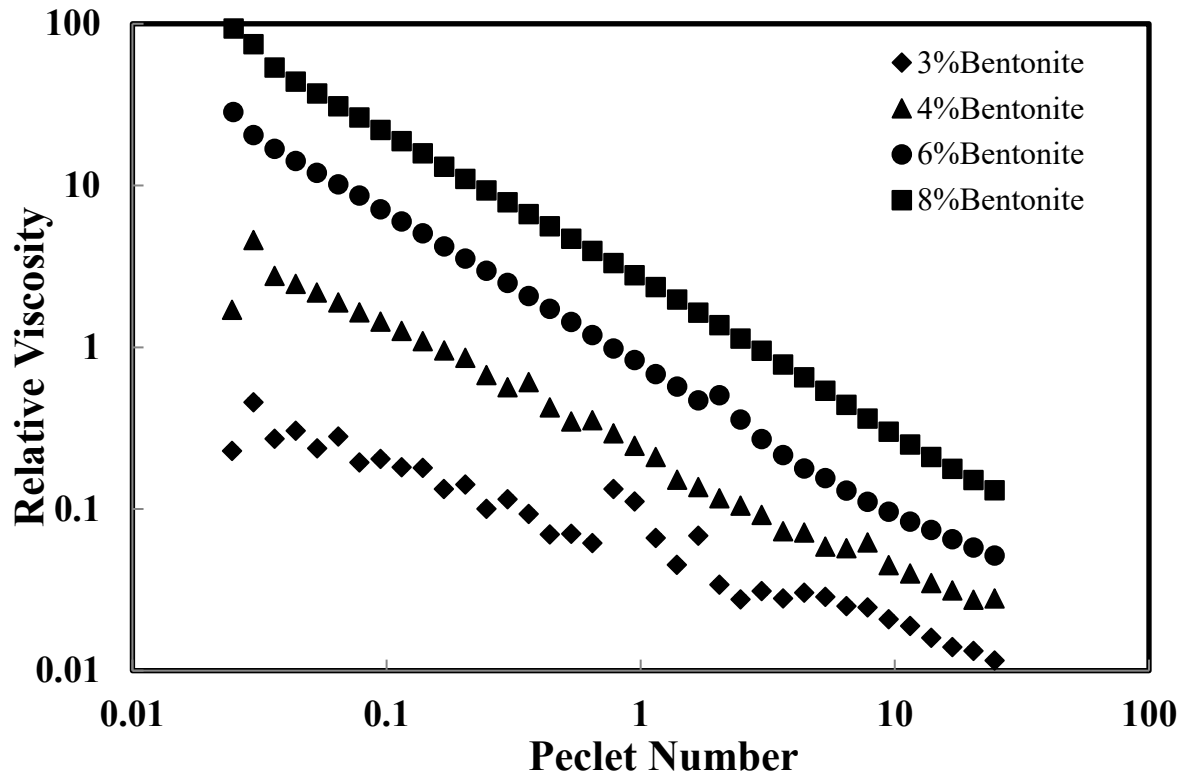


**Figure 5.6. Rheological behaviour of bentonite suspensions with different concentrations**

Viscosity behaviour of clay suspensions was also plotted as a function of clay volume fraction at shear rate =  $0.1 \text{ s}^{-1}$  in Figure 5.7.

Likewise, 3% w/v bentonite ( $\phi = 1.30\%$ ) is located in the dilute suspension regime and behaves linearly.

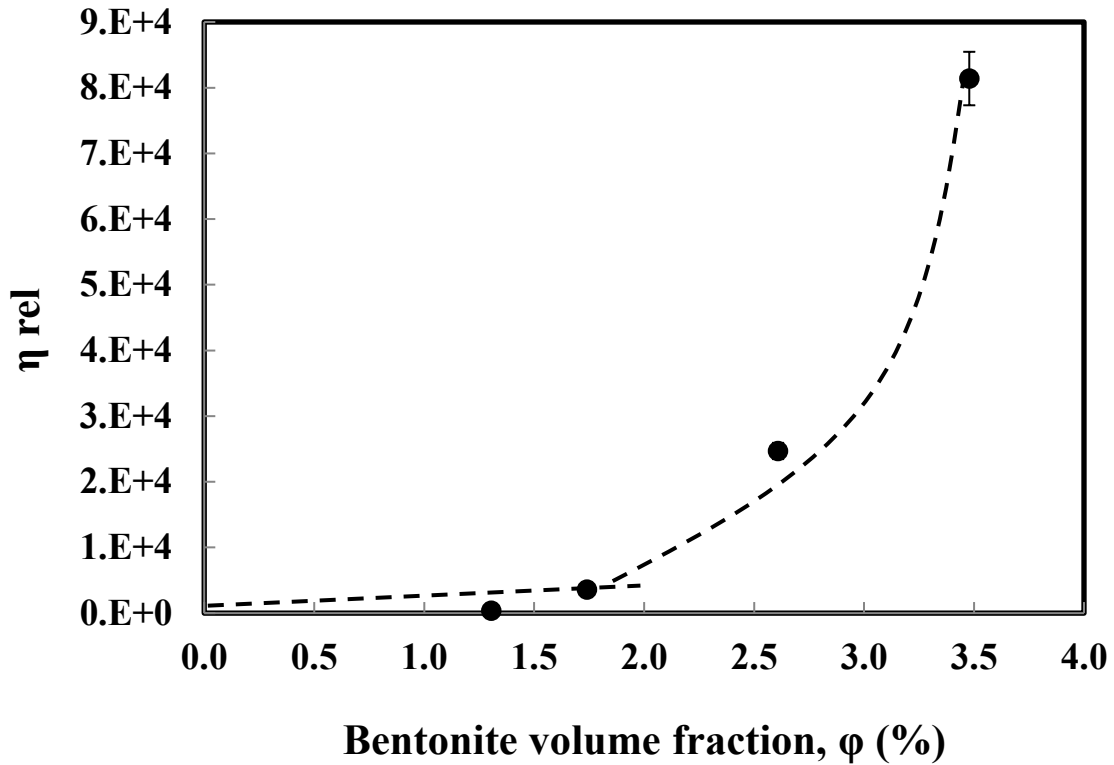


**Figure 5.7. Bentonite suspension viscosity as a function of concentration.**

**The dashed lines are guides for the eye.**

It can be observed that the difference in viscosities is more highlighted in higher bentonite concentrations. Low shear viscosity values are shown in Figure 5.8 for better comparison. Viscosities in higher shear rates are presented in Table 5.1. For example, viscosity values for 8% bentonite suspension are 93.8, 9.4, and 1.1 Pa.s for shear rates of 0.1, 1.0, and 10  $s^{-1}$ , respectively, while their values for 3% bentonite suspension are 0.4, 0.1, and 0.04 Pa.s for the same shear rates. This phenomenon may be explained as follows: High concentration of solids in such suspensions builds a structure by grain-to-grain contact. This structure resists shear because of inter-particle friction such as inter-particle attractive forces. Once the yield point is passed, and laminar flow begins, the particles are presumed to interact no longer, and to influence viscosity just by the volume fraction they occupy [1].

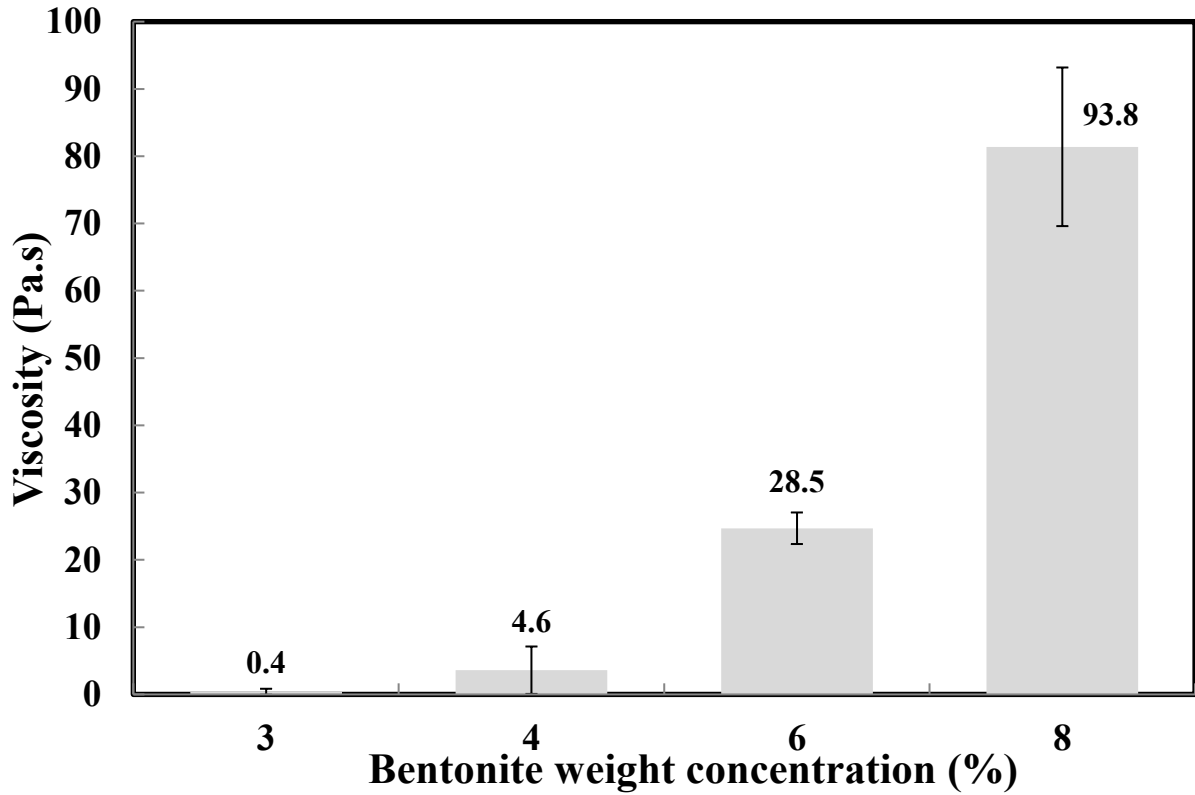


Figure 5.8. Low shear viscosity values for bentonite suspensions at shear rate = 0.1 s<sup>-1</sup>

At low shear rates the behaviour of the clay particles is influenced by attractive and repulsive surface interactions, and the viscosity is relatively high consequently. As the shear rate increases, the particles gradually align themselves in the direction of flow, and the viscosity becomes mostly dependent on the concentration of all solids in the mud suspension.

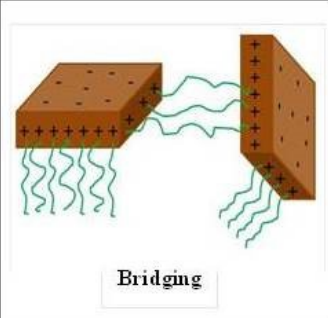
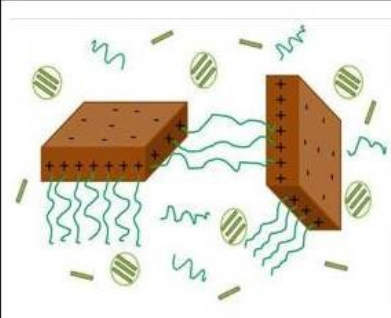
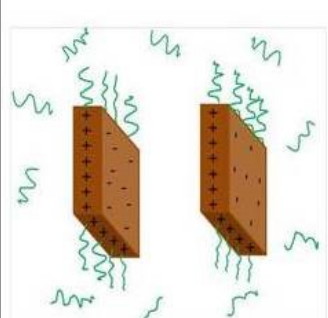
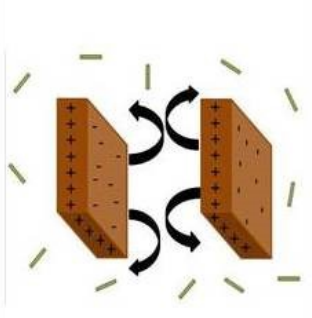
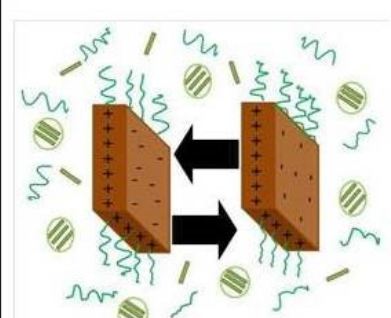
Table 5.1. Viscosity values for bentonite clay suspensions at different shear rates and mud concentrations

Bentonite Weight Percentage (%)	Viscosity (Pa.s)		
	Shear Rate of 0.1 s <sup>-1</sup>	Shear Rate of 1.0 s <sup>-1</sup>	Shear Rate of 10 s <sup>-1</sup>
3	0.4	0.1	0.04
4	4.6	0.6	0.1
6	28.5	2.9	0.3
8	93.8	9.4	1.1

To investigate the contribution of additives (CMC, CNC, and both) on the rheological behaviour of clay suspensions, a decision has been made to set the concentration of clay to 3%. This concentration is very commonly used in the formulation of drilling muds [45, 78, 79].

## 5.4. Rheology of CNC/CMC-rich drilling mud suspensions

Figure 5.9 illustrates all the potential mechanisms involved when bentonite particles are interacting with CMC polymer and/or CNC particles.

Potential mechanisms	Mud formulations		
	Bentonite + CMC	Bentonite + CNC	Bentonite + CMC + CNC
Adsorption	 <p>Bridging</p>	<p>Low possibility</p>	
Depletion attraction			

**Figure 5.9. Potential mechanisms for different mud formulations**

All the possibilities will be discussed in the following sections (5.4.1 – 5.4.3). Effect of each polysaccharide material will be investigated individually. Afterwards, their synergistic effect will be discussed when both are added to the clay suspension.

### 5.4.1. Effect of cellulose nanocrystals (CNC)

Recently, CNC effect on rheological properties of mud suspensions was investigated [21]. They showed the effect of CNC concentration on viscosity of drilling fluids. By increasing CNC concentration up to 0.5%, the viscosity of drilling fluid increased by 2 orders of magnitude at shear rate of  $0.1 \text{ s}^{-1}$ . A shear thinning behaviour was observed by adding CNC to the fluid. Increasing CNC concentration resulted in more obvious shear thinning behaviour in such a way that at shear rate of  $1000 \text{ s}^{-1}$ , the viscosity increases from 0.01 to 0.1 Pa.s (1 order of magnitude) [21]. The absence of CNCs yielded a unique shear-thinning curve with two stages. In the first stage, the viscosity decreased linearly for shear rates  $0.1\text{-}100 \text{ s}^{-1}$ . In the second region, an evident plateau was observed as shear rate increase from 100 to  $1000 \text{ s}^{-1}$ . Without the use of CNCs, the surface interaction among polysaccharide polymer, bentonite and water molecules was relatively weak. Consequently, the viscosity quickly reached the leveling-off plateau at a much lower shear rate [21].

Figure 5.10 illustrates the effect of CNC addition to bentonite suspensions of different concentrations. All viscosity values for bentonite – CNC suspensions are tabulated in Table 5.2 for better comparison and low shear viscosity values are illustrated in Figure 5.11. Likewise Figure 5.6, shear thinning behaviour is observed when CNC is added to clay suspensions, but comparing Figure 5.6 and Figure 5.10 highlights the effect of CNC to increase the low shear viscosity of drilling muds. The low shear viscosities increase at least by one order of magnitude when 1% CNC is added to the clay suspension. This phenomenon is in good agreement with previous works. This considerable effect is illustrated in Figure 5.12.

**Table 5.2. Viscosity values for suspensions including CNC at different shear rates**

1% CNC & Bentonite Concentration (%)	Viscosity (Pa.s)		
	Shear Rate of $0.1 \text{ s}^{-1}$	Shear Rate of $1.0 \text{ s}^{-1}$	Shear Rate of $10 \text{ s}^{-1}$
3	2.3	0.8	0.2
4	6.9	1.9	0.3
6	71.2	7.7	0.9
8	235.3	25.9	2.9

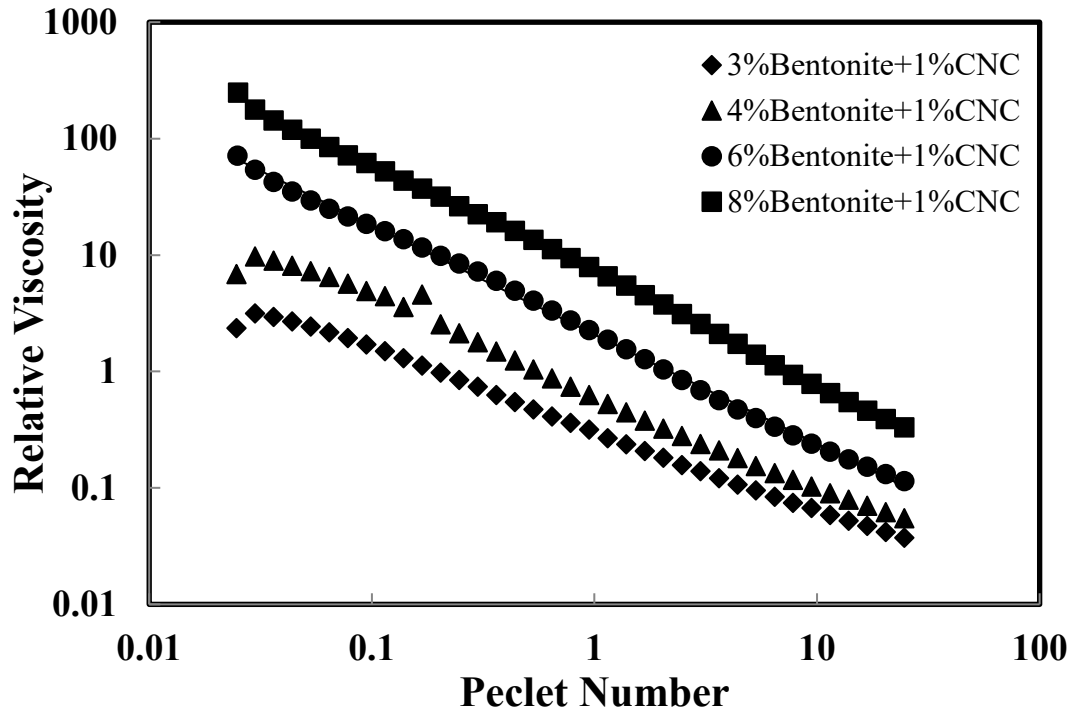


Figure 5.10. Rheological behaviour of bentonite suspensions containing 1% CNC

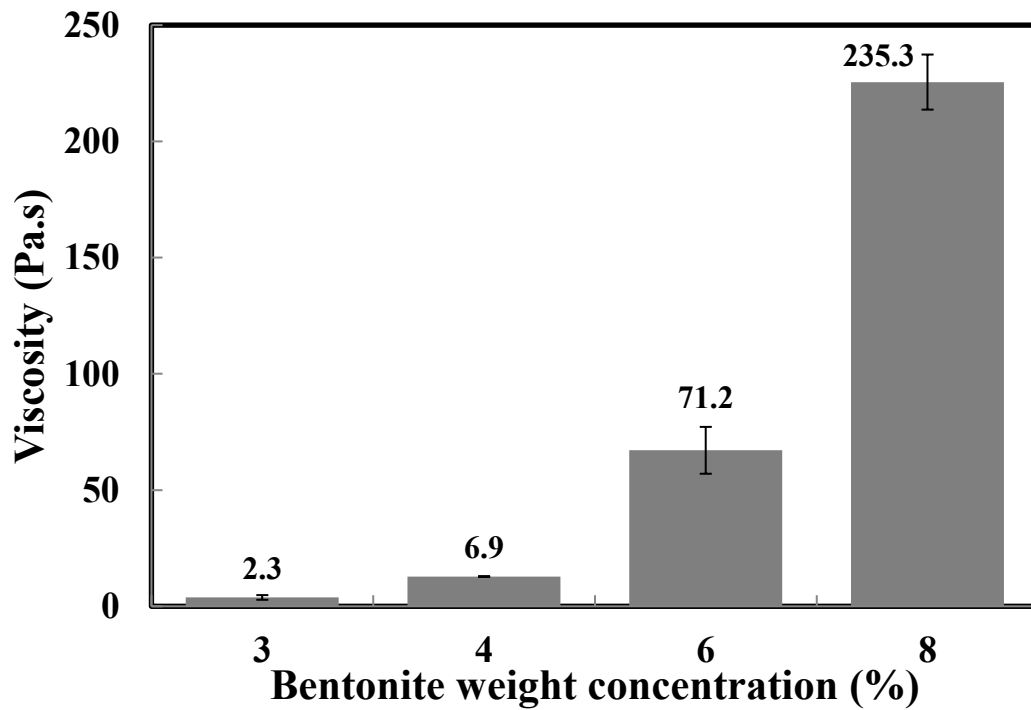
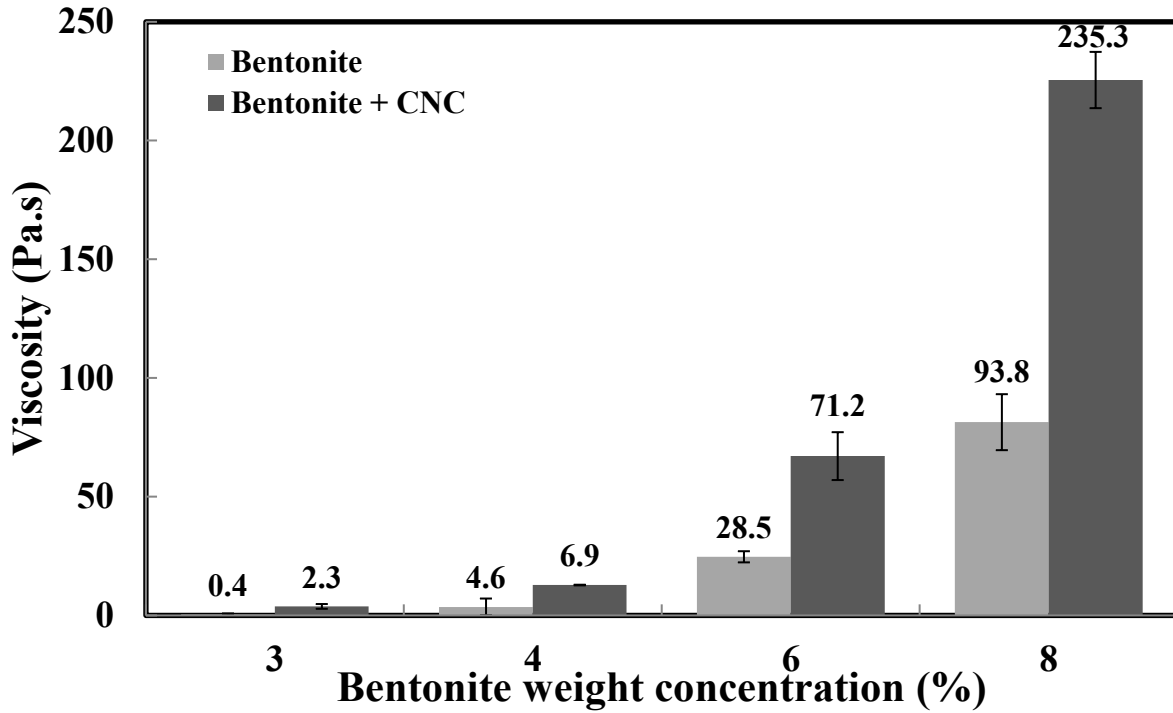


Figure 5.11. Low shear viscosity values for CNC enhanced bentonite suspensions at shear rate =  $0.1 \text{ s}^{-1}$



**Figure 5.12. Effect of 1% CNC addition in rheological behaviour of clay suspensions at shear rate =  $0.1 \text{ s}^{-1}$**

Rheological behaviour of bentonite clay suspensions with and without CNC was plotted at different bentonite volume fractions at  $0.1 \text{ s}^{-1}$  shear rate. Figure 5.13 illustrates the effect of CNC addition to enhance rheological properties of clay suspensions. More highlighted differences are observed at higher volume fractions of bentonite. This supports the decision to select 3% w/v ( $\phi = 1.30\%$ ) bentonite in the final formulation of drilling mud.

Increase in viscosity values in the presence of CNC particles is attributed to the depletion effect induced by CNC particles. This interaction results in bridging of bentonite particles and further gelation in the suspension. As a consequence, viscosity of the suspension including CNC particles increases considerably. Figure 5.14 illustrates the possible depletion attraction interaction between bentonite platelets and CNC rod-like particles. Li et al. attributed this viscosity increase to a typical core-shell structure created in CNC-Bentonite drilling fluids due to the strong surface interactions among bentonite layers, CNCs, and water molecules [21].

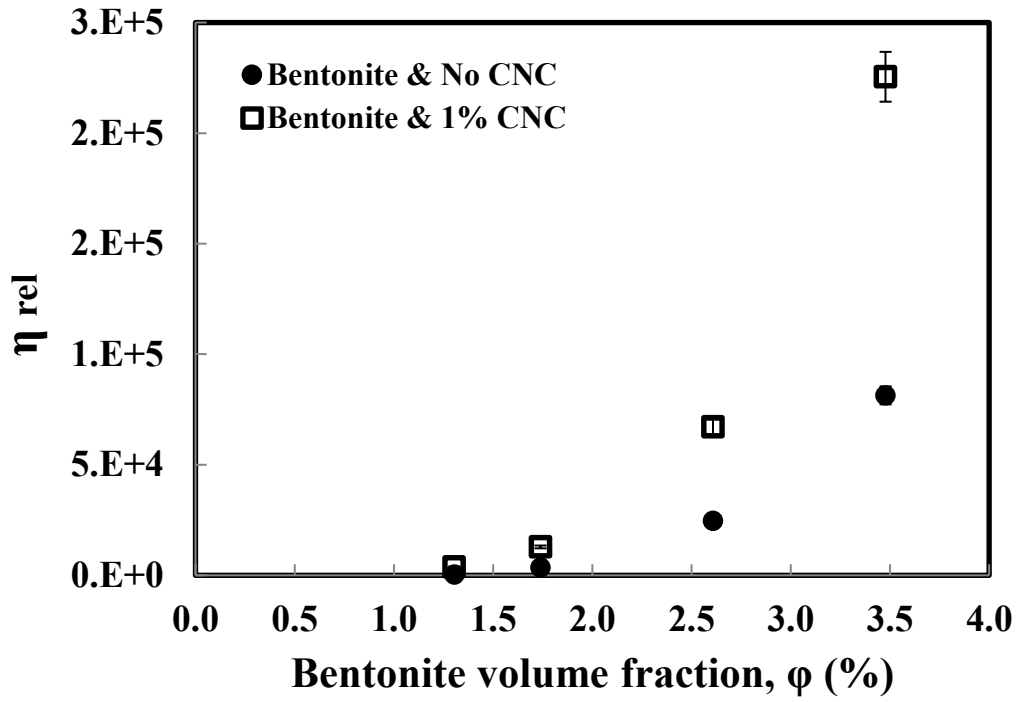


Figure 5.13. Effect of CNC addition in rheological behaviour of bentonite suspensions at different volume fractions

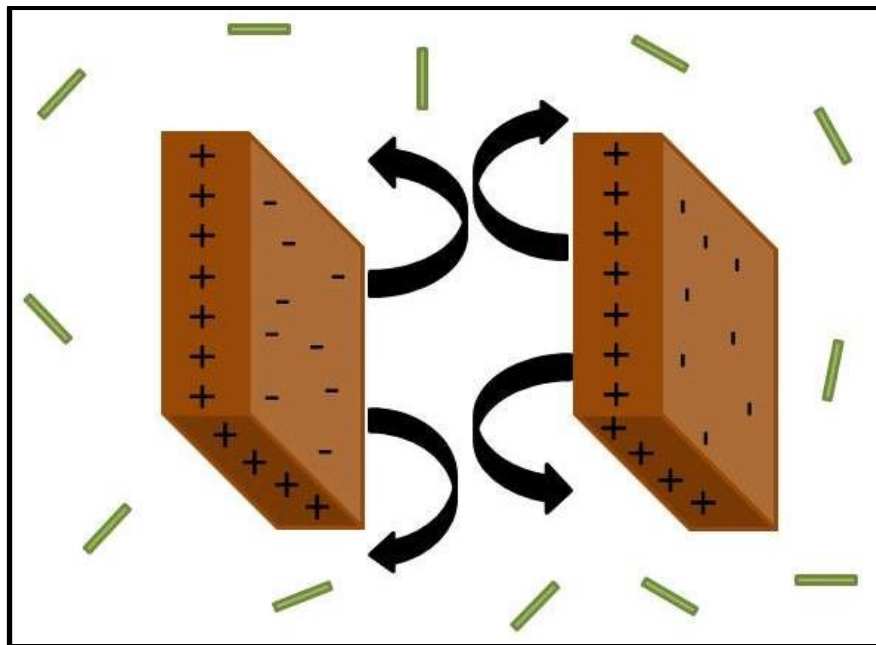


Figure 5.14. Bentonite - CNC depletion interaction

### 5.4.2. Effect of carboxymethyl cellulose (CMC) polymer

Many researchers investigated the effect of polysaccharide materials especially CMC and PAC on the rheological behaviour of clay suspensions [18, 21, 45]. M. Li et al. investigated the effect of polyanionic cellulose (PAC) on the rheological behaviour of drilling muds [21]. They found out that adding PAC to the clay suspension increases the viscosity and reveals shear thinning behaviour, but no significant change was observed when PAC concentration increased from 0% to 0.5% in such a way that the viscosity at  $0.1 \text{ s}^{-1}$  increased from 10 to 100 Pa.s (1 order of magnitude) and at  $1000 \text{ s}^{-1}$  from 0.01 to 0.1 Pa.s (1 order of magnitude) [21]. K. Benyounes et al. investigated the effect of adding CMC on the rheological properties of the 3% bentonite suspensions [45]. CMC concentration was in the range of 0 – 2%. They observed an increase in viscosity as CMC concentration increased. CMC long chains cause a number of entanglements when added to the clay suspension. Therefore, higher viscosity was observed in bentonite-CMC mixtures compared to bentonite suspensions. In addition, the yield stress existing in bentonite solutions was reduced when CMC was added. There is a possible reason behind this phenomenon. CMC has flexible character and possess a high negative charge, which favors the deflocculating of bentonite-CMC suspension and dispersion of clay particles [45].

As illustrated in Figure 5.9, the positive charges in bentonite platelets are distributed over the edges, while the negative charges are located in the upper and lower surfaces. It has been reported that bentonite is composed of a large number of plate-like layers with a permanent negative charge on the flat surface and usually positive charge on the edge [41, 80]. Consequently, two potential mechanisms may occur between CMC polymer chains and bentonite platelets due to the conformational status of bentonite platelets. The first possible scenario is shown in Figure 5.15 and takes place when the bentonite platelets edges are facing each other. In this situation, the CMC polymer may adsorb to the edges of bentonite platelets partially. It then may happen that some polymer chains adsorb on two or more different bentonite particles and pulling them together. Therefore, bridging may occur. The other possibility shown in Figure 5.16 happens when bentonite platelets conformation is in such a way that the surfaces are facing each other. Due to approximately no polymer adsorption on these surfaces, more volume fraction is available for CMC polymer chains and bentonite

platelets may be depleted by excess CMC polymer in the suspension. This creates a subtle osmotic attraction between the bentonite particles, which can lead to aggregation.

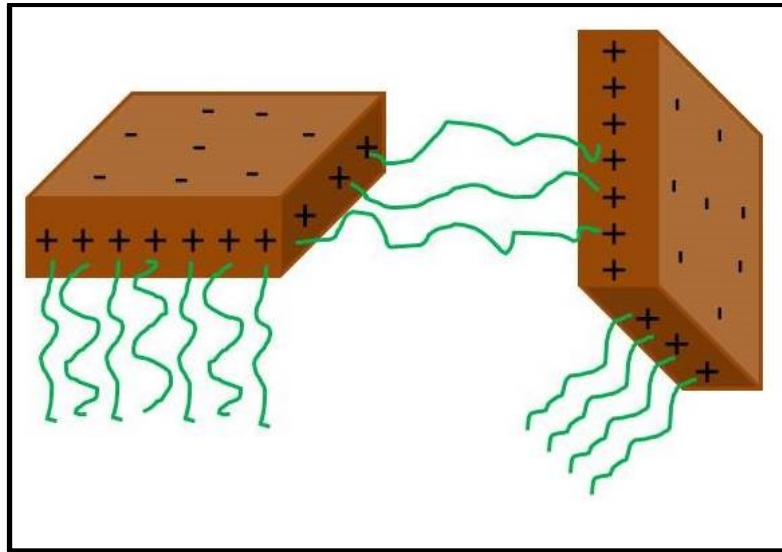


**Figure 5.15. Bridging mechanism between bentonite platelets and CMC polymer chains**

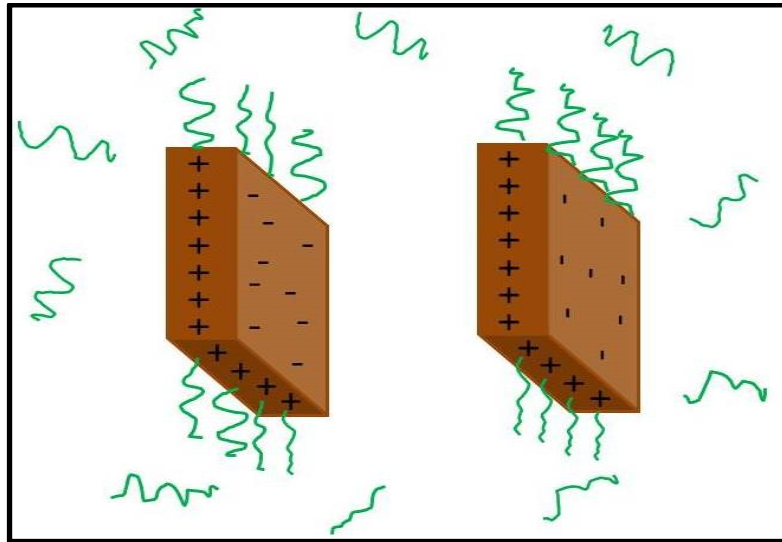


**Figure 5.16. Depletion mechanism between bentonite platelets and CMC polymer chains**

Anticipation of the most probable mechanisms in colloid – polymer suspension can be made using the following equations:

$$C_p = \frac{3\phi\Gamma}{R} \quad (\text{For Spheres}) \quad [5.6]$$

$$C_p = \frac{2\phi\Gamma}{R} \quad (\text{For rods}) \quad [5.7]$$

Where  $C_p$  is the saturated polymer concentration,  $\phi$  the particle volume fraction,  $\Gamma$  the saturation value of the polymer coverage ( $\Gamma_{\max} = 1 \text{ mg/m}^2$ ) [81, 82], and  $R$  the particle radius. The polymer concentration used in the experiments ( $0.25\% \text{ w/v} = 2.5 \text{ kg/m}^3$ ) will be compared with the saturated polymer concentration. The different possibilities are shown in Table 5.3.

**Table 5.3. Anticipation of interaction mechanisms based on saturated polymer concentration**

Below $C_p$	At $C_p$	Above $C_p$
Bridging (Attraction)	Steric stabilization (Repulsion)	Depletion of soft surfaces (Attraction)

Assuming spherical bentonite volume fraction  $\phi = 0.013$  (3% w/v),  $\Gamma = 1 \text{ mg/m}^2$ , and bentonite particles radius  $R = 10^{-6} \text{ m}$ , the saturated polymer concentration is calculated as  $0.039 \text{ kg/m}^3$ . Therefore, comparing  $2.5 \text{ kg/m}^3$  CMC used in the experiments with the calculated saturation concentration leads us to conclude that bridging of bentonite particles are more probable through partially adsorbed CMC polymers, which results in higher viscosity of the suspension. It should be noted that we cannot certainly predict the mechanism(s) occurring between polymers and particles unless X-Ray images are taken from the suspensions.

### 5.4.3. Rheology of drilling mud containing both CMC and CNC

Cellulosic polymers and particles increase the stability of clay suspension. Rheological behaviours of clay, CMC, CNC, clay + CMC, clay + CNC, and clay + CMC + CNC suspensions are shown in Figure 5.17. It can be observed that the addition of CMC increased the viscosity of the suspension considerably by one order of magnitude. Similarly, CNC addition improves the rheological behaviour of clay suspension approximately in the same manner which CMC does. But, the most considerable effect was observed when CMC and

CNC were added together to the clay suspension. The addition of CNC even at very low concentration (1% w/v) along with low dosage of CMC (0.25% w/v) increased the low shear viscosity by approximately two orders of magnitude.

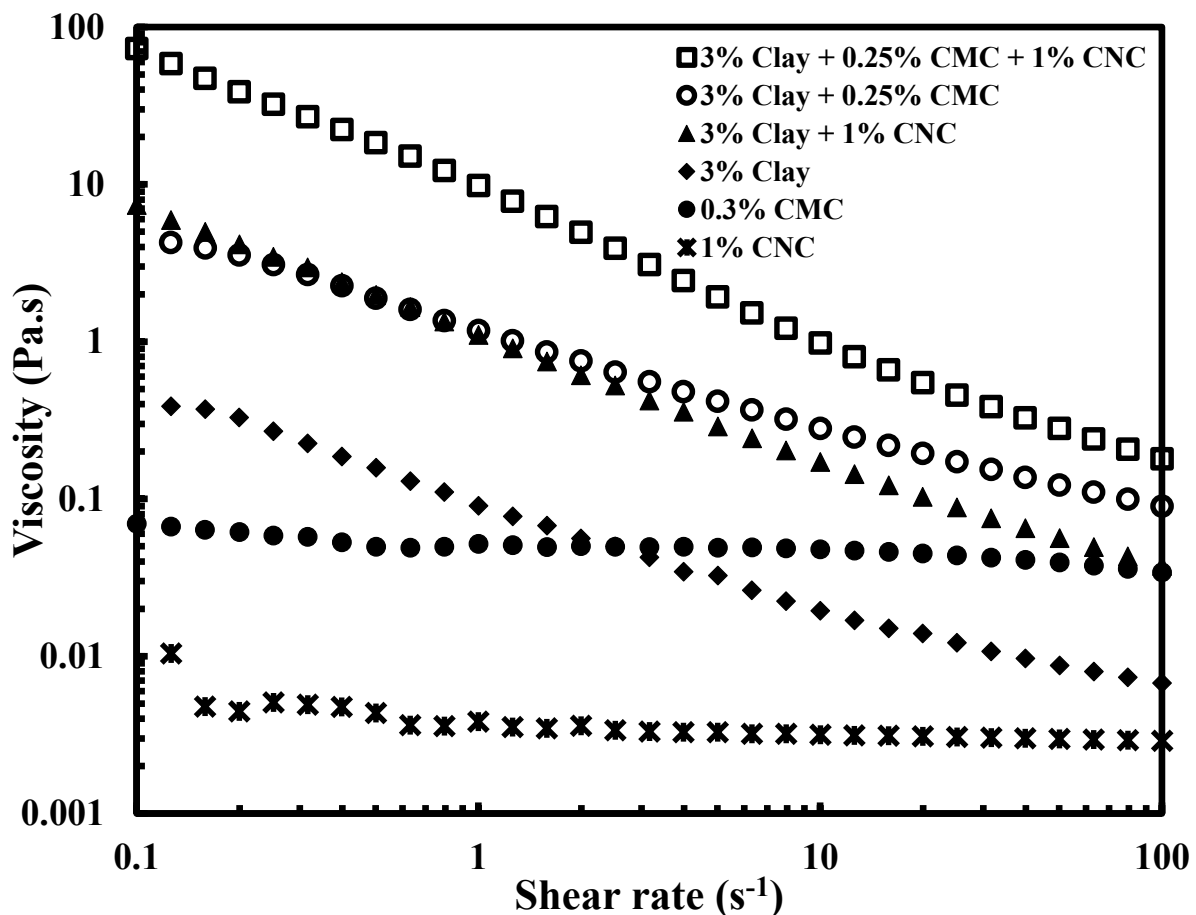
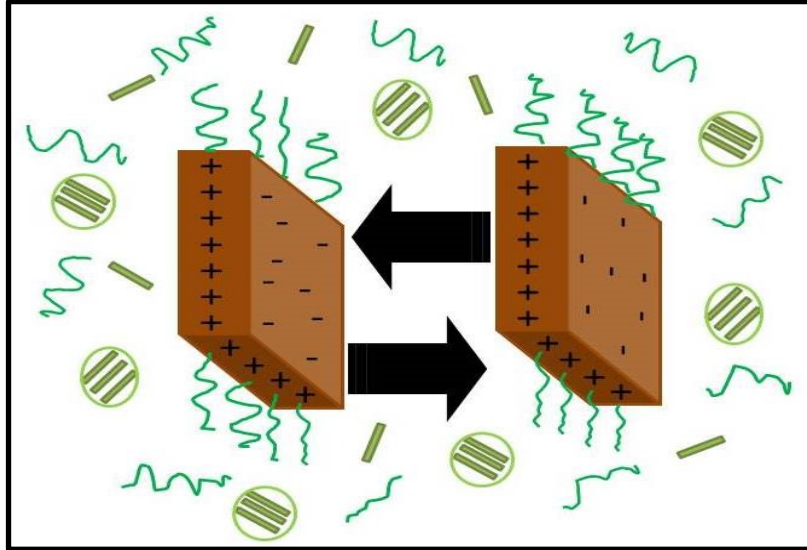


Figure 5.17. Viscosity vs. shear rate for different suspensions

This viscosity increase may originate from the nematic flocculation of CNC particles in the presence of CMC polymer that result in formation of pockets of CNC flocs. In other words, the unusual behaviour of CNC suspension in CMC polymer solution is explained by depletion flocculation phenomenon [13, 83]. Once CNC particles are added to the suspension, they occupy higher volume fraction than their real one due to flocculation and formation of nematic floc pockets with entrapped CMC free water. Therefore, the available volume of water for CMC polymer chains decreases and CMC concentration will increase.

Consequently, apparent CMC concentration shifts the solution state to concentrated network solution state and yields a high viscosity increase in the suspension. In this situation, bentonite platelets are trapped in a gel-like structure of CMC and CNC.



**Figure 5.18. Aggregation of bentonite platelets by CNC-CMC, CNC-bentonite, and CMC-bentonite depletion**

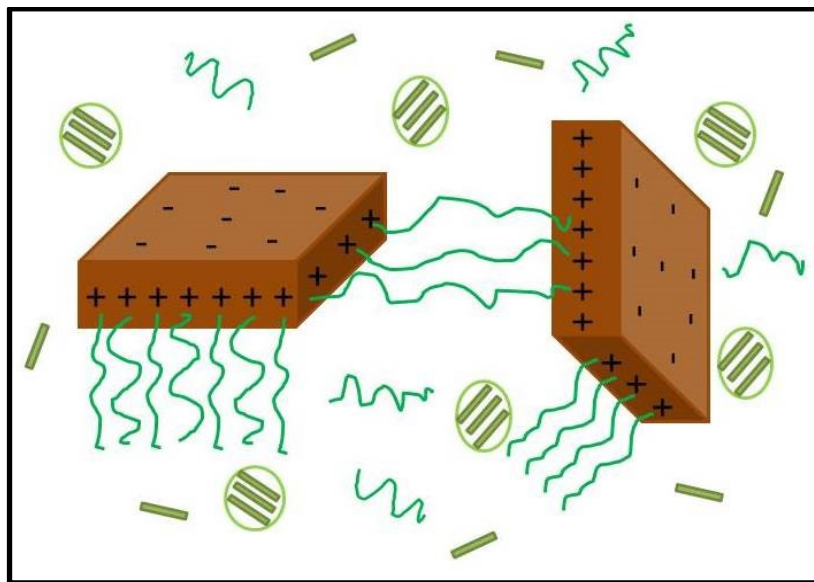


**Figure 5.19. Aggregation of bentonite platelets by CNC-CMC, and CNC-bentonite depletion, and CMC-bentonite bridging**

Equation [5.7] also confirms the depletion flocculation of CNC rod-like particles by CMC polymer. Assuming CNC volume fraction  $\phi = 6.66 \times 10^{-3}$  (1% w/v),  $\Gamma = 1 \text{ mg/m}^2$ , and CNC particle radius  $R = 4 \times 10^{-9} \text{ m}$ , the saturated polymer concentration is calculated as  $3.33 \text{ kg/m}^3$ . Therefore, comparing  $2.5 \text{ kg/m}^3$  CMC used in the experiments with the calculated saturation concentration leads us to conclude that CNC particles are possibly depleted by CMC polymer. Figure 5.18 and Figure 5.19 show the possible interactions between bentonite platelets, CMC polymer chains and CNC rod-like particles.

Figure 5.20 illustrates the synergistic effect of CNC and CMC in bentonite clay rheological behaviour. As it can be observed, the experimental viscosity data are considerably larger than the additive data for CMC and CNC enhanced bentonite suspensions. This difference is more highlighted in low shear rates. For example, the viscosity of CMC/CNC-enhanced bentonite suspension in the experiment at shear rates of  $0.1 - 1 \text{ s}^{-1}$  is one order of magnitude larger than when viscosities of bentonite – CMC and bentonite – CNC viscosities are added together.

It can be concluded that there should be an interaction between CMC and CNC to make such a difference in rheological data. This effect was mentioned above and is known as depletion flocculation. In other words, CNC particles are depleted and flocculated in the presence of CMC polymer.

Many studies have been carried out to investigate the effect of CMC and/or CNC on clay suspensions [18, 21, 45]. It has been shown that presence of each or both of them in the clay suspension increases the viscosity of the mixture, but not a quite clear understanding was achieved about the function of each CMC or CNC to enhance the rheological properties of clay suspensions. M. Li et al. did the rheological tests for CMC/CNC suspensions with 0 – 6% bentonite. They showed that increase in bentonite concentration results in viscosity increase by at least two orders of magnitude. They also observed the shear thinning behaviour of polyanionic cellulose (PAC)/CNC suspension without bentonite (0%), revealing the potential use of the combined PAC/CNC additives as effective rheological modifiers for drilling fluids [21]. PAC is water-soluble anionic cellulose ether, which is synthesized using

an alkali-catalyzed method. The primary difference between CMC and PAC is the degree of substitution (DS). PAC has higher purity and DS compared with CMC [19].

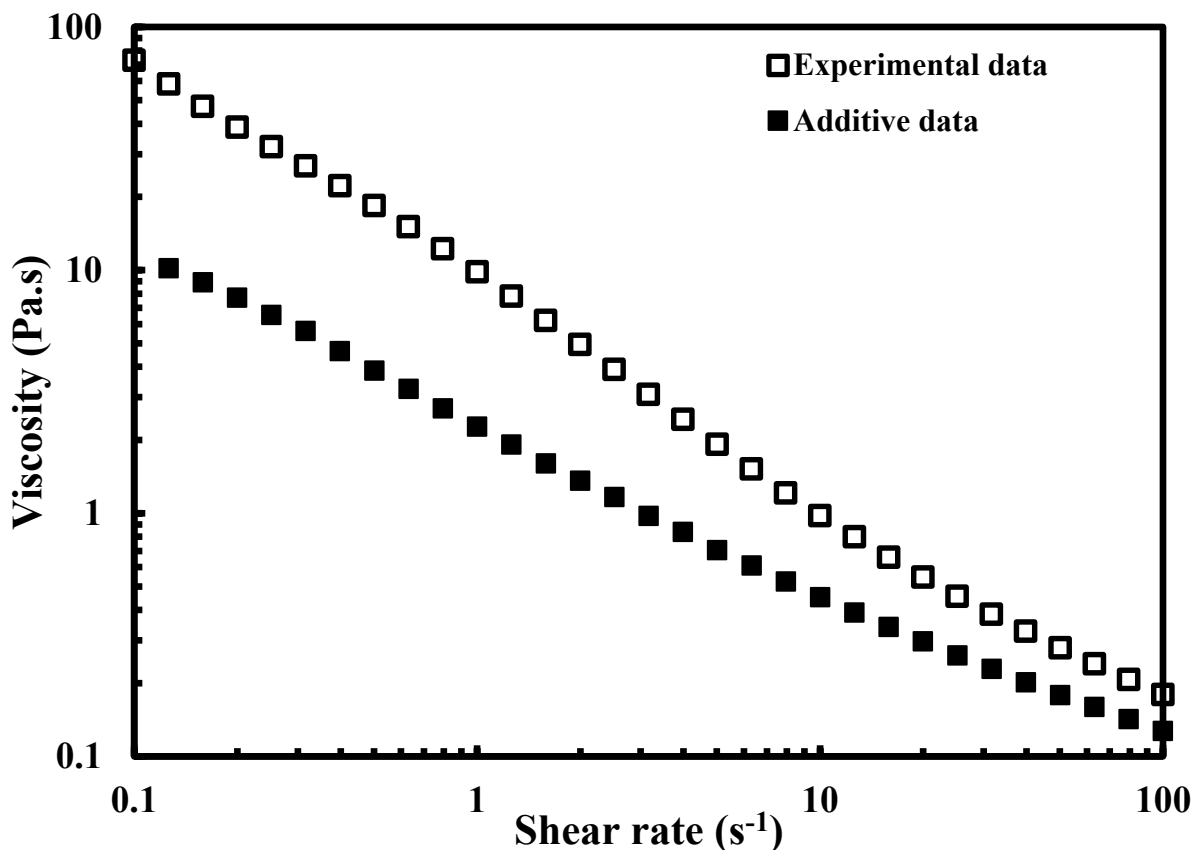


Figure 5.20. Synergistic effect of CMC/CNC addition to bentonite suspension

Interactions of colloidal particles and polymers in the solution have been studied by many researchers [84, 85]. Several phenomena may occur when a soluble, flexible polymer surrounds dispersed colloidal particles that are illustrated in Figure 5.21.

First of all, the swollen polymer coils are forced to leave from the surface of the particle that induces an elusive osmotic attraction between the particles, which can result in aggregation. This phenomenon is called “depletion” effect (B). Secondly, the polymer may adsorb to the surface of the particles. Therefore, some chains may adsorb on two or more

different particles, thereby pulling them together. This is called “bridging” (C). Alternatively, the polymer may develop a protective case around each particle, thereby preventing them from aggregation or bridging. This is usually called “steric stabilization” (D). Finally, if no polymer exists in the solution, the dispersed particles are usually stabilized by electrostatic interactions (A) according to DLVO theory.

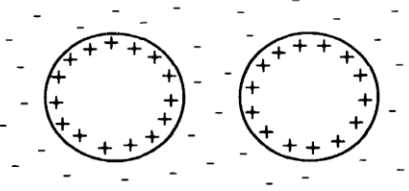
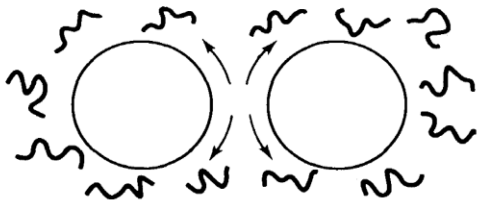
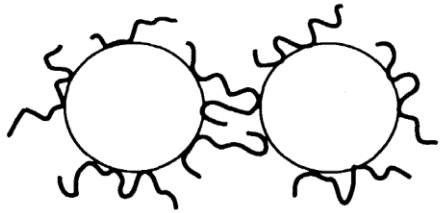
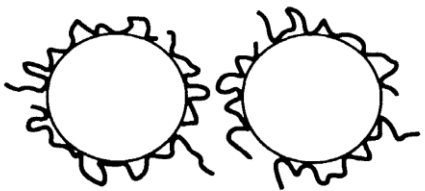
MECHANISM	FORCE LAW
<p>(A) bare particles</p> 	<p><u>Van der Waals attraction</u></p> <p><u>electrostatic repulsion</u></p>
<p>(B) particles + non-adsorbing polymer</p> 	<p>weak (osmotic) attraction</p> <p><u>"depletion attraction"</u></p>
<p>(C) particles + low polymer dose adsorbed</p> 	<p>strong attraction</p> <p><u>"bridging"</u></p>
<p>(D) particles + excess adsorbing polymer</p> 	<p>strong repulsion</p> <p><u>"steric repulsion"</u></p>

Figure 5.21. Schematic overview for different mechanisms colloids - polymer suspensions [84]

In conclusion, different scenarios were taken into account and possible effects on the rheological behaviour of bentonite suspensions were investigated. However, the viscosity of the mud suspension is dictated by bentonite concentration and conformation. Viscosity values and stability of different mud formulations are tabulated in Table 5.4.

**Table 5.4. Rheological data for different mud formulations**

<b>Clay (wt%)</b>	<b>CMC (wt%)</b>	<b>CNC (wt%)</b>	<b>Rate index n</b>	<b>Yield stress (Pa)</b>	<b>Suggested model</b>
3	0	0	0.64	0.06	Herschel-Bulkley
3	0.25	0	0.58	0.50	Herschel-Bulkley
3	0	1	0.54	1.02	Herschel-Bulkley
3	0.25	1	0.68	7.71	Herschel-Bulkley

## **5.5. Best rheological models for cellulose-based drilling mud**

The rheological behaviour of bentonite suspension has been correlated by Herschel – Bulkley model [45, 86, 87]. The model was described earlier in Chapter 2.

$$\tau = \tau_0 + \mu\gamma^n \quad [5.8]$$

Herschel-Bulkley schematic model is illustrated in Figure 5.22. According to this model, the suspension has an initial yield stress at low shear rates, and afterwards presents pseudoplastic or “shear-thinning” type behaviour at higher shear rates. In other words, the viscosity decreases with shear rate. The advantage of using this model is that it covers a broader shear rate scope, giving a better estimate of the yield stress. Also, it is useful for obtaining other parameters such as the flow behaviour index  $n$ , consistency factor  $k$ , and effective viscosity  $\mu$  [44]. This model has been used extensively to describe the rheology of drilling mud suspensions [18, 45, 88, 89] due to its high compatibility with experimental data.

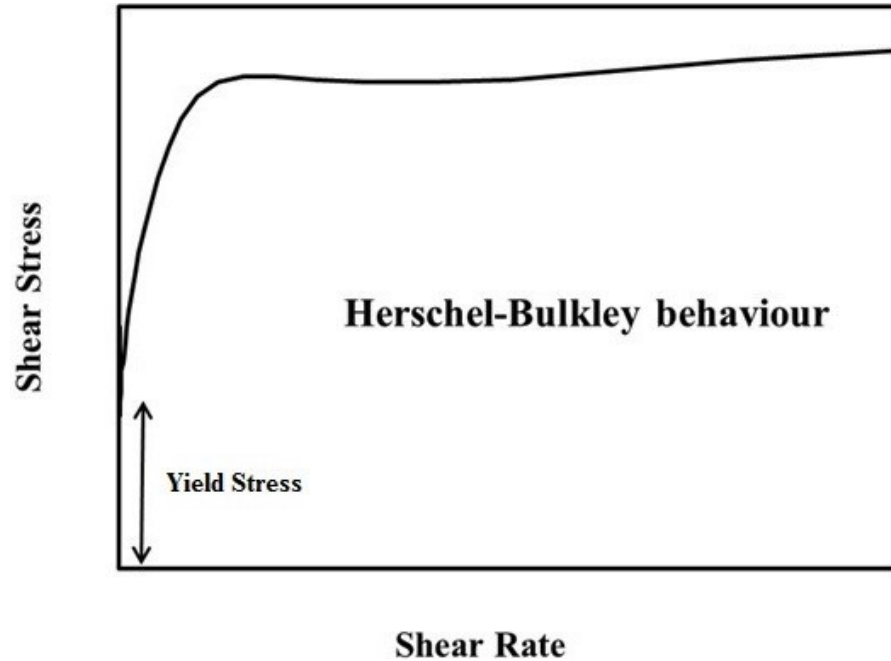


**Figure 5.22. Herschel - Bulkley schematic model**

As it is illustrated in Table 5.4 and Figure 5.23 the yield stress values are comparable for different mud formulations. The 3% bentonite suspension with no CMC/CNC has a yield stress of 0.06 Pa. When 0.25% CMC is added to the suspension, yield stress increases by one order of magnitude and has a value of 0.50 Pa. This is in good agreement with the aforementioned possibility of bridging of bentonite particles by the partially adsorbed CMC polymer chains. The yield stress is double when CNC replaces CMC in bentonite suspension. This will be also investigated in Chapter 6 and attributed to depletion of bentonite particles due to the rod-like CNC particles. Finally, when both CMC and CNC are added to the bentonite suspension, yield stress value will be about 7.71 Pa that is two orders of magnitude larger than when no additives exist in the bentonite suspension. This can be justified by the fact that CMC and CNC have a synergistic effect in mud suspension. As discussed earlier in section 5.4.3, this may originate from the nematic flocculation of CNC particles in the presence of non-adsorbing CMC polymer that result in formation of pockets of CNC flocs. As a result, a gel-like structure forms that surrounds the bentonite particles and deplete them.

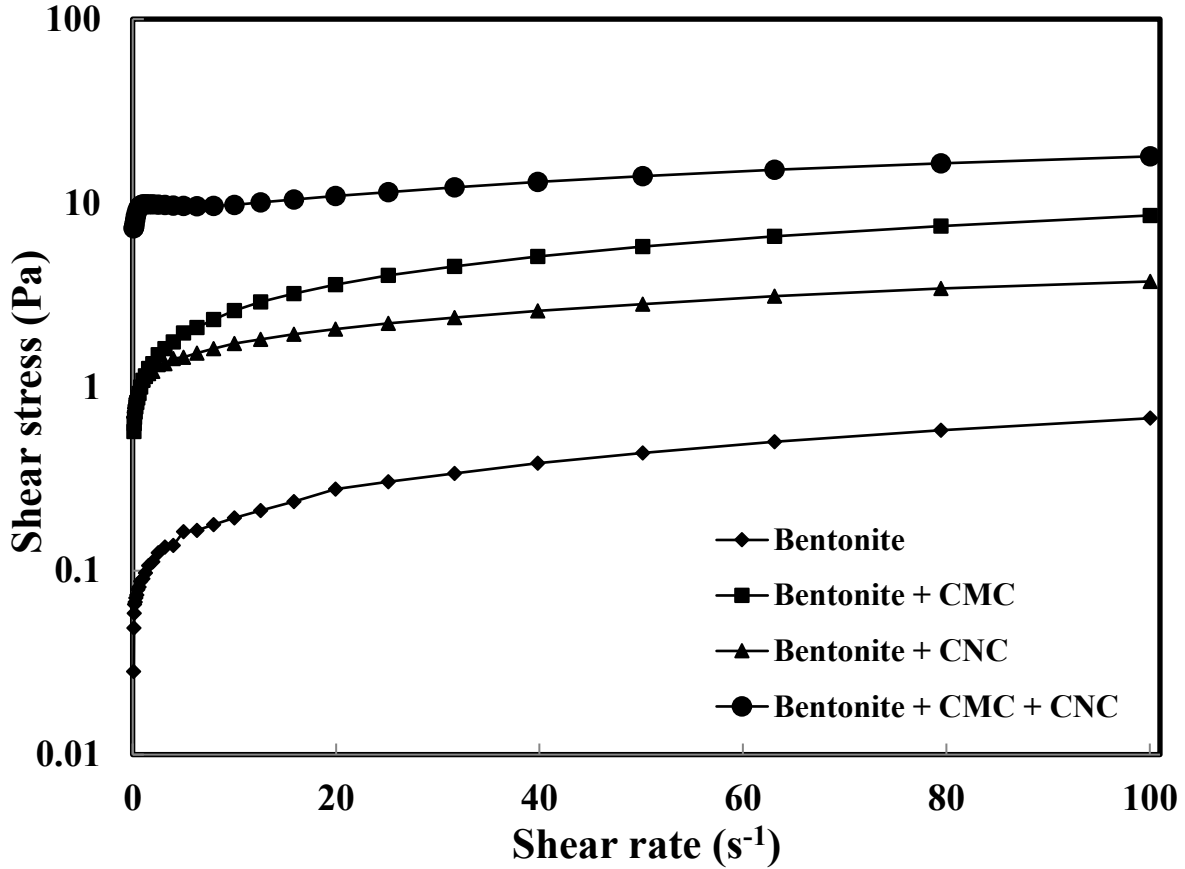


Figure 5.23. Herschel - Bulkley rheological behaviour of mud suspensions

## 5.6. Summary

The addition of cellulose-based additives to clay suspensions has been taken into account significantly due to their colloidal and rheology modifying capacity. They enable clay-based drilling mud to fulfill its functions such as stabilizing the borehole (cake formation), cleaning the hole (evacuating the cuttings), and cooling and lubricating the string and the bit. Among many cellulose-based additives, CMC polymer and CNC particles are great materials for increasing the viscosity, controlling the mud fluid loss, and maintaining enough flow properties at high temperature-high pressure (HPHT) condition.

The effect of CMC polymer on the rheological properties of the bentonite clay suspensions has been studied and experimented thoroughly. An increase in apparent viscosity is observed with CMC concentration. This is because of more polymer chain entanglements

due to concentration increment. Additionally, the partially adsorbed polymer chains bridge the bentonite particles and forms networks of bentonite platelets.

The effect of CNC particles on the rheological behaviour of clay suspensions was experimented and investigated completely in this chapter; however, the depletion interaction between bentonite – CNC will be investigated in detail in Chapter 6.

The rheological behaviour of the additives predominates that of the bentonite suspension alone. The addition of merely a small amount of these additives in the suspension makes a considerable increase in viscosity value that makes cellulose-based polymers (CMC) and particles (CNC) interesting in water-based drilling mud.

## **6. Particle deposition onto model surfaces: A microscopic approach**

In Chapter 4, particle pore plugging was confirmed to be the main and governing mechanism during filtration due to the invasion of particles. Since we found out this fact, we investigate the particle deposition mechanisms in microscopic level. Governing interactions between particles and pore surfaces through flow in porous media and filtration could be investigated through particle deposition study. In other words, particle deposition study onto different model surfaces will give us a clue about what mechanism(s) are involved in interactions between particles and pore surfaces. Figure 6.1 illustrates a schematic of the study approach for the interpretation of dynamic filtration results.

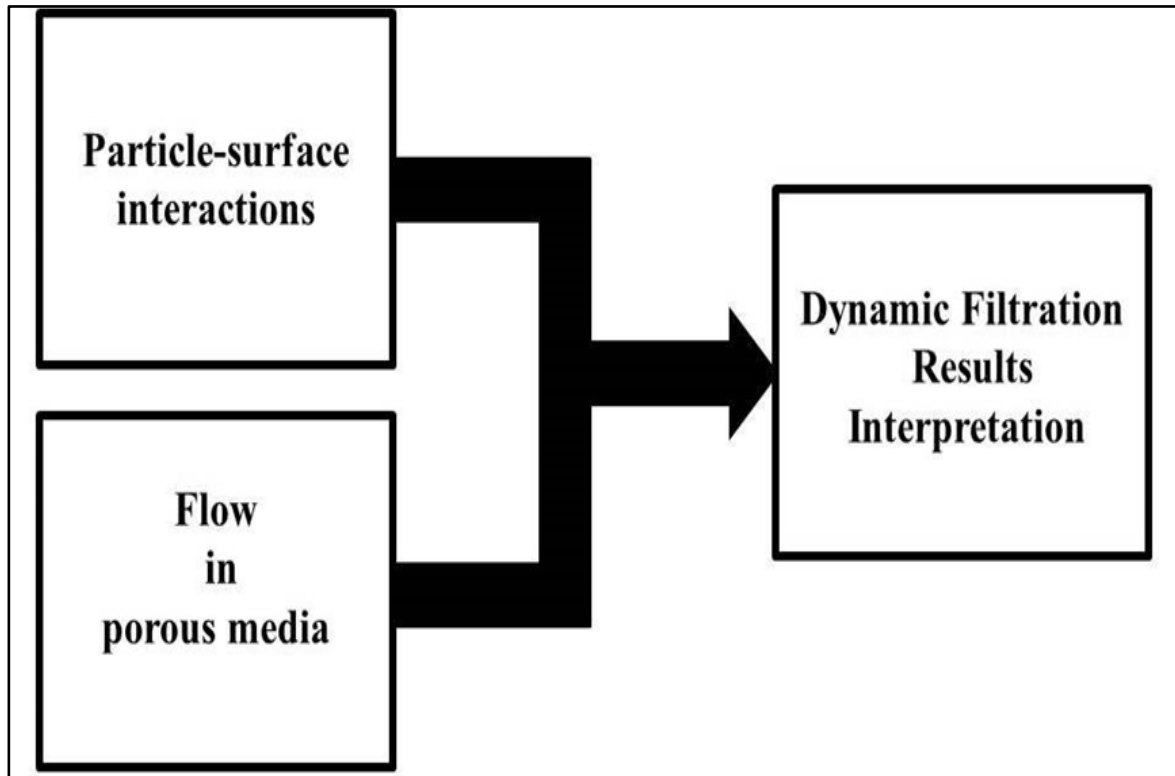


**Figure 6.1. The schematic relationship between microscopic and macroscopic studies of cake formation**

Role of particle deposition in dynamic filtration results of bentonite suspensions can be investigated by observing it in microscopic level. When filtration happens, particles move towards the inner surface of filter core due to hydrodynamic forces. A portion of them passes through the filter and transports through porous medium of the filter, while the other portion may be deposited onto the inner surface of the filter. Figure 6.2 shows a schematic representation of a spherical particle of radius  $a_p$  and a collector of radius  $a_c$  interacting across gap with  $h$  in a suspension of spherical nonadsorbing particles of radius  $a_d$  and bulk concentration  $\rho_\infty$ .

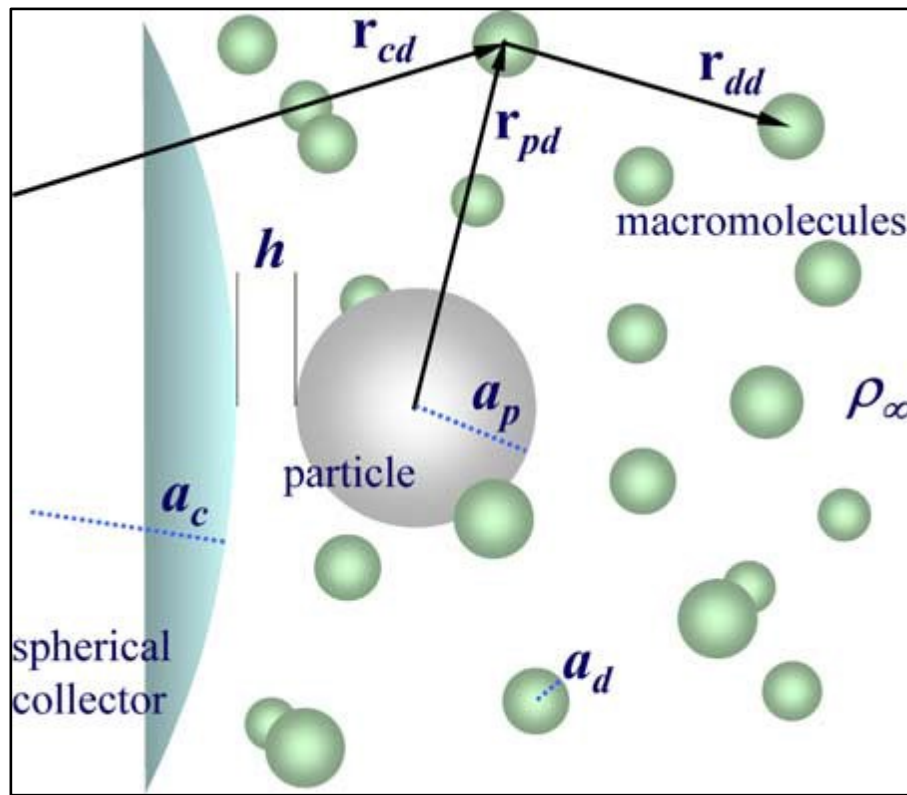


**Figure 6.2. Schematic of a suspension containing spherical particles of different radii interacting with a collector surface [1]**

The total interaction energy between a single particle and a collector consists of three primary components: an electrostatic repulsion due to the charged surfaces, an attractive van der Waals (London dispersion) interaction, and a depletion/structural interaction produced by the presence of the nonadsorbing nanoparticles (smaller spheres in Figure 6.2). The first two interactions are categorized into the well-known Derjaguin-Landau-Verwey-Overbeed

(DLVO) theory. The theory explains the aggregation of aqueous dispersions quantitatively and describes the force between charged surfaces interacting through a liquid medium. It combines the effects of the van der Waals attraction and the electrostatic repulsion due to the so-called double layer of counter ions. The latter component, known as depletion, does not follow the DLVO concept. Depletion interaction arises between large colloidal particles that are suspended in a dilute solution of depletants, which are smaller solutes that are preferentially excluded from the vicinity of the large particles. It is regarded as an entropic interaction as it was first explained by Asakura-Oosawa model [83]. The model described that the depletion force comes from an increase in osmotic pressure of the surrounding solution while colloidal particles get close enough such that the excluded depletants cannot fit in between them. It has to be noted that the particles are considered as hard (completely rigid) particles that are non-interacting and impenetrable spheres.

Investigation of particle deposition mechanism onto model surfaces (collectors) was carried out using Quartz Crystal Microbalance with Dissipation (QCM-D) apparatus. Model collectors include different geometries such as the rotating disk, stagnation-point flow, isolated sphere, porous medium composed of uniform spheres, and parallel-plate channel. One of the most common methods to investigate the kinetics of particle deposition is the parallel-plate channel geometry. They have been used in several theoretical and experimental studies of particle deposition [90-94].

Two dimensional parallel-plate channel is illustrated in Figure 6.3. Fluid suspension passes through the channel with the constant flow rate,  $Q$ , with a fully developed, laminar regime. The quartz collector sensor is located inside the channel. The mass of particles deposited onto the quartz sensor is measured and will be used for further deposition analysis.

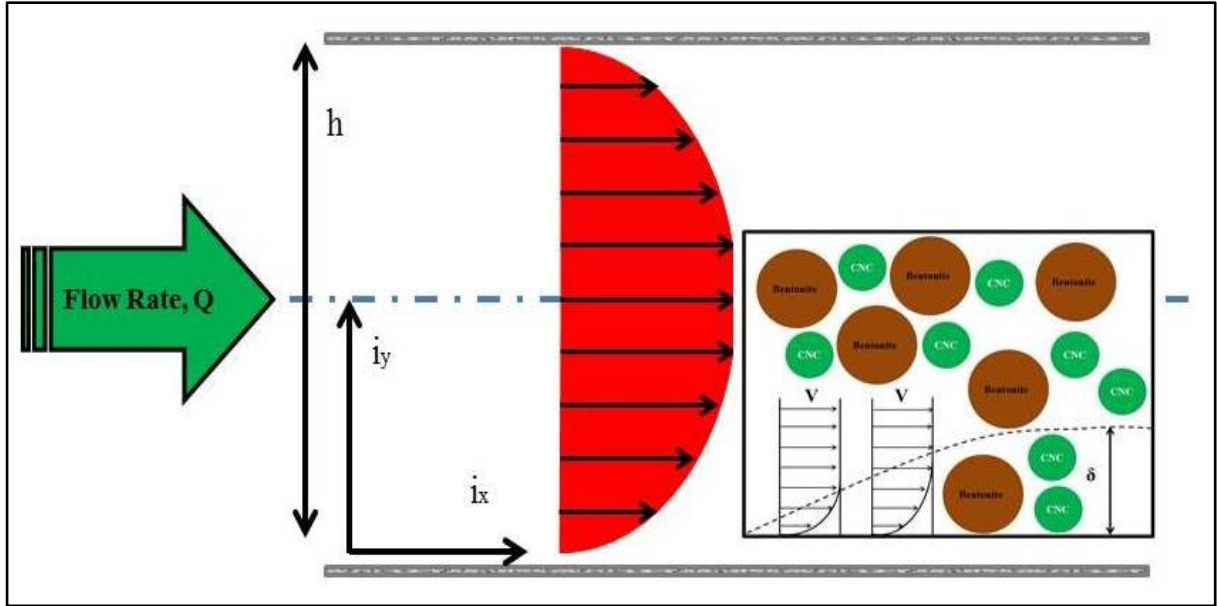


**Figure 6.3. 2-D parallel-plate channel; large and small spheres represent bentonite and CNC particles, respectively**

The transport and deposition of colloidal particles in saturated homogeneous porous media is governed by the convective-diffusion equation. The convective-diffusion equation in its general form is given by:

$$\frac{dC}{dt} + \nabla N = Q \quad [6.1]$$

where  $N$  is the mass/particle flux and  $Q$  is the bulk reaction (source) term.

$$N = u \cdot C - D \cdot \nabla C - \frac{D}{kT} \cdot C \cdot \nabla F \quad [6.2]$$

Assuming no bulk reaction yields:

$$\nabla N + \frac{dC}{dt} = 0 \quad [6.3]$$

Therefore, one can obtain:

$$\frac{\partial C}{\partial t} + \nabla \cdot (uC) = \nabla \cdot (D \cdot \nabla C) - \nabla \cdot \left( \frac{DF}{kT} C \right) \quad [6.4]$$

where  $C$  is the particle concentration,  $t$  time,  $u$  the particle velocity induced by the fluid (medium),  $D$  the particle diffusion tensor,  $F$  the external forces exerted on the particles,  $k$  the Boltzmann constant, and  $T$  is the absolute temperature. Applications of this equation to coagulation and deposition phenomena illustrate that a steady state is established in a very short period of time that is much smaller compared to the time scales of interest in studying most particle deposition phenomena. Therefore, the accumulation term “ $\partial C/\partial t$ ”, can be eliminated from the equation. The remained equation is in fact a balance of convection, diffusion, and migration mechanisms. It has to be noted that all experimental conditions such as flow rate were set in order to meet the perfect sink model. In this model, it is assumed that the source term in convection-diffusion equation is zero and all particles arriving at the distance  $h = \delta$  disappears from the system.  $\delta$  is the minimum gap width between particle and collector surface and sometimes assumed to be zero. All classical analytical solutions for particle deposition, such as Smoluchowski-Levich approximation [94] were obtained using this model. In this approach it is assumed that the increase in hydrodynamic drag a particle experiences when approaching the collector surface, is cancelled out by attractive dispersion forces. It has been found that neglecting hydrodynamic and dispersion forces results in very close outcome to the exact solution of convection-diffusion equation [58, 93, 94].

The fluid velocity profile in Cartesian coordinate  $(x,y,z)$  is expressed as:

$$v = \frac{3}{2}V_m \frac{z}{B} \left(2 - \frac{z}{B}\right) i_x \quad [6.5]$$

Where  $V_m$  is the mean fluid velocity, and  $B$  the half of channel width ( $B = 1\text{mm}$ ). Due to the effect of hydrodynamic interactions, the velocity of the particles in the vicinity of the upper and lower walls of the channel deviates from the fluid velocity field. Approximations to the particle flow field in the absence of sources and sinks, and under steady conditions introduced by Adamczyk and van de Ven, resulted in the dimensionless “ $Pe$ ” number for this geometry as:

$$Pe = \frac{3V_m a_p^3}{2B^2 D_\infty} \quad [6.6]$$

where  $a_p$  is the particle radius, and  $D_\infty$  is the diffusion coefficient for dilute suspension defined as:

$$D_\infty = \frac{kT}{6\pi\mu a_p} \quad [6.7]$$

where  $k$  is the Boltzmann constant,  $T$  the absolute temperature and  $\mu$  the solvent viscosity.

Peclet number is a dimensionless number used in all three sections of transport phenomena including momentum, heat and mass transfer. It is defined as the ratio of the rate of advection of a physical quantity by the flow to the rate of diffusion of the same quantity driven by an appropriate gradient.

$$Pe = \frac{\text{Convective transport rate}}{\text{Diffusive transport rate}} = Re.Sc = Re.Pr \quad [6.8]$$

The Peclet number is the product of Reynolds number ( $Re$ ) and the Schmidt number ( $Sc$ ) in mass transfer, while is equivalent to the product of Reynolds number and Prandtl number ( $Pr$ ) in heat transfer. Qualitatively speaking,  $Pe$  number is a comparison between convection and diffusion mechanisms involved in particle transport and deposition. In other words, high  $Pe$  numbers illustrate that the governing mechanism is convection while low  $Pe$  numbers imply that diffusion of particles controls the deposition and transport process.

By applying the usual perfect sink boundary conditions to the upper and lower surfaces of the channel, the deposition rate for the particles can be written as dimensionless Sherwood number ( $Sh$ ):

$$Sh = \frac{1}{\Gamma\left(\frac{4}{3}\right)} \left(\frac{2Pe}{9x^*}\right)^{\frac{1}{3}} \quad [6.9]$$

where  $x^*$  is a dimensionless variable and defined as:

$$x^* = \frac{x}{B} = \frac{B}{a_p} \quad [6.10]$$

Sherwood number is another dimensionless number used specifically in mass transfer. It represents the ratio of total mass transfer rate to the diffusive mass transport rate.

$$Sh = \frac{\text{Mass transfer rate}}{\text{Diffusion rate}} = f(Re, Sc) = f(Pe) \quad [6.11]$$

The particle deposition flux onto model surfaces can be expressed by dimensionless Sherwood number. Likewise, low “Sh” numbers imply low deposition rates while large “Sh” numbers illustrate high deposition rates [58].

Initial mass deposition rates ( $j_0$ ) of different fluids can be calculated as:

$$Sh = \frac{j_0 a_p}{D_\infty C_0} \quad [6.12]$$

where  $C_0$  is the mass bulk concentration of constituents in the solution.

More detailed procedure and all the equations used here ([6.1] – [6.12]) can be found in M. Elimelech’s work [58]. Equation [6.9] will be used to investigate the effect of cellulose nanocrystals on deposition of bentonite particles onto silica sensors. It should be noted that both CNC and bentonite particles were assumed to be spherical in order to use the derived equations and for simplicity. In fact, CNC and bentonite particles have rod-like and platelet geometries, respectively.

## **6.1. Experimental set-up for bentonite – CNC particles system**

In larger scale or macroscopic view, the question of why CNC improves cake formation in dynamic filtration process can be answered by calculating initial deposition rates of clay samples with/without CNC. Higher deposition rates of bentonite particles in presence of CNC particles reveal the efficiency of CNC particles to improve filtration and rheological properties of clay suspensions. In order to investigate the effect of CNC on bentonite deposition, three samples were prepared as follows:

1. 0.1 % (wt) bentonite in water
2. 0.1 % (wt) CNC in water
3. 0.1 % (wt) bentonite + 0.1 % (wt) CNC in water

The experimental conditions are presented in Table 6.1.

**Table 6.1. QCM-D experimental parameters**

<b>Experimental parameters</b>	<b>unit</b>	<b>Value</b>
Flow rate, Q	ml/min	0.3
Reynolds number, Re	-	0.5
Mean flow velocity, $V_m$	m/s	$2.5 \times 10^{-4}$
Boltzmann constant, k	$m^2kg/s^2K$	$1.38 \times 10^{-23}$
Temperature, T	K	302.15
Channel height, $h = 2B$	m	$2 \times 10^{-3}$
Channel width, w	m	$1 \times 10^{-2}$
Bentonite particle size, $a_{p1}$	m	$1 \times 10^{-6}$
CNC particle size, $a_{p2}$	m	$1 \times 10^{-7}$
Solvent (water) viscosity, $\mu$	pa.s	$1 \times 10^{-3}$
Bentonite concentration, $C_0$	kg/m <sup>3</sup>	1
CNC concentration, $C_0$	kg/m <sup>3</sup>	1

Deposition of clay particles with/without CNC particles onto quartz sensor was carried out in order to verify the colloidal forces including DLVO and non-DLVO interaction forces. Silica sensor was coated with positively charged Polyethyleneimine (PEI) in one set of experiments in order to verify the QCM-D instrument capability and use maximum capacity of deposition. Deposition of clay particles in presence of CNC particles with/without PEI surface coating will be described in sections 6.2 and 6.3, respectively.

## 6.2. Particle deposition onto uncoated quartz sensor (similarly charged particles and collector)

The deposition of negatively charged clay particles in the presence/absence of CNC particles onto negatively charged silica (quartz) collector was investigated both theoretically via DLVO theory and experimentally via QCM-D device. Effect of CNC particles on deposition of bentonite particles was highlighted.

### 6.2.1. Similarly charged particles and collectors interactions

In case of both similar charges (negatively charged particles and surface), according to the electrical double layer (EDL) equation, repulsive interaction is expected. In other words, higher energy barriers must be observed in DLVO curve. Van der Waals (VDW) interactions are dependent on separation distance, Hamaker constant, and particle size only and always negative and attractive. Electrical double layer and van der Waals interactions between spherical particles and flat surfaces are given below:

$$V_{EDL} = 64\pi\epsilon_0\epsilon_r a_p \left(\frac{KT}{ze}\right)^2 \Gamma_1 \Gamma_2 \exp(-kh) \quad [6.13]$$

where

$$\Gamma_i = \tanh\left(\frac{ze\psi_i}{4KT}\right) \quad [6.14]$$

And

$$k = \left(\frac{2000z^2 e^2 N_A M}{\epsilon_0 \epsilon_r KT}\right)^{1/2} \quad [6.15]$$

$$V_{VDW} = -\frac{A_H}{6} \left[ \frac{a_p}{h} + \frac{a_p}{h + 2a_p} + \ln\left(\frac{h}{h + a_p}\right) \right] \quad [6.16]$$

$A_H$  is the overall effective Hamaker constant for the particles (p) and collector (c) being intervened by water (w) as the medium. Therefore one can write:

$$A_H = (A_c^{0.5} - A_w^{0.5})(A_p^{0.5} - A_w^{0.5}) \quad [6.17]$$

According to DLVO theory, total interaction energy,  $V_T$ , is the summation of electrical double layer and van der Waals interaction energies:

$$V_T = V_{EDL} + V_{VDW} \quad [6.18]$$

All the parameters and values are tabulated in Table 6.2. Total interaction energies between bentonite/CNC particles and quartz surface are plotted for 0.1 M electrolyte concentration and shown in Figure 6.4.

**Table 6.2. DLVO parameters for Bentonite-CNC-Silica system**

Constants	Description	Value	unit
$a_p$ for CNC	CNC particles size <sup>a</sup>	$1 \times 10^{-7}$	m
$a_p$ for bentonite	Bentonite particle size <sup>b</sup>	$1 \times 10^{-6}$	m
$\epsilon_0$	Permittivity of vacuum	$8.85 \times 10^{-12}$	C/V.m
$\epsilon_r$	Dielectric constant of medium (water)	78.5	-
$K$	Boltzmann constant	$1.38 \times 10^{-23}$	J/K
$T$	Absolute temperature	298.15	K
$z^{\text{e}}$	Absolute value of valence of a (z:z) electrolyte	1	-
$e$	Elementary charge	$-1.60 \times 10^{-19}$	C
$\psi_{CNC}^{\text{d}}$	Zeta potential of CNC particles	-51.5	mV
$\psi_B^{\text{e}}$	Zeta potential of bentonite particles	-35	mV
$\psi_S^{\text{f}}$	Zeta potential of silica surface	-60	mV
$M$	Molarity (ionic concentration)	0.1	mol/lit
$k$	Inverse Debye length	variable with molarity	$\text{m}^{-1}$
$h$	Separation distance	variable	m

$A_H^{c-s}$ <sup>g</sup>	Hamaker constant for Silica-CNC	$4.45 \times 10^{-21}$	J
$A_H^{B-s}$ <sup>g</sup>	Hamaker constant for Silica-Bentonite	$1.50 \times 10^{-20}$	J
$N_A$	Avogadro's Number	$6.022 \times 10^{+23}$	mol <sup>-1</sup>
$KT$	Brownian energy	$4.11 \times 10^{-21}$	J
$\Gamma_{CNC}$	Reduced surface potential for CNC particles	0.5455	-
$\Gamma_B$	Reduced surface potential for Bentonite particles	0.3284	-
$\Gamma_S$	Reduced surface potential for Silica surface	0.5260	-

---

**Note:** a & b: spherical shape assumption for CNC and bentonite particles, respectively; c: 0.1 M NaCl electrolyte solution was assumed; d: Ref. [13]; e: [95]; f: [27]; g: [17, 27]

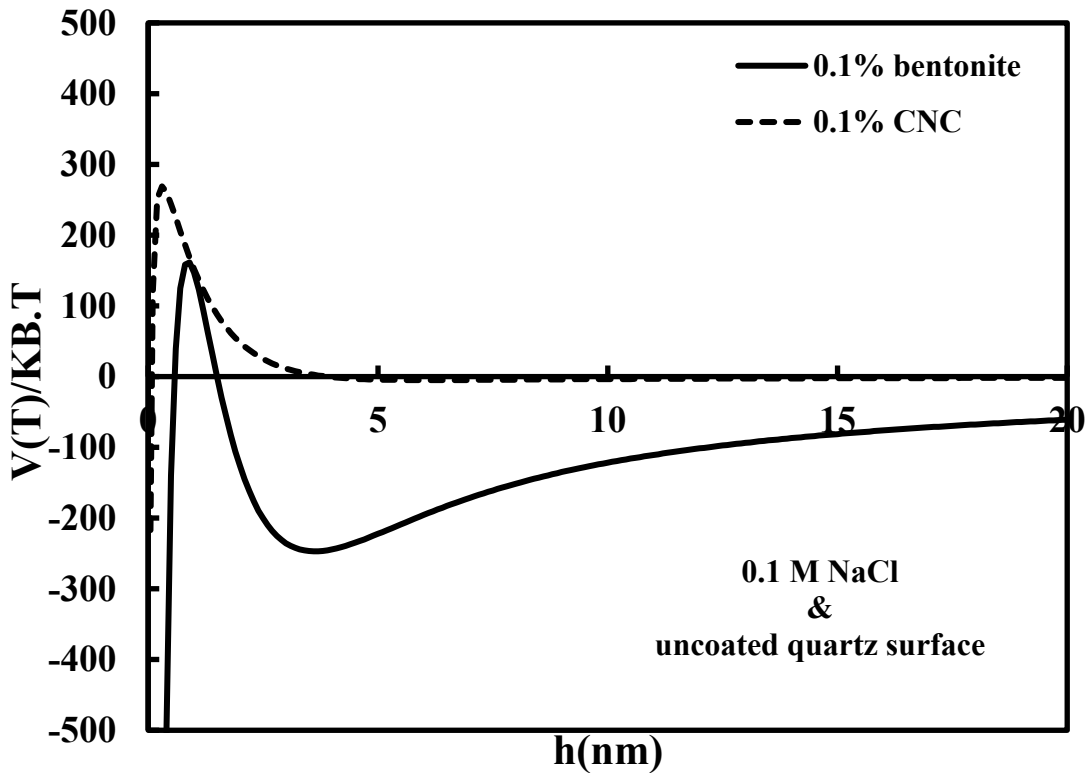


Figure 6.4. Interaction potentials between bentonite/CNC particles and uncoated quartz surface

As it is shown, high energy barriers of 150 KT and 280 KT are observed for deposition of similarly charged bentonite and CNC particles on quartz surface, respectively. No deposition is expected for total interaction energies of 5 KT and more [17]. Therefore, theory expects no deposition for similarly charged particles like CNC and bentonite on silica surface.

### 6.2.2. QCM-D experimental data

The deposition of negatively charged clay particles in the presence/absence of negatively charged CNC particles onto negatively charged silica collector was investigated experimentally via QCM-D device. Figure 6.5 illustrates the deposition of bentonite particles on quartz surface. It is observed that low amounts of mass (up to hundred nanograms) were deposited in the first hundred seconds of experiment. Fluctuations in data reveal the possible attachment-detachment processes during the deposition of clay particles onto naked silica

surface. S. Varennes and T.G.M van de Ven studied the deposition and attachment of latex particles at similarly charged glass surfaces exposed to flow [96]. They observed a sudden change from almost no deposition to fast deposition at a well-defined electrolyte concentration. It was also shown that particle escape is not only governed by hydrodynamic forces exerted on particles, but also by a convective-diffusive transport out of an energy minimum. In other words, surface collisions between suspended and deposited particles play an important role in the detachment process. During a surface collision the hydrodynamic force on a deposited particle is increased, thus increasing even further the probability of escape [96].

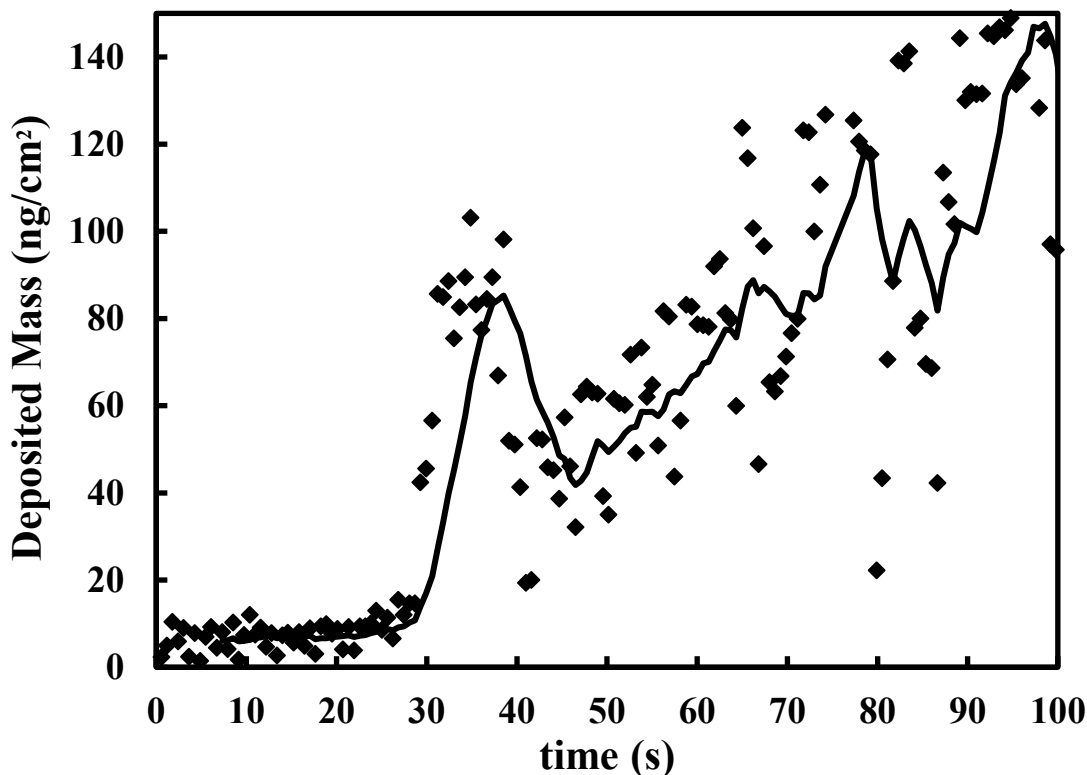


Figure 6.5. Deposition of similarly charged clay particles on uncoated silica surface (The line is guide for the eye).

### 6.2.3. Effect of CNC particles on clay particles deposition

Figure 6.6 illustrates an enhancement in deposition when 0.1% CNC is added to the clay suspension. This considerable increase is about three orders of magnitude, but not stable. Fluctuations in deposition data can be observed likewise. Table 6.3 presents the effect of CNC particles on the deposition of clay particles in terms of initial deposition rate,  $J_0$ , maximum level of deposition (leveling-off),  $M_\infty$ , and particle sensor surface coverage by particles.

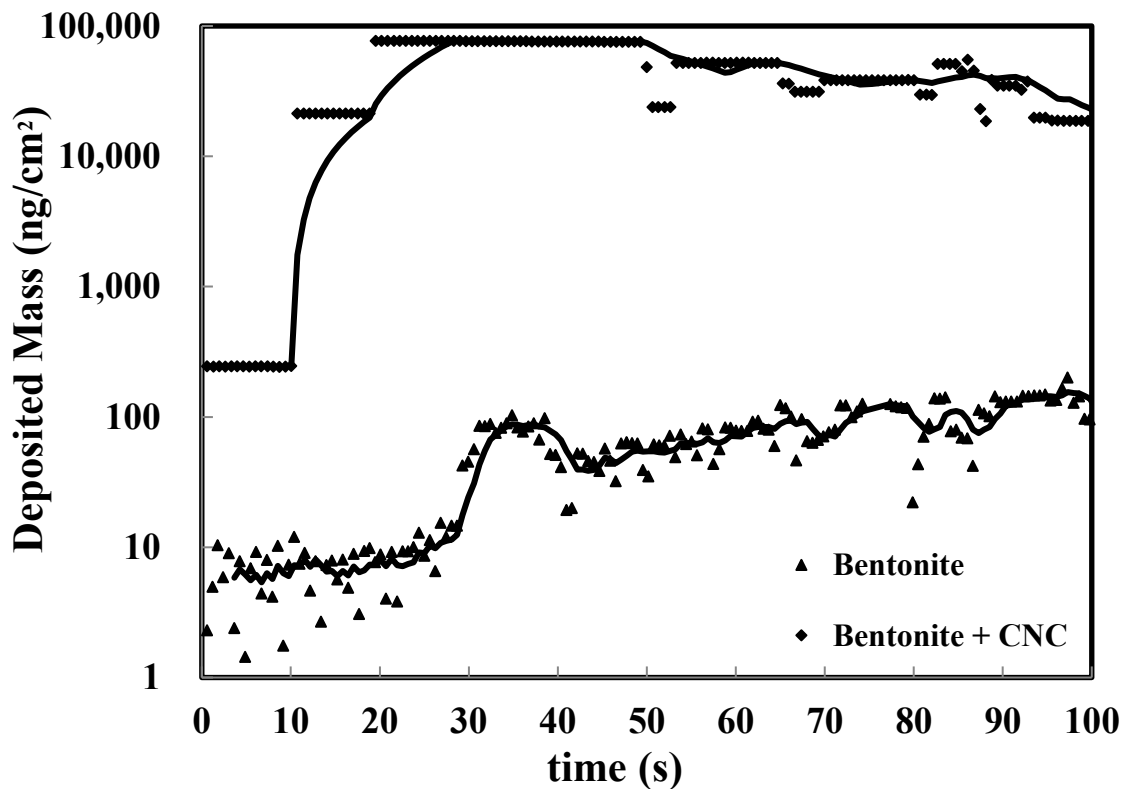


Figure 6.6. Effect of CNC on deposition of similarly charged clay particles on uncoated silica surface (The lines are guide for the eye)

**Table 6.3. Deposition of bentonite/CNC particles on uncoated silica surface**

Condition	Comment	Initial Deposition flux, $J_0$ (ng/cm <sup>2</sup> .s)	Maximum Plateau, $M_\infty$ (ng/cm <sup>2</sup> )	Surface Coverage (%)
Theory (bentonite+quartz)	No deposition	-	-	
Experiment (bentonite+quartz)	Low deposition	0	$\sim 10^2$	0.13 <sup>a</sup>
Theory (bentonite+CNC+quartz)	No deposition	-	-	
Experiment (bentonite+CNC+quartz)	Enhanced deposition	0.13	$\sim 10^4$ - $10^5$	13

**Note:** <sup>a</sup>: calculations based on spherical bentonite and CNC particles in Appendix C.

Initial deposition rates of bentonite particles with and without CNC particles can be measured using the early stage deposition data in the first seconds of experiments. As shown in Figure 6.7, approximately zero deposition flux is illustrated for the deposition of bentonite particles on silica surface, while an average of 0.13 ng/cm<sup>2</sup>.s deposition flux is obtained when CNC was added.

Moreover, Figure 6.6 illustrates that higher deposition is obtained when CNC particles are added to the bentonite suspension. This huge difference may be originated from the depletion effect of CNC particles on bentonite particles [27, 97, 98]. Bentonite particles are pushed to the surface of sensor due to electrostatic and depletion of CNC particles. This depletion-induced deposition is a reversible process involving secondary energy wells. Because such secondary wells happen at relatively large separation distances from the collector surface (bulk), particles captured in such wells are probably mobile and can translate along the collector surface in addition to attachment, detachment, and reattachment processes [97]. That increases the deposition amount significantly. However, due to similar charge of sensor surface, this deposition is not stable because the deposited particles may be repelled due to repulsive electrostatic interaction between bentonite particles and silica surface. In other words, a particle that is deposited may be detached again due to the repulsive interactions. Also, due to the relatively weak attractive depletion force, the hydrodynamic drag force exerted on particles trapped near the surface may contribute significantly to the detachment rate [97].

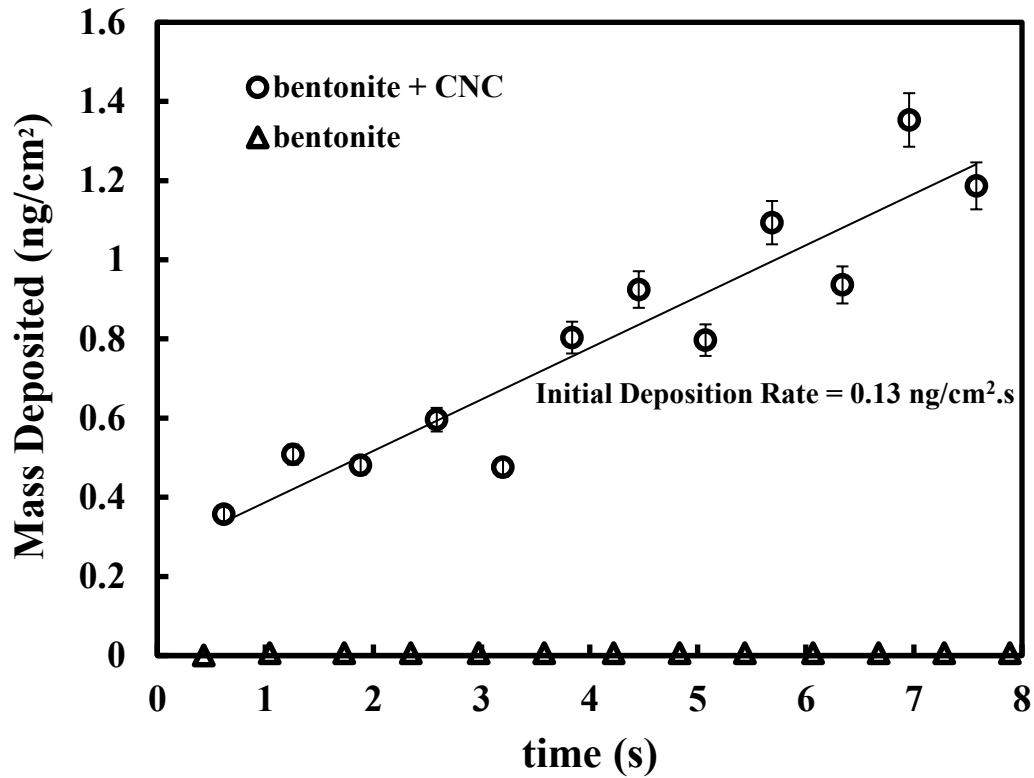


Figure 6.7. Initial deposition rates for bentonite particles with and without CNC particles

Surface coverage calculations were done based on spherical particle assumption. 0.13% surface coverage for bentonite particles reveals the instability of their deposition. However, 13% of the sensor surface was covered by particles when CNC is added. That is 100 times bigger and in good agreement with Figure 6.6 trend.

In conclusion, the secondary energy wells produced by a depletion attraction have a considerable effect on the transport and deposition of particles through similarly charged collectors. In addition, hydrodynamic drag force exerted on captured particles can enhance particles detachment altogether with repulsive electrostatic interactions between particles and similarly charged collectors [97].

### **6.3. Particle deposition onto coated quartz sensor (oppositely charged particles and collector)**

The deposition of negatively charged clay particles in the presence/absence of CNC particles onto positively charged silica (quartz) collector was investigated both theoretically via DLVO theory and experimentally via QCM-D device. As shown in Chapter 3, silica sensor was coated with a thin layer of polyethyleneimine (PEI) and the surface of the sensor was positively charged. This was carried out to stabilize the obtained deposition data and smoother behaviour and to use the maximum capacity of silica sensor to adsorb nanoparticles. PEI makes the surface positively charged and controls the deposition of particles. The PEI chains were considered fully extended due to electrostatic repulsion between the protonated amine groups, therefore, accelerating the attachment of negatively charged bentonite particles onto the surface of silica sensor [62, 99]. Effect of CNC particles on deposition of bentonite particles was also highlighted.

#### **6.3.1. Oppositely charged particles and collectors interactions**

In case of oppositely charged particles and collectors (negatively charged particles and positively charged surface), according to Equation [6.13], electrical double layer is negative (attractive). It means lower energy barrier must be observed in DLVO curve, because van der Waals interactions do not change. In other words, enhanced particle deposition is expected, because both electrical double layer and van der Waals interactions act in the same direction.

Figure 6.8 shows approximately no energy barrier for any of bentonite or CNC particles to be deposited on quartz surface. High deposition of particles is expected according to DLVO theory.

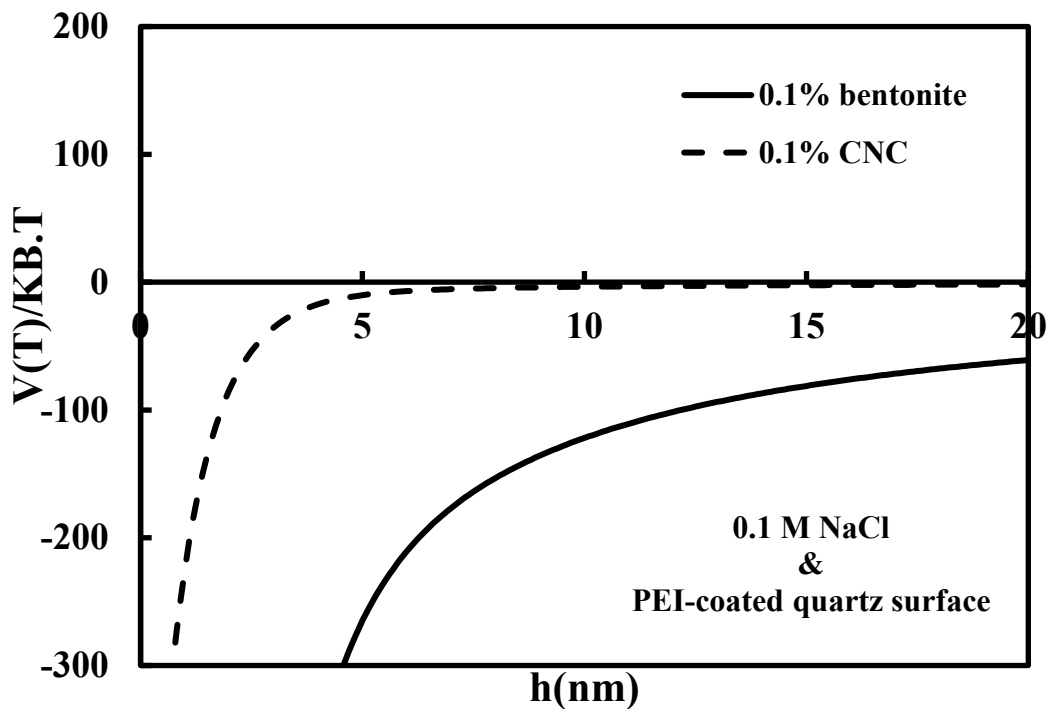


Figure 6.8. Interaction potentials between bentonite/CNC particles and PEI-coated silica surface

### 6.3.2. QCM-D experimental data

The deposition of negatively charged clay particles in the presence/absence of negatively charged CNC particles onto positively charged silica collector was investigated experimentally via QCM-D device. The mass deposition analysis can be done by splitting it into two different zones: 1. the initial mass flux, and 2. the mass deposition leveling-off at steady-state.

Figure 6.9 illustrates the mass deposited over time for CNC, bentonite and both CNC and bentonite particles. The leveling off mass deposition for the CNC-bentonite suspension is roughly 2.5 times higher than bentonite suspension. Additionally, more stability is observed in deposition data compared to the uncoated silica surface (section 6.2). The addition of CNC is considerably important to enhance the deposition of bentonite particles. Likewise, the depletion interactions induced by CNC particles pushes the bentonite particles towards the collector surface. Moreover, the electrostatic interaction between PEI-coated silica surface

and bentonite particles is now attraction. Therefore, the particles deposited on the sensor are more likely to stay on the surface than leaving it. That is why smoother data and fewer fluctuations are observed in Figure 6.9. As experiment reaches steady-state, the level-off deposited mass for CNC particles is less than bentonite. The CNC particles which are deposited may repel the other ones that approach the sensor surface due to electrostatic repulsions. Another probability may be the blocking of sensor active surface area by the CNC particles that results in less deposition later on.

Table 6.4 shows the initial deposition rate, maximum leveling off, and sensor surface coverage for oppositely charged particles and collector. In this case, higher surface coverages are expected. 2.9% of sensor was covered by bentonite particles when deposited on oppositely charged collector. This value is about 22 times larger than when the sensor surface was uncoated. 7.9% of the sensor surface area was covered by particles which is slightly lower than the one for uncoated sensor. This may be due to the high surface coverage for CNC particles (about 20%) that may block the bentonite particles to deposit on the surface furthermore. In other words, due to the attractive electrostatic interaction between CNC particles and silica surface, CNCs are also deposited on the sensor surface and occupy an area that might block other bentonite particles to be deposited.

Figure 6.9 clearly shows that the deposition of CNC and CNC - bentonite suspensions have been already started before the onset of experiment. That implies the fact that CNC addition to bentonite particles solution results in bentonite particles flocculation and sedimentation without considering any hydrodynamic/attractive interactions with the collector. This type of phenomenon is called perikinetic flocculation when it is only caused by Brownian motion (diffusion mechanism). As experiment starts, the deposition of particles is governed by orthokinetic flocculation and other interactions when hydrodynamic and other forces are involved in deposition.

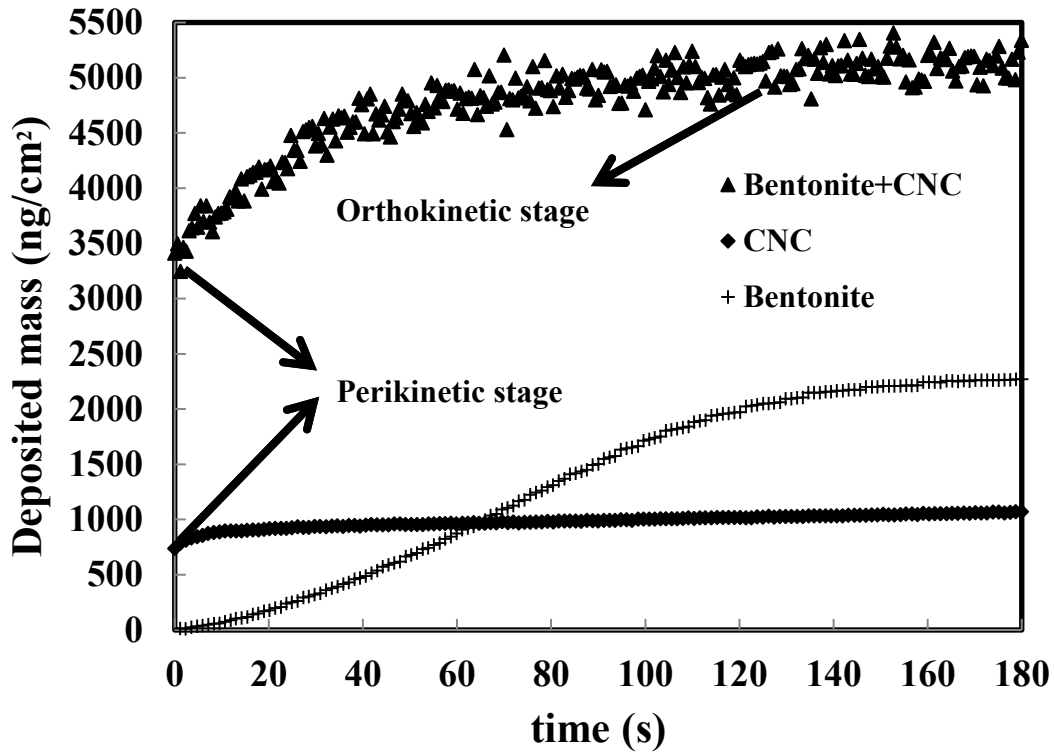


Figure 6.9. Particle mass deposition on PEI-coated silica surface

Figure 6.10 depicts the initial deposition rates in the first 20 seconds of the experiments. It is illustrated that cellulose nanocrystal particles are deposited with a higher rate compared to bentonite, while both together have higher initial mass flux. Table 6.4 presents the initial deposition flux for bentonite, CNC, and both as 8.9, 41.5, and 57.1  $\text{ng}/\text{cm}^2\cdot\text{s}$ , respectively. The size of CNCs is at least one order of magnitude smaller than bentonite particles. This allows CNCs to be deposited with a higher initial rate. This may also happen due to the alignment of CNC or bentonite particles on the sensor. More numbers of CNCs are probable to be deposited on the surface compared to bentonite particles in a period of time. The suspension of CNC and bentonite has the highest initial flux. The depletion of bentonite particles and the attractive interactions between particles and collector surface work together in order to increase the rate and the amount of deposition as illustrated in Figure 6.9 and Figure 6.10.

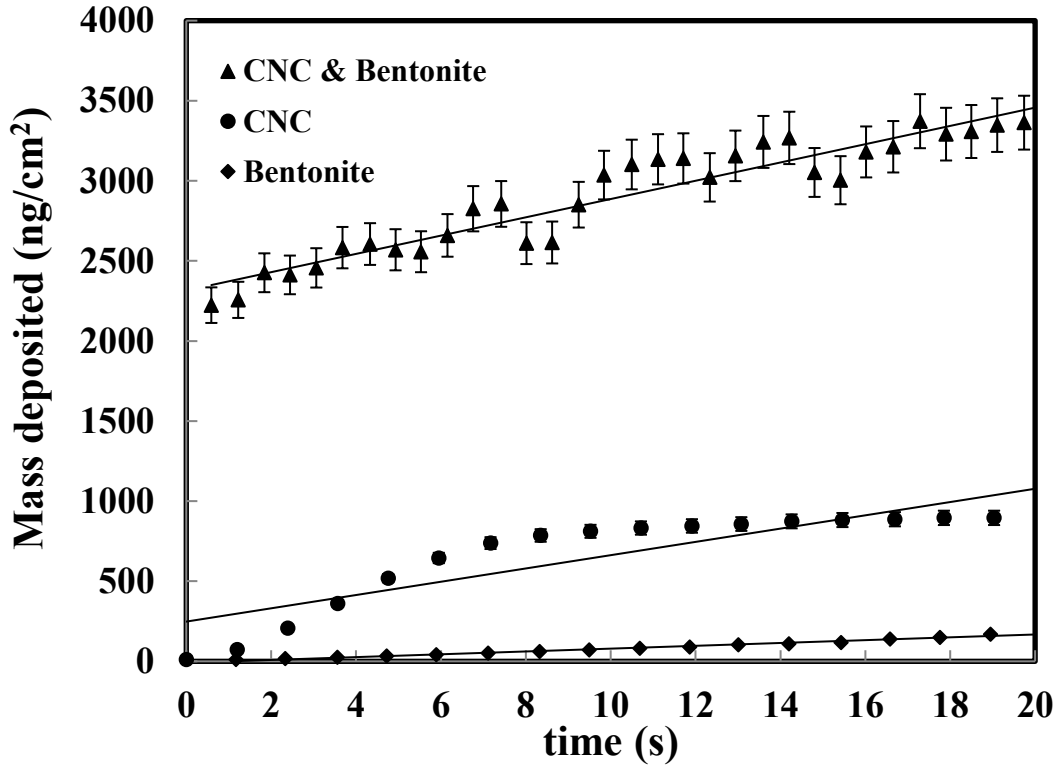


Figure 6.10. Initial deposition rates for oppositely charged particles and collector

Table 6.4. Particle deposition studies for oppositely charged particles and collector

Condition	Sh-Pe relationship	Deposition Rate, Sh	Initial Deposition flux, $J_0$ (ng/cm <sup>2</sup> .s)	Maximum Plateau, $M_\infty$ (ng/cm <sup>2</sup> )	Surface Coverage (%)
Theory (bentonite+quartz)	$\sim Pe^{1/3}$	$8.12 \cdot 10^{-3}$	$1.79 \cdot 10^{-2}$	-	
Experiment (bentonite+quartz)	-	-	8.9	$\sim 2.2 \cdot 10^3$	2.9
Theory (CNC+quartz)	$\sim Pe^{1/3}$	$1.75 \cdot 10^{-4}$	$3.87 \cdot 10^{-1}$	-	
Experiment (CNC+quartz)	-	-	41.5	$\sim 1 \cdot 10^3$	20
Theory (bentonite+CNC+quartz)	-	-	-	-	
Experiment (bentonite+CNC+quartz)	-	-	57.1	$\sim 5 \cdot 10^3$	7.9

### **6.3.3. Effect of CNC particles on clay particles deposition**

The most important target of deposition studies was to investigate the effect of CNCs on bentonite particles deposition. The initial deposition flux is the highest value and the finite deposition plateaus are higher than those of each CNC or bentonite. Having considered all the potential forces/interactions that may be involved in deposition mechanism of bentonite particles, two main interactions are the attractive electrostatic interactions between oppositely charged bentonite/CNC particles and collector sensor and the flocculation of bentonite particles due to the depletion of CNC particles [13, 16, 83].

The kinetics of capture of suspended colloidal particles by collectors in the presence of attractive double layer interactions have been investigated thoroughly [100, 101]. A notable increase was observed in colloidal deposition rates which were attributed to the range and magnitude of the attractive double layer interactions. When attractive double layer interactions extend to large distances from the collector surface, the transport of particles toward the collector increases beyond that of pure convective diffusion. As a result, colloid deposition rates also increase.

The enhanced deposition of bentonite colloidal deposition is not limited to the presence of attractive double layer interactions between oppositely charged particles and collector. The presence of CNC particles induces another interaction that cannot be described by DLVO theory. This steric interaction that arises between large colloidal particles that are suspended in a dilute solution of depletants, which are smaller solutes, is known as depletion interaction. Depletion forces are often considered as entropic forces, as was first explained by Asakura et al. [83]. In this theory the depletion force arises from an increase in osmotic pressure of the surrounding solution when larger colloidal particles get close enough such that the excluded depletants cannot fit in between them. That leads to an attractive interaction between larger particles and makes them flocculated consequently. In other words, a repulsive interaction is induced by smaller particles (depletants) that pushes the flocculated large particles toward the collector surface.

Table 6.3 and Table 6.4 illustrate that more surface area of silica sensor was covered by bentonite particles when the surface of the sensor was pretreated by PEI (positively charged). An order of magnitude surface coverage difference simply confirms that the deposition of bentonite particles in the absence of CNCs on oppositely charged silica sensor was higher. In the theory, we assume deposition occurs when a suspended particle comes within a distance  $\delta$  of the collector surface. By coating the collector with polymer, loops and tails protruding from the surface of the collector increase the region where a suspended particle can be captured. Therefore,  $\delta$ , deposition rate, and Sh increase accordingly. In addition, the bonds formed by polyelectrolyte are definitely strong enough to prevent the release of deposited particles. In other words, cationic polyelectrolyte enhances deposition of colloidal particles onto collector surface and prevents the release of these particles once contact has been established [102]. Boluk and van de Ven carried out some experiments on the deposition of titanium dioxide particles onto a cellophane surface in the presence of cationic polyelectrolyte [103]. They found out that the deposition rate in the case of bare particles and coated cellophane surface was pretty higher compared to the conditions when coated particles deposit on the bare surface and coated particles deposit on coated surface. In other words, the deposition of particles was enhanced when the similarly charged collector was coated with a cationic polyelectrolyte and was positively charged [103].

Figure 6.11 illustrates the adsorbed polyelectrolyte on the (a) particles and (b) collector surface. As already mentioned before in this chapter, treating the substrate surface with a polymer solution (polyelectrolyte) gives rise to loops and tails extending from the surface out into the aqueous phase, and yields in an increase in the distance where particles are captured. The capture of particles by extended chains increases the deposition rate [103]. Boluk and van de Ven showed that deposition experiments in the presence of cationic polymers results in charge reversal of collector surface and barrierless deposition of particles on oppositely charged surfaces [103].

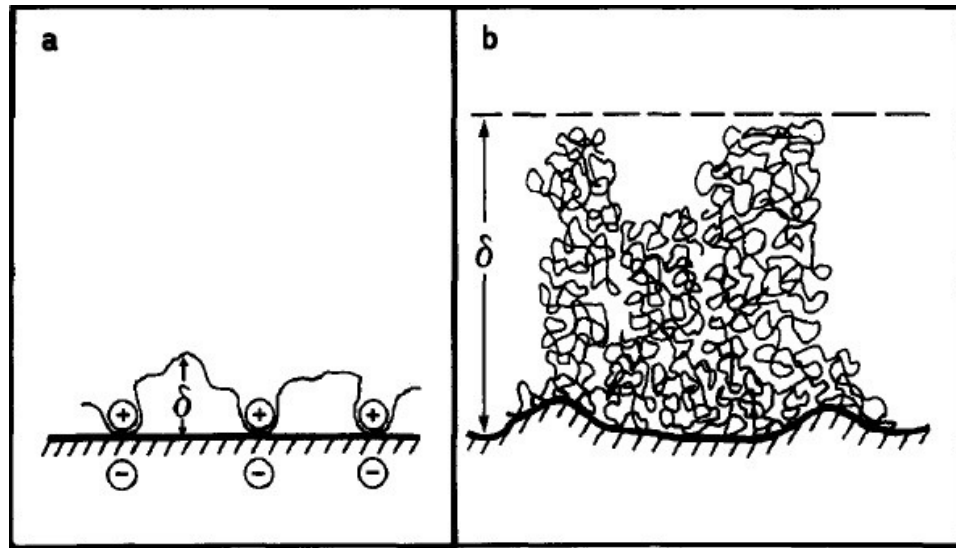


**Figure 6.11. Schematic representation of adsorbed polyelectrolyte (a) on the particle; (b) on a collector surface [103]**

On the other hand, the deposition of bentonite particles onto bare surface in the presence of CNC was a little higher compared to coated surface. This may be due to the blocking effect that was induced by trapped CNC particles. CNC particles are trapped faster because of their size, therefore, due to the electrical double layer repulsion between bentonite and CNC particles, fewer number of bentonite particles can be deposited, however, the detachment process is still controlled better when the surface of collector is coated [102].

The rate of deposition declines with time and a non-linear trend is observed for the number of colloidal particles deposited versus time. That is also due to the blocking effects of the already deposited particles. It was found that one particle is able to block an area of 20 to 30 times its geometrical cross-section [104]. Non-linear trend may be attributed to one or a combination of the following reasons:

- Particle detachment from the collector surface,
- Blocking effects by deposited particles,
- Coagulation of colloidal particles prior to the deposition (perikinetic flocculation of CNC and CNC-bentonite particles onto coated silica surface), and
- Changes in the energy of interaction between collector and particle.

Figure 6.12 illustrates the synergistic effect of CNC particles on bentonite particles deposition. CNC addition to bentonite suspension had a synergistic effect compared to the situation when any of them was deposited individually. It also illustrates how fast steady-state condition is reached due to the CNC particles effect. The approximate time to reach steady-state (leveling-off) condition is about three times less when CNC is added to bentonite suspension. In addition, the mass deposited onto the sensor surface is larger than the one in superposition of CNC and bentonite deposition data in the first initial 50 seconds. This significant effect is crucial to justify the better filtration and rheological properties of drilling muds formulated with CNC particles. Novel, low cost, environmentally friendly cellulose nanocrystals play an essential role in improving bentonite colloidal suspensions which results in better filtration performance for bentonite drilling muds.

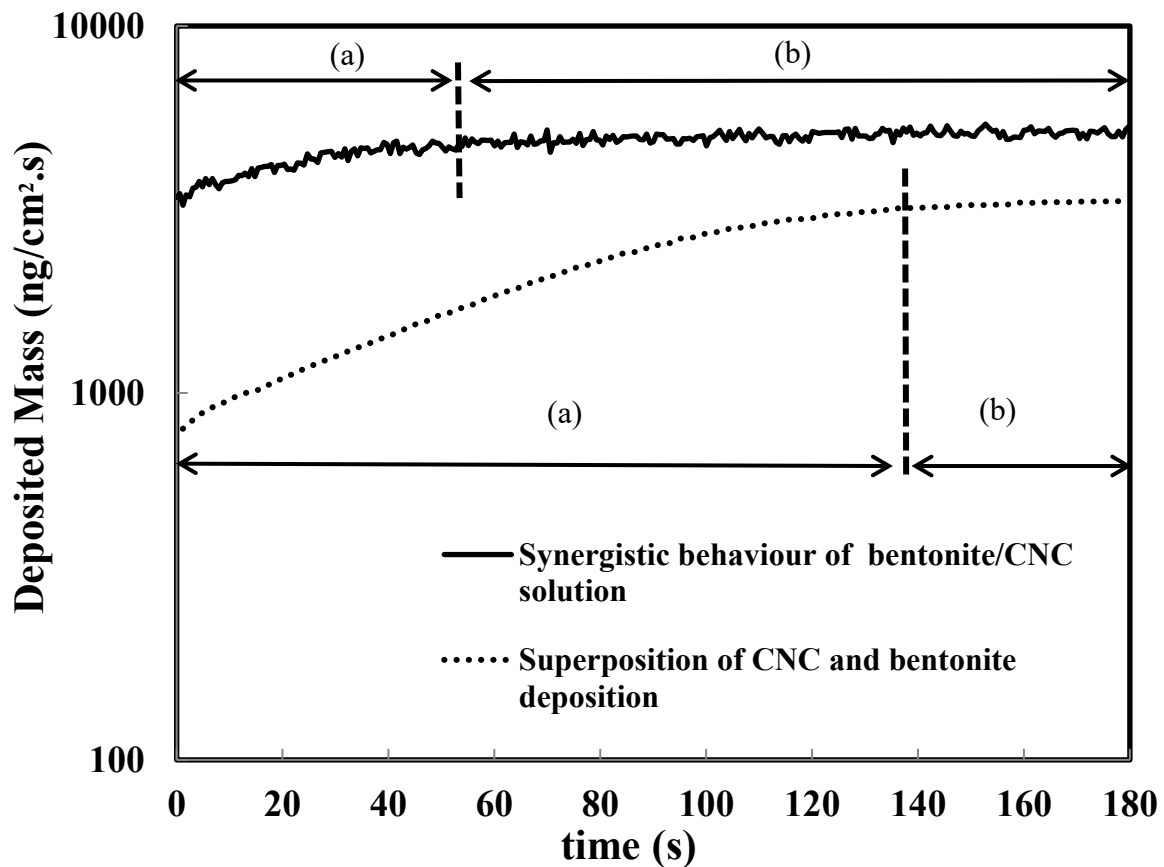


Figure 6.12. (a) Progressive and (b) steady-state regions of deposition

### 6.3.4. Effect of surface potentials and ionic strength on deposition of colloidal particles

Two main parameters affecting the colloidal deposition results are surface potential of particles and collector and ionic strength of the electrolyte. According to DLVO interactions, increasing the surface potentials, regardless of the sign, increases the magnitude of electrical double layer interactions. Moreover, increasing the ionic strength results in Debye length increase, so higher electrical double layer is expected. Ionic strength can be manipulated by changing the valence of ions in electrolyte or changing the molarity of electrolyte solution. Equation 13 defines the ionic strength of an electrolyte consisting of  $n$  components.

$$I = \sum_{i=1}^n c_i z_i^2 \quad [6.19]$$

where  $c_i$  and  $z_i$  are the concentration and the valence of of  $i^{\text{th}}$  ion, respectively.

## 6.4. Summary

Particle deposition studies were carried out using QCM-D technique to investigate dynamic filtration mechanisms of cellulose-based drilling mud suspensions. Governing interactions between clay particles and pore surfaces were studied thoroughly. Cellulose nanocrystals (CNCs) played a significant role to enhance clay particles deposition onto silica collector surface. They improved fluid loss control in dynamic filtration of drilling muds by enhancing the deposition of clay particles onto filter surface. The depletion interaction induced by rod-like shape CNCs pushed the bentonite particles toward the collector surface. Bentonite particles plugged the pores at the beginning and start to form a cake gradually. As a result, fluid loss issue (large permeate flow from filter) was controlled and the involved mechanisms were investigated completely.

## **7. Morphology of filter cake and structure analysis**

As observed in Chapters 4 and 5, the mud formulation consisting of Wyoming clay, cellulose nanocrystal particles, and carboxymethyl cellulose polymer exhibited acceptable performance in dynamic filtration and rheological experiments under different experimental conditions. Not only the mechanism of clay particles deposition from a flow onto a model surface is investigated in Chapter 6, but also a good fundamental knowledge of clay mineralogy is required to investigate filtration and rheological properties of drilling muds in a more comprehensive way. Clay is the basic component of approximately all aqueous muds. The stability of borehole depends largely on interactions between the drilling fluid and the exposed formation surface. Moreover, colloid chemistry is of great importance in drilling fluid technology, as clays form colloidal suspensions in water. Both clay mineralogy and colloid chemistry are significant topics to investigate the drilling mud behaviour under wellbore condition. Colloid chemistry of drilling fluids was discussed comprehensively in the previous chapter.

In this chapter, morphology and mineralogy of filter cakes (deposited particles) will be investigated. Scanning electron microscopy (SEM) images of the dried filter cakes will be studied and cake structure analysis will be done.

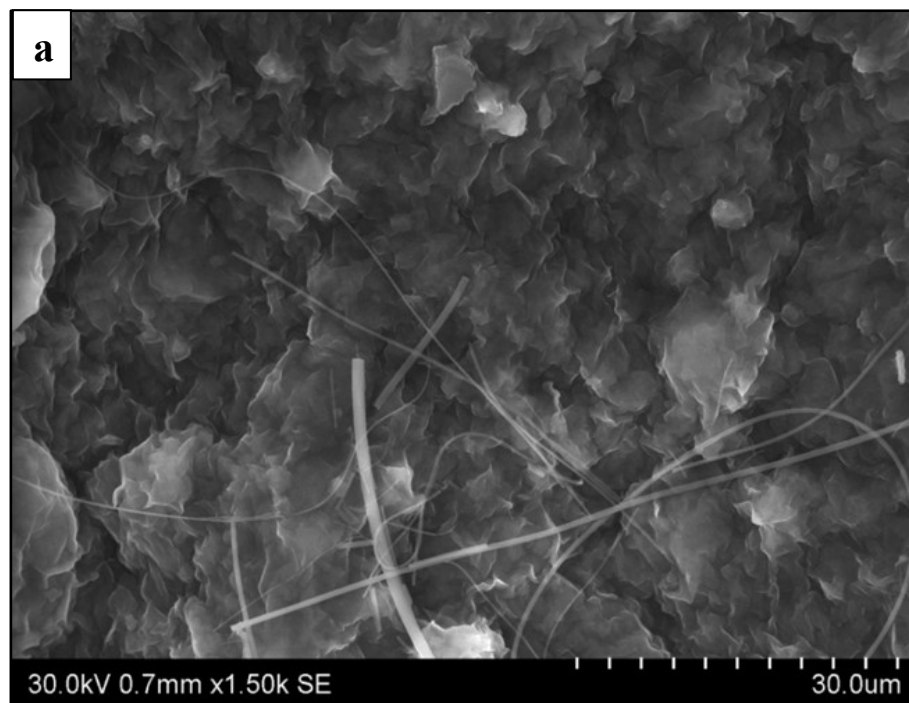
### **7.1. The origin of fibrous structure in dried filter cakes**

Figure 7.1 indicates scanning electron microscopy (SEM) images of the filter cake collected from dynamic filtration apparatus, which includes Wyoming clay, CNC particles, and CMC polymer. As shown in Figure 7.1, fibrous structure is observed in different sections of the filter cake with various magnifications. Presence of these structures can be attributed to one or a combination of the following reasons:

- Sepiolite mineral in the composition of Wyoming Gel,
- Effect of shear force exerted on the clay particles and the cake during rheological and filtration experiments,
- The addition of CNC rod-like particles to the mud suspension and mud rheology enhancement.

Not many researchers investigated the origin of fibrous structures in mud suspensions to the best of our knowledge. In 1940, Bradley found out that when slurries of sepiolite are subjected to high shear rates, the bundles of fibers separate to innumerable individual fibers. Mechanical interference between these fibers is primarily responsible for the rheological properties, and sepiolite muds are therefore little affected by the electrochemical environment. The suspension properties of the mineral itself are stable up to at least 700°F (371°C). Sepiolite-based muds are recommended for use in deep wells because of their high rheological stability under high temperatures [105]. Further information on sepiolite minerals and their structural properties are discussed in Chapter 3 and Reference [1].

As illustrated in Figure 7.1 (a-c), fibrous structure exists in different sections of the filter cake with different magnifications. This may confirm the presence of sepiolite minerals in Wyoming clay. To support this hypothesis, elemental analysis was carried out on mud suspension before filtration, filtrate, and dried filter cake after filtration. The results are explained in the following section.



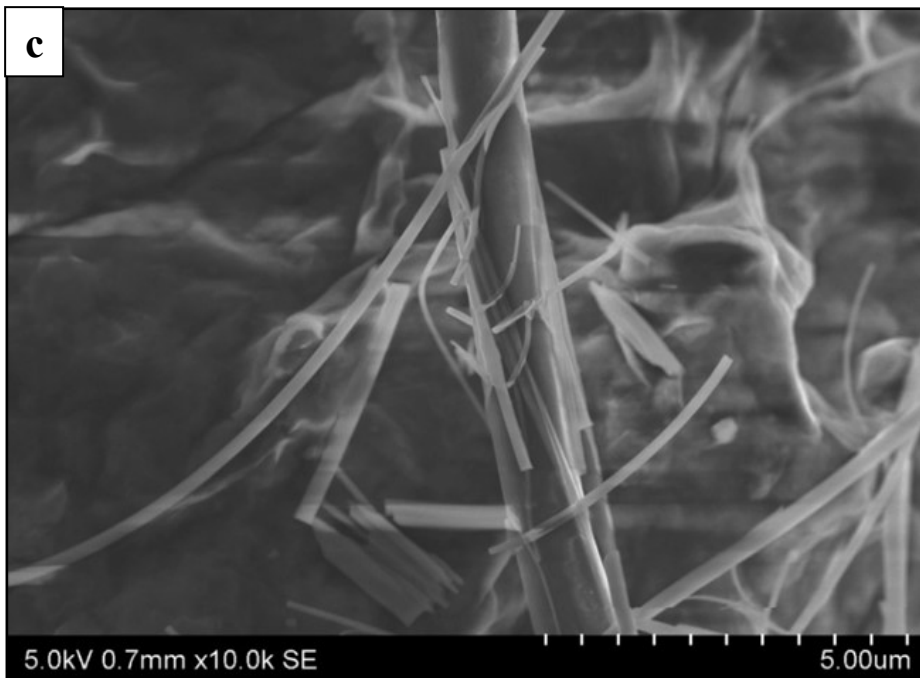
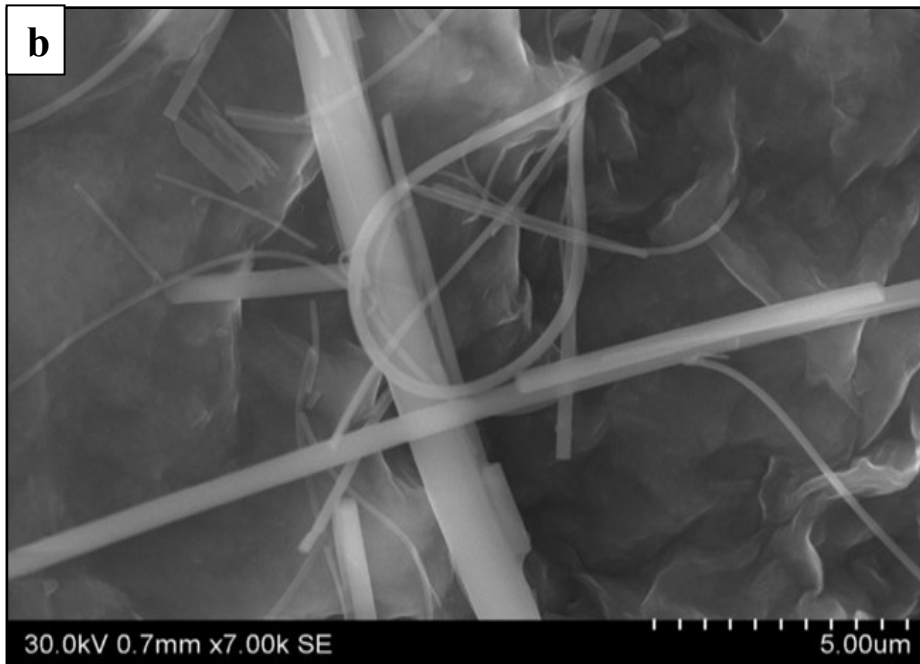


**Figure 7.1. SEM images of filter cake**

## 7.2. Elemental analysis of dried cake filters and filtrate suspension

Wyoming clay used in our experiments is composed of several minerals with different structures. Among them, sepiolite with chain-type structure is consisted of bundles of fibers. Sepiolite mineral is differed from other types of clay minerals due to the presence of iron (Fe) element in its chemical composition. Therefore, inductively coupled plasma (ICP) and energy dispersive X-Ray (EDX) characterization tests were carried out. As illustrated in Figure 7.2, iron element (Fe) along with other main constituents of sepiolite mineral is distributed through the sample. ICP test results shown in Table 7.1 confirmed the presence of iron metal (sepiolite mineral element) together with other sepiolite constituent elements before and after filtration and in the cake.

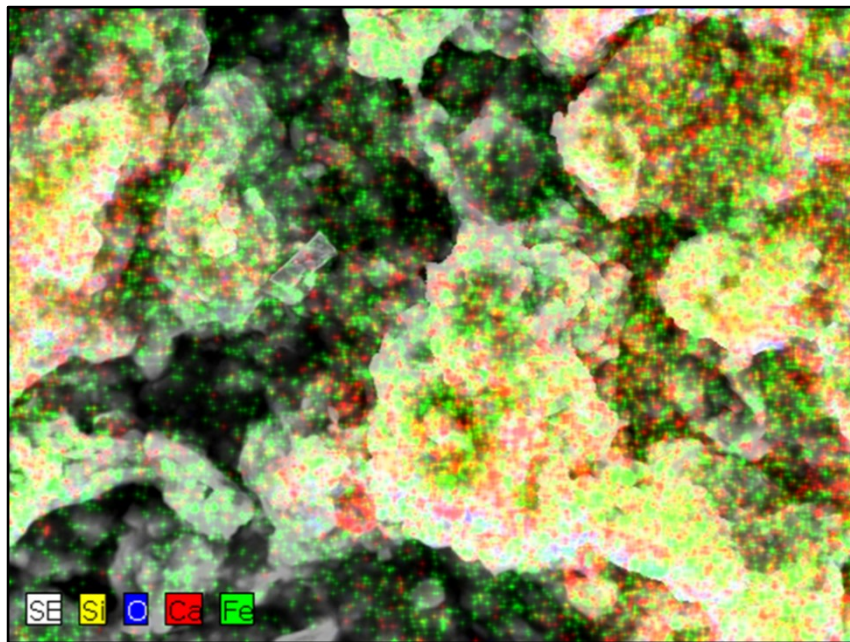


Figure 7.2. EDX elemental analysis for filter cake

**Table 7.1. Inductively Coupled Plasma (ICP) elemental analysis results**

Analyte	Mg	Al	Si	Ca	Fe
Units	ppm	ppm	ppm	ppm	ppm
Before filtration (mud suspension)	13.4	7.5	43.6	64.6	2.9
After filtration (filtrate)	0.3	0.06	1.4	0.9	0.3
Filter cake (retentate)	13.0	7.4	42.2	62.9	2.6

As it is illustrated in Table 7.1, presence of iron metal in all three samples can be explained as one of the probable reasons of fibrous structure in Wyoming clay.

However, a complimentary explanation for observing fibrous structure can be the effect of shear forces exerting on bentonite clay platelets [106]. Even if no fibrous structure exists in the clay mineralogy analysis, shear forces exerted on the particles during cross-flow filtration may produce fibrous structures in the cake. In the fiber mechanism, bentonite fibers form, tying the grains together. These fibers form as the bentonite platelets slip, like a deck of cards across a table as shown in Figure 7.3. This explanation is supported by considering the fact that fiber formation requires less energy than complete dissociation of platelets from each other and hence energetically preferred. A rope-like structure is formed by the entanglements and rotational movements of bentonite platelets. This mechanism is shown in Figure 7.4.

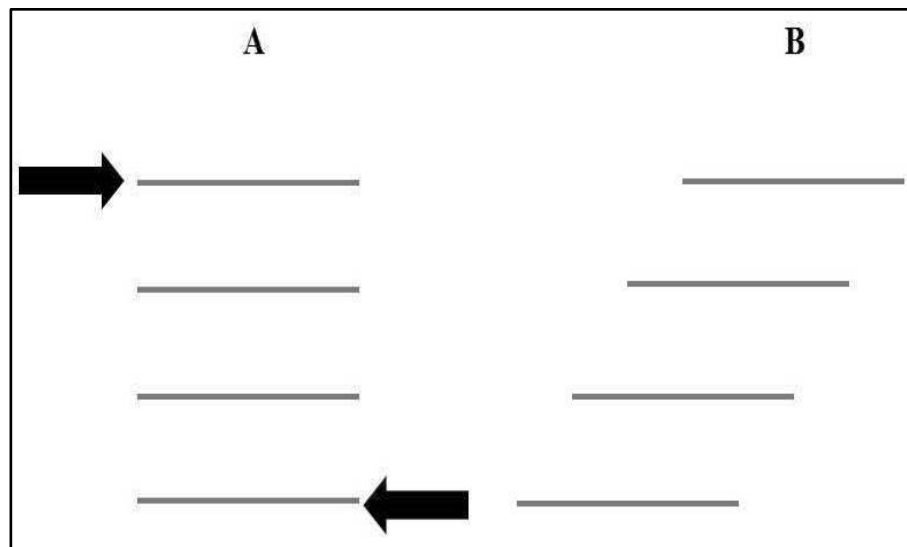


**Figure 7.3. The shear forces in A develop the bentonite particle into the fiber in B**



**Figure 7.4. Rope-like structure in clay due to shear force effect**

There might be a third complimentary scenario in the case of filter cakes containing clay particles, CMC polymer and CNC particles. In the case of clay suspension with cellulosic materials, shear forces exerted on the clay platelets may also make them move resulting in entanglement of bentonite layers and polymer chains. Due to depletion force induced by the presence of rod-like cellulose nanocrystals (CNCs), clay particles may flocculate in the suspension creating larger aggregates. In addition, presence of CMC helps the flocculation process of clay particles. It has shown that when the concentration of CMC exceeds 1g/350ml (0.28%), flocculation occurs [5]. An increase in apparent viscosity of bentonite-CMC mixture was observed when CMC concentration increased [45]. This is due to the number of entanglements caused by long polymer chains. Under high shear conditions, the flocculated clay aggregates are broken either by disruption of the attachment points on a particle surface or by the scission of covalent bonds within the bridging polymer chains, followed by reformation of the polymer to form a positive patch on the particle surface [107]. The effect of CMC and CNC on the rheological properties of drilling muds was discussed comprehensively in Chapter 5.

### **7.3. Summary**

Having considered all the possible reasons for fibrous structures in filter cakes during dynamic filtration tests, the first and second scenario are more probable compared to the third one. In other words, due to the different elemental analyses on the dried filter cake, presence of sepiolite structure was confirmed. In addition, due to the presence of CMC and CNC in the system, flocculation of clay particles and formation of aggregates are confirmed. Therefore,

shear stress exerting on these aggregates can be considered as the second possibility to form fibrous structure out of previously aggregated flocs. As it is observed in Figure 7.1, the diameter of the fibers is in micron scale, so it can not represent the CNC rods in the cake. Both CMC and CNC help indirectly to form such fibrous structures.

## 8. Conclusions and recommendations for future work

In this study, the environmentally friendly, high performance water-based drilling fluids were successfully prepared by the addition of low dosages of green, biodegradable, abundant, renewable cellulose-based nanoparticles and polymers. Rod-like cellulose nanocrystals (CNCs) with about 6-10 nm width and 80-200 nm length were added in drilling fluids to enhance the rheological properties and control the dynamic filtration fluid loss. Carboxymethyl cellulose polymer (CMC) was also added mainly as a viscosity – modifier agent. After sample preparation stage, different experiments such as dynamic filtration, rheology, colloidal deposition, and morphological characterization were carried out to better understand the mechanisms involved between colloidal particles.

In Chapter 4, drilling mud flow behaviour was investigated during two separate stages: between the drilling bit and porous media (concentric annuli), and through porous media (filter pores). Flow regime was laminar in both stages and laminar flow assumptions were used to develop fundamental transport equations. Darcy flow through porous media was established and pressure loss through the filter was calculated and compared for samples including/excluding CNC particles. Effect of different physical/chemical parameters such as differential pressure, temperature, porosity of filters, shear rate, and mud formulation on the total volume loss and filtration rate of drilling mud was investigated. Governing filtration mechanisms were investigated under different experimental conditions. Pore plugging due to the invasion of particles was confirmed to be the main and governing mechanism during filtration. Fluid loss additives (CMC/CNC) was evaluated on their ability to both block pore space and to form a filter cake under applied differential pressures and shear forces by examining the slopes of plots of  $t/V$  vs.  $V$  and  $t/V$  vs.  $t$ . Drilling fluids can be formulated to deposit a filter cake that can be eroded under laminar flow. Finally, a proper mathematical model to fit dynamic fluid loss data was achieved, which covered both early wall-building and equilibrium periods during dynamic filtration.

The second objective of this thesis was to find out if CNC is workable and feasible to be used as a fluid loss additive in drilling fluids formulation. Comparisons made with other

nanoparticles already used in drilling fluids in Chapter 4 along with superior features of CNC such as rod-like shape, high dispersion in aqueous medium and low environment contamination, made CNC a good candidate to be used as fluid loss additive. The addition of cellulose-based additives to clay suspensions has been taken into account significantly due to their colloidal and rheology modifying capacity. They enable clay-based drilling mud to fulfill its functions such as stabilizing the borehole (cake formation), cleaning the hole (evacuating the cuttings), and cooling and lubricating the string and the bit.

In Chapter 5, the effect of CMC polymer and CNC particles on the rheological properties of the bentonite clay suspensions was studied and experimented thoroughly by doing viscosity measurements versus shear rate. An increase in apparent viscosity was observed with CMC concentration by one order of magnitude. This is because of more polymer chain entanglements due to concentration increment. Additionally, the partially adsorbed polymer chains bridge the bentonite particles and forms networks of bentonite platelets. The effect of CNC particles on the rheological behaviour of clay suspensions was experimented and investigated completely in this chapter. One order of magnitude increase in low shear viscosity was observed by the addition of 1% CNC to the bentonite suspension. Addition of both CMC and CNC increased the low shear viscosity of the suspensions by two orders of magnitude. That implies a synergistic effect between CMC and CNC. The rheological behaviour of the additives predominates that of the bentonite suspension alone. The addition of merely a small dosage of these additives in the suspension makes a considerable increase in viscosity value that makes cellulose-based polymers (CMC) and particles (CNC) interesting in water-based drilling mud.

In Chapter 6, particle deposition experiments were carried out using QCM-D technique to better understand the mechanisms involved in dynamic filtration properties of CNC-formulated drilling fluids. Governing interactions between clay particles and pore surfaces were investigated completely. DLVO interactions including van der Waals attraction and electrical double layer repulsion forces were quantified for particle – surface systems. The magnitude of these interactions for bentonite particle – silica surface and bentonite and CNC particles – silica surface were calculated. Enhanced deposition of bentonite particles were associated with these DLVO interactions. However, the synergistic impact of CNC on the

deposition of bentonite particles was attributed to a non-DLVO interaction called depletion interaction induced by rod-like CNC particles. Cellulose nanocrystals (CNCs) played a significant role to enhance clay particles deposition onto silica collector surface. They improved fluid loss control in dynamic filtration of drilling muds by enhancing the deposition of clay particles onto filter surface. Bentonite particles plugged the pores at the beginning and start to form a cake gradually. As a result, fluid loss issue (large permeate flow from filter) was controlled and the involved mechanisms were investigated completely.

In Chapter 7, morphological and mineralogical characterization of filter cakes collected from dynamic filtration experiments was investigated. Scanning electron microscopy (SEM) images of the dried filter cakes was analyzed and filter cake elemental analysis was carried out. As shown in SEM images, fibrous structure was observed in dried filter cake samples that could not be attributed to the CMC polymer and CNC rods because of micron-range size of these fibers. Presence of these fibers was ascribed to one or a combination of the following scenarios:

- Sepiolite mineral in the composition of Wyoming Gel,
- Effect of shear force exerted on the clay particles and the cake during rheological and filtration experiments,
- The addition of CNC rod-like particles to the mud suspension and mud rheology enhancement.

Having considered all the possible reasons for fibrous structures in filter cakes during dynamic filtration tests, the first and second scenario were more possible compared to the third one. In other words, different elemental analyses on the dried filter cake confirmed the presence of sepiolite structure due to the presence of iron (Fe) element. In addition, presence of CMC and CNC in the system accelerates the flocculation of bentonite clay particles and formation of aggregates. Therefore, shear stress exerting on these aggregates can be considered as the second possibility to form fibrous structure out of previously aggregated flocs. As it was shown in Figure 7.1, the diameter of the fibers is in micron scale, so it can not represent the CNC rods in the cake. Both CMC and CNC help indirectly to form such fibrous structures by aggregating the bentonite platelets.

The following conclusions could be drawn from this research:

- The mechanisms involved in dynamic filtration of CNC-dosed bentonite drilling fluids. Pore plugging due to the rapid invasion of particles into filter medium pores was confirmed to be the governing and controlling mechanism followed by gradual filter cake formation on the inner surface of the filter. This objective was achieved by plotting inverse of filtration rates versus a) total volume loss, and b) time. Plotting inverse of filtration rate versus time resulted in linear relationship confirming the standard blocking law or pore plugging mechanism. The initial particle penetration under a shear force into the porous filter medium greatly influences the final deposition of the filter cake formed on the surface of the medium.
- CNC was confirmed to be a fluid-loss material in this study. First of all, its unique characteristics such as rod shape, nano-size dimensions, high dispersion in water medium, and low environment contamination along with its depletion and flocculation capacity made it an interesting topic to investigate. In addition, dynamic filtration and rheological experiments carried out on CNC-dosed drilling fluids demonstrated high viscosity modifying and fluid-loss capacity of CNC. The filtration results in this research were compared with other similar results with different fluid loss nanoparticle additives. CNC improved the total volume loss by approximately 60% and was comparable with other nanoparticles. In addition, this accomplishment was achieved under dynamic conditions, while the other nanoparticles were tested under static filtration conditions. Synergistic effect of CNC made it an appropriate replacement for other nanoparticles already used as fluid loss additives.
- “Why CNC was effective” was answered by investigation of the involved interactions between particles and model surface. DLVO interactions including van der Waals attraction and electrical double layer repulsion forces were calculated for particle – surface systems. The magnitude of these interactions for bentonite particle – silica surface and bentonite and CNC particles – silica surface were quantified. Deposition of bentonite particles were associated with these DLVO interactions between particles and silica model surface. However, the synergistic impact of CNC on the deposition of

bentonite particles was attributed to a non-DLVO interaction called depletion interaction induced by rod-like CNC particles.

- Finally, SEM images revealed a fibrous structure in the dynamic filtration dried filter cakes. Some elemental analyses were carried out on the dried filter cake samples using EDX and ICP. They confirmed the presence of bundles of sepiolite fibers in the cake. Also, shear stress exerting on these aggregates due to the shaft rotation can be considered as the second possibility to form fibrous structure out of previously aggregated flocs [108]. The sepiolite unique structure is very sensitive to applied mechanical processes.

This research opens a new point of view to the applications of cellulose nanocrystals. This work is an initiative to use CNC particles in CMC-dosed bentonite-base drilling fluids. In this research, an attempt was made to understand and investigate the mechanisms involved in dynamic filtration of CNC-dosed drilling muds in order to minimize the risk of fluid loss and prevent formation damage in drilling operations. It shows the considerable effect of CNC particles compared to other nanoparticles to enhance filtration and rheological properties of bentonite drilling fluids. It also explains the scientific concept behind the synergistic effect of CNC rod-like particles by quantifying and analyzing the microscopic interactions between CNC, CMC and bentonite clay particles. CNC can potentially be used in drilling fluids formulation as fluid loss and viscosity modifier material. It is biodegradable, smart, and environment-friendly material that can be utilized in several applications including drilling fluids technology.

However, more comprehensive investigation is necessary to confirm the findings that were out of the scope of this study. For example, the presence of sepiolite mineral in Wyoming clay can be further investigated by X-Ray image analysis on bentonite suspension samples without any additives. Moreover, the synergistic effect due to the addition of CNC to the bentonite suspensions can be analyzed in more details. In conclusion, the following recommendations are listed below for future studies:

- Permeability analysis for filter cakes collected from dynamic filtration experiments,
- Porosity measurements on different filter cores used in dynamic filtration apparatus,

- Dynamic filtration tests under elevated temperatures and pressures for more realistic wellbore conditions,
- Rheological measurements at high temperature, high pressure conditions to better evaluate the performance of drilling muds additives,
- Colloidal deposition tests for tertiary suspensions including bentonite, CMC, and CNC,
- More characterization tests on the drilling fluids suspension before and after filtration tests, and
- Cost analysis on the feasibility of CNC usage in large-scale industry level operations.

In summary, this research was based on the hypothesis of “CNC as an effective fluid loss additive in cross-flow filtration”. Different experimental procedures and methodologies were carried out in order to confirm or reject it. Dynamic filtration, rheological experiments (viscosity behaviour vs. shear rate), and colloidal particles deposition experiments were considered to check the hypothesis. They confirmed the effectiveness and workability of CNC in drilling fluids formulation to control fluid loss issue. However, there is still so much work to do in this journey.

## References

- [1] R. Caenn, H. C. H. Darley and G. R. Gray, *Composition and Properties of Drilling and Completion Fluids*. USA: Elsevier, 2011.
- [2] IHS Global, "Trends in U.S. oil and natural gas upstream costs," The US Energy Information Administration, Washington, DC, March. 2016.
- [3] N.L. Fischer Supervision & Engineering Ltd., "PSAC 2015 well cost study," Petroleum Services Association of Canada (PSAC), Calgary, AB, April. 2015.
- [4] M. Zakaria, M. M. Husein and G. Harland, "Novel Nanoparticle-Based Drilling Fluid with Improved Characteristics," /1/1/, 2012.
- [5] A. G. Iscan and M. V. Kok, "Effects of Polymers and CMC Concentration on Rheological and Fluid Loss Parameters of Water-Based Drilling Fluids," *Energy Sources, Part A: Recovery, Utilization, and Environmental Effects*, vol. 29, pp. 939-949, 05/31; 2014/02, 2007.
- [6] J. Walker, J. J. Miller, K. Burrows, T. Mander and J. Hovan, "Nonaqueous, Salt-Free Drilling Fluid Delivers Excellent Drilling Performance with a Smaller Environmental Footprint," /3/1/, 2016.
- [7] R. F. Krueger, "Evaluation of Drilling-Fluid Filter-Loss Additives Under Dynamic Conditions," /1/1/, 1963.
- [8] D. V. Kosynkin, G. Ceriotti, K. C. Wilson, J. R. Lomeda, J. T. Scorsone, A. D. Patel, J. E. Friedheim and J. M. Tour, "Graphene Oxide as a High-Performance Fluid-Loss-Control Additive in Water-Based Drilling Fluids," *ACS Appl. Mater. Interfaces*, vol. 4, pp. 222-227, 01/25, 2012.
- [9] B. Fazelabdolabadi, A. A. Khodadadi and M. Sedaghatzadeh, "Thermal and rheological properties improvement of drilling fluids using functionalized carbon nanotubes," *Applied Nanoscience*, vol. 5, pp. 651-659, 2015.
- [10] H. Mao, Z. Qiu, Z. Shen, W. Huang, H. Zhong and W. Dai, "Novel hydrophobic associated polymer based nano-silica composite with core-shell structure for intelligent drilling fluid under ultra-high temperature and ultra-high pressure," *Progress in Natural Science: Materials International*, vol. 25, pp. 90-93, 2, 2015.
- [11] G. Cheraghian, M. Hemmati, M. Masihi and S. Bazgir, "An experimental investigation of the enhanced oil recovery and improved performance of drilling fluids using titanium dioxide and fumed silica nanoparticles," *Journal of Nanostructure in Chemistry*, vol. 3, pp. 1-9, 2013.

- [12] J. K. M. William, S. Ponmani, R. Samuel, R. Nagarajan and J. S. Sangwai, "Effect of CuO and ZnO nanofluids in xanthan gum on thermal, electrical and high pressure rheology of water-based drilling fluids," *Journal of Petroleum Science and Engineering*, vol. 117, pp. 15-27, 5, 2014.
- [13] Y. Boluk, L. Zhao and V. Incani, "Dispersions of nanocrystalline cellulose in aqueous polymer solutions: structure formation of colloidal rods," *Langmuir*, vol. 28, pp. 6114-6123, 2012.
- [14] A. Lu, Y. Wang and Y. Boluk, "Investigation of the scaling law on gelation of oppositely charged nanocrystalline cellulose and polyelectrolyte," *Carbohydr. Polym.*, vol. 105, pp. 214-221, 5/25, 2014.
- [15] H. Oguzlu, C. Danumah and Y. Boluk, "The role of dilute and semi-dilute cellulose nanocrystal (CNC) suspensions on the rheology of carboxymethyl cellulose (CMC) solutions," *The Canadian Journal of Chemical Engineering*, vol. 94, pp. 1841-1847, 2016.
- [16] X. Sun, C. Danumah, Y. Liu and Y. Boluk, "Flocculation of bacteria by depletion interactions due to rod-shaped cellulose nanocrystals," *Chem. Eng. J.*, vol. 198–199, pp. 476-481, 8/1, 2012.
- [17] X. Sun, Q. Lu, Y. Boluk and Y. Liu, "The impact of cellulose nanocrystals on the aggregation and initial adhesion of *Pseudomonas fluorescens* bacteria," *Soft Matter*, vol. 10, pp. 8923-8931, 2014.
- [18] M. Dolz, J. Jiménez, M. J. Hernández, J. Delegido and A. Casanovas, "Flow and thixotropy of non-contaminating oil drilling fluids formulated with bentonite and sodium carboxymethyl cellulose," *Journal of Petroleum Science and Engineering*, vol. 57, pp. 294-302, 6, 2007.
- [19] O. U. Nwosu and C. M. Ewulonu, "Rheological Behaviour of Eco-friendly Drilling Fluids from Biopolymers," *Journal of Polymer and Biopolymer Physics Chemistry*, vol. 2, pp. 50-54, 08/28; 2014/08, 2014.
- [20] A. E. Osgouei, M. H. Ozyurtkan and G. Altun, "Dynamic Filtration Properties of Fresh Water Sepiolite-based Muds," *Energy Sources, Part A: Recovery, Utilization, and Environmental Effects*, vol. 36, pp. 2079-2086, 10/02, 2014.
- [21] M. Li, Q. Wu, K. Song, C. F. De Hoop, S. Lee, Y. Qing and Y. Wu, "Cellulose Nanocrystals and Polyanionic Cellulose as Additives in Bentonite Water-Based Drilling Fluids: Rheological Modeling and Filtration Mechanisms," *Ind Eng Chem Res*, vol. 55, pp. 133-143, 01/13, 2016.
- [22] D. W. Green and R. H. Perry, "Liquid-solid operations and equipment," in *Perry's Chemical Engineers' Handbook*, 8th ed. Anonymous McGraw-Hill: New York, Chicago, San

Francisco, Lisbon, London, Madrid, Mexico City, Milan, New Delhi, San Juan, Seoul, Singapore, Sydney, Toronto, 2008, .

[23] C. Tien, *Introduction to Cake Filtration: analyses, Experiments and Applications*. Amsterdam, Boston: Elsevier, 2006.

[24] C. Tien, *Principles of Filtration*. Great Britain: Elsevier, 2012.

[25] Don W. Green and Robert H. Perry, "Liquid-solid operations and equipment," in *Perry's Chemical Engineers' Handbook, Eighth Edition*, Eighth ed. Anonymous McGraw-Hill: New York, Chicago, San Francisco, Lisbon, London, Madrid, Mexico City, Milan, New Delhi, San Juan, Seoul, Singapore, Sydney, Toronto, 2008, .

[26] J. V. Fisk, S. S. Shaffer and S. Helmy, "The Use of Filtration Theory in Developing a Mechanism for Filter-Cake Deposition by Drilling Fluids in Laminar Flow," *SPE Drilling Engineering*, September, 1991.

[27] J. H. Masliyah and S. Bhattacharjee, *Electrokinetic and Colloid Transport Phenomena*. John Wiley & Sons Inc., 2005.

[28] Z. Adamczyk, B. Senger, J. -. Voegel and P. Schaaf. Irreversible adsorption/deposition kinetics: A generalized approach. *J. Chem. Phys.* 110(6), pp. 3118-3128. 1999. . DOI: <http://dx.doi.org/10.1063/1.477908>.

[29] L. Song, "Flux decline in crossflow microfiltration and ultrafiltration: mechanisms and modeling of membrane fouling," *J. Membr. Sci.*, vol. 139, pp. 183-200, /2/18/, 1998.

[30] L. Song and M. Elimelech, "Theory of concentration polarization in crossflow filtration," *J. Chem. Soc. {,} Faraday Trans.*, vol. 91, pp. 3389-3398, 1995.

[31] P. E. Clark, "Analysis of fluid loss data II: Models for dynamic fluid loss," *Journal of Petroleum Science and Engineering*, vol. 70, pp. 191-197, 2010.

[32] J. Y. Park, C. K. Choi and J. J. Kim, "A study on dynamic separation of silica slurry using a rotating membrane filter 1. Experiments and filtrate fluxes," *J. Membr. Sci.*, vol. 97, pp. 263-273, 12/27, 1994.

[33] J. Lieberherr, "Hydrodynamics of the annular gap flow between permeable cylinder walls," *Escher Wyss New*, vol. 2, pp. 24-30, 1979.

[34] K. H. Kroner and V. Nissinen, "Dynamic filtration of microbial suspensions using an axially rotating filter," *J. Membr. Sci.*, vol. 36, pp. 85-100, 1988.

[35] N. Tufenkji and M. Elimelech, "Correlation equation for predicting single-collector efficiency in physicochemical filtration in saturated porous media," *Environ. Sci. Technol.*, vol. 38, pp. 529-536, 2004.

- [36] T. Ozgumus, M. Mobedi and U. Ozkol, "Determination of Kozeny Constant Based on Porosity and Pore to Throat Size Ratio in Porous Medium with Rectangular Rods," *Engineering Applications of Computational Fluid Mechanics*, vol. 8, pp. 308-318, 01/01; 2015/09, 2014.
- [37] D. Tiab and E. C. Donaldson, "Chapter 3 - porosity and permeability," in *Petrophysics (Fourth Edition)*, D. Tiab and E. C. Donaldson, Eds. Boston: Gulf Professional Publishing, 2016, pp. 67-186.
- [38] J. L. Duda, S. Hong and E. E. Klaus, "Flow of polymer solutions in porous media: inadequacy of the capillary model," *Ind. Eng. Chem. Fund.*, pp. 299, .
- [39] R. E. Sheffield and A. B. Metzner, "Flows of nonlinear fluids through porous media," *AIChE J.*, vol. 22, pp. 736-744, 1976.
- [40] J. M. Gonzalez, A. J. Muller, M. F. Torres and Saez. A.E., "The role of shear and elongation in the flow of solutions of semi-flexible polymers through porous media," vol. 44, pp. 396-405, 2005.
- [41] P. F. Luckham and S. Rossi, "The colloidal and rheological properties of bentonite suspensions," *Adv. Colloid Interface Sci.*, vol. 82, pp. 43-92, 10/1, 1999.
- [42] H. van Olphen. Internal mutual flocculation in clay suspensions. *J. Colloid Sci.* 19(4), pp. 313-322. 1964. . DOI: [http://dx.doi.org/10.1016/0095-8522\(64\)90033-9](http://dx.doi.org/10.1016/0095-8522(64)90033-9).
- [43] R. K. Khandal and T. F. Tadros, "Application of viscoelastic measurements to the investigation of the swelling of sodium montmorillonite suspensions," *J. Colloid Interface Sci.*, vol. 125, pp. 122-128, 9, 1988.
- [44] S. Rossi, P. Luckham and T. F. Tadros, "Influence of non-ionic polymers on the rheological behaviour of Na<sup>+</sup>-montmorillonite clay suspensions—I Nonylphenol–polypropylene oxide–polyethylene oxide copolymers," *Colloids Surf. Physicochem. Eng. Aspects*, vol. 201, pp. 85-100, 2002.
- [45] K. Benyounes, A. Mellak and A. Benchabane, "The Effect of Carboxymethylcellulose and Xanthan on the Rheology of Bentonite Suspensions," *Energy Sources, Part A: Recovery, Utilization, and Environmental Effects*, vol. 32, pp. 1634-1643, 07/09; 2015/09, 2010.
- [46] A. Benchabane and K. Bekkour, "Rheological properties of carboxymethyl cellulose (CMC) solutions," *Colloid Polym. Sci.*, vol. 286, pp. 1173-1180, 09/01, 2008.
- [47] A. Benchabane and K. Bekkour, "Effects of anionic additives on the rheological behavior of aqueous calcium montmorillonite suspensions," *Rheologica Acta*, vol. 45, pp. 425-434, 04/01, 2006.

- [48] E. İ̇sci and S. İ̇ Turutođlu, "Stabilization of the mixture of bentonite and sepiolite as a water based drilling fluid," *Journal of Petroleum Science and Engineering*, vol. 76, pp. 1-5, 2011.
- [49] S. Beck-Candanedo, M. Roman and D. G. Gray, "Effect of Reaction Conditions on the Properties and Behavior of Wood Cellulose Nanocrystal Suspensions," *Biomacromolecules*, vol. 6, pp. 1048-1054, 03/01, 2005.
- [50] X. M. DONG, J. REVOL and D. G. GRAY, "Effect of microcrystallite preparation conditions on the formation of colloid crystals of cellulose," *Cellulose*, vol. 5, pp. 19-32, 1998.
- [51] W. Y. Hamad and T. Q. Hu, "Structure–process–yield interrelations in nanocrystalline cellulose extraction," *The Canadian Journal of Chemical Engineering*, vol. 88, pp. 392-402, 2010.
- [52] Y. Habibi, L. A. Lucia and O. J. Rojas, "Cellulose Nanocrystals: Chemistry, Self-Assembly, and Applications," *Chem. Rev.*, vol. 110, pp. 3479-3500, 06/09, 2010.
- [53] Y. Boluk, R. Lahiji, L. Zhao and M. T. McDermott, "Suspension viscosities and shape parameter of cellulose nanocrystals (CNC)," *Colloids Surf. Physicochem. Eng. Aspects*, vol. 377, pp. 297-303, 3/5, 2011.
- [54] S. Shafiei-Sabet, W. Y. Hamad and S. G. Hatzikiriakos, "Rheology of Nanocrystalline Cellulose Aqueous Suspensions," *Langmuir*, vol. 28, pp. 17124-17133, 12/11, 2012.
- [55] A. Lu, U. Hemraz, Z. Khalili and Y. Boluk, "Unique viscoelastic behaviors of colloidal nanocrystalline cellulose aqueous suspensions," *Cellulose*, vol. 21, pp. 1239-1250, 2014.
- [56] M. H. Ozyurtkan, G. Altun, A. Etehadı Osgouei and E. Aydilsiz, "Dynamic filtration properties of clay based drilling muds under elevated temperatures," in *2012 SPE Kuwait International Petroleum Conference and Exhibition, 2012*, .
- [57] A. L. J. Olsson, I. R. Quevedo, D. He, M. Basnet and N. Tufenkji, "Using the Quartz Crystal Microbalance with Dissipation Monitoring to Evaluate the Size of Nanoparticles Deposited on Surfaces," *ACS Nano*, vol. 7, pp. 7833-7843, 09/24; 2014/02, 2013.
- [58] M. Elimelech, "Particle deposition on ideal collectors from dilute flowing suspensions: Mathematical formulation, numerical solution, and simulations," *Separations Technology*, vol. 4, pp. 186-212, 10, 1994.
- [59] T. NypelÄ¶, H. PynnÄ¶nen, M. Ä¶sterberg, J. Paltakari and J. Laine, "Interactions between inorganic nanoparticles and cellulose nanofibrils," *Cellulose*, vol. 19, pp. 779-792, 2012.

- [60] M. Suchy, M. B. Linder, T. Tammelin, J. M. Campbell, T. Vuorinen and E. Kontturi, "Quantitative Assessment of the Enzymatic Degradation of Amorphous Cellulose by Using a Quartz Crystal Microbalance with Dissipation Monitoring," *Langmuir*, vol. 27, pp. 8819-8828, 07/19, 2011.
- [61] J. Fatisson, R. F. Domingos, K. J. Wilkinson and N. Tufenkji, "Deposition of TiO<sub>2</sub> Nanoparticles onto Silica Measured Using a Quartz Crystal Microbalance with Dissipation Monitoring," *Langmuir*, vol. 25, pp. 6062-6069, 06/02, 2009.
- [62] V. Incani, C. Danumah and Y. Boluk, "Nanocomposites of nanocrystalline cellulose for enzyme immobilization," *Cellulose*, vol. 20, pp. 191-200, 02/01, 2013.
- [63] M. M., *An Introduction to Marine Drilling*. Dayton's, 1987.
- [64] M. R. Rojas, A. J. Müller and A. E. Sáez, "Shear rheology and porous media flow of wormlike micelle solutions formed by mixtures of surfactants of opposite charge," *J. Colloid Interface Sci.*, vol. 326, pp. 221-226, 10/1, 2008.
- [65] D. Jiao and M. Sharma, "Formation damage due to static and dynamic filtration of water-based muds," in *SPE Formation Damage Control Symposium*, 1992, .
- [66] J. McGowen and S. Vitthal, "Fracturing-fluid leakoff under dynamic conditions part 1: Development of a realistic laboratory testing procedure," in *SPE Annual Technical Conference and Exhibition*, 1996, .
- [67] E. Fischer and J. Raasch, "Model tests of the particle deposition at the filter medium in cross-flow filtration," in *Proc. 4th World Filtration Congress*, 1986, pp. 11.11-11.17.
- [68] M. M. Husein, M. F. ZAKARIA and G. Hareland, "Novel nanoparticle-containing drilling fluids to mitigate fluid loss," 01/14, 2016.
- [69] M. Bercea and P. Navard, "Shear Dynamics of Aqueous Suspensions of Cellulose Whiskers," *Macromolecules*, vol. 33, pp. 6011-6016, 08/01, 2000.
- [70] E. E. Ureña-Benavides, G. Ao, V. A. Davis and C. L. Kitchens, "Rheology and Phase Behavior of Lyotropic Cellulose Nanocrystal Suspensions," *Macromolecules*, vol. 44, pp. 8990-8998, 11/22, 2011.
- [71] S. Shafeiei-Sabet, W. Y. Hamad and S. G. Hatzikiriakos, "Influence of degree of sulfation on the rheology of cellulose nanocrystal suspensions," *Rheologica Acta*, vol. 52, pp. 741-751, 2013.
- [72] M. T. Ghannam and M. N. Esmail, "Rheological properties of carboxymethyl cellulose," *J Appl Polym Sci*, vol. 64, pp. 289-301, 1997.

- [73] M. Edali, M. N. Esmail and G. H. Vatistas, "Rheological properties of high concentrations of carboxymethyl cellulose solutions," *J Appl Polym Sci*, vol. 79, pp. 1787-1801, 2001.
- [74] W. Kulicke, A. H. Kull, W. Kull, H. Thielking, J. Engelhardt and J. Pannek, "Characterization of aqueous carboxymethylcellulose solutions in terms of their molecular structure and its influence on rheological behaviour," *Polymer*, vol. 37, pp. 2723-2731, 6, 1996.
- [75] C. Clasen and W. -. Kulicke, "Determination of viscoelastic and rheo-optical material functions of water-soluble cellulose derivatives," *Progress in Polymer Science*, vol. 26, pp. 1839-1919, 11, 2001.
- [76] M. Guaita, O. Chiantore, A. Munari, P. Manaresi, F. Pilati and M. Toselli. A general intrinsic viscosity-molecular weight relationship for linear polydisperse polymers—3. applicability to the evaluation of the mark-houwink-sakurada k and a constants. *European Polymer Journal* 27(4), pp. 385-388. 1991. . DOI: [http://dx.doi.org/10.1016/0014-3057\(91\)90193-R](http://dx.doi.org/10.1016/0014-3057(91)90193-R).
- [77] W. Kulicke, A. H. Kull, W. Kull, H. Thielking, J. Engelhardt and J. Pannek, "Characterization of aqueous carboxymethylcellulose solutions in terms of their molecular structure and its influence on rheological behaviour," *Polymer*, vol. 37, pp. 2723-2731, 6, 1996.
- [78] V. Mahto and V. P. Sharma, "Rheological study of a water based oil well drilling fluid," *Journal of Petroleum Science and Engineering*, vol. 45, pp. 123-128, 11/30, 2004.
- [79] Y. Yan, L. Liang and W. Feng, "Rheological study on natural heteropolysaccharide based drilling fluid," *Journal of Central South University of Technology*, vol. 14, pp. 188-191, 2007.
- [80] Y. Jung, Y. Son, J. Lee, T. X. Phuoc, Y. Soong and M. K. Chyu, "Rheological Behavior of Clay Nanoparticle Hybrid-Added Bentonite Suspensions: Specific Role of Hybrid Additives on the Gelation of Clay-Based Fluids," *ACS Appl. Mater. Interfaces*, vol. 3, pp. 3515-3522, 09/28, 2011.
- [81] J. Wang and P. Somasundaran, "Adsorption and conformation of carboxymethyl cellulose at solid-liquid interfaces using spectroscopic, AFM and allied techniques," *J. Colloid Interface Sci.*, vol. 291, pp. 75-83, 11/1, 2005.
- [82] J. Gregory, "Polymers at interfaces, by G. J. Fleer, M. A. Cohen Stuart, J. M. H. M. Scheutjens, T. Cosgrove and B. Vincent. Chapman and Hall, London, 1993. Pp. xv + 502, price £65.00. ISBN 0-412-58160-4," *Polym. Int.*, vol. 36, pp. 102-102, 1995.

- [83] S. Asakura and F. Oosawa, "Interaction between particles suspended in solutions of macromolecules," vol. 33, pp. 183-192, 1958.
- [84] M. A. C. Stuart, "Adsorbed Polymers in Colloidal Systems: from Statics to Dynamics," *Polym. J.*, vol. 23, pp. 669-682, print, 1991.
- [85] F. Lafuma, K. Wong and B. Cabane. Bridging of colloidal particles through adsorbed polymers. *J. Colloid Interface Sci.* 143(1), pp. 9-21. 1991. . DOI: [http://dx.doi.org/10.1016/0021-9797\(91\)90433-9](http://dx.doi.org/10.1016/0021-9797(91)90433-9).
- [86] V. C. Kelessidis and R. Maglione, "Yield stress of water–bentonite dispersions," *Colloids Surf. Physicochem. Eng. Aspects*, vol. 318, pp. 217-226, 4/1, 2008.
- [87] P. Coussot, A. I. Leonov and J. M. Piau. Rheology of concentrated dispersed systems in a low molecular weight matrix. *J. Non Newtonian Fluid Mech.* 46(2), pp. 179-217. 1993. . DOI: [http://dx.doi.org/10.1016/0377-0257\(93\)85046-D](http://dx.doi.org/10.1016/0377-0257(93)85046-D).
- [88] B. Abu-Jdayil, "Rheology of sodium and calcium bentonite–water dispersions: Effect of electrolytes and aging time," *Int. J. Miner. Process.*, vol. 98, pp. 208-213, 3/9, 2011.
- [89] K. Bekkour, M. Leyama, A. Benchabane and O. Scrivener. Time-dependent rheological behavior of bentonite suspensions: An experimental study. *J. Rheol.* 49(6), pp. 1329-1345. 2005. . DOI: <http://dx.doi.org/10.1122/1.2079267>.
- [90] B. D. Bowen, S. Levine and N. Epstein. Fine particle deposition in laminar flow through parallel-plate and cylindrical channels. *J. Colloid Interface Sci.* 54(3), pp. 375-390. 1976. . DOI: [http://dx.doi.org/10.1016/0021-9797\(76\)90317-9](http://dx.doi.org/10.1016/0021-9797(76)90317-9).
- [91] B. D. Bowen and N. Epstein. Fine particle deposition in smooth parallel-plate channels. *J. Colloid Interface Sci.* 72(1), pp. 81-97. 1979. . DOI: [http://dx.doi.org/10.1016/0021-9797\(79\)90184-X](http://dx.doi.org/10.1016/0021-9797(79)90184-X).
- [92] J. Yang, R. Bos, A. Poortinga, P. J. Wit, G. F. Belder and H. J. Busscher, "Comparison of Particle Deposition in a Parallel Plate and a Stagnation Point Flow Chamber," *Langmuir*, vol. 15, pp. 4671-4677, 06/01, 1999.
- [93] Z. Adamczyk and T. Van de Ven, "Deposition of particles under external forces in laminar flow through parallel-plate and cylindrical channels," *J. Colloid Interface Sci.*, vol. 80, pp. 340-356, 1981.
- [94] Z. Adamczyk, J. Czarnecki and T. Van De Ven, "Particle transfer to solid surfaces," *Adv. Colloid Interface Sci.*, vol. 19, pp. 183-252, 1983.
- [95] R. Goh, Y. Leong and B. Lehane, "Bentonite slurries' zeta potential, yield stress, adsorbed additive and time-dependent behaviour," *Rheologica Acta*, vol. 50, pp. 29-38, 2011.

- [96] S. VARENNES and T. VANDEVEN, "Deposition and Detachment of Latex-Particles at Glass Surfaces Exposed to Flow," *Physicochemical Hydrodynamics*, vol. 9, pp. 537-559, 1987.
- [97] P. Weroński, J. Y. Walz and M. Elimelech, "Effect of depletion interactions on transport of colloidal particles in porous media," *J. Colloid Interface Sci.*, vol. 262, pp. 372-383, 2003.
- [98] D. Grasso\*, K. Subramaniam, M. Butkus, K. Strevett and J. Bergendahl, "A review of non-DLVO interactions in environmental colloidal systems," *Reviews in Environmental Science and Biotechnology*, vol. 1, pp. 17-38, 2002.
- [99] E. D. Cranston, D. G. Gray and M. W. Rutland, "Direct Surface Force Measurements of Polyelectrolyte Multilayer Films Containing Nanocrystalline Cellulose," *Langmuir*, vol. 26, pp. 17190-17197, 11/16, 2010.
- [100] M. Elimelech, "Kinetics of capture of colloidal particles in packed beds under attractive double layer interactions," *J. Colloid Interface Sci.*, vol. 146, pp. 337-352, 1991.
- [101] Z. Adamczyk, B. Siwek, M. Zembala and P. Warszyński. Enhanced deposition of particles under attractive double-layer forces. *J. Colloid Interface Sci.* 130(2), pp. 578-587. 1989. . DOI: [http://dx.doi.org/10.1016/0021-9797\(89\)90133-1](http://dx.doi.org/10.1016/0021-9797(89)90133-1).
- [102] S. Varennes and T. G. M. Van De Ven. Effects of polyelectrolyte on the deposition and detachment of colloidal particles subjected to flow. *Colloids and Surfaces* 33pp. 63-74. 1988. . DOI: [http://dx.doi.org/10.1016/0166-6622\(88\)80049-0](http://dx.doi.org/10.1016/0166-6622(88)80049-0).
- [103] M. Boluk and T. Van de Ven, "Effects of polyelectrolytes on flow-induced deposition of titanium dioxide particles onto a cellophane surface," *Colloids and Surfaces*, vol. 46, pp. 157-176, 1990.
- [104] T. Dabro and d. V. van, "A direct method for studying particle deposition onto solid surfaces," *Colloid Polym. Sci.*, vol. 261, pp. 694-707, 1983.
- [105] L. L. Carney and R. L. Meyer, "A New Approach to High Temperature Drilling Fields," /1/1/, 1976.
- [106] S. K. Kawatra and S. J. Ripke, "Developing and understanding the bentonite fiber bonding mechanism," *Minerals Eng.*, vol. 14, pp. 647-659, 6, 2001.
- [107] S. Yoon and Y. Deng, "Flocculation and reflocculation of clay suspension by different polymer systems under turbulent conditions," *J. Colloid Interface Sci.*, vol. 278, pp. 139-145, 10/1, 2004.
- [108] M. F. Can, M. Çınar, B. Benli, O. Özdemir and M. S. Çelik, "Determining the fiber size of nano structured sepiolite using Atomic Force Microscopy (AFM)," *Appl. Clay. Sci.*, vol. 47, pp. 217-222, 2, 2010.

## Appendix A: Cross-flow and porous media calculations

### Cross-flow calculations in concentric cylinders geometry

Here, Taylor number calculations will be presented in detail. Equations [2.11] to [2.15] will be used in order to calculate the Taylor number for the experimental set-up and a practical example for comparison purpose.

#### Taylor number for experimental data (FANN90 device)

Calculations are done using specifications in Table 4.1. Angular velocity,  $\omega$ , is calculated at shear rates = 10 and 100  $s^{-1}$ .

$$\omega = \frac{\dot{\gamma}}{c} = \begin{cases} 3.13 s^{-1} & , for \dot{\gamma} = 10 s^{-1} \\ 31.35 s^{-1} & , for \dot{\gamma} = 100 s^{-1} \end{cases} \quad [A.1]$$

Kinematic viscosities are available from Figure 5.17 and assuming the mud density of 2300  $kg/m^3$ .

$$\nu = \frac{\mu}{\rho} = \begin{cases} 4.2 \times 10^{-4} \frac{m^2}{s} & , for \dot{\gamma} = 10 s^{-1} \\ 7.8 \times 10^{-5} \frac{m^2}{s} & , for \dot{\gamma} = 100 s^{-1} \end{cases} \quad [A.2]$$

Taylor numbers at  $\dot{\gamma} = 10 s^{-1}$  and  $\dot{\gamma} = 100 s^{-1}$  are calculated as 0.13 and 7.05, respectively.

#### Taylor number for industrial data (Example)

Calculations are done using specifications in Table 4.2. The same procedure is followed for Taylor number calculations. The shear rate ranges from 50 – 100 RPM (0.83 – 1.67  $s^{-1}$ ). Working in low shear rate region results in larger kinematic viscosities than the experimental ones.

$$\omega = \frac{\dot{\gamma}}{c} = \begin{cases} 0.15 s^{-1} & , for \dot{\gamma} = 0.83 s^{-1} \\ 0.31 s^{-1} & , for \dot{\gamma} = 1.67 s^{-1} \end{cases} \quad [A.3]$$

$$v = \frac{\mu}{\rho} = \begin{cases} 4.8 \times 10^{-3} \frac{m^2}{s} & , for \dot{\gamma} = 0.83 s^{-1} \\ 2.4 \times 10^{-3} \frac{m^2}{s} & , for \dot{\gamma} = 1.67 s^{-1} \end{cases} \quad [A. 4]$$

Taylor numbers at  $\dot{\gamma} = 0.83 s^{-1}$  and  $\dot{\gamma} = 1.67 s^{-1}$  are calculated 0.38 and 1.59, respectively.

## Porous media calculations

Here, porosity and flow velocity calculations in porous media will be presented. In Afterwards, pressure drop ( $\Delta P/L$ ) comparison in porous media with polymer flow will be done for bentonite – CMC (B-C) and bentonite – CMC – CNC (B-C-C) mud formulations.

Equations [2.49] – [2.51], [4.1] – [4.3], and Table 4.3 were used for the following calculations.

According to Table 4.3, filter surface area is calculated from:

$$A = \pi . d . L = \pi \times 1.014 \times 1.114 = 3.55 \text{ in}^2 = 0.0023 \text{ m}^2 \quad [A. 5]$$

Mean velocities for (B-C) and (B-C-C) are:

$$\bar{V}_{m,B-C} = 0.3 \frac{ml}{min} \times 1 \frac{min}{60 s} \times 1 \frac{m^3}{10^6 ml} \times \frac{1}{0.0023 m^2} = 2.17 \times 10^{-6} \frac{m}{s} \quad [A. 6]$$

$$\bar{V}_{m,B-C-C} = 0.25 \frac{ml}{min} \times 1 \frac{min}{60 s} \times 1 \frac{m^3}{10^6 ml} \times \frac{1}{0.0023 m^2} = 1.8 \times 10^{-6} \frac{m}{s} \quad [A. 7]$$

Corresponding Re numbers at  $\dot{\gamma} = 100 s^{-1}$  are as follows:

$$Re_{B-C} = \frac{2.17 \times 10^{-6} \frac{m}{s} \times 35 \times 10^{-6} m \times 2300 \frac{kg}{m^3}}{0.089 \frac{kg}{m.s}} = 1.96 \times 10^{-6} \quad [A. 8]$$

$$Re_{B-C-C} = \frac{1.8 \times 10^{-6} \frac{m}{s} \times 35 \times 10^{-6} m \times 2300 \frac{kg}{m^3}}{0.18 \frac{kg}{m.s}} = 8.05 \times 10^{-7} \quad [A. 9]$$

$$\frac{Re_{B-C}}{Re_{B-C-C}} = \frac{1.96 \times 10^{-6}}{8.05 \times 10^{-7}} = 2.4 \quad [A. 10]$$

In conclusion, higher Re number is expected when no CNC was added to the mud suspension or CNC addition increased the viscosity of the mud suspension.

Pressure drop comparison between muds including CMC (B-C) and CMC/CNC (B-C-C) are carried out at  $Re = 0.1$  using the following equations:

$$\frac{\Lambda_{B-C}}{\Lambda_W} = \frac{\mu_{B-C}}{\mu_W} \xrightarrow{\text{yields}} \frac{\Lambda_{B-C}}{200} = \frac{0.14}{0.001} = 28 \times 10^3 \quad [A. 11]$$

$$\frac{\Lambda_{B-C-C}}{\Lambda_W} = \frac{\mu_{B-C-C}}{\mu_W} \xrightarrow{\text{yields}} \frac{\Lambda_{B-C-C}}{200} = \frac{0.37}{0.001} = 74 \times 10^3 \quad [A. 12]$$

$$\frac{\Lambda_{B-C}}{\Lambda_{B-C-C}} = \frac{(\Delta P/L)_{B-C}}{(\Delta P/L)_{B-C-C}} = \frac{28 \times 10^3}{74 \times 10^3} = 0.38 \quad [A. 13]$$

It shows the fact that more pressure drop is expected to observe while CNC particles are added to the B-C suspension.

## Appendix B: CMC characterization via intrinsic viscosity

In this Appendix, molecular weight of the CMC polymer used in the experiments will be calculated in details via intrinsic viscosity method. Equations [5.2] – [5.5] will be used.

Table below illustrates all the calculations required to find intrinsic viscosity (y-intercept) from the graph of reduced viscosity versus concentration.

C (g/ml)	$\eta_0$ (zero-shear viscosity) (Pa.s)	$\eta_{rel}$	$\eta_{sp}$	$\eta_r$
0.001	$8.50 \times 10^{-3}$	9.55	8.55	$8.55 \times 10^3$
0.002	0.024	27.0	26.0	$1.30 \times 10^4$
0.003	0.050	56.2	55.2	$1.84 \times 10^4$
0.004	0.113	127	126	$3.15 \times 10^4$
0.005	0.200	225	224	$4.47 \times 10^4$
0.006	0.250	281	280	$4.66 \times 10^4$

C represents the concentration of CMC solutions, and  $K_H = 0.281$ ,  $B_n = 4.80 \times 10^{-4}$ , and  $n = 4.34$  are constants for CMC in 0.01 M NaCl solution at  $T = 298$  K. Using linear regression, intrinsic viscosity and the consequent molecular weight of the CMC polymer were calculated as  $3466.3 \text{ cm}^3/\text{g}$  and 961 K, respectively.

## Appendix C: Sensor surface coverage calculations

In this Appendix, the surface area of the sensor covered by nanoparticles is calculated for different sensor conditions. The surface coverage values are estimated for uncoated and coated silica sensor. Both bentonite and CNC particles are assumed to be spherical for the simplicity of the calculations. Their approximate radii are  $10^{-6}$  and  $10^{-7}$  m, respectively.

Volume of one bentonite and one CNC particle can be calculated as:

$$V = \frac{4}{3}\pi r^3 \xrightarrow{\text{yields}} \begin{cases} V_B = 4.19 \times 10^{-12} \text{ cm}^3 \\ V_C = 4.19 \times 10^{-15} \text{ cm}^3 \end{cases} \quad [C.1]$$

Surface area of one bentonite and one CNC particles can also be calculated as:

$$A = 4\pi r^2 \xrightarrow{\text{yields}} \begin{cases} A_B = 1.26 \times 10^{-7} \text{ cm}^2 \\ A_C = 1.26 \times 10^{-9} \text{ cm}^2 \end{cases} \quad [C.2]$$

Sensor surface area is reported as  $0.2 \text{ cm}^2$ .

### Uncoated silica surface and bentonite particles coverage

As shown in Figure 6.6, the maximum mass deposited for bentonite particles is  $100 \text{ ng/cm}^2$ . Therefore, the maximum amount deposited on the sensor will be  $20 \text{ ng}$ . Using the following equation, the number of deposited bentonite particles will be about 2076.

$$m_p = \rho_p \times V_p \times \#_p \xrightarrow{\text{yields}} 20 \times 10^{-9} \text{ g} = 2.3 \frac{\text{g}}{\text{cm}^3} \times 4.19 \times 10^{-12} \text{ cm}^3 \times \# \quad [C.3]$$

$$\text{Surface coverage}(\%) = \frac{\text{Area of deposited particles}}{\text{Area of sensor}} = \frac{2076 \times 1.26 \times 10^{-7} \text{ cm}^2}{0.2 \text{ cm}^2} = 0.13\%$$

### Uncoated silica surface and bentonite + CNC particles coverage

As illustrated in Figure 6.6, the maximum mass deposited for bentonite + CNC particles is about  $10^4 \text{ ng/cm}^2$ , which will be  $2000 \text{ ng}$  on the sensor. Equation [C.3] may be applied to calculate the number of particles deposited on the sensor. Assuming the density and volume values of bentonite (larger particles), the number of deposited particles is 207583.

Therefore,

$$\text{Surface coverage(\%)} = \frac{\text{Area of deposited particles}}{\text{Area of sensor}} = \frac{207583 \times 1.26 \times 10^{-7} \text{ cm}^2}{0.2 \text{ cm}^2} = 13.0\%$$

### **Coated silica surface and bentonite particles coverage**

As shown in Figure 6.9, the maximum mass deposited for bentonite particles is 2250 ng/cm<sup>2</sup>. Using Equation [C.3], the number of deposited bentonite particles is 46706.

Therefore,

$$\text{Surface coverage(\%)} = \frac{\text{Area of deposited particles}}{\text{Area of sensor}} = \frac{46706 \times 1.26 \times 10^{-7} \text{ cm}^2}{0.2 \text{ cm}^2} = 2.9\%$$

### **Coated silica surface and CNC particles coverage**

As shown in Figure 6.9, the maximum mass deposited for CNC particles is about 1000 ng/cm<sup>2</sup>. Using Equation [C.3], the number of deposited bentonite particles is  $3.18 \times 10^7$ .

So,

$$\text{Surface coverage(\%)} = \frac{\text{Area of deposited particles}}{\text{Area of sensor}} = \frac{3.18 \times 10^7 \times 1.26 \times 10^{-9} \text{ cm}^2}{0.2 \text{ cm}^2} = 20\%$$

### **Coated silica surface and bentonite + CNC particles coverage**

Finally, the maximum mass deposited for bentonite + CNC particles is about 5000 ng/cm<sup>2</sup>. Using Equation [C.3], the number of deposited bentonite particles is  $1.2 \times 10^5$ .

Hence,

$$\text{Surface coverage(\%)} = \frac{\text{Area of deposited particles}}{\text{Area of sensor}} = \frac{1.2 \times 10^5 \times 1.26 \times 10^{-7} \text{ cm}^2}{0.2 \text{ cm}^2} = 7.9$$